Morphology dependent voltage sensitivity of gold nanostructures

Yu Huang, MSc, BEng

Thesis submitted to the University of Nottingham for the

degree of Doctor of Philosophy

June 2010

Abstract

In this thesis, the sensitivity of a range of plasmonic gold nanostructures to changes in ambient electric potential has been studied using a high quality objective-type dark-field imaging spectrometer, which was capable of measuring the signal from single nanoparticles. Optical response of the nanostructure to the change of physiologically relevant potential has been investigated experimentally and theoretically. Simulations to predict the sensitivity to potential changes were in good qualitative agreement with experimental data.

The similar transients of scattering produced by potential cyclic voltammetry and potential step for gold film and gold nanoprism indicated that the mechanism of potential perturbation on the gold nanostructures was independent of their morphologies. The relationship between the morphologies of the gold nanostructure and their ability for voltage sensing had been investigated in detail. The cost-effective ultrathin gold film provides the highest voltage sensitivity and appears to be extremely promising as the basis for the design of an ultrasensitive plasmonic nanostructure sensor for electrical signals.

Acknowledgments

I would like to sincerely thank my supervisors, Dr Mark Pitter and Professor Mike Somekh for their guidance and support throughout the course of my study. Their patience, encouragement and educational philosophy consolidate my confidence to finish this work.

I would also like to thank Dr Jing Zhang for her essential help and advice with the optics, Mr. Rod Dykeman and Mr. Paul Moss for their technical support and assistance, my colleagues for the extensive idea and knowledge, and my close friends, Bo Fu, Zhongcheng Duan, especially Qing Ye, for their invaluable help and soothing conversation during the course of my study.

Finally, I would like to thank my dearly beloved parents, who constantly give me their generous support and encouragement, not only over these years of my study, but throughout my life.

Contents

Contents

Contents

Chapter 1   Introduction

1.1   Motivation

Noble metal nanoparticles have attracted considerable interest due to their remarkable optical properties, which are dominated by the phenomenon of localised surface plasmon resonance (LSPR). Nanoparticles are capable of confining the interaction of metal conduction band electrons and incident light within extremely small dimensions. The resonant photons dramatically enhance the electromagnetic field at the particle surface and lead to the particle characteristic radiative and nonradiative properties of wavelength dependent photon scattering and absorption [1-3].

The manifestation of localised plasmon resonance is dependent on the particle's size, shape, and composition. Study of the geometry-dependent resonance is encouraged by rapid progress in synthesis strategies developed for the creation of nano-objects. Both 'top-down' lithography and 'bottom-up' self-assembly techniques have provided various kinds of nanoparticle of controlled size, shape and material, from the most simple geometries of nanospheres and nanorods, to silica/gold nanoshells and exotic structures such as nanorices and nanocrescents [4-5]. By tailoring the particles' geometry, their resonant frequency can be tuned across the whole visible and near-infrared spectrum. A powerful attribute of the surface plasmon resonance frequency is

that it is strongly dependent on the dielectric constant of the surrounding environment. For example, increasing the refractive index of the ambient medium shifts the LSPR wavelength towards the red. This provides great opportunities to monitor changes of the environment and renders particles as suitable candidates for chemical and biological sensing applications [6]. The LSPR is dependent on the particle size, shape, the dielectric constant of the metal and the surrounding medium because all of these factors have an effect on the electron density at the particle surface[7] .

Extracellular and intracellular neural recording are the prime techniques to access the neural network in order to try to monitor and understand neural activity. Traditionally, direct electrical access to nerve tissue *in vitro* and *in vivo* is achieved by the patch-clamp method, where sensors ranging from metal wire to micropipettes are inserted directly into the nerve [8-9]. However, simultaneous recording the activities of even a small number of cells over extended periods of time requires a strategic innovation to replace the invasive microelectrode method. To this end, voltage-sensitive fluorescence dyes have been developed as a noninvasive method to optically record the neural signal. Fluorescence probes the change in membrane potential and transduces it as a change in its emission intensity or spectrum. But fluorescent dyes' inherent drawbacks of photobleaching and phototoxicity, severely restrict their applications [10]. The plasmon frequency of noble metal nanostructure is determined by its electron density. An increase in the electron density results in

an increase of the plasmon frequency, and leads to a blue shift of the plasmon band, as demonstrated by either adding chemical reductant [11] or with the aid of an electrode to transfer electrons to particle [12]. The existence of an electron density dependent LSPR response opens a new possible application for metal particles in monitoring the neural activities. The nanosized dimension of the nanoparticles makes them convenient to be incorporated into biological systems, while the intensity of the light scattered by particles can be higher than that emitted by dye molecules which potentially makes them suitable for optical imaging and labeling of biological cells. The wide spectral tunability could allow a choice of incident wavelength to suit the bioapplication. The fluorescent dye bleaching could therefore be eliminated by using photostable metal nanoparticles so that longer probing time becomes possible [7].

The study of nanoparticles directed towards recording cellular activity is encouraged by these advantages. The cellular electrical signal is extremely small and fast. A neural action potential has a maximum amplitude of around 150 mV [13-14], in contrast to most previous studies which used much higher potentials, where the contrast is dramatically increased by chemical activity that does not occur at action potentials [15-16]. A high sensitivity of the plasmon resonance scattering or absorption band in response to the cellular activity is the fundamental factor to determine the success of the sensing. The prime objective of this thesis is to investigate the voltage sensitivity of gold nanocrystals to physiologically relevant voltages of a wide range of

morphologies. The tunable nanostructure geometry not only offers the plasmon resonance tunability, but provides a handle to discover high plasmon sensitivity without reducing the particle volume [6, 10], and hence retaining sufficient signal strength for optical observation.

In order to observe the performance of single Au nanocrystals under potential control, reflected light dark-field illumination was chosen for the optical microscope, as it has been demonstrated as an efficient single particle technique and allows free access to one side of the sample to apply complementary techniques. The magnitude of potential applied on these Au nanostructures was limited to be within their double layer charging region. Therefore, the optical signals recorded here truly reflect pure electron transport to and from the particles without interference from the redox reaction.

A custom objective-type dark-field imaging spectrometer was designed, constructed and used to simultaneously acquire spatial and spectral information from Au nanostructure. Instead of measuring the spectral shift directly, the existence of potential was detected as the alteration of scattering at a carefully optimised single wavelength. The scattering response of Au nanostructure to a series of modulated potentials was measured to quantify the capability of Au nanostructure to sense potential. Time dependent scattering was studied to understand the response time of Au nanostructure to dynamic potential.

The design of the LSPR sensing experiment and the morphology of the Au nanostructure were considered as two possible routes to enhance the Au

nanostructure's sensitivity. Modelling of Au nanostructure's response to potential was also used to investigate the influence of these two factors. The behaviour predicted by the simulations not only improves the understanding of the optical properties of Au nanostructure but also indicates the direction in which to design and develop plasmonic nanoparticle based potential sensors.

1.2   Thesis outline

Extensive research of nanoparticles has been propelled by the need for progress in understanding the nanoparticles' physical properties and their promising potential for sensing applications. The deeper the understanding of the nanoparticles, the better predictions can be made to advance the utility of these plasmonic nanoparticles in monitoring, for example, cellular activity. Chapter 2 presents an overview of the recent and rapid upsurge in the research of nanostructure carried out to purse ultrasensitive plasmonic sensors. Nanoparticles' sensitivity to changes in dielectric and charge transport has been exploited by tuning their morphologies to find the best configuration to enhance the sensitivity, which is supported by the sophisticated nanoparticle synthetic methods.

In chapter 3, size and aggregation effects on the dielectric constant of gold nanostructure, together with the impact of charge transport are described.

Chapter 4 outlines the design and construction of the objective-type

dark-field imaging spectrometer, which is capable of investigating single nanocrystals under potential control. The experimental preparation and procedure for the measurement of Au nanostructures are also described in this chapter.

Chapters 5, 6 and 7 present the optical responses of Au nanostructures to potential. The relationship between their voltage sensitivity and their morphologies is investigated and used to propose rules to select the type of particle and design sensitive LSPR based sensors.

Finally, a summary of the work in this thesis and recommendations for future work are stated in chapter 8.

Chapter 2   Literature review: Optical properties of noble metal subjected to an applied potential

Exploration of the properties of noble metal nanostructure is one of the most exciting contemporary nanosciences. The precious and unique optical properties exhibited by these nanostructures promote the exploitation and applications of noble metal systems. The manipulation of light with noble metals is a utilisation of the phenomenon of surface plasmon resonance (SPR), the coherent oscillation of electrons in the conduction band excited by electromagnetic radiation [7, 17]. Surface plasmon polaritons are generated by coupling of the free electrons with an electromagnetic field near the metal-dielectric interface. They are generated at and propagate along the metal-dielectric interface[18]. However, the electron motion is also dependent on the space accessible for its movement. When bulk noble metal is reduced to the nano-dimensions, the resonant electrons are confined within its small size and a localised surface plasmon oscillation of conduction band electrons is induced, known as localised surface plasmon resonance (LSPR) or particle plasmon resonance [1]. The intense scattering and absorption of light from noble metal nanoparticles is the result of its unique interaction with the incident light.

Due to the extreme sensitivity to the refractive index of the dielectric

medium, surface plasmon resonance has been extensively used as an analytical technology in both chemical and biological sensing. Most of the widely employed optical surface plasmon resonance biosensors are based on surface plasmon polaritons excited on thin metal films. However, the advancement of biotechnology towards nanoscale design and the need for high spatial resolution give rise to new requirements for the development of nano-biosensors. Localised surface plasmon biosensors are expected to match this new trend. Plasmonic metallic nanostructures are capable of being incorporated into biological systems because of their nanometer scale [7]. The shorter EM-field-decay length in the vicinity of the nanoparticle surface, relative to film supported SPR, can provides greater sensitivity to short-range changes in the refractive index due to the molecular adsorption layer [19]. High throughput and label-free analysis in diagnostics are feasible to be implemented simultaneously with LSPR based sensors [20-21]. Moreover, various synthesis techniques have been developed over recent decades in order to manipulate and optimise the nanostructures' functionality. By varying the particle's size, shape and composition, the LSPR wavelength is able to be tuned throughout the visible, near-infrared, and even the infrared region, which is extremely useful to optimise the design of LSPR sensors and maximise the biosensing response [19, 21].

Systematically exploring the optical properties of noble metal nanoparticles provides the means to predict a nanoparticle's behaviour.

Functionalising nanoparticles to achieve high sensitivity, selectivity, rapidity and simplicity for biosensing motivates researchers to rationally design the nanostructure on the same scale as the biological system [22].

Rather than choosing specific application to suit the characteristics of nanoparticles that are currently available, the ability to select nanoparticles based on the requirements of new applications gives more flexibility to attain desirable properties and expand the utility of nanoparticles [17]. The development of new synthesis methods makes tunable plasmon resonance achievable and allows the appropriate nanostructure to be selected for expectant bio-applications. The emerging understanding of the diverse properties of nanoparticles has driven interest in enhancing nanoparticle's ability to probe and modify the biological systems. This chapter is a review of the recent advances in the study of noble metal nanoparticles in order to design and develop ultrasensitive LSPR-based sensing device.

2.1   Surface plasmons on a planar metal-dielectric interface

Surface plasmons, also known as surface plasmon polaritons, are an electromagnetic wave coupled with a metal film and a dielectric to raise resonance at their interface. The electromagnetic wave not only propagates in a direction parallel to the interface, but its field intensity decays exponentially in both media at a direction normal to the surface as shown in Fig. 2.1. By absorbing incident light under certain conditions, free electrons of the metal are

converted into surface plasmon waves localised at the vicinity of the surface. Due to substantial enhancement of the electric field and the corresponding extremely short length of penetration, surface plasmons are highly sensitive to the refractive index of the dielectric adjacent to the metal surface. This advantageous property is exploited to detect and transfer a change of local environment to an optical signal for not only binding events, for example, but also binding kinetics [20, 23-24].
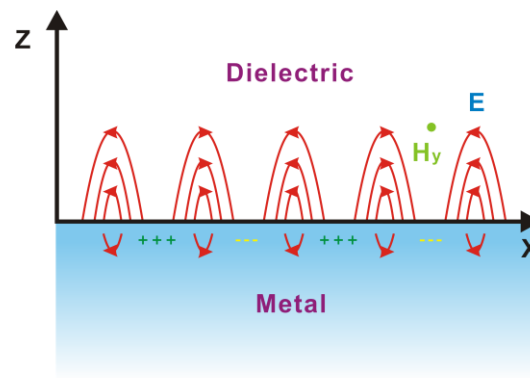
Figure 2.1 Propagation of a surface plasmon wave

2.1.1   Surface plasmons

Surface plasmons are coupled oscillations of electrons and the electromagnetic field at the metal-dielectric interface. The frequency dependent surface plasmons wave vector k_{sp} is given by[23]

$$k_{sp} = k_0 \sqrt{\frac{\varepsilon_1 \varepsilon_2}{\varepsilon_1 + \varepsilon_2}} \qquad (2.1)$$

where $k_0 = \omega/c$ is the free-space wave vector. At optical wavelengths,

because of the complex permittivity of metal, ε_1 ($n_1 = \sqrt{\varepsilon_1}$, $\varepsilon_1 = \varepsilon_1' + i\varepsilon_1''$), and the dielectric material ε_2 ($n_2 = \sqrt{\varepsilon_2}$), this condition enables the surface plasmons wave to propagate along the surface but attenuate gradually due to absorption in the metal.

Moreover, the surface plasmon field decays exponentially into both sides of the media. On the dielectric side, the penetration depth is several hundreds of nanometres whereas the penetration depth at the metal side is determined by the wavelength but only has about 20 nm [25]. The sensing properties of surface plasmons are dependent on the strong concentration of the electromagnetic field due to this penetration [25-27].
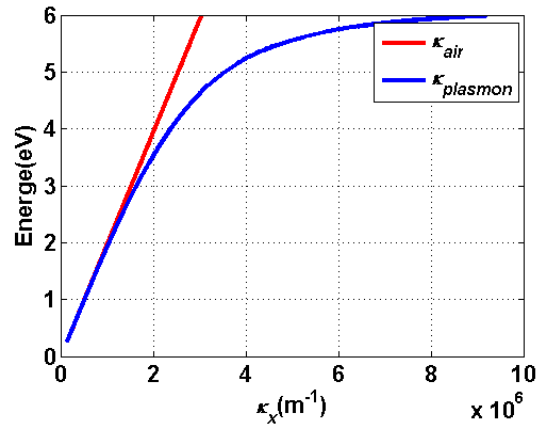
Figure 2.2   Dispersion of plasmons at a gold-air interface

Considering the dispersion of surface plasmons at the gold-air interface compared to the dispersion of a plane electromagnetic wave in air shown in Fig. 2.2, the momentum of the surface plasmons, $\hbar k_{sp}$, is larger than that of a plane wave $\hbar k_0$, but they do not intersect, so surface plasmons cannot be excited by a freely propagating plane wave. A detailed description of the surface plasmon resonance can be found in Appendix A.1.

2.1.2   Excitation of surface plasmons

In order to excite surface plasmons, it is necessary to enhance the momentum of the incident light, which also means that the dispersion line of the plane electromagnetic wave in air shown in Fig. 2.2 is to intersect that of the surface plasmons. Generally speaking, this can be achieved either by placing a grating on the metallic surface or by introducing a dielectric with high refractive index such as a prism [23-26]. The latter configuration is widely applied and there are two arrangements available as depicted in Fig. 2.3. The first setup is known as the Otto-configuration. A very small separation is present between the dielectric and metal surface. However, the requirement to maintain a spacing of less than 1 μm restricts its applicability. In the alternative choice of the Kreschmann-Raether configuration, a thin metal layer is formed on a dielectric substrate. The correct thickness of metal layer and incident angle allow an evanescent field to couple into the resonance mode of the metal layer and excite surface plasmons.

(a) Otto-configuration   (b) Kreschmann-Raether configuration
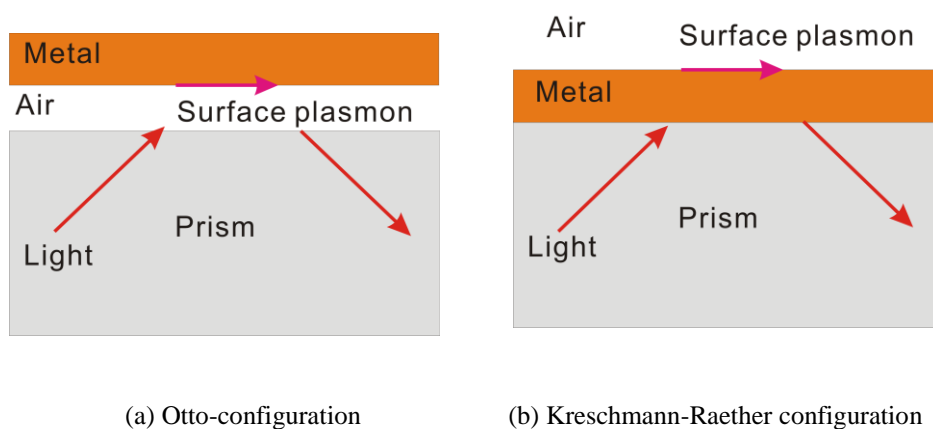
Figure 2.3 Configurations for excitation of surface plasmons resonance

2.2   Plasmon resonances in noble metal nanoparticles

When the size of a noble metal particle is reduced to be comparable to the illumination wavelength, the oscillating electric field leads the free-electrons in the metal to oscillate coherently as represented in Fig. 2.4 [7, 19, 28]. The electron cloud is displaced with respect to the positive nucleus, and a restoring force arising from Coulombic interaction drives the electrons to oscillate in resonance with the light frequency. The metal nanoparticle exposed to light resonant with its surface plasmon oscillations strongly absorbs the light and rapidly converts it into heat or scattered photons. The oscillation frequency can be determined from the absorption and scattering spectroscopy and is found to be dependent on the particle's size, shape, material, interparticle spacing and the properties of the surrounding medium [7, 28-29].
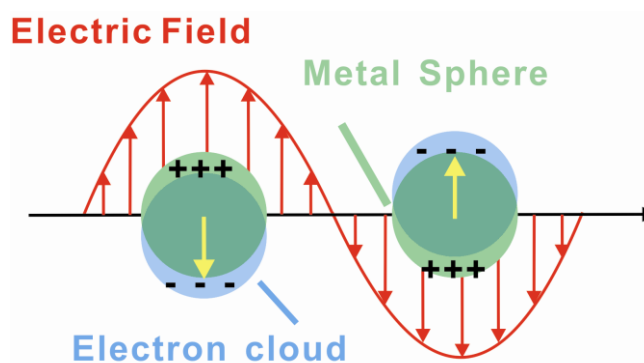
Figure 2.4   Plasmon oscillations surrounding a sphere

2.2.1   Excitation of electrons
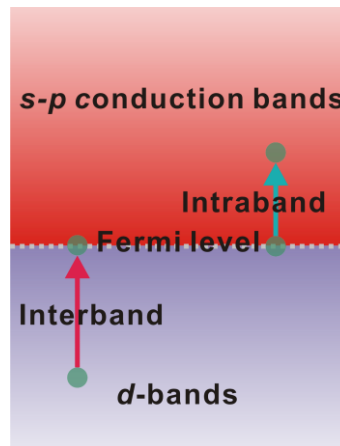
Figure 2.5 Electron transition. Electrons are excited within the conduction band or from the

upper *d*-bands to the conduction band.

On the atomic level of a noble metal, each electron is accommodated in its orbital according to its rotational energy. The equilibrium of a free atom is disrupted by the perturbation of an electromagnetic wave. Radiant energy absorbed by the atom thermally excites the electrons to undergo intraband and interband transitions. Small energy absorption promotes intraband transition so that conduction band electrons oscillate at their original state. Absorbed energy larger than the energy gap excites the electron to jump from the upper *d*-band to the partially filled conduction band in the noble metal (Fig. 2.5) [30-34]. During an interband transition, the electrons may jump to the conduction band either in a direct process with a creation of a hole at its original orbital or an indirect way needing the assistance of a phonon to satisfy the requirement of conversation of wave vector [35].

2.2.2 Energy release of excited electrons
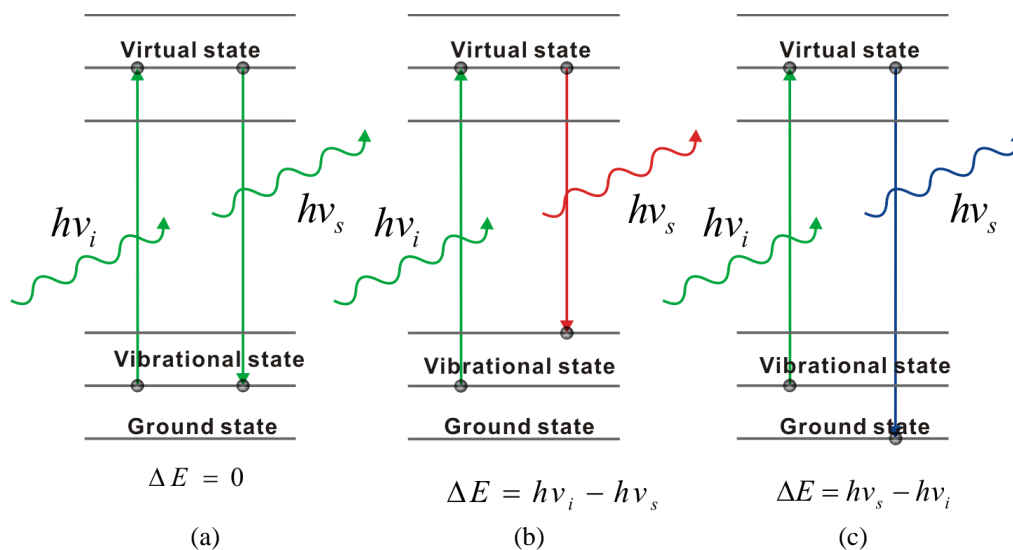
Figure 2.6   Different mechanisms of scattering. (a) Rayleigh scattering: emission of a photon

(b) Stokes Raman scattering: emission of a photon and a phonon (c) Anti-Stokes Raman

scattering: emission of a photon and absorption of a phonon

Electrons in the excited state release their absorbed energy over femtosecond to nanosecond time scales and spontaneously return to a lower energy state [36-37]. The energy is either converted to heat due to interatomic collisions, which is the origin of light absorption, or is emitted as scattered photons in any direction (Fig. 2.6). The majority of light is emitted at the same frequency as the incident light, such as Rayleigh scattering. This is referred to as elastic scattering, because the electron releases the same energy as it has briefly absorbed. Another possibility is inelastic scattering where the outgoing light has a different frequency from the incident, such as Raman scattering. Here, the polarisability of the atom changes during the release of energy with

the creation or the elimination of a phonon. In the case that the outgoing photon possesses less energy than the incoming photon, associated with the emission of a phonon, it is referred to as a Stokes transition. The other case is an Anti-Stokes transition when the photon emits as a higher energy by absorbing a phonon.

2.3   Optical Properties of metal nanoparticles

The intriguing optical properties of noble metal nanoparticles contributed by the localised surface plasmons are due to the dynamic response of its conduction band electrons to incident light. The range of nanoparticles provided by the modern synthesis techniques allows the possibility of insight into the LSPR dependent on the particle size, shape, topology and the properties of the metal and its surrounding medium, which all ultimately affect the electron density at the particle's surface [1].

Spectroscopic measurements are commonly adopted to observe the LSPR, that is tunable from the ultraviolet to the visible and near-infrared regions [3], while TEM and SEM are used as the complementary tools to monitor their morphologies [38]. The absorption of nanoparticles is usually measured in transmission spectrometry, where an ensemble of nanoparticles are dispersed in solution or immobilised on a substrate. Dark-field spectroscopy improves the characterisation method to enable the detection of the scattering of single

particles [39].

The bright colours exhibited by colloidal gold attracted early pioneers in the 19th century, especially Faraday, Zsigmondy, Svedberg, Rayleigh, Mie and Gans, to experimentally and theoretically study the properties of noble metal colloids [40]. Mie and Gans' theories are the most popular and simple analytical methods to understand the scattering and absorption of noble metal particles. Various numerical methods have been developed to solve the interaction between the light and the complex nanostructure. Among them, the discrete dipole approximation (DDA), finite element and finite difference time domain methods (FEM and FDTD) and T-matrix are widely applied [39-40] .

2.3.1   The effect of aspect ratio

The spectra of gold nanorods are characterised by a strong longitudinal resonance at a longer wavelength and a relatively weak transverse resonance band at a shorter wavelength. The prediction from Gans' theory that drastic changes in the longitudinal plasmon mode would be caused by the small changes in the nanorod aspect ratio was modelled by El-Sayed et al. [41]. The consequences of increasing the nanorod's aspect ratio are a red-shifted longitudinal and a blue-shifted transverse wavelength (Fig. 2.7). The pronounced longitudinal wavelength is usually the object of interest to be observed since it can be tuned over a wide wavelength range. A linear

relationship between the absorption maximum of the longitudinal mode (λ_{max}),

the aspect ratio (AR=length/width) and the medium dielectric constant (ε_m)

deduced and corrected [42] by them is

$$\lambda_{max} = (53.71AR - 42.29)\varepsilon_m + 495.14 \quad (2.2)$$

Pileni and co-workers prepared Au nanorods with aspect ratios varying

from 2.2 to 4.0 by the seed-mediated growth method. They measured the

longitudinal wavelength of gold nanorods in solvent from their absorption

spectra, and compared the experimental wavelength positions with the

absorption efficiency using the DDA method [43], as shown in Fig. 2.8.
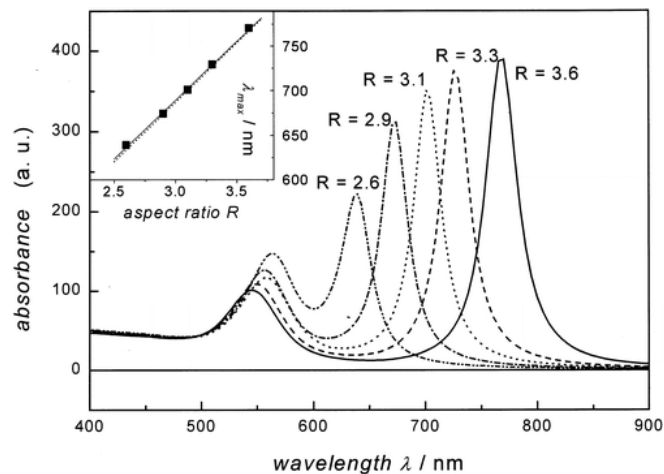
Figure 2.7 Calculated absorption spectra of elongated ellipsoids with varying aspect ratio

according to Gans' theory. The dielectric constant used in the calculation was 4. The inset

shows the longitudinal wavelength peaks as a function of aspect ratio. The solid line is a linear

fit to the five calculated peak wavelengths (square) and the dotted line is the plot of Eq. (2.2).

[41]

The longitudinal wavelength peaks undergo red-shift when the gold nanorods aspect ratio increases. The linear variation for the maximum of longitudinal wavelength with respect to the nanorod aspect ratio was $\lambda_{max} = 93.72AR + 392.6$ from the experimental data, which is close to the $\lambda_{max} = 96AR + 418$ obtained by the DDA method, assuming the dielectric constant of the solvent was constant at 1.77.
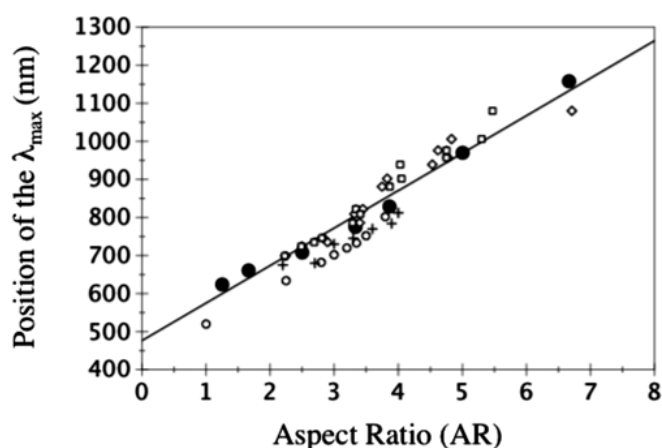
Figure 2.8 The longitudinal wavelength peaks versus the aspect ratio of Au nanorods. DDA calculation results (black circles) and the corresponding fit (straight line). Experimental data from the work of Al-Sayed et al.(diamonds), Pérez-Juste et al. (squares) and M.P.Pileni et al (crosses). [43]

2.3.2   The effect of the refractive index of the surrounding medium

The spectrum of a nanoparticle is expected to shift when its surrounding environment is changed because of the varying refractive index [41, 44]. El-Sayed et al. [41] employed Gans' theory to show that the absorption

maximum of the longitudinal wavelength depends on the refractive index of surrounding medium in a linear fashion for a fixed aspect ratio nanorod (Fig. 2.9). The absorption of this nanorod (aspect ratio: 3.3) shifts to longer wavelengths and the intensity increases with the increasing dielectric constant of the surrounding medium.
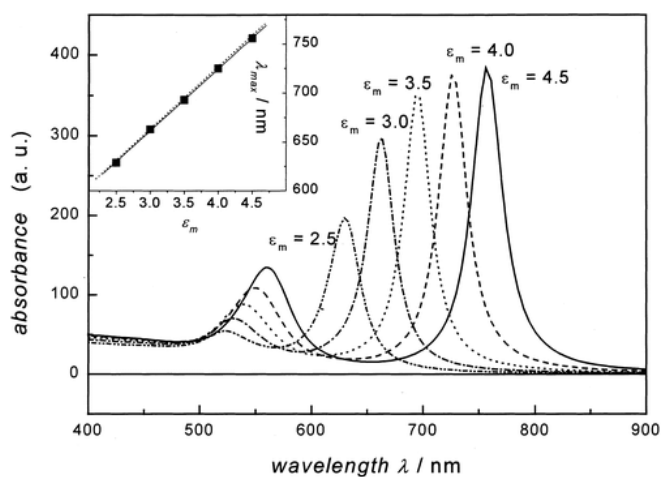
Figure 2.9   Calculated absorption spectra of elongated ellipsoids with different refractive index media using Gans' theory. The aspect ratio was 3.3. The inset shows the longitudinal wavelength peaks as a function of dielectric constant. The solid line is a linear fit to the five calculated peak wavelengths (square) and the dotted line is the plot of Eq. (2.2). [41]
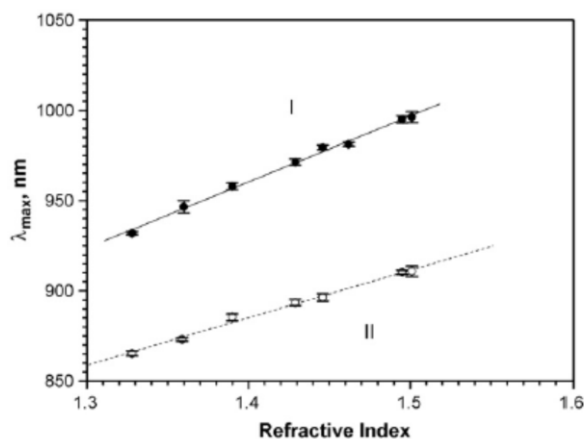
Figure 2.10 The absorption maxima of longitudinal plasmon bands of Au nanorods in different

solvents with the refractive index varied from 1.328 to 1.501. The aspect ratios for (I) and (II)

were 5.2 and 4.6 respectively. The lines are drawn for eye-guiding. [45]

Wang et al. conducted the experimental measurement for the refractive index dependent absorption of two types of nanorods, with aspect ratios of 5.2 and 4.6 respectively [45]. The Au nanorods immobilised on a glass slide were exposed to different solvents whose refractive indices increased from 1.328 to 1.501. As a result of the increased refractive index, the longitudinal plasmon band of Au nanorods was red-shifted, illustrated in Fig. 2.10 as the measured longitudinal peak wavelength as a function of the refractive index.

2.3.3   The shape-dependent refractive index sensitivity of nanoparticles

The localised surface plasmon resonance of noble metal nanoparticles is

highly dependent on the refractive index of the surrounding environment and has attracted a great deal of interest because of its potential to be employed in the biological sensing applications [6, 46]. The binding of organic and biological molecules on the surface of a nanoparticle leads to a change of the nanoparticle's local environment and a consequent change of the LSPR as monitored from its scattering or absorption. The magnitude of a nanoparticle's spectral response to the local environment varies according to its properties, which are determined by its size, shape and composition.
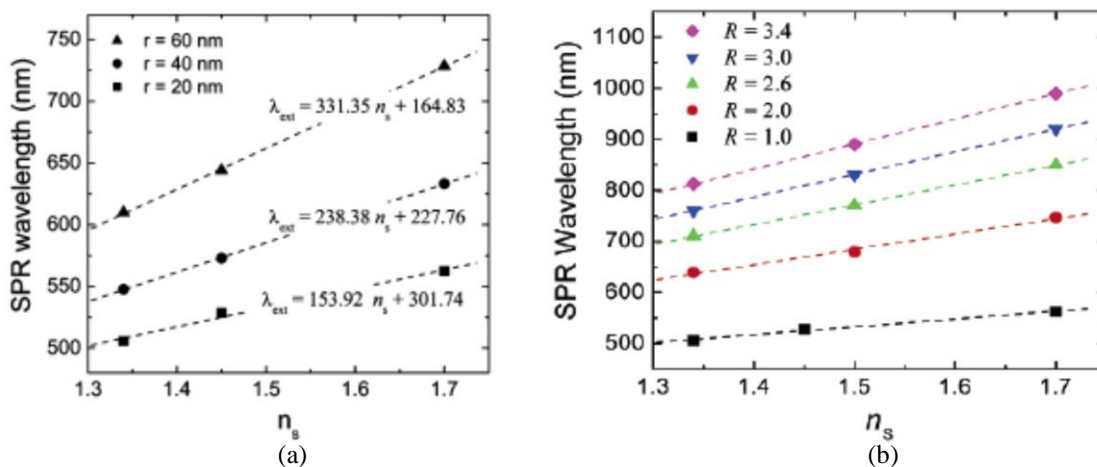
Figure 2.11 Sensitivity of nanosphere and nanorod deduced from DDA simulation. (a) Size dependence of the SPR wavelength response to the change in the refractive index of the surrounding medium from 1.34 to 1.7. (b) The aspect ratio dependence of the SPR wavelength response to a medium refractive index change from 1.34 to 1.7. [6]

In recent decades, the sensitivity of nanoparticles has been investigated for realising an ultrasensitive plasmonic sensor.   The dependence of the SPR

sensitivity for Au nanospheres and nanorod had been discussed by Lee and El-Sayed [6]. The aspect ratio of nanorods plays an important role to determine their sensitivity. Enlarging the size of a nanosphere (Fig. 2.11 a) or changing the nanoparticle from a spherical to a rod-like shape significantly improves the magnitude of wavelength shift of the long wavelength SPR band under a given change in the refractive index. Therefore, the sensitivity of nanorods, estimated from the slope of the linear plot, increases with increasing aspect ratio through the shape factor, as demonstrated by the DDA simulation of Au nanorods in Fig. 2.11 b.

Miller and Lazarides investigated the plasmon resonance wavelength dependent sensitivity of nanoparticle of various sizes and shapes, including Au nanocylinders, nanodiscs and nanoshells by using the discrete dipole approximation (DDA) [47-48]. The extinction and scattering spectral peak wavelengths of these nanoparticles undergo a red-shift as their aspect ratio increases and their sensitivity to the bulk refractive index of the surrounding medium also increases. A linear analytic expression for the sensitivity of nanoparticle correlated to the slope of the real part of the noble metal dielectric function, can be expressed as

$$\frac{d\lambda^*}{dn} = \frac{2}{n}\lambda^* + \frac{2}{n}\frac{b}{m} \qquad (2.3)$$

23

where λ^* and n are the peak wavelength and refractive index of the medium, m and b are two parameters used in a linearisation for the real part of the noble metal dielectric constant as a function of wavelength λ derived from the Drude model, $\varepsilon' \approx m\lambda + b$, is used for comparing the sensitivity determined by the DDA method.

(a)   (b)
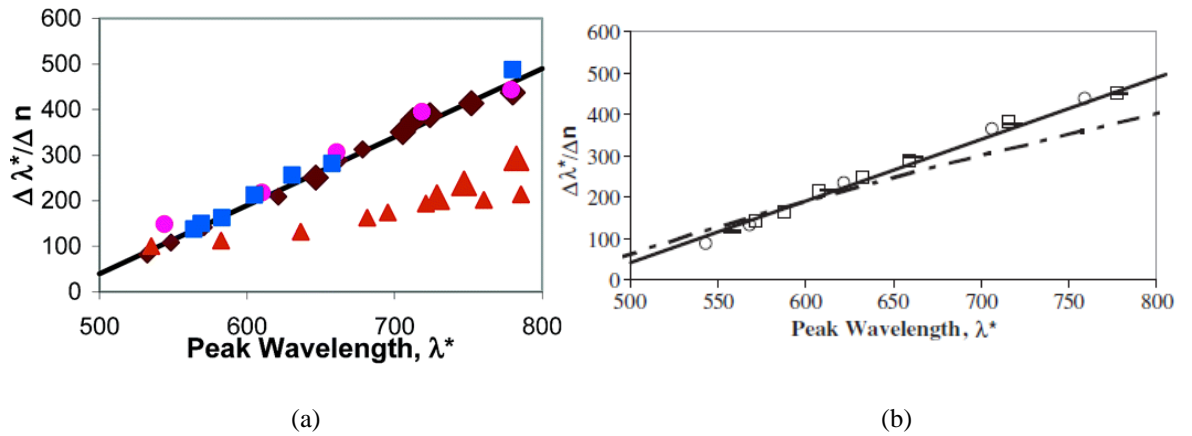
Figure 2.12 Sensitivity of plasmon resonance to bulk refractive index as a function of peak wavelength. (a) is the extinction sensitivity for Au nanocylinders (circles), Au nanodisks (squares) and hollow nanoshells (diamonds, larger diamonds). Solid nanoshells (triangles) are linear except for larger particles (larger triangles). (b) is the scattering sensitivity for Au nanocylinders (dashes), nanodiscs (open squares) and hollow nanoshells (open circles). The solid lines show the analytical fit of Eq. (2.3) using the parameters for gold in the visible range. The dash-dot line in (b) is a quadratic approximation based on a true Drude metal which is less accurate than the predication provided by Eq. (2.3). (a) [47] (b) [48]

Both the sensitivity of extinction and scattering plasmon resonance as a function of peak wavelength for different sizes and shapes of Au nanoparticles

derived from electrodynamic calculations and the analytic approximation of Eq. (2.3) are illustrated in Fig. 2.12. The linear description matches well with the trend of the sensitivity of nanoparticles determined by the DDA method. The sensitivities of extinction and scattering also have a good agreement with each other and both of them increase linearly with the resonant wavelength.

The sensitivity of nanoparticles increases with their plasmon resonance wavelength and its relationship with the curvature of particles was summarised by Wang and co-workers when they compared the sensitivity of nanoparticles measured by their group and other's [49]. The refractive index based sensitivity for Au nanospheres and Au nanorods of plasmon wavelength 527 nm, 653 nm, 728 nm and 846 nm are 44 nm/RIU, 195 nm/RIU, 224 nm/RIU and 288 nm/RIU respectively, while the sensitivity of Au nanobranches of plasmon wavelength at 1141 nm and Au nanocrescents of plasmon wavelength at 2640 nm approach 703 nm/RIU and 801 nm/RIU respectively [4, 50]. In order to distinguish the effect of plasmon resonance wavelength and nanoparticle shape on the sensitivity, they prepared seven different shapes of Au nanoparticles that exhibited the same longitudinal wavelength of nearly 730 nm. The extinction spectra of Au nanoparticles suspended in the water-glycerol mixture were red-shifted as the result of increasing the refractive index of this liquid mixture from 1.33 to 1.46. The sensitivity of the large Au nanorod (length = 108 nm, diameter = 44 nm, aspect ratio = 2.5) was the highest within the seven shape categories at 326 nm/RIU, while the small Au nanorod (length = 26 nm,

diameter = 10 nm, aspect ratio = 2.6) had the lowest sensitivity of 156 nm/RIU

(Fig. 2.13).
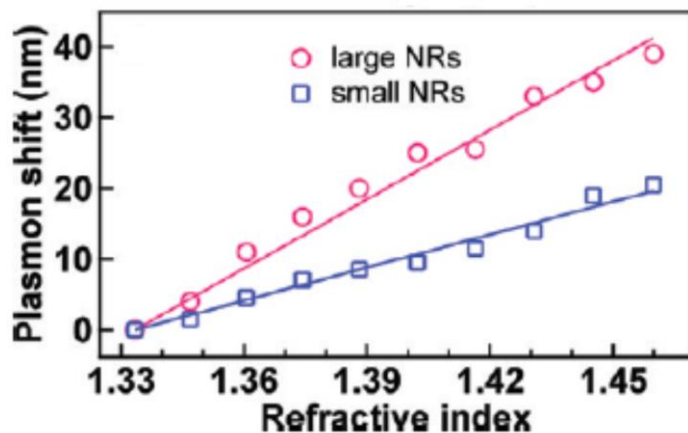
Figure 2.13 Sensitivity of large and small Au nanorods. The lines are linear fits. [49]
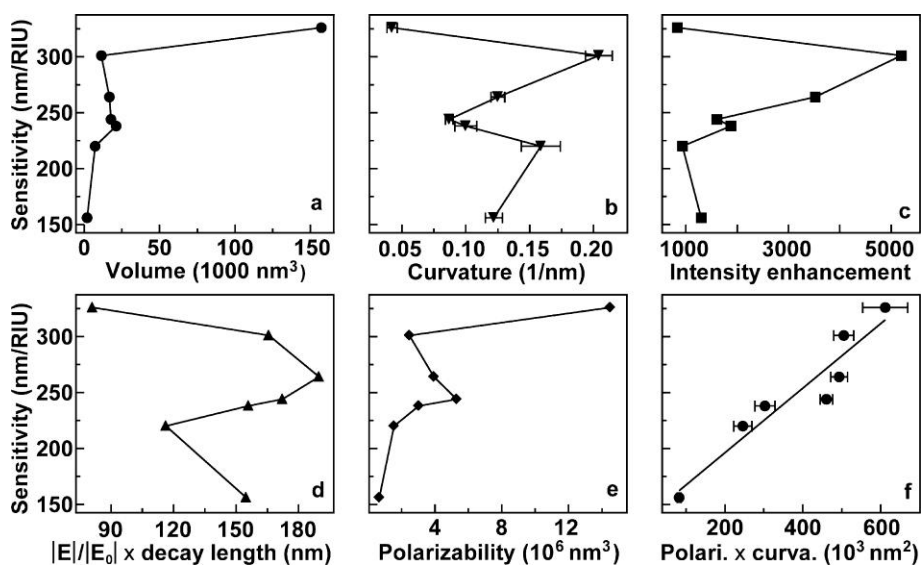
Figure 2.14 Relationship between the refractive index sensitivity and different

parameters of the Au nanocrystals: (a) nanocrystal volume; (b) end curvature; (c) maximum

electric field intensity enhancement; (d) product of the maximum field enhancement and the

decay length of the field intensity enhancement along the central length axis of the Au

nanocrystals; (e) polarisability; (f) product of the polarisability and the end curvature. [49]

The effect of six parameters of Au nanoparticles, including nanoparticle volume, the curvature, maximum electric field intensity enhancement, the product of the maximum field enhancement and the decay length, the polarisability and the product of polarisability and local curvature on the sensitivity was carried out in FDTD simulation. None of the factors had any positive correlation with the index sensitivity except the latter (Fig. 2.14). The sensitivity increases approximately linearly with the polarisability-curvature product.

The consequence of increasing medium refractive index is a decreasing surface plasmon resonance frequency, which is equivalent to a red-shift of the plasmon wavelength. In physical terms, the Coulombic restoring force acting on the electrons cloud at the particle's surface decreases while the electric dipole moment of the particle increases as a result of the increasing medium refractive index [49, 51]. The greater the screening of the Coulombic restoring force is, the less the displacement of the electron cloud with respect to the ionic core of the nanoparticle and the greater the reduction of surface plasmon resonance energy produced. Therefore, the refractive index based sensitivity of a nanoparticle is determined by the degree of how easily the electron cloud is displaced by the medium change. The easier it is to move the free electrons in a noble metal nanoparticle, the higher the refractive index change-based sensitivity is. Higher electron density presenting at sharp curvatures of a nanoparticle enhances the electric field around its tip and will also contribute to

the net polarisability, which is known as "lightning rod effect" [52-53]. Taking the polarisability and the shape into consideration, both of them play important roles in determining the nanoparticle's sensitivity simultaneously, which is supported from the linear relationship between the sensitivity and the polarisability-curvature product.

2.4   Electrochemical reaction of Au nanostructure

Electrochemistry deals with the transfer of electronic charge. The application of potential to the electrolyte solution is generally accompanied by the formation of an electrical double layer at the electrode surface where the electrons and ions transfer between the neighbouring phases of electrode and electrolyte solution. A wide range of noble metal nanoparticles with different morphologies can be synthesised and organised in a desired pattern by assembly methods, which provide an abundant variety of conditions in which to investigate the charge transport taking place on particles immersed in solution.

Traditional techniques of studying electrochemical process are to measure the current, potential, charge and capacitance. The requirement of acquiring surface structure information of a geometric, electronic and vibronic nature stimulates the incorporation of non-invasive optical methods alongside conventional electrochemical techniques [54-55]. Surface plasmon

spectroscopy of the noble metal nanocrystals is a versatile technique for studying the electrochemical process. The absorption and scattering resonance depending on the electron density of metal nanocrystals perform as the essential elements to study the charge transfer reaction on nanoparticles.

2.4.1   Surface plasmon resonance for the investigation of electrochemistry

(a)   (b)
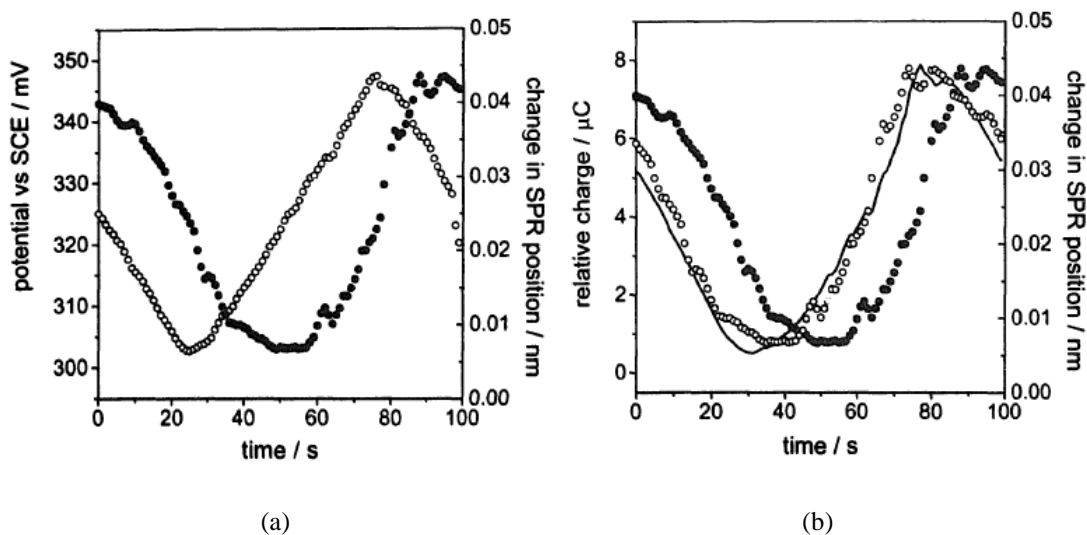
Figure 2.15 SPR position associated with the potential. (a) Potential of Au film versus time (open circles). Change in SPR position versus time (solid circles). (b) Relative charge oscillation with time (solid line) compared to change in the SPR position (solid circles). The open circles are the same SPR data shifted by 14 s. [56]

Surface plasmon resonance is a sensitive technique to monitor the change of environment adjacent to the metal surface, realised by measuring the reflectivity of light from the metal surface either as a function of

angle-of-incidence at a constant wavelength, or a function of wavelength for a fixed incident angle [19]. The electrochemical reactions taking place at the metal surface promotes the development of electrochemical SPR (EC-SPR). The ion adsorption/desorption, and charge redistribution in the double layer and metal film, have been studied by using SPR [57-59].
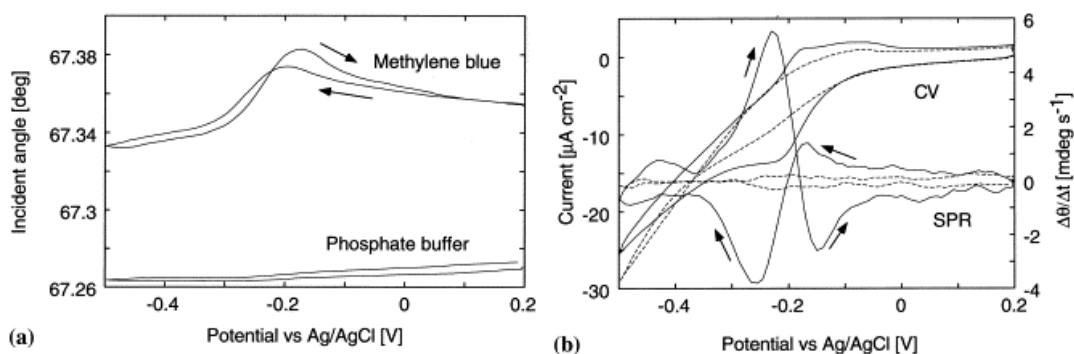
Figure 2.16 Comparison of CV, SPR angle shift and time differential SPR resonance angle. (a) Electrochemical SPR voltammogram of MB (17.9 μM) and 0.1 M phosphate buffer pH 7 (background). (b) Cyclic voltammogram and potential dependence of $\Delta\theta / \Delta t$ for MB (solid line) and phosphate buffer (dashed line). The scan rate was 10 mVs^{-1}. [60]

M.J.Jory et al. employed an acousto-optic tunable filter (AOTF) to tune the incident wavelength at a fixed incident angle and recorded the SPR position. The application of potential using cyclic voltammetry (CV) on Au film resulted in the SPR position oscillating with the potential cycles [56]. The 14 seconds delay between the SPR oscillations and the potential sweep was determined by shifting the charge oscillation curve to match the SPR response (Fig. 2.15). Lioubimov et al. also observed this hysteresis phenomenon between the SPR

angle shift and the potential scan between 1.5 V and -1.5 V [61]. The slow chemical oxidation-reduction process accounted for this behaviour. Anodic polarisation exceeding 1.35 V produced an Au_2O_3 oxide layer on the Au surface. The time dependent diffusion of the oxide near the Au surface led to the retardation of the SPR angle shift.

Time differential SPR resonance angle has been used to characterise the electrochemical reaction of 17.9 μM methylene blue (MB, 3.7-Bis(dimethylamino)-phenothiazin-5-ium chloride) in 0.1 M phosphate buffer (PH 7), instead of only relying on the SPR angle and CV [60]. The cathodic potential scan induced the reduction of MB in the bulk solution and the adsorption of reduced MB on the Au surface. The anodic potential scan caused desorption of the MB film from the Au surface. The SPR angle shift in the presence of only phosphate buffer was therefore obviously smaller than the SPR angle shift when the MB was present. The redox reaction of MB had been observed not only from the SPR angle shift, but the exhibition of two pronounced peaks in $\Delta\theta/\Delta t$ corresponding to the redox reaction, which was not easily identified from the current peak in the CV graph (Fig. 2.16). The time differential SPR data provided qualitative diagnostic information as useful as the conventional CV. When this feature was not legible from the CV, $\Delta\theta/\Delta t$ actually provided better information.

2.4.2   Potential controlled absorption

Most surface plasmon absorption bands are observed in particles larger than 10 nm because the extremely weak signal exhibited by small particles constrains observation. Potential dependent plasmon absorption bands have been reported both from Ag and Au nanospheres dissolved in an aqueous solution [62-63] and Ag and Au nanospheres immobilised on an ITO electrode [12, 64-65].
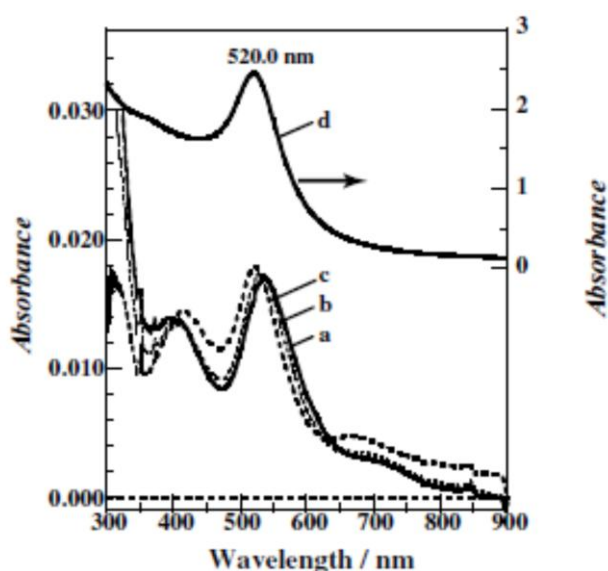
Figure 2.17 The absorption spectra of Au nanospheres on a modified ITO electrode at three different potentials. The potentials were 0.6 V (solid line, a), 0.0 V (thick broken line, b) and -0.9 V (c). Line d represents the absorption spectrum of the Au colloidal solution. [12]

The spectral shift is mainly attributed to the charging and discharging of the particles. The application of potential to the electrode results in movement of the electrons to and from the particles via the double layer. When the electrons are transferred to the particle in the case of negative potential, this leads to an

increase of the electron density of the particle and hence the plasmon frequency. As a result, the plasmon absorption is enhanced and blue-shifted. On the contrary, positive potential depletes the particle's electrons and induces a plasmon absorption red-shift.

The spectral shift induced by the potential can be seen in Fig. 2.17, measured from 11 nm citrate capped Au nanospheres immobilised on amineterminated siloxane (ABSiO) modified ITO electrode. The plasmon absorption peak was about 530 nm at 0.0 V. After the application of potential at 0.6 V, the absorption spectrum red shifted to a new position with a maximum around 534 nm. When the potential was step to -0.9 V, the absorption spectrum blue shifted to about 520 nm.

2.4.3   Particle morphology dependent charge transport

The shift of absorption spectrum accompanying potential application indicates that metal nanoparticles experience charge transport at their electrified interface. The amount of transferred electrons regulated by the potential control is determined by the double layer capacitance of the nanoparticle. Varying nanoparticle sizes and shapes produce different capacitances and electron densities which are sensitive to their morphologies. The accumulation and depletion of a particle's electrons leads to a wide degree of alternation of the particle's plasmon frequency and results in its different

magnitude of spectral change.

The size effect on the capacitance of Au nanospheres was investigated by Toyota and Sagara using electrochemical method [66]. Citrate-stabilised Au nanospheres with five different diameters (3.7, 11.0, 11.5, 21.7 and 40.8 nm) were immobilised on an ABSiO-ITO electrode. Potential step coulometry measurements were conducted to obtain the equilibrium charge at constant potentials. The potential E_f was stepped from -0.4 V to 0.6 V at 0.02 V intervals as a potential step for a duration of 1 s [12]. The charge *q(t)* at each step was obtained by the integration of current with time. Within the potential step, *q(t)* was linear at *t* > 0.8 s regardless of the potential. The intercept to the time zero line of the straight line fit of *q(t)* in 0.8-1.0 s was equated to $Q(E_f)$, ensuring as the amount of charge to reach a new equilibrium state. The charge at each potential step relative to the charge at the initial potential of -0.4 V was $\Delta Q(E_f)$, which was presumably equal to the change of electrons to charge the particle and the space charge layer of the ITO from that at -0.4 V.

The graph of $\Delta Q(E_f)$ before and after the immobilisation of 21.7 nm Au nanospheres on an identical ABSiO-ITO electrode is illustrated in Fig. 2.18 a. $\Delta Q(E_f)$ was greater in the presence of the particles. The change of total charge on the particles for 23 % (5.6×10^{10} particles cm^{-2}) and 34 % (8.2×10^{10} particle cm^{-2}) coverage were 58 μCcm^{-2} and 87 μCcm^{-2} respectively, which were equated to the difference of $\Delta Q(0.6V)$ before and after the immobilisation of particles. The number of electrons *q* transferred at each

particle was estimated at 6.5×10^3 electrons V^{-1} particle^{-1}, and this value was equal to a capacitance of 70 μFcm^{-2} for a single particle.

(a)   (b)
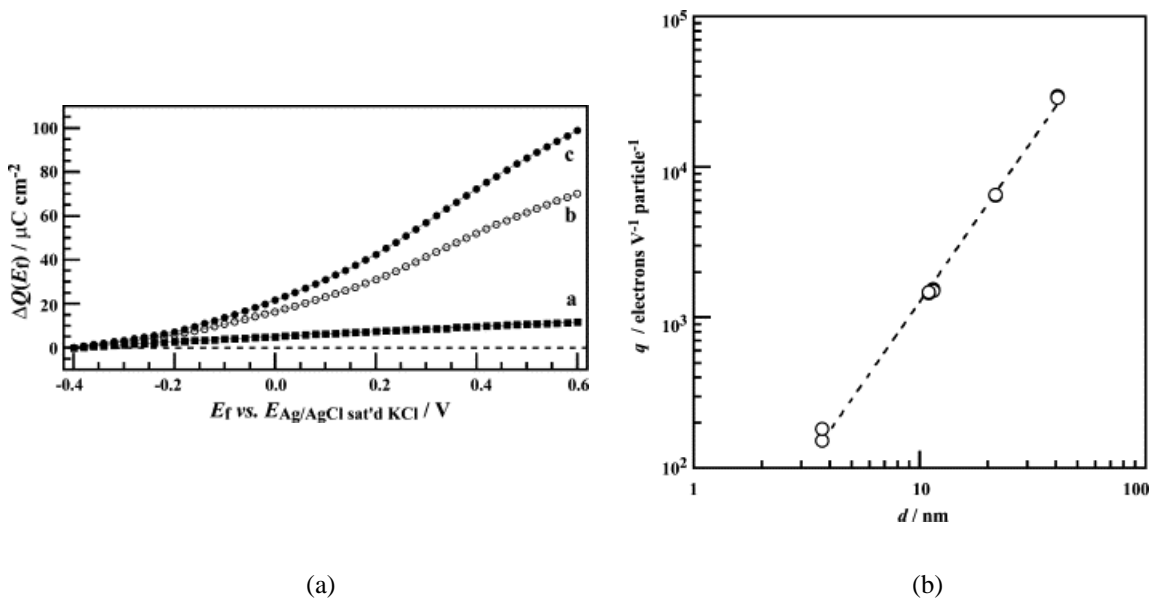
Figure 2.18 (a) Plot of relative charge $\Delta Q(E_f) = Q(E_f) - Q(-0.4V)$ obtained by the potential step coulometry as a function of E_f for 21.7 nm Au nanospheres. Line a (solid square, ▮), before immobilisation of the particles. Line b (open circle, ○) and line c (solid circle, ●), after the immobilisation of Au nanospheres of 5.6×10^{10} particles cm^{-2} and 8.2×10^{10} particles cm^{-2} respectively. The potential sequence was $E_f = -0.4V + n \times 0.02V$ with n = 1-50. (b) The number of electrons per particle transferred when a 1.0 V potential step coulometry was implemented as a function of particle diameter. The immobilisation densities for 3.7 nm particles were 1.1 and 1.3×10^{12} particles cm^{-2}, for 11.0 nm particles were 3.0 and 3.6×10^{11} particles cm^{-2}, for 11.5 nm particles were 2.0 and 2.8×10^{11} particles cm^{-2}, for 21.7 nm particles were 5.6 and 8.2×10^{10} particles cm^{-2}, and for 40.8 nm particles were 3.5 and 7.1×10^9 particles cm^{-2}. [66]

Potential step coulometry from -0.4 V to 0.6 V was implemented on the other four particles with different diameters. The electrons q obtained for each type of particle was proportional to the square of the particle diameter, as shown in Fig. 2.18 b as a log-log plot. This indicated that the amount of electron transport and capacitance per unit surface area was independent of the particle's diameter, and was 69 ± 12 µFcm^{-2} in the range of 3.7-40.8 nm diameter.

The absorption spectral shift of these five kinds of Au nanospheres induced by the potential changing in the range of -0.3 V to 0.6 V was quantified by using spectroelectrochemical methods. That the absorption peak wavelength was located at a shorter wavelength when the potential was negative and shifted to a longer wavelength when the potential became more positive was observed in all the particles' measurement results. The peak shift $\Delta\lambda$ which is the difference of peak wavelengths at 0.6 V and -0.3 V was greater for small particles. 3.7 nm Au nanospheres exhibited 38 nm shifts while 40.8 nm particles had only a 9 nm shifts due to the change of potential of 0.9 V.

Toyota and Sagara's work raised the question: "which particle has the largest peak wavelength shift within the constant potential range?" Ung et al. proposed a relationship between the spectral shift and the change of particle charge amount according to the Mie-Drude theory [62],

$$\frac{\lambda_f^2}{\lambda_i^2} = 1 + \frac{1}{d}\frac{6CV_m\Delta E}{F} \qquad (2.4)$$

where C is the double layer capacitance per unit area [Fm^{-2}], λ_i [nm] and λ_f [nm] are the plasmon peak wavelengths at initial E_i [V] and final $E_f = E_i + \Delta E (\Delta E > 0)$ [V] potential, d [m] is the diameter of the nanosphere, F is the Faraday constant of 96487 Cmol^{-1}, and V_m [m^{3}mol^{-1}] is molar volume. At constant ΔE and certain C irrespective of particle diameter, λ_f^2/λ_i^2 is proportional to the reciprocal of d. This predicts that the spectral shift is greater for smaller nanospheres at a given ΔE [66].

Beside nanospheres, there are several other shapes of nanocrystals available to be used under potential control. Mulvaney el al. deduced a relationship between the surface plasmon resonance shift $\Delta\lambda$ and the alteration of the nanoparticle electron density ΔN within the dipole approximation [67],

$$\Delta\lambda = -\frac{\Delta N}{2N}\lambda_p\sqrt{\varepsilon_\infty + (\frac{1}{L}-1)\varepsilon_m} \qquad (2.5)$$

Here N is the electron density of the uncharged metal, ε_∞ is the high frequency contribution from interband transitions, ε_m is the dielectric constant of the medium, λ_p is the bulk plasmon wavelength, and L is the nanoparticle shape factor.

The number of electrons transported at the metal nanoparticle-electrolyte

interface is determined by the potential and the double layer capacitance, which

is proportional to the surface area of the particle, while the electron density is

inversely proportional to the volume of the particle [65]. Therefore, high

surface area-to-volume ratio particles, where the large surface provides a large

number of electrons transferred in a small volume, experience drastic change in

the electron density ΔN and greater peak wavelength shifts. Equation (2.5)

predicts that for a constant value of ΔN, the wavelength shift is larger for the

particle with small depolarisation factor L resulted from the large aspect ratio,

such as nanorods.
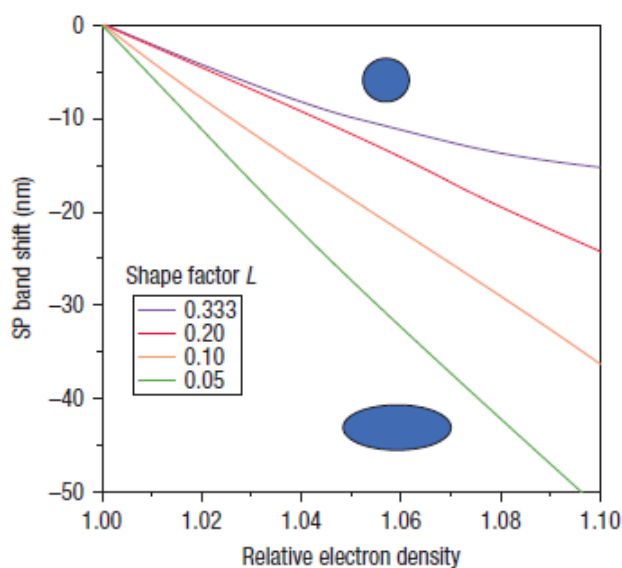
Figure 2.19   Sensitivity of the surface plasmon resonance band to changes in electron density

for different shaped gold nanocrystals. The dielectric constant of the medium was 2.25, *L* is the

depolarisation factor describing the nanocrystal morphology. [68]

The spectral shift of gold particles as a function of change in electron

density is shown in Fig. 2.19 calculated from Eq. (2.5) [68]. All the Au particles, whatever the shape, experience peak wavelength blue shift when more electrons are injected. At a given relative electron density, spherical particle exhibits the smallest shift, whereas the rods and other needle-like particles with smaller depolarisation factor exhibit higher spectral shifts.

2.4.4   Electron-transfer study of single nanoparticles

Electron-transfer to and from particle have been studied on large ensembles of metal nanoparticles by using the spectroelectrochemical method. Adding soluble reductant to the colloid to inject electrons into particles is one way to change the particle charge [11, 67-68]. Another approach is to apply a potential on an electrode immersed in the solution to transfer electrons to the particles as described in the previous section [12, 62, 69]. The study of single metal particles can avoid the inhomogeneity problems which occur in the ensemble measurements, such as the distribution of size, shape and structural defects during the particle synthesis process. The interaction between particles when they are in close proximity can also be eliminated as well [70]. Dark-field microscopy is the most common technique to image single metal particles, using either dark-field illumination or total internal reflection [71-74]. All of these methods aim to detect the scattered light from metal particles. Rayleigh scattering decreases with the sixth power of particle diameter, so

particles with sizes larger than 40 nm can be typically used in dark-field microscopy [71, 73].

Because the size and shape are important factors to determine the particle's optical and electrochemical properties, dark-field microscopy is an elegant technique to meet this challenge to investigate the electrochemical reaction on single metal particle.
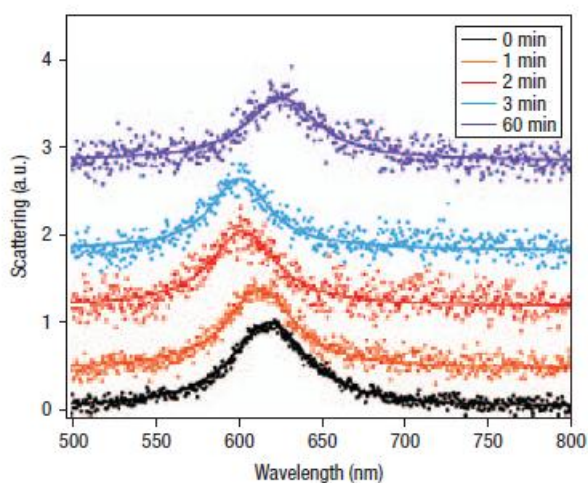
Figure 2.20 Scattering spectra of a gold decahedron before and at 1, 2, 3 and 60 minutes after

electron injection by ascorbate ions. [68]

Direct observation of gold decahedra-catalysed oxidation of ascorbic acid was achieved by Novo et al using a dark-field microscope [68]. The gold nanocrystals in the solution act as an electron reservoir in the presence of oxidation of ascorbic acid followed by the reduction of oxygen to water. Oxidated ascorbic acid transferred the electrons into the Au nanocrystal and the consequence was a blue-shift of the surface plasmon band. The SP band shifted

almost 20 nm during catalysis from 620 nm to 600 nm. When the scattering of this single Au nanocrystal became stable after 3 minutes of electron injection, it shifted back to its initial position at a longer wavelength region (Fig. 2.20). According to Eq. (2.5), a 7 % increase in the electron density is required to achieve 20 nm shifts, which is equivalent to 830,000 electrons transported in the 3 minutes, or 4,600 electrons per second.

(a)   (b)
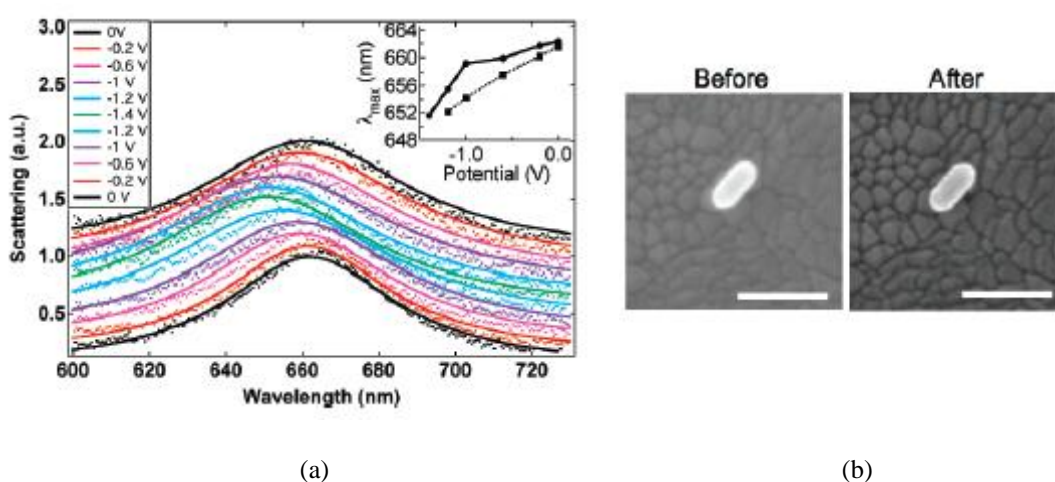
Figure 2.21 Normalised scattering spectra of the gold nanorod (a) shown in the SEM images (b)

before and after charging. The potential was varied from 0 V to -1.4 V. The solid lines are

Lorentzian fits to the spectra. The granular structure is ITO surface. Scale bars= 100 nm. [75]

The process of electron injection into a single Au nanoparticle immobilised on an ITO coated glass slide by the electrochemical method can also be monitored using dark-field microscopy [75]. In a comparison of an Au nanosphere, an Au trigonal prism and an Au nanorod, the Au nanorod exhibited the largest scattering spectral blue-shift of 11 nm as the result of potential

applied from 0 V to -1.4 V. Reversing the bias potential back to 0 V made the scattering peak wavelength red-shift back to its original position (Fig. 2.21 a). The observation of SEM images on the Au nanoparticle before and after the potential application indicated that there was no significant change in the particle's morphology (Fig. 2.21 b). Considering the geometry of this Au nanorod, 11 nm blue-shift resulted from the application of 1.4 V, 85,000 electrons were estimated to have transported implying a double layer capacitance of 150 μFcm^{-2}.

2.4.5   Biosensor applications of electron transport in nanoparticles

Because the surface plasmon resonance frequency of noble metal nanoparticles is highly dependent on the dielectric constant of the surrounding medium, either the wavelength shifts in the absorption/ scattering, or the absorption/scattering intensity change at a single wavelength, provide great opportunities to detect the adsorbate-induced change in the local environment of nanoparticle [1-2, 76-77].

In addition, metal particles performing as electron relays to catalyse the electron transfer in the redox-active species was directly monitored by surface plasmon spectroscopy [11, 67-68, 71, 78]. The alteration of absorption and scattering is able to be achieved by the electrochemical method. All of these experiments raise the possibilities that metal particle could provide a potential

route to the detection of electron transfer by optical methods.
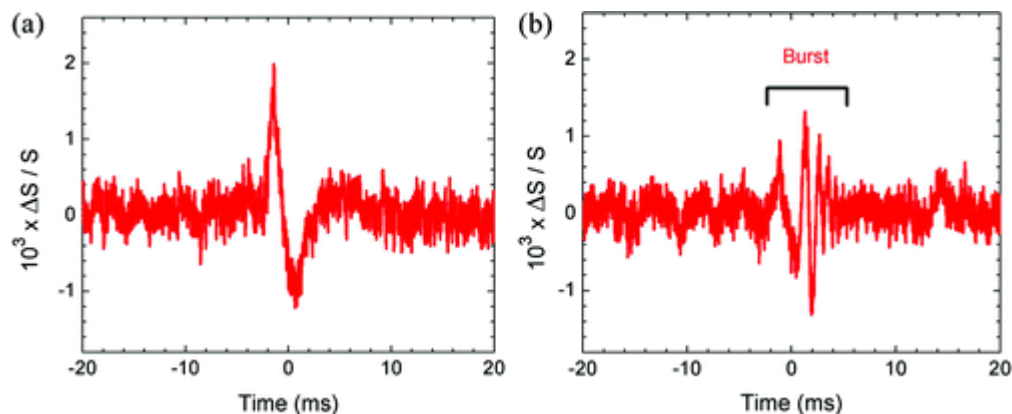
Figure 2.22   Differential scattering signal of neural activity. (a) A single spike activity. (b)A

burst of spikes. Each trace represents a single shot recording from a single neural cell. [9]

The traditional technique for recording cellular electrical activity is to insert a sensor electrode into the cellular medium/tissue to measure the voltage generated from cells and their response to electrical charges [9]. This very invasive method is often replaced by less invasive optical labelling methods. The most commonly used labels are voltage-sensitive dyes, which change their optical properties in response to the cellular membrane potential. Although they are capable of detecting the cellular electrical activity, the drawbacks of photobleaching and the resultant toxicity inherent to fluorescent markers limit their application [9, 73]. The advantage of non-photobleaching possessed by the noble metal nanoparticles and its optical properties related to the interaction between metal conduction electrons and the electric field across cellular membranes make the particle a potential substitute for fluorescent dyes to

record the cellular electrical activity.

The optical detection of brain cell activity using Au particles array has been reported by Zhang and co-workers [9]. An array of gold particles of 160 nm diameter and 40 nm height was fabricated on ITO coated glass by electron beam lithography. This high density Au nanoparticle substrate was used for the growth of hippocampal neural cells and as an electrical to optical signal transducer. A laser with wavelength of 850 nm, where the highest gradient presented in the transmission spectrum of this particle array, was chosen as the probe wavelength in the neuron-sensing experiment. The hippocampal neuron rested on the particle array was stimulated by the injection of glutamate into the neuron's surrounding medium of artificial cerebrospinal fluid to generate spontaneous microsecond duration bursts of electrical activity. The neural cell activity triggered by the injection of glutamate is shown in Fig. 2.22. A single spike and a burst of spikes from two different neurons are identified from this graph. The successful recording of neural spiking activity in real time proves the capability of nanoparticles in biosensing applications and encourages the extensive study of metal nanoparticle in the detection of neuron activities.

Chapter 3   Optical properties of gold and its local

environment

Recent advances in technology have enabled the fabrication of various noble metallic nanostructures. This has raised interest in characterising the optical properties of such nanostructures because of their potential applications in many diverse fields. Distinctive optical features have been revealed as their dimensions have been scaled down from the micron to the submicron region [79] and their shape modified from spherical to nonspherical, for example rodlike or triangular [44, 80-82]. Among a wide range of techniques available to study nanostructure, optical methods are often preferred because of their non-destructive nature [28, 79]. Optical measurements are able to operate from the near field to the far field, which gives a wide degree of flexibility and allows insight into the nanostructure.

Although optical measurement and imaging can be implemented in several ways, the understanding of nanostructure through optical methods involves investigating the dielectric function of noble metals to determine its optical response. The range of optical features are correlated to the geometry and size of nanostructure implying morphology related effects on the properties of the material that are absent from the bulk metal. The discontinuous structures presenting on metal film surfaces prepared by thermal evaporation consist of metal nanocrystals intersecting with the surrounding dielectric. This

metal-dielectric composite supports a drastic change in its optical response, as compared to the bulk material, attributed to the interface with an aggregate particle topology [83-84]. The dielectric function of noble metal is dependent on its free electron density. The application of potential to a submersed metal induces charge transport between the metal and the surrounding electrolyte solution. The change in the electron density leads to an alteration of the metal's dielectric constant, and consequently its optical properties [57].

The purpose of this chapter is to understand the dielectric function of gold. The dielectric function of bulk gold will be briefly described. Then, small metal particles will be explained followed by the dielectric function of an effective medium at a rough metal film surface that consists of interlaced metal and dielectric particles. Dielectric function adjustments for small particles and the surface of gold films are applied to that of bulk gold. Finally, the alteration of gold's properties by the presence of potential will be presented at the end of this chapter.

3.1   The dielectric function of gold

It is well known that the polarisability of a material is proportional to its dielectric function. An applied electric field driving the electrons to oscillate with the atomic nuclei in the matter was thought of as a harmonic oscillator by H. A. Lorentz. Each oscillator driven by the time harmonic electric field

contributes to the overall induced dipole moment in the material [85]. The perception of matter and its interaction with light has been developed by quantum mechanics. The photon absorbed in the matter releases its energy and produces quantum excitation, which has unique quantised energy and momentum. The energy of an electron is altered by the effects of optical and thermal excitation. Understanding of the energy states of the electrons improves the prediction of dielectric function [37].

3.1.1   Dielectric function for bulk gold

| (a) | (b) | (c) |
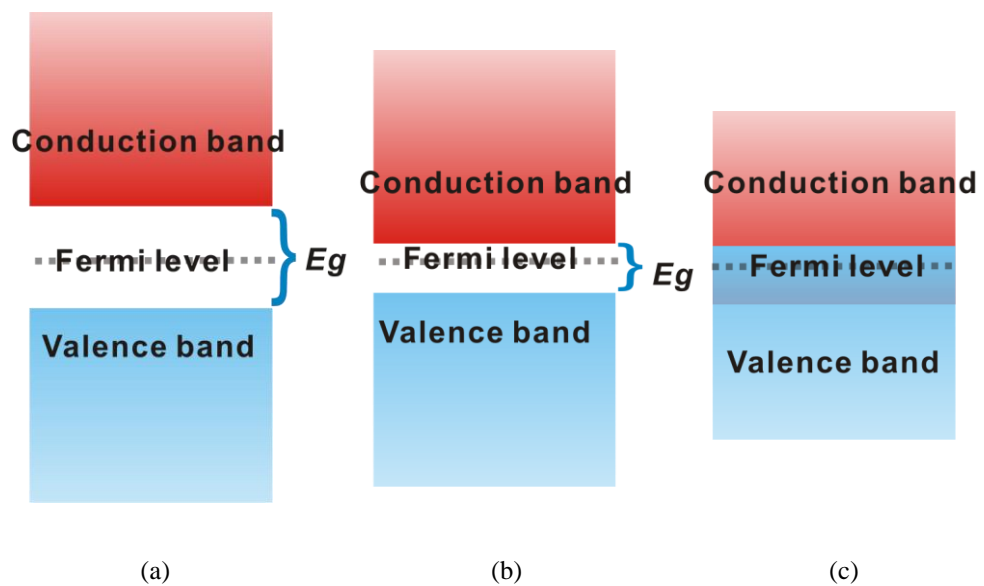
Figure 3.1   Diagrams of the electronic band structure of (a) an insulator, (b) a semiconductor

and (c) a metal.

The electron spins around the atomic nucleus in discrete energy levels. A

solid is composed of a large number of atoms as a periodic crystal lattice. In a solid, the difference between energy levels become smaller and these energy levels form broad and continuous bands as shown in Fig. 3.1. For the cases of insulators and semiconductors, the valence band is completely filled and the conduction band is empty of electrons. There is an energy gap E_g between these two bands that forbids the electron to transit at absolute zero temperature. If excited by absorbing energy, electrons tend to transfer from a lower to a higher energy level. The probability of an electron transferring from the valence to the conduction band is determined by the size of energy gap and the absorbed energy. The large band gap in insulators deters the electron from completing this transition. No current flow can be caused by applying an electric field. The energy gap in semiconductors is smaller than that of insulators. By absorbing energy greater than the energy gap, an electron in the valence band is able to move to the conduction band as a charge carrier [35, 85].

The band structure of a noble metal is different from that of either insulators or semiconductors. The valance band is partially filled with electrons. It overlaps in energy with the conduction band. An applied electromagnetic field distorts the distribution of electrons in the metal and induces electrons to experience intraband $\varepsilon_{intra}(\omega)$ and interband $\varepsilon_{inter}(\omega)$ transitions, which contribute to its wavelength dependent dielectric constant $\varepsilon_r(\omega)$,

$$\varepsilon_r(\omega) = \varepsilon_{intra}(\omega) + \varepsilon_{inter}(\omega) \qquad (3.1)$$

An intraband transition can occur when electrons at the Fermi level are excited by photons of very small energies, usually at the near-infrared region, to achieve collective free movement in the conduction band. The Drude model empirically explains the dielectric function contribution from the collective oscillation of free electrons.

$$\varepsilon_{intra}(\omega) = \varepsilon_\infty - \frac{\omega_D^2}{\omega(\omega + i\gamma_D)} \qquad (3.2)$$

where ω is the angular frequency of light [rad s^{-1}], ε_∞ is the dimensionless high frequency limit contributed from the interband transition of electrons and has the value of unity if only free-electron oscillation is present (a 'perfect' metal), and $\gamma_D = 1/\tau$ [Hz] is the damping coefficient due to the dispersion of the electrons where τ is the relaxation time [s].

The plasmon frequency ω_D is given by

$$\omega_D = \sqrt{\frac{Ne^2}{m^*\varepsilon_0}} \qquad (3.3)$$

where N [m^{-3}] is the free electron density, e [C] is the charge of an electron, ε_0 [Fm^{-1}] is the permittivity of vacuum and m^* [kg] is the effective mass of an

electron. Since m^* in the gold conduction band is approximately the same as m_e, the mass of an electron [86], the figure 9.109×10^{-31} kg is used in the following calculations.

However, noble metals also exhibit strong absorption in the visible and ultraviolet, as well as the near-infrared region, and this is attributed to the electron's interband transitions. Noble metals have a distinct and high energy gap between the occupied highest point in the *d*-band and the lowest unoccupied level of s-*p* conduction band. An interband transition occurs when an electron jumps from a state below the Fermi surface to the conduction band when it is excited by energy of more than the interband transition threshold. For the case of gold, electrons transfer from the narrow and flat *d*-bands 5d^{10} to the Fermi level (6s^{1}), which is the only band participating in the interband transition [32, 34, 87]. The first interband excitation occurs from *d* bands in the *X* point of the first Brillouin zone to the conduction band, with an energy of 1.7 eV. The second interband transition threshold near *L* point of the Brillouin zone is about 2.5 eV [31, 33, 88-90]. To extend the model of the relative permittivity of gold from the near-infrared into the visible range by taking the contribution of interband transitions into account, the permittivity of gold can be better estimated by introducing one Lorentz oscillator into the Drude model [91],

$$\varepsilon_{DL}(\omega) = \varepsilon_\infty - \frac{\omega_D^2}{\omega(\omega + i\gamma_D)} - \frac{\Delta\varepsilon\Omega_L^2}{(\omega^2 - \Omega_L^2) + i\Gamma_L\omega} \qquad (3.4)$$

where Ω_L [Hz] and Γ_L [Hz] are respectively the strength and spectral width

of the Lorentz oscillator and $\Delta\varepsilon$ is a weight factor.

The real, $\varepsilon^{'}$, and imaginary part, $\varepsilon^{''}$, of the dielectric function of gold

for wavelengths of 500 nm to 1000 nm is illustrated in Fig. 3.2.

| (a) | (b) |
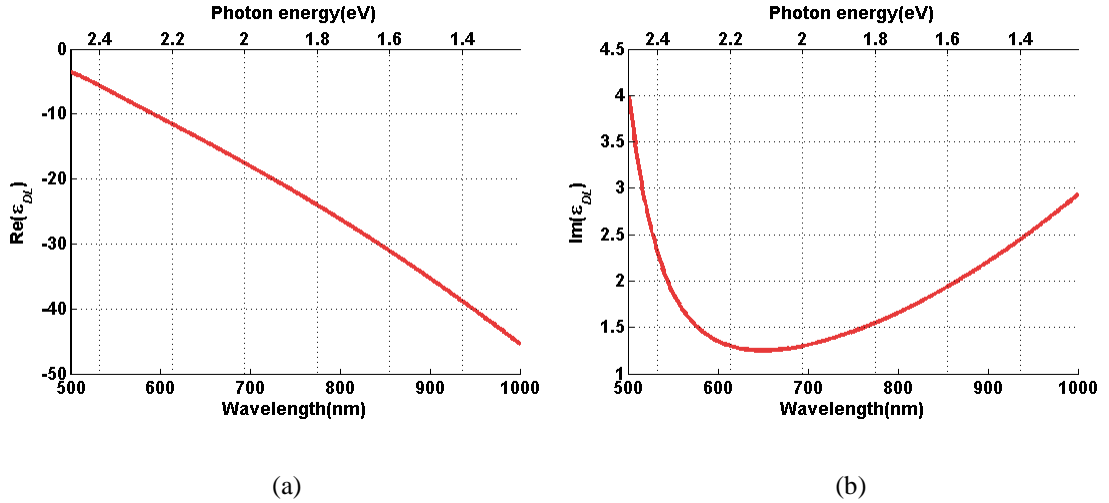
Figure 3.2 The real (a) and imaginary (b) part of the dielectric function of gold from 500 nm to

1000 nm

For gold at low frequency (long wavelength), $\varepsilon^{'}$ is large and negative.

Its magnitude increases monotonically with increasing frequency (reducing

wavelength). $\varepsilon^{''}$, which is related to the energy loss, presents a parabolic curve

and has a consistently positive value between the low and high frequency

regions illustrated.

One of the interesting optical properties of noble metals is their optical

reflectivity. The plasmon frequency determined from the electron intraband and

interband transitions is defined as where $\varepsilon^{'} = 0$. In the spectral region below

the plasmon frequency (the infrared and visible), the metal presents as opaque

due to the high reflectivity. Above the plasmon frequency into the ultraviolet

region, the sign of ε' changes. Here, the metal is highly transmitting since the

reflectivity approaches zero [35, 85].

3.1.2   Size effects on the dielectric function

Due to the Pauli-exclusion principle and screening of coulomb

interactions, conduction band electrons in a bulk metal move freely for a

certain distance λ_τ before they experience a collision, even if they are

crowded together [35]. The scattering of the electrons by other electrons,

phonons, lattice defects and impurities is described by the damping coefficient

γ_D. In a bulk metal,

$$\gamma_D = \frac{v_F}{\lambda_\tau} \qquad (3.5)$$

where v_F is the electron velocity at the Fermi surface [ms^{-1}] and λ_τ is the

mean free path for electrons in the bulk metal [m]. The mean free path of the

electrons in gold is of the order of 40-50 nm [92].

For a particle whose size is comparable to or smaller than λ_τ, the mean

free path of electron becomes dominated by collisions with the particle

boundary [85]. The smaller the particle, the faster the electron reaches the

particle surface.   Surface scattering leads to a reduced effective mean free path L_{eff} and an increased damping term γ_{eff} (the inverse of the collision time) in the Drude model to account for these additional surface collisions. As a consequence, the resonance linewidth of particles' spectra, which provides a measure of the damping process for the collective plasmon oscillation, has been shown theoretically and experimentally that it is relative to the nanoparticles with various geometries [92-93]. γ_{eff} can be written as

$$\gamma_{eff} = \gamma_D + \frac{A v_F}{L_{eff}} \qquad (3.6)$$

where γ_D is the bulk metal damping constant [Hz], v_F is the electron velocity at the Fermi surface [ms^{-1}] and L_{eff} is the effective mean free path for collisions with the boundary [m]. A is a dimensionless parameter related to the details of the scattering processes. It is nearly unity assuming that conduction electron scattering at the surface is totally inelastic. Surface scattering compels the electrons to move randomly at the Fermi velocity by an average chord length until the next surface collision. The chord length between the two points on the surface where the electron loses its energy is the effective mean free path L_{eff}. In terms of the volume V and surface area S of an arbitrary shape particle [94],

$$L_{eff} = \frac{4V}{S} \qquad (3.7)$$

The dielectric function of small gold particles, with consideration of intraband and interband transitions and the size effect, is given by

$$\varepsilon_{NP}(\omega) = \varepsilon_{\infty} - \frac{\omega_D^2}{\omega(\omega + i\gamma_{eff})} - \frac{\Delta\varepsilon\Omega_L^2}{(\omega^2 - \Omega_L^2) + i\Gamma_L\omega}$$

$$= \varepsilon_{DL}(\omega) + \frac{\omega_D^2}{\omega(\omega + i\gamma_D)} - \frac{\omega_D^2}{\omega(\omega + i\gamma_{eff})} \qquad (3.8)$$

In Chapter 6, the investigation of small Au nanospheres and Au nanorods is carried out. The dielectric function of gold including the size effect is employed for the calculation of their dielectric functions in that Chapter.

3.1.3   Aggregation effects

Thermal evaporation of bulk gold onto a substrate such as glass, mica or quartz, can be used to fabricate gold films of varying thickness. Initially, bulk gold at high temperature is ionised. Charged and neutral clusters nucleate in the gas phase [95]. These Au clusters initially land on the bare substrate as isolated 'islands' to form a discontinuous scattering structure. Neutral clusters experience Brownian coagulation to form particles while Coulomb force is repulsive for charged clusters with similar sizes but changes to be attractive

when their size difference is large. The attachment of several clusters constructs larger clusters. As evaporation continues, a percolation threshold is approached due to the continuous growth of both the cluster size and its distribution on the substrate. Gold islands coalesce on the substrate and eventually create a continuous and electrically conductive film. The size of the Au islands increases with the nominal thickness of the film and their presence becomes less distinguishable in thicker films as compared to thin ones [84].

The metallic nano-islands at the surface of a film embedded in the surrounding ambient medium (which is typically insulating) can be regarded as a composite system [96-97].   When the metallic islands are much smaller than the incident wavelength, this inhomogeneous medium can be approximated as a quasi-homogeneous effective-medium material, whose dielectric function has contributions from both the insulating medium and the metallic particles.

The Maxwell-Garnett (MG) theory is one of the earliest and most well known approximations that can be used to interpret the properties of such an inhomogeneous medium. Assuming the local electric field generated by the interaction of the metallic particle and the external electric field is of Lorentz type [83], the effective dielectric constant ε_{eff} of the composite is related to those of the metal particles ε_p and the insulating medium ε_i as

$$\frac{\varepsilon_{eff} - \varepsilon_i}{L_p \varepsilon_{eff} + (1 - L_p)\varepsilon_i} = f_p \frac{\varepsilon_p - \varepsilon_i}{L_p \varepsilon_p + (1 - L_p)\varepsilon_i} \quad (3.9)$$

where L_p is the depolarisation factor determined by the shape and orientation of the particles and f_p is the volume fraction of metal particles within the film. (The depolarisation factor L_p will be described in detail in Sec. 6.1.1. For a spherical particle, $L_p = 1/3$).

MG theory is applicable when there are only a small proportion of metal particles which are widely separated. For the situation of a high particle volume fraction, Bruggeman provided the effective dielectric constant of a random mixture of two component materials that is expressed as

$$f_p \frac{\varepsilon_p - \varepsilon_{eff}}{\varepsilon_{eff} + (\varepsilon_p - \varepsilon_{eff})L_p} + (1 - f_p) \frac{\varepsilon_i - \varepsilon_{eff}}{\varepsilon_{eff} + (\varepsilon_i - \varepsilon_{eff})L_p} = 0 \quad (3.10)$$

ε_{eff} can be solved as [98]

$$\varepsilon_{eff} = \frac{\varepsilon_i}{2(1 - L_p)} [1 - 2L_p + \frac{L_p - f_p}{s} \pm \frac{\sqrt{s^2 - 2(f_p + L_p - 2f_p L_p)s + (L_p - f_p)^2}}{s}]$$

$$(3.11)$$

where s has the form $\varepsilon_i / (\varepsilon_i - \varepsilon_p)$. One branch in the solutions of Eq. (3.11) which has positive values in the imaginary part is chosen as the effective dielectric function ε_{eff}.

(a)   (b)
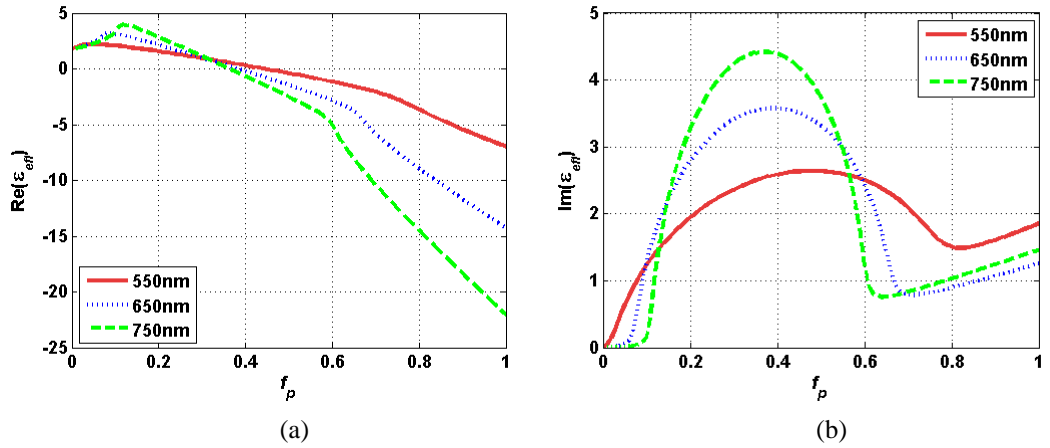
Figure 3.3 Evolution of the real (a) and imaginary part (b) of the dielectric constant of a

gold-water mixture as a function of the volume fraction of gold particles. The solid red, dotted

blue and dashed green lines represent the dielectric constant at 550 nm, 650 nm and 750 nm

respectively.

The dielectric constant of an effective medium formed by gold and water

(n=1.33) as a function of volume fraction is shown in Fig. 3.3. $\varepsilon^{'}$ and $\varepsilon^{''}$ vary

in a non-monotonic fashion as the volume ratio of gold is increased.

Considering the volume fraction f_p extending beyond 0.8, $\varepsilon^{'}$ decreases and

$\varepsilon^{''}$ increases quasi-linearly with f_p.

Au film fabricated on a coverslip by thermal evaporation is investigated in

Chapter 5, and the effective medium theory is employed to calculate the

dielectric constant of the interface between the gold surface and the ambient

environment in that Chapter.

3.2   The electrical double layer

Polarising an electrode alters the metal's Fermi level and induces the movement of electrons at the metal surface. The charged surface attracts opposite charges towards the neighbourhood of the electrode and sets up an electrical double layer at the metal-solution interface. The different Fermi levels between the metal and the ions and neutral molecules in the electrolyte solution are balanced by the convection of electrons through the double layer. Many natural phenomena, such as biological membranes, crystal growth and colloid stability, are related to the construction of the double layer [54-55].

Helmholtz was the first pioneer [54-55, 99] to think about the distribution of charges on the metal surface. He raised the concept of the double layer to explain the consequence of opposite charges residing on the surface of metals separated by distances of molecular order. The charges approaching the metal are regarded as point charges by Gouy and Chapman and are distributed in a diffuse layer as the result of electrical force competing with thermal diffusive force. A high concentration of electrolyte causes excess charge to align at the region near the metal surface, while charges are distributed further from the surface of the metal in the case of lower concentrations since the electrostatic force is weaker. Stern combined the merits of both Helmholtz's and Gouy-Chapman's explanations for the double layer and envisaged the ions as having finite size. He also proposed a more elaborate theory for the electrical double layer.

Emerging theoretical models have begun to account for the ion-specific behaviour and the assumption of ions as hard spheres [100-102] to improve the double layer theory. However, in this thesis, Stern's modification is used as the primary model to investigate the electrical double layer constructed at an Au film-electrolyte interface in Chapter 5 and an Au nanoparticle-electrolyte interface in Chapter 6 respectively.

3.2.1   Gouy-Chapman-Stern (GCS) model
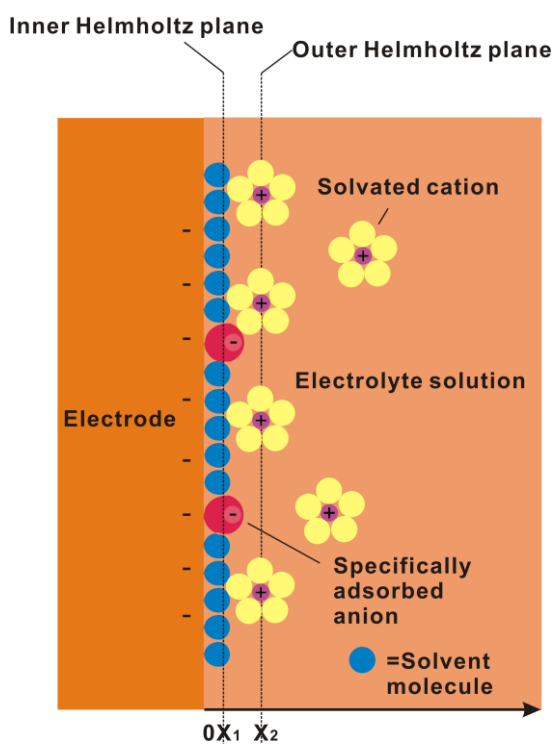
Figure 3.4 GCS model of the double layer under the condition of anions specifically adsorbed

on the electrode

The Gouy-Chapman-Stern model gives a general description of the

electrical double layer. The behaviour of the electrode and the electrolyte solution resembles a capacitor that can accumulate and release charges at the electrode-solution interface. At a given potential, the charges existing on the metal electrode induce an equal quantity but opposite sign of ions to reside in the vicinity of the metal-solution interfacial region together with the presence of oriented molecule dipoles. A schematic representation of the GCS model is illustrated in Fig. 3.4.

The electrical double layer consists of three regions, the inner Helmholtz layer, the outer Helmholtz layer and the diffuse layer [103-104]. Solvent molecules together with some specially adsorbed anions adsorb on the surface of the electrode through Coulombic and van der Waals interactions. Because anions are less strongly hydrated than cations, they are formed more commonly as the specific adsorption ions. The orientation of the solvent dipole is dependent on the polarisation of the electrode and the adsorbed anions. The solvent molecules and the anions adsorb firmly on the metallic surface, to form an inner layer called the compact layer. The locus of the centre of this layer at x_1 is called the inner Helmholtz plane. Meanwhile, additional hydrated cations are attracted by the metal surface. Water molecules have a strong dipole moment so they prefer to bind to ions, especially cations. The locus of the centre at x_2 of these non-specially adsorbed ions with closest approach to the electrode surface is called the outer Helmholtz plane. These excess hydrated cations are repelled by the outer Helmholtz layer as well as by competition

from other cations moving towards the electrode. Thermal motion makes these ions distribute in a three dimensional region called the diffuse layer to achieve equilibrium. The diffuse layer extends from the outer Helmholtz plane x_2 into the bulk of the solution.

The capacitance of this electrical double layer C_D is made up of two capacitors in series, the capacitance of the Helmholtz plane C_H at $0 < x < x_2$ and the capacitance of the diffuse layer C_{diff} extending from x_2 into the bulk solution. In the assumption that there are no specially adsorbed ions on the metal electrode, the double layer capacitance C_D [Fm^{-2}] for a symmetrical $z : z$ electrolyte with the bulk concentration n^0 [mol L^{-1}] is given as [103]

$$C_H = \frac{\varepsilon_0 \varepsilon_r}{x_2} \tag{3.12a}$$

$$C_{diff} = \sqrt{\frac{2\varepsilon_0 \varepsilon_r z^2 e^2 10^3 N_A n^0}{kT}} \cosh(\frac{ze\psi_2}{2kT}) \tag{3.12b}$$

$$\frac{1}{C_D} = \frac{1}{C_H} + \frac{1}{C_{diff}} = \frac{x_2}{\varepsilon_0 \varepsilon_r} + \frac{1}{\sqrt{\frac{2\varepsilon_0 \varepsilon_r z^2 e^2 10^3 N_A n^0}{kT}} \cosh(\frac{ze\psi_2}{2kT})} \tag{3.12c}$$

where ε_0 is the permittivity of vacuum, ε_r is the relative static permittivity of the medium and x_2 is the closest distance that the counterion can approach the metallic surface. A molecular thickness of 5 Å is used here [9]. N_A is Avogadro's number, z is the valence of the ion, *e* is the electron charge [C], *k* is Boltzmann's constant [JK^{-1}], *T* is the absolute temperature [K], and ψ_2 [V]

is the electrical potential at position x_2.

Considering that specially adsorbed ions are absent in the region $0 \le x \le x_2$, the charge density is zero. The electric field $d\psi / dx$ is constant and the potential varies linearly in the Helmholtz layer from the electrode surface, where the potential is ψ_0 [V], to the potential ψ_2 at position x_2,

$$\psi_0 = \psi_2 - (\frac{d\psi}{dx})_{x=x_2} x_2 \qquad (3.13)$$

ψ_2 can be solved graphically and substituting it into Eq. (3.12) to obtain C_D.

Therefore, the total capacitance C_D is lower than that of either C_H or C_{diff}. The potential alters linearly from the electrode surface $(x=0)$ to the outer Helmholtz plane $(x=x_2)$. Then, the potential exponentially changes from the outer Helmholtz plane to the interior of the electrolyte. The derivation of the double layer capacitance is described in detail in Appendix A.2.

The reciprocal of κ is the Debye length used to characterise the thickness of the double layer [m],

$$\kappa = \sqrt{\frac{2 \times 10^3 N_A n^0 z^2 e^2}{\varepsilon_0 \varepsilon_r kT}} \qquad (3.14)$$

and is dependent on the concentration of electrolyte n^0.

The capacitance profile for a 1:1 electrolyte is shown in Fig. 3.5. At lower

electrolyte concentration, the capacitance C_D is dominated by the diffuse capacitance C_{diff} indicated by the presence of a parabolic curve. At larger electrolyte concentration, the double layer is compressed and the increased C_{diff} is comparable to C_H. The constant Helmholtz capacitance begins to dominate the overall double layer capacitance.
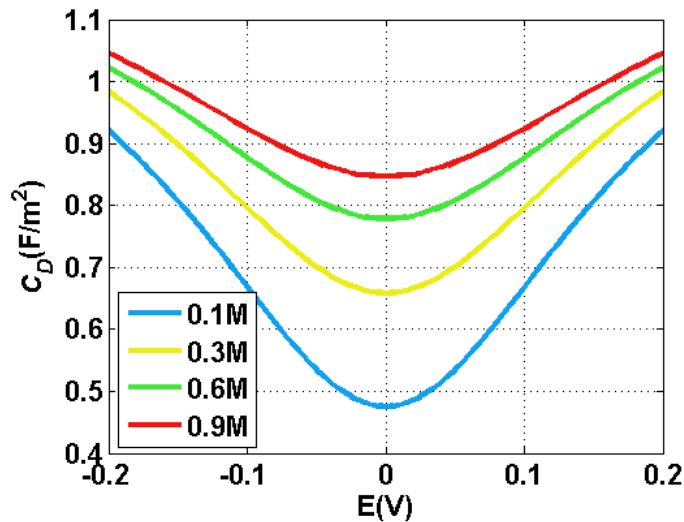
Figure 3.5   Double layer capacitance C_d as a function of potential and electrolyte

concentration. The electrolyte is assumed as a 1:1 electrolyte, such as NaCl.

The minimum capacitance is observed at 0 V, which is assumed as the point of zero charge (PZC) in this calculation. Solvents in contact with the electrode surface may have preferential orientation in the presence of specially adsorbed cations or anions. The applied potential on the electrode is adjusted to be the point of zero charge to achieve the condition that no free excess charges exist on the metal electrode surface, where the charge density of cations is equalised to that of anions. Because the GCS model treats the ions as

dimensionless and does not account for the specificities and non-specificities of ions, the saturation effect of the electrical double layer from the finite size of the ions is not considered by this approach [101-102, 105].

3.2.2   Charge transfer process

The equilibrium potential may be achieved when the metal is immersed in an electrolyte. The electrochemical potentials in the metal and the electrolyte, depending on their Fermi energy, govern the direction of electron transfer. Initially, the Fermi levels of the metal and electrolyte are different. Electrons will transfer from the substance with a higher to that of a lower Fermi level through the quantum tunnelling effect to overcome the work function. Releasing electrons from the metal into the electrolyte generates a cathodic current while removing electrons from the electrolyte to the metal generates an anodic current. The potential between the metal and electrolyte caused by the electron flow creates a double layer at their interface to counterbalance the cathodic and anodic reaction. Eventually, the net current approaches zero as the balanced result of the cathodic and anodic reaction. At the equilibrium state, equal Fermi energy of the two phases is attained [103-104].
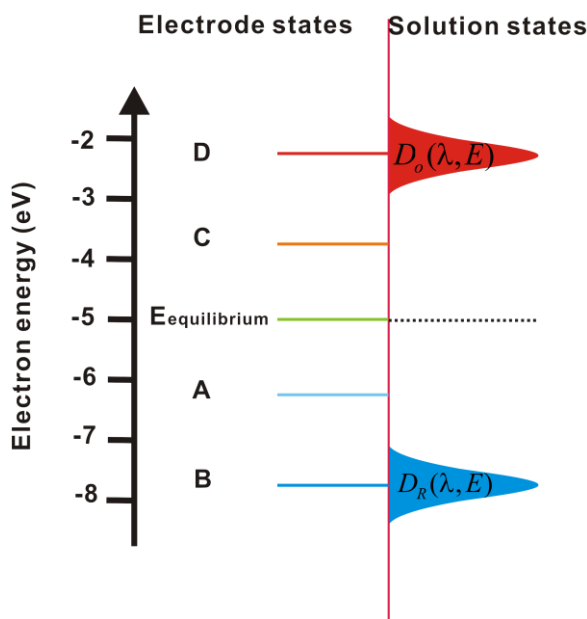
Figure 3.6   Relationships of the electronic energy states between a metal electrode and an electrolyte solution containing one oxidised and one reduced species. $D_0(\lambda, E)$ and $D_R(\lambda, E)$ are the energy state distributions for the oxidised and reduced species respectively, which are determined by the reorganisation energy λ and the electron energy E.

Considering an electrochemical experiment with one redox-active couple employing a three-electrode system, where the potential of the working electrode is controlled with respect to the reference electrode, the measurement of current generated by scanning the potential gives useful information about the nature of the reaction in the solution. Overpotential applied on the working electrode either accelerates the anodic reaction rate and slow down the cathodic reaction rate or vice versa, depending on the direction of overpotential. If driving the electrode to a positive potential, the Fermi level of atoms in the

electrode is decreased. An anodic process takes place where the electron is transferred from an occupied state of the ion or neutral molecule (reduced species) in the double layer, or adsorbed on the electrode surface to an unoccupied state in the conduction band of the metal electrode. Conversely, a cathodic reaction occurs at negative potential and the Fermi level of atoms in the metal is elevated as a consequence. An electron is transferred from the conduction band of the metal electrode to an unoccupied state of the ion or neutral molecule in solution (oxidised species).

Suppose the initial potential on the working electrode is at the equilibrium potential located between the Fermi levels of the reduced and oxidised species, as shown in Fig. 3.6, driving the potential in a positive direction (*A*) induces the Fermi level of the metal electrode towards a lower energy level, but unoccupied states on the electrode do not match the Fermi level of the reduced species. The current flow at this condition is only to charge the electrical double layer. When the potential is continually increased (*B*) to satisfy the requirement of overlapping the Fermi level of the electrode and that of the reduced species, oxidation is activated effectively in that electrons are transferred from the reduced species to the electrode. A sharply rising faradaic current dominates the current-potential curve at this moment. When the potential is negatively scanned, the anodic reaction is decelerated and the Fermi level of the electrode is raised. When the overpotential is reduced to point *C* where the Fermi level of the electrode is lower than that of the oxidised

species, a charging current is observed in the current-potential curve. Increased negative potential (*D*) effectively boosts the Fermi level of the electrode to overlap that of the oxidised species and enable electrons to transfer from the metal electrode to the oxidised species.

The thermodynamic potentials for deposition of Na^+ and evolution of Cl^- are -2.911 V vs. Ag/AgCl (sat. NaCl) and 1.161 V vs. Ag/AgCl (sat. NaCl) respectively [103-104]. Both of them lie appreciably below and above the potentials required to evolve oxygen and hydrogen. If aqueous NaCl is used as the supporting electrolyte, it improves the conductivity of the solution and meanwhile avoids the redox reaction taking place on Na^+ and Cl^-.

3.3   The space charge region

The electron density of the metal electrode adjusts in the presence of an external electric field. The induced electric field caused by the separated equal density of electrons and holes in the space charge region near the metal surface neutralises the effect of the external electric field to approach the equilibrium state [103, 106].

The plasmon frequency determining the dielectric constant of noble metal is dependent on the electron density. Adjustment of the electron density in the space charge region consequently affects the metal's dielectric constant in this region as the result of electric field. Therefore, the modeling in Chapter

5 and 6 related to the investigation of the influence of potential on Au film and Au nanoparticle has employed the space charge region to take account of the change in the gold's dielectric constant caused by the potential.

3.3.1   Electron screening

Potential applied to the metal electrode perturbs the initial equilibrium. Creation of the electrical double layer at the metal-solution interface intensifies the external electric field. An excess of electrons move towards the bulk metal in the case of a positive potential on the metal electrode. Remaining holes act as positive charges and flow towards the metal surface. Excess electrons and holes distributed at the space charge region develop the induced electric field to decrease the influence of the external electric field. The resultant electric field affects the energy of electrons in the space charge region but its effect is negligible beyond this layer. The Fermi level at the metal surface decreases due to the accumulation of positive charges as compared to the bulk metal. The energy band is bent upward. In the case of a negative potential applied on the electrode, electrons flow to the surface in the opposite direction to the external electric field, whilst the holes move towards the bulk metal. Their movement is confined to the surface space charge region. The band energy at the metal surface is bent downward because of the positive energy level at the surface compared to the field free bulk metal.

The interaction of electron screening was elucidated in the Thomas-Fermi approximation. The external electric field is able to penetrate but exponentially decays into the metal, characterised by λ_{TF}, the Thomas-Fermi screening length. Beyond this screening distance, the absence of an external electric field enables the electrons move freely in the metal.

The Thomas-Fermi screening length λ_{TF} is given by [107]

$$\lambda_{TF} = \left(\frac{e^2}{\varepsilon_0} D_m(\varepsilon_F) \right)^{-\frac{1}{2}}$$

$$= \frac{\pi \hbar}{e} \sqrt{\frac{\varepsilon_0}{m}} \left(3\pi^2 N \right)^{-\frac{1}{6}} \qquad (3.15)$$

where ε_0 is the permittivity of vacuum, e is the electron charge, $D_m(\varepsilon_F)$ is the density of states for the energy of an electron at the Fermi level, $\hbar = h/(2\pi)$, where h is Planck's constant, m is the mass of electron and N is the free electron density. Usually, this screening length, which is the penetration depth of the electric field into the metal, is extremely short, typically less than 1Å.

3.3.2   The effect of potential on the dielectric function

As described above, an applied potential on the metal electrode results in an electrical double layer at the metal-solution interface and the space charge

region inside the metal. The very small thickness of the space charge region as compared to the thickness of the electrical double layer at a metal-solution interface makes the contribution of capacitance from the space charge region to the overall capacitance negligible compared to the capacitance of the electrical double layer since they are in series[103]. Most of the potential drops on the solution side across the double layer rather than across the space charge region.

When a noble metal electrode is electrochemically polarised, the modification of the dielectric function was considered by McIntyre [57]. The perturbation caused by the potential induces impurity atoms and ions to adsorb on the metal surface via the bridge of the electrical double layer in solution phase. The electrons in the valence and conduction energy band in the metal self adapt according to the electric field. The penetration of the electric field is confined to the space charge region as the result of screening. The electronic band structure of the bulk metal retains its original configuration.

The distribution of electrolyte ions with different charges in the double layer is compensated by the electronic charges localised at the metal surface dependent on the capacitance of the electrical double layer.

An applied potential ψ [V] decaying from the metal surface into the bulk electrolyte solution induces a surface charge density Q [Cm^{-2}] at the metal surface,

$$Q = C_D \psi \qquad (3.16)$$

where C_D is the capacitance [Fm^{-2}] of the double layer.

The electron density [m^{-3}] in the space charge region within the Thomas-Fermi screening length is adapted according to these excess charges residing on the metal surface,

$$\Delta N = \frac{Q}{\lambda_{TF}} \qquad (3.17)$$

The adjustment of electron density in the conduction band leads the plasmon frequency of the noble metal to be

$$\omega_{D\_V} = \sqrt{\frac{(N+\Delta N)e^2}{m^* \varepsilon_0}} \qquad (3.18)$$

where N is the unperturbed free electron density.

The tuned plasmon frequency results in the potential induced dielectric function of bulk metal in the space charge region as

$$\varepsilon_{DL\_V}(\omega) = \varepsilon_\infty - \frac{\omega_{D\_V}^2}{\omega(\omega+i\gamma_D)} - \frac{\Delta\varepsilon\Omega_L^2}{(\omega^2-\Omega_L^2)+i\Gamma_L\omega} \qquad (3.19)$$

Substituting Eqs. (3.18) and (3.19) into Eqs. (3.8) and (3.11) can obtain the dielectric function of nano-sized particle and composite system at metal

film surfaces respectively.

3.4   Summary

The dielectric constant of noble metals in the infrared region is described well by the Drude model by accounting for electron intraband transitions. Considering the contribution of electron interband transitions in the visible region, one Lorentz oscillator is added to the Drude model to improve the analysis of the dispersion of the noble metal's dielectric function.

The adjustments to the dielectric function of metal caused by the size effect and aggregation are modifications to their bulk counterpart. The consequence of scaling down a metallic particle's size to the submicron region is an increase in surface scattering. As a result, the electron collision rate increases significantly. Islands resembling metallic particles reside on the metal surface as a result of the fabrication process. The interaction of these metallic nano-islands with incident light was treated by Bruggeman. Both the metal nano-islands and the surrounding insulating medium contribute to the optical properties of the metal-dielectric interface.

The electric field resulting from the potential applied to the metal electrode is eliminated at the vicinity of the metal surface by the electrical double layer in the electrolyte solution and the space charge region in the metal. The charges accumulated by the electrical double layer capacitor at the

metal-electrolyte interface are compensated by the induced charges distributed in the space charge region near the metal surface. The penetration depth of an external electric field into the metal is limited to the Thomas-Fermi screening length because of the screening effect. The change in the dielectric function of a metal electrode affected by potential due to the adjustment of electron density is confined to the space charge region.

Chapter 4   Objective-type dark-field imaging spectrometer and experimental methods

Noble metal nanostructures have been studied for several decades due to their unique optical properties related to the phenomenon of localised surface plasmon resonance (LSPR) [108]. Light scattering and absorption by the particles are dominated by this resonance as the result of the collective oscillation of conduction electrons [109]. Charge transport on the surface of noble metal particles has dramatic consequences on their optical properties [11-12, 110]. The potential application of noble metal nanoparticles designed as chemical and biological sensors for the electrochemical reactions can be accessed by spectroelectrochemical techniques, which can provide a definitive description of the metal-solution interface and a breadth of information on the reactions occurring at the interfacial region. The exploration of the perturbed optical signal from nanostructure maintained under potential control provides complementary compositional and structural information to investigate the electrical influence with conventional electrochemical techniques [55, 103].

Traditional absorption spectroscopy of colloids collects information from an ensemble of many particles, and is therefore affected by fluctuations in particle size and shape. This limitation is circumvented by taking advantage of single particle technologies. The development of spatial modulation spectroscopy [111] and the photothermal interference contrast method [73]

allow the absorption of single particle smaller than 40 nm to be examined. However, most absorption-based techniques need to scan the nanoparticle in the focal plane, which is complex and time-consuming. In the work presented in this thesis, objective-type dark-field illumination is used, which achieves high contrast to allow detection of single particles under potential control, while allowing full access to the sample from above.

In this chapter, the main experimental methods used in this work are introduced. Firstly, the primary instrument, a custom objective-type dark-field imaging spectrometer is described. Several metal nanostructures were prepared for study, including gold films and gold nanoparticles of various shapes and sizes. The fabrication of Au film by thermal evaporation and Au nanoparticles arrays by nanosphere lithography (NSL) will be introduced before the drop-casting of gold nanoparticle suspensions on substrates. The preparation and procedure of the electrochemical experiment are presented towards the end of this chapter.

4.1   The epi-illuminated dark-field imaging spectrometer

On impinging an object, an illuminating beam produces two resultant components. The first is an undeviated (zero-order) wave, which only passes through the object without any interaction with it. The second is the deviated wave (diffracted wave) that is scattered by the object in many directions.

Dark-field microscopy is a sensitive technique because the nondiffracted rays are removed and the image formation is based solely on the diffracted wave component. By illuminating the object at an oblique angle, only the diffracted light from the specimen is collected by the objective lens whereas the nondiffracted rays are excluded. The visibility of the object is enhanced as the result of the absence of nondiffracted background light [112].

The investigation of single noble metal nanocrystal has been performed by collecting its scattered light using dark-field illumination [50, 108], where the zero-order, unscattered light is blocked and only the higher orders of diffracted light are collected. Thus the scattering from nanocrystals is detected in the presence of a low background. The observation of single nanoparticles under the perturbation of potential whose magnitude is limited to be within the nanocrystal's double layer charging region gives rise to the challenge to extract the weak scattered light produced by the potential.

The custom dark-field spectrometer was developed to study the nanoparticles under the potential control. A linear variable interference filter was integrated into a dark-field microscope that used epi-illumination through the objective lens, with two CCD cameras as imaging and reference sensors respectively. Only the scattered light from the nanocrystal is collected by the imaging camera. The reference camera is used to directly monitor the stability of light from the light source. A micromotion stage translated the interference filter to scan the illumination wavelength, and quasi-monochromatic images

were acquired at many different wavelengths. Analysis of regions of interest from these images was used to calculate the scattering spectra of the nano-objects.

4.1.1   Wavelength calibration of the interference filter

A HG-1 Mercury Argon source (Ocean Optics) was used as a calibration source for the linear variable interference filter (VIS-NIR 200, Edmund Optics, with a 400 nm to 1000 nm spectral range, bandwidths from 40-65 nm) to characterise a dispersion curve that describes the position of the central wavelength with respect to the filter position, which can be expressed as

$$\lambda_X = LD \times X + B \qquad (4.1)$$

where λ_X [nm] is the transmission wavelength corresponding to the position X [mm] on the filter, LD [nm/mm] is the linear dispersion, intercept B [nm] is the offset wavelength at the beginning of the filter.

The filter was mounted on a motorised stage (8MT175-200, Standa) directly between the calibration source and a CCD camera (SXVF-M7, Starlight Xpress, pixel size: 8.2 μm×8.4 μm, image format: 752 × 580). Several Hg and Ar spectral lines were available from the calibration source. The filter was translated from its initial position at 0 mm along the full range of 200 mm,

so that separated emission lines were sequentially projected onto the CCD camera. By recording two positions on the filter where the emission peaks were the strongest, namely 546.08 nm (measured at 63.6 mm), and 763.51 nm (measured at 112.8 mm), the linear dispersion *LD* was determined as 4.42 nm/mm. The slight variation from the linear dispersion of 3.6-4.4 nm/mm provided by manufacturer was considered acceptable.
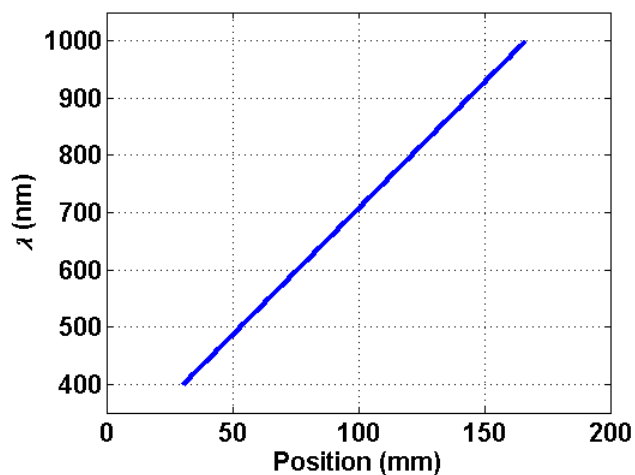
Figure 4.1 Relationship between transmission wavelength and the position of the linear

variable interference filter

Substituting the linear dispersion *LD* and one pair of position and wavelength into Eq. (4.1) can evaluate the dispersion curve for this filter,

$$\lambda_X = 4.42X + 265 \qquad (4.2)$$

A graph of the dispersion curve for this filter is shown in Fig. 4.1.

4.1.2   Sampling and magnification requirements

The central component of the spectrometer is a Zeiss objective, NA=1.25, 100x oil-immersion. The back aperture *BA* [m] of this objective is written as [113]

$$F\_mo = \frac{F\_tube}{M} \qquad \text{(4.3a)}$$

$$BA = 2 \times F\_mo \times NA \qquad \text{(4.3b)}$$

where *F_mo* and *F_tube* are the focal lengths of the microscope objective and the tube lens respectively [m], *NA* is the numerical aperture and *M* is the magnification. This infinity corrected objective lens is specified for a 165 mm tube lens, so the diameter of this objective's back aperture is approximate 4.125 mm.

The spatial resolution, or the minimum distance that two adjacent points on a sample can be distinguished by the objective lens, is defined by the Rayleigh criterion as

$$d_{Rayleigh} = \frac{0.61\lambda}{NA} \qquad \text{(4.4)}$$

Nyquist-Shannon's theorem requires that a minimum of two pixels on the CCD are used to correctly sample the smallest resolvable feature on the

specimen. Taking the vertical scan line into account, the 8.4 µm height of one pixel should represent 122 nm in object space, for the case of visible light at 500 nm. The focal length of the objective used was 1.65 mm. Therefore, a minimum magnification of approximately 69x was required, that is a minimum tubes lens focal length of 113 mm, to ensure adequate spatial sampling. A lens with 125 mm focal length was selected as the tube lens for this microscope to satisfy this magnification requirement.

4.1.3   Dark-field and total internal reflection epi-illumination

Considering light propagating to the sample plane through a glass coverslip, the critical angle for total internal reflection (TIR) is given by

$$\theta_c = \sin^{-1}(\frac{n_1}{n_2}) \quad (4.5)$$

where n_1 and n_2 are the refractive indices of the sample medium and the coverslip respectively.

A coverslip with refractive index $n_2 = 1.517$ at 550 nm was used which gave a critical angle of 41.23 ° for a glass-air interface ($n_1 = 1.0$) and 61.25 ° for a glass-water interface ($n_1 = 1.33$).

The maximum illumination angle θ_m that the light emerging from the objective can impinge on the sample plane depends on the numerical aperture

NA of the objective,

$$NA = n_2 \sin \theta_m \qquad (4.6)$$

For the objective used, 55.48 ° is the maximum illumination angle and therefore TIR illumination can be implemented on a glass-air interface (Fig. 4.2 a). Exclusion of light below the critical angle produces a hollow cone of supercritical angle light in the 41.23 °-55.48 °angular range which converges on the sample plane, and creates an evanescent wave at the interface.

(a)   (b)
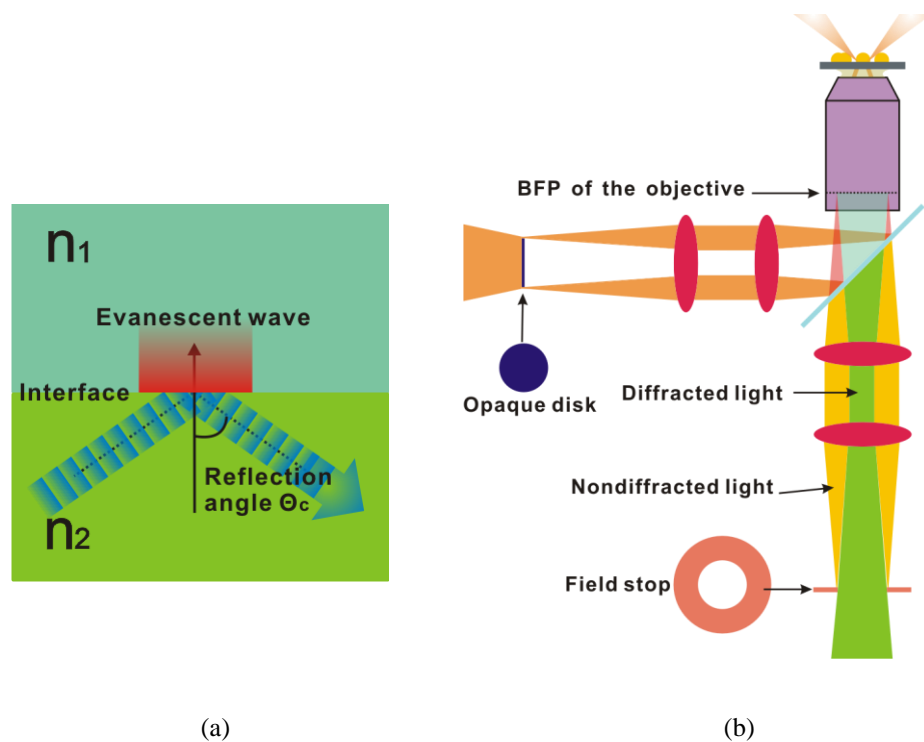
Figure 4.2   (a) Dielectric interface (b) Illustration of the epi-illumination dark-field

microscopy scheme

Dark-field microscopy is capable of studying single metal nanoparticles,

81

and an epi-illumination dark-field scheme permits the working electrode with immobilised nanoparticles to be arranged in the three-electrode cell, so the reference and counter electrodes can be configured above it (see Sec. 4.3 below). The key element of dark-field microscopy design is to isolate the nondiffracted and diffracted rays emerging from the object so that they locate at different regions in the diffraction plane at the back aperture of the objective lens. In order to achieve dark-field epi-illumination through the objective lens, the central, on-axis region of the illumination beam is typically blocked at the back focal plane (BFP), so that only oblique rays can strike the specimen [114-115]. The angle of light emerging from the objective to the immersion oil and coverslip is dependent on the radial position of the beam with respect to the optical axis when it transmits through the back focal plane of the objective. Placing an opaque disk of a certain diameter at the back focal plane excludes the subcritical rays. The back focal plane is located inside the objective lens and therefore inaccessible, so a conjugate plane was used. An aluminium disk of 3.3 mm diameter was chosen and located at one conjugate plane in the illumination path, so that the beam emerging from the objective was designed to have a $44\,^\circ$ minimum incident angle. When the specimen is excited by the illumination light, part of the nondiffracted wave which does not interact with it is reflected and focused as a bright ring in the back focal plane of the objective (the diffraction plane). The diffracted light reflected from the specimen occupies various locations across the entire back aperture of the

objective lens [112]. Since the nondiffracted and diffracted light are spatially separated at the diffraction plane, an aperture stop whose size matched that of the aluminium disk was placed at one conjugate plane at the imaging path to select the diffracted rays and form the dark-field image (Fig. 4.2 b).

4.1.4   Dark-field spectrometer optical arrangement
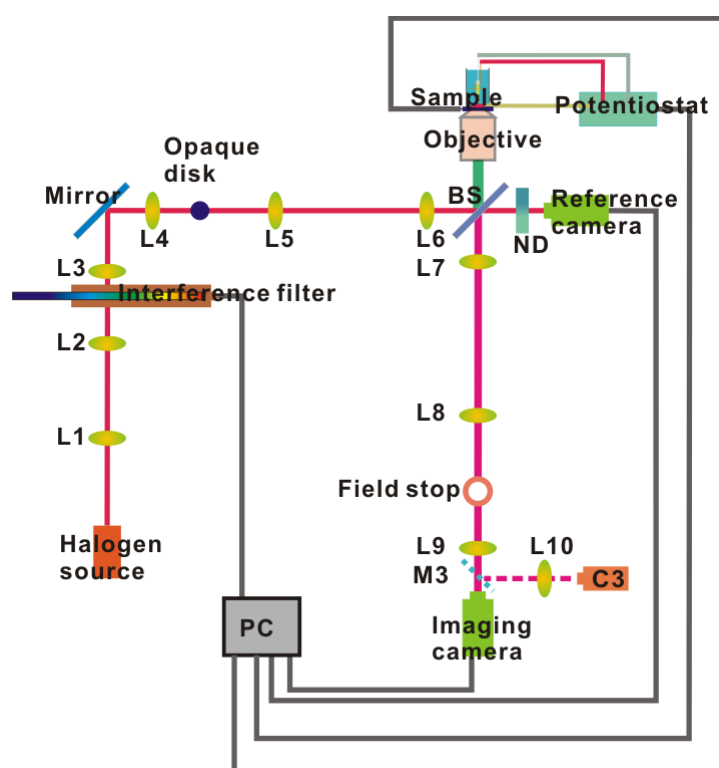
Figure 4.3   Dark-field imaging spectrometer schematic. L1-achromatic lens (f = 200 mm). L2-achromatic lens (f = 100 mm). L3-achromatic lens (f = 50 mm). L4- achromatic lens (f = 200 mm). L5- achromatic lens (f = 160 mm). L6- achromatic lens (f = 160 mm). L7-achromatic lens (f = 160 mm). L8-achromatic lens (f = 160 mm). L9- achromatic lens (f = 125 mm). L10- achromatic lens (f = 50 mm). C3- camera. BS- Pellicle beamsplitter (R/T ratio: 45/55 %). ND-Neutral density filter. M3-Mirror.

The dark-field spectrometer utilises the microscope's objective for both the illumination and the imaging of the sample. A schematic and a photograph of the dark-field spectrometer are shown in Figs. 4.3 and 4.4 respectively. White light illumination was provided by a halogen lamp. The source was imaged as an approximately 1 mm diameter spot by a pair of lens (L1, L2) onto the linear variable interference filter. The filter was mounted on a motorised stage and positioned at a plane conjugate to the back focal to the microscope objective lens.
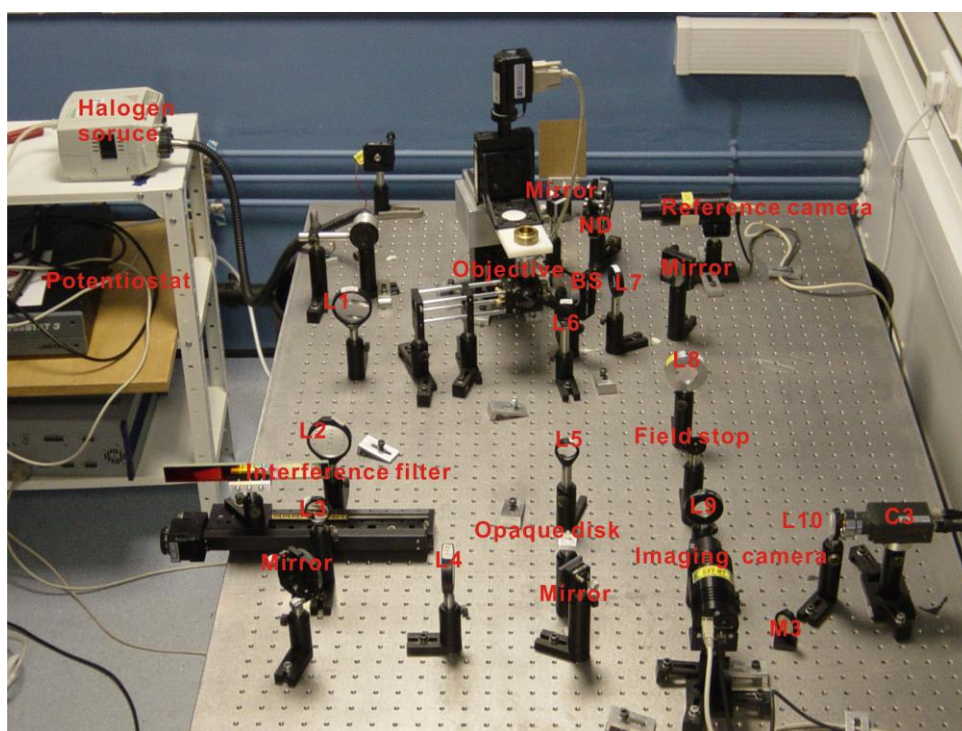
Figure 4.4   Photograph of objective-type dark-field imaging spectrometer. Part numbers of elements are corresponding to these labelled in Fig. (4.3)

A second pair of lenses (L3, L4) magnified the illumination source four-fold

and reimaged the spectrally filtered light onto the 3.3 mm diameter opaque disk located at a second conjugate back focal plane. This disk blocked the central portion of the beam from entering the objective lens. The annulus of rays created by this disk was directed into the back focal plane of the objective by a third pair of lens (L5, L6) and a beam splitter (BS). Light scattered by the sample and returned to the objective, passed through the beam splitter, and was directed by the fourth pair of lens (L7, L8) to an aperture stop placed at a third conjugate back focal plane in the imaging path. Only high order backscattered light was allowed to pass through the centre of the field stop and the lens L9 to produce a dark-field image at the imaging CCD camera. Although the field stop reduced the effective NA of the objective to be approximately 1.0, this was considered an acceptable trade-off to achieve dark-field imaging through the objective. Mirror M3 and lens L10 were used to image the back focal plane of the objective on the camera C3 when this was necessary for alignment purposes.

The transmitted illumination beam from the beam splitter was recorded by a second CCD camera and used as a reference to monitor the intensity stability at each wavelength and therefore minimised the effect of any fluctuations in the light source.

4.1.5   Imaging and processing of the recorded spectra

The motorised stage translated the variable interference filter to scan across the spectral ranges, sequentially illuminating the sample with a range of wavelengths. The imaging CCD camera recorded an image corresponding to each wavelength band. These quasi-monochromatic, high resolution images were stored as an image stack for post-processing. Images of a spectrally flat standard (WS-1-SL, Ocean Optics) were also collected with this system to characterise the spectrum of the lamp. Since the spectrometer was imaging the sample at many wavelengths, chromatic aberration had to be overcome in order to maintain high spatial resolution throughout the spectrum. To this end, the sample was mounted on a motorised z-stage (Physik Instrument) for automated fine focussing. The empirical relationship between the focus positions of the sample at each illumination wavelength was used to generate a mapping table for refocusing. Therefore, the image of the sample was recorded after it was refocused at each wavelength automatically. Software written in C++ language was used to control the imaging process.

Figure 4.5 illustrates the technique used to acquire the resonant scattering spectrum of single Au nanoparticles facilitated by an image processing program written in Matlab. The scattered light was calculated by integrating the gray intensity values in a small region containing the object of interest. An adjacent empty region of substrate of the same dimensions was also analysed for background subtraction. The background corrected spectrum was

normalised to the light source spectrum to yield the final scattering spectrum.

The spectrum was smoothed and typically fitted to a third-order polynomial to

determine its peak wavelength [74, 116-118].

(a)

(b)

(c)

(d)

(e)

(f)

(g)
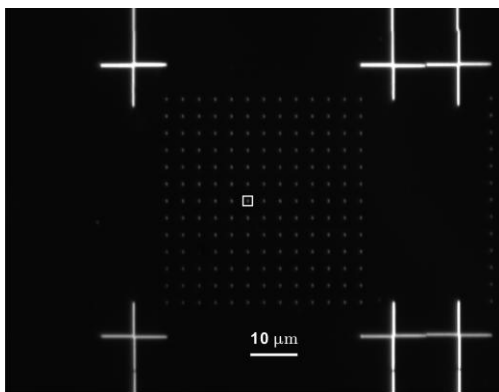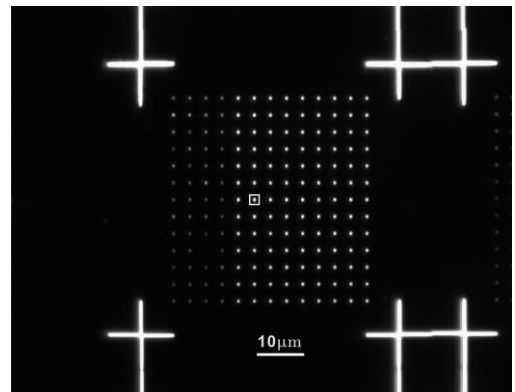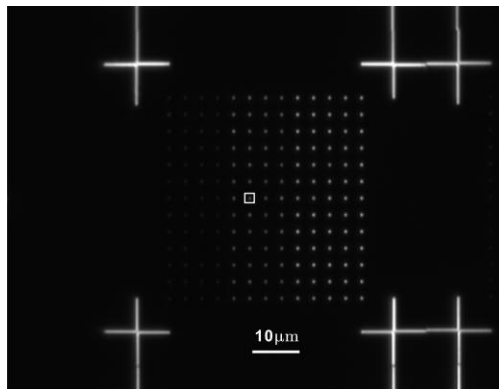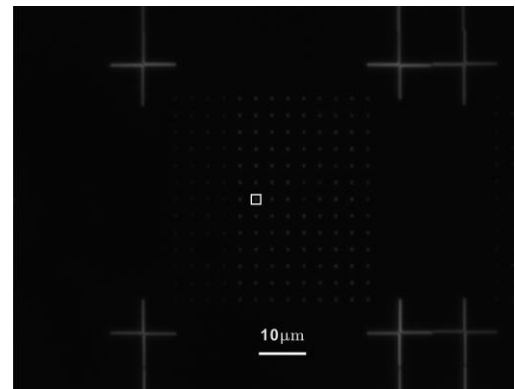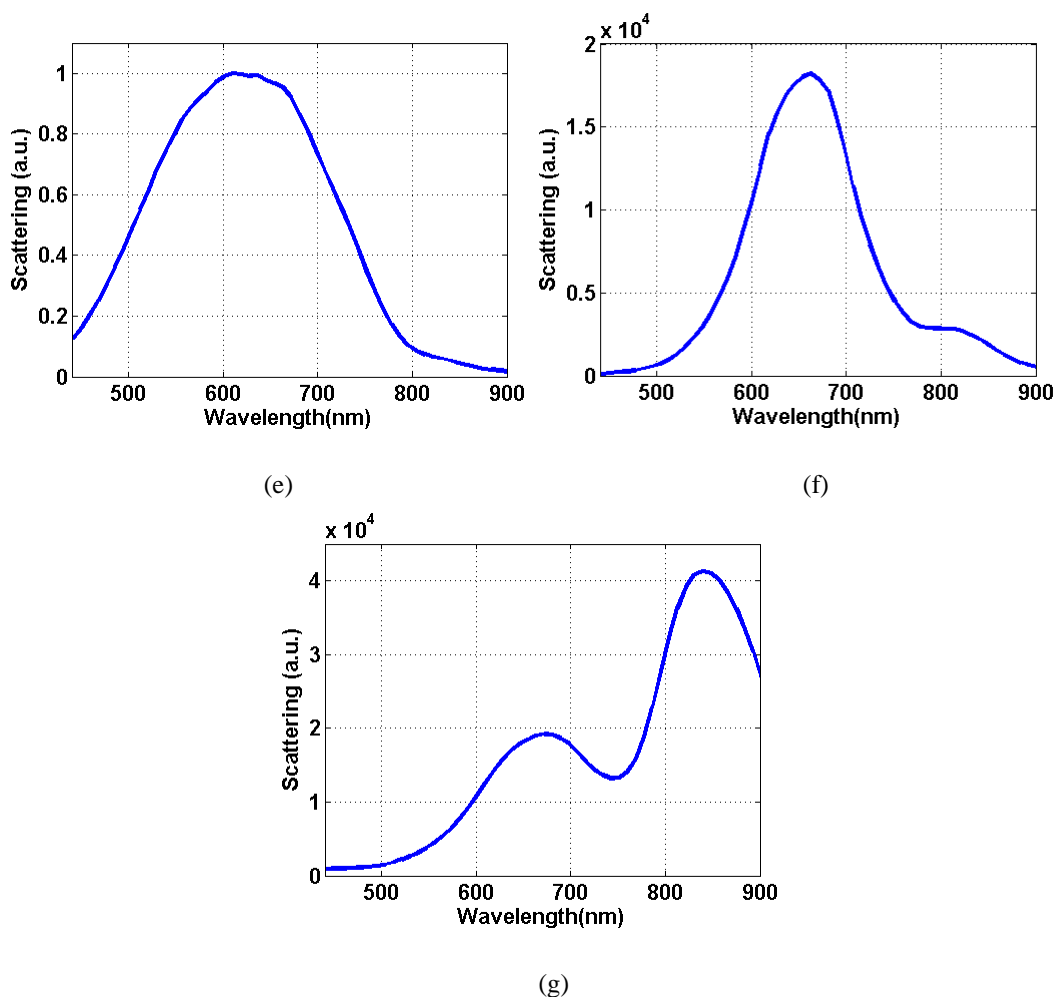
Figure 4.5 Image processing to calculate the spectrum. Dark-field images of Au cylinder

particles immersed in silicone oil at (a) 556.72 nm, (b) 653.96 nm, (c) 751.2 nm and (d) 839.6

nm. The Au particle of interest identified by the white box had an elliptical basis. The axes of

the ellipse were 120 nm and 60 nm respectively. (e) Lamp spectrum used for the normalisation

of the scattering spectrum (f) Raw scattering spectrum of Au particle of interest (g) Spectrum

of Au particle of interest with a peak scattering wavelength of 828.5 nm

4.1.6   Procedure for the detection of potential-induced scattering

The scattering strength of the nanostructure under potential control depends on both the intensity of the light source and the magnitude of the applied potential. Considering the transformation from electrical effects to the optical signal, the potential is transferred as scattered light but the signal is weak and imposed on a strong background. It is essential to reduce the noise coming from several sources, especially from fluctuations of the lamp.

Due to the small magnitude of potential applied to the nanocrystals, it was extremely difficult to observe the spectral shift directly by scanning scattering strength consecutively at several wavelengths under different potentials. To observe the influence of potential on the Au nanostructure, recording the scattering strength at a single wavelength was preferred. The synchronised imaging camera, reference camera and potentiostat began to record images and apply potential simultaneously. The beam from the lamp was divided into two at the beamsplitter. The sample beam was utilised to illuminate the nanostructure to obtain scattering I_s. The reference beam was diverted for the reference recording as I_r. The imaging camera and reference camera were triggered simultaneously to ensure accurate calibration. Division of the scattering from the nanocrystal and the reference recording, I_s/I_r, was used to extract the synchronised scattering component associated with the potential.

4.2   Sample preparation

Noble metal nanostructures exhibit localised surface resonance, which strongly depends on their geometric size and shape. Advances in nanoparticle synthesis techniques provide a wide range of nanostructure, such as nanorods, nanocubes, nanobranches [50]. The wide choices of fabrication techniques have boosted research efforts to investigate nanoparticles' various properties.

Two sets of gold films with nominal thickness of 16 nm and 50 nm were prepared in a thermal evaporation system with control of the deposition rate and pressure.

Nanosphere lithography creates regions of periodic, highly monodisperse nanostructure. The Au nanoprisms with 16 nm and 50 nm heights were fabricated on indium tin oxide (ITO) coated coverslips by nanosphere lithography.

Colloidal suspensions of Au nanospheres and nanorods solution were diluted to deposit these nanoparticles on ITO coated coverslips respectively. A low concentration of Au particle suspension was used to ensure that single Au particles could be resolved and isolated on the ITO substrate and analysed individually.

4.2.1   Materials

Polystyrene polymer 2 μm diameter nanospheres were purchased from

Invitrogen Detection Technologies. The density of nanospheres in the supplied suspension was 2 % by volume.

100 nm gold sphere colloidal suspension was purchased from BBInternational. The coefficient of shape variation was less than 8 %.

Two types of cetyltrimethylammonium bromide (CTAB) stabilised gold nanorods with length $L = 60$ nm, width $d = 25$ nm and $L = 73$ nm, $d = 25$ nm were purchased in colloidal solution from Nanopartz Inc. The shape monodispersity was greater than 95 %.

ITO coated coverslips (surface resistivity 15-30 Ω/sq) were supplied by Structure Probe, Inc.

The water was purified through a Milli-Q 18 MΩ cm system.

4.2.2   Thermal evaporation of Au films

Au films with nominal thickness of 16 nm and 50 nm were evaporated on glass coverslips at an evaporation rate of 0.1-1.5 nm/s. Evaporation was performed under high vacuum with a base pressure of 1×10^{-6}-2×10^{-6} Torr. The gold wire (99.99 % purity, Advent Research Materials Ltd) was heated up to fusion. The samples were mounted on an aluminium plate having four regularly spaced 24 mm diameter apertures and placed about 200 mm above the source. The evaporation rate and the thickness of the Au film were monitored using an Edwards FTM-5 film thickness monitor. The thickness of

the Au film was measured by a Rank Taylor Hobson Talystep surface profilometer. SEM images of the Au films are shown in Fig. 4.6.

<div align="center">(a)   (b)</div>
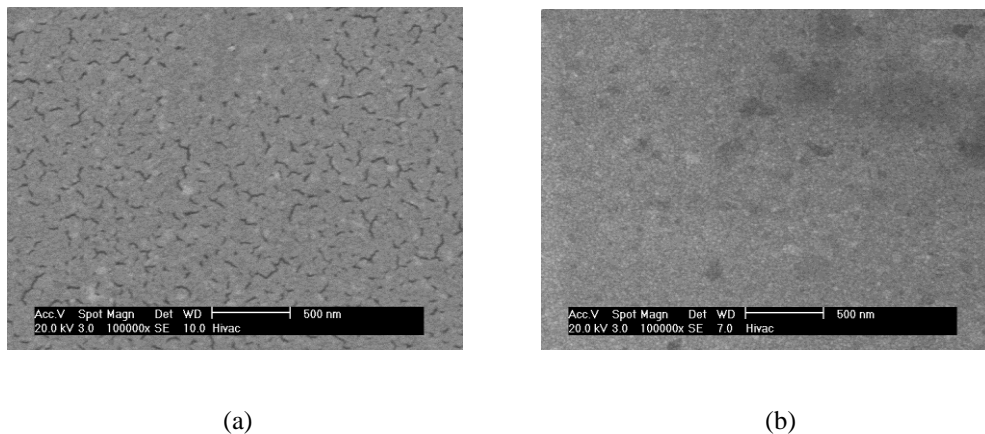
<div align="center">Figure 4.6 SEM images of (a) 16 nm Au film and (b) 50 nm Au film</div>

4.2.3   Nanosphere lithography

Nanosphere lithography is an inexpensive, flexible and high-throughput technique to fabricate nanoparticles array with controlled shape, size and interparticle spacing [44, 119-120].

The ITO coated coverslips were cleaned by immersing in acetone and isopropanol for 5 minutes each in an ultrasonic bath and then rinsed copiously with water. This procedure was repeated at least three times and then the coverslips were dried at room temperature.

The nanoprism fabrication process is shown in Fig. 4.7. 2 to 4 μl of nanosphere suspension was stirred with 10 to 20 μl of deionised water for dilution. The 5 μl of the mixture was drop-coated onto the substrate. The

nanospheres dispersed freely across the substrate allowing self assembly into a close-packed, hexagonal 2D colloidal crystal on the substrate. The boundary region of the droplet of diluted nanosphere suspension generally deposited multiple layers of nanospheres. During solvent evaporation, capillary force drew the nanospheres within the droplet together to crystallise as a single mask inside the droplet boundary. The size of the resultant relatively defect-free monolayer domain was usually 2-4 mm^2.

(a)   (b)

(c)   (d)
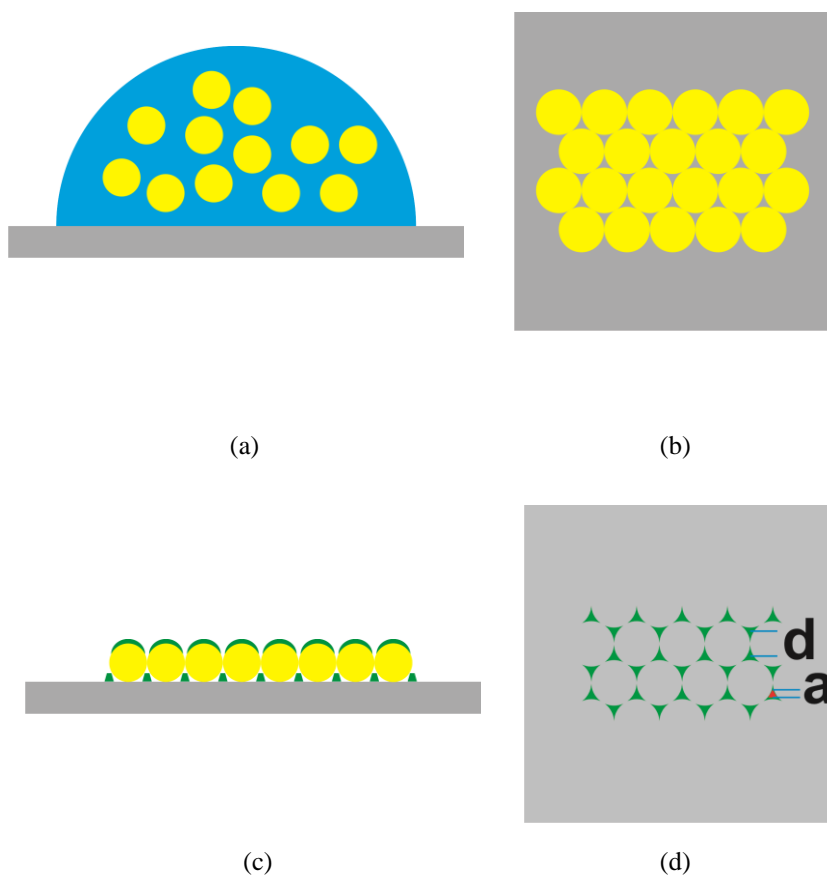
Figure 4.7 Schematics of the nanosphere lithograph fabrication process. (a) Drop-coating of the polystyrene nanospheres (b) Nanosphere monolayer mask (c) Deposition of Au metal on the nanosphere mask (d) Removal of the polystyrene nanospheres.

16 nm and 50 nm thickness Au films were thermally evaporated over the nanosphere masks. After gold deposition, the mask was removed to leave the gold nanostructure by ultrasonicating the sample in ethanol. The in-plane particle length *a*, defined as the perpendicular bisector of the largest inscribed equilateral triangular and the interparticle spacing *d* relative to the nanosphere diameter *D* are given by [120]

$$a = \frac{3}{2}(\sqrt{3} - 1 - \frac{1}{\sqrt{3}})D = 0.233D \qquad (4.7a)$$

$$d = \frac{D}{\sqrt{3}} = 0.577D \qquad (4.7b)$$
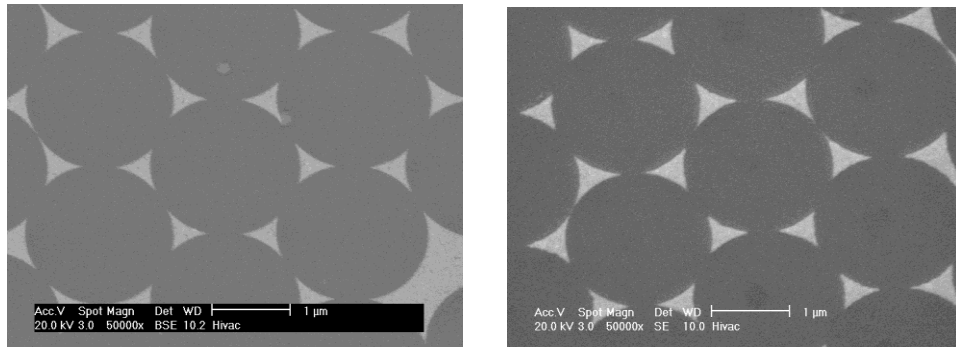
(a)   (b)

Figure 4.8   SEM images of nanosphere lithography fabricated nanoparticles. in-plane length ~ 466 nm, interparticle spacing ~ 1.1 μm, height ~ (a) 16 nm, (b) 50 nm.

The density of triangular nanoparticles, whose in-plane length was ~466 nm, interparticle spacing was ~1.1 μm, and out of plane height were ~16 and

~50 nm respectively, was roughly 6.93×10^6 mm^{-2}. SEM images of nanoparticles with triangular structure are shown in Fig. 4.8.

4.2.4   Immobilisation of Au nanoparticles on a substrate

Commercially obtained nanoparticles were stored in aqueous suspension. The colloidal solution was diluted in deionised water to a concentration of approximately 2.6×10^8 nanoparticles per millilitre. The ITO coated coverslips were cleaned as described in Sec. 4.2.3. A drop of diluted colloidal suspension was placed on the centre of the coated coverslip and allowed to dry at room temperature. ITO is a highly degenerate n-type semiconductor and the gold nanoparticle surface is positively charged because of the CTAB capping molecules. The gold nanoparticles are immobilised on the ITO coated coverslip via the electrostatic interaction. Figure 4.9 shows SEM images of spherical and rod-shaped nanoparticles. On the basis of the measurement of 40-50 nanoparticles for each type, the sizes of nanoparticles have an average diameter 100 nm, with a standard deviation 9 % in Fig. 4.9 (a), length of 60 nm with a standard deviation 14 % and width of 25 nm with a standard deviation 15 % in Fig. 4.9 (b), length of 73 nm with a standard deviation 18 % and width of 25 nm with a standard deviation 16 % in Fig. 4.9 (c) respectively.

(a)

(b)

(c)
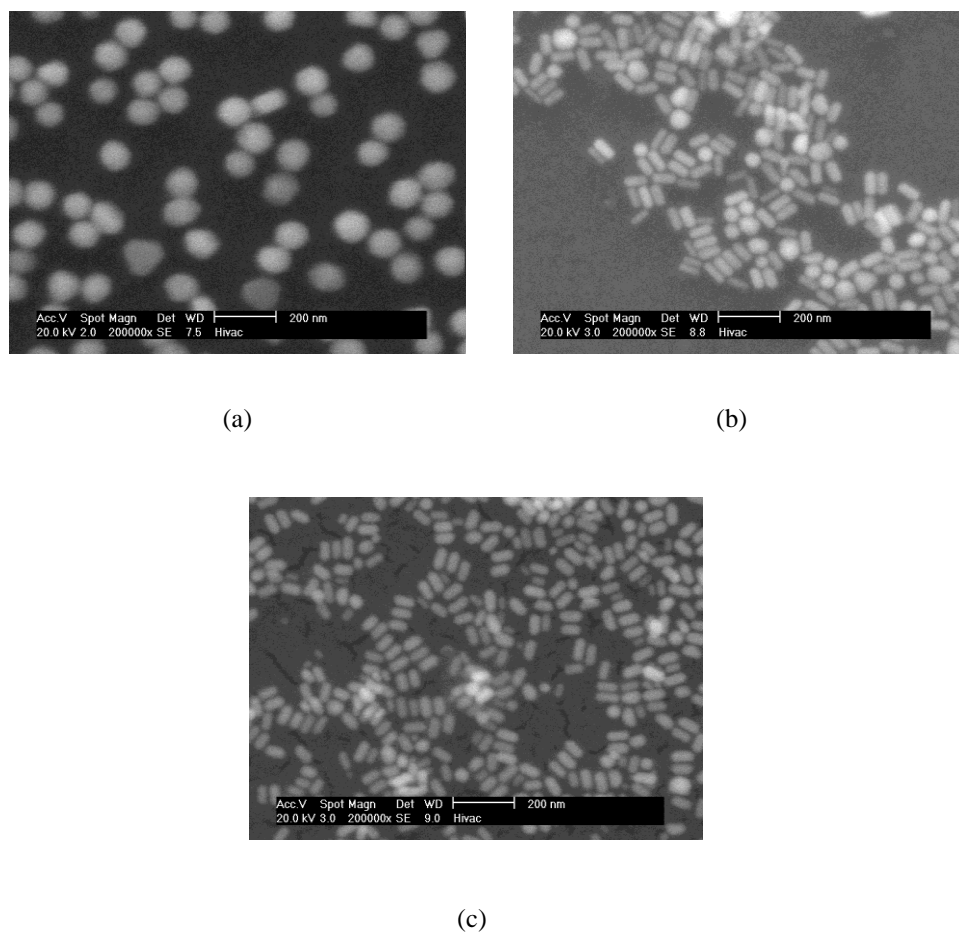
Figure 4.9   SEM image of (a) nanospheres d = 100 nm (b) nanorods L = 60 nm, d = 25 nm (c)

nanorods L = 73 nm, d = 25 nm.

(a)

(b)
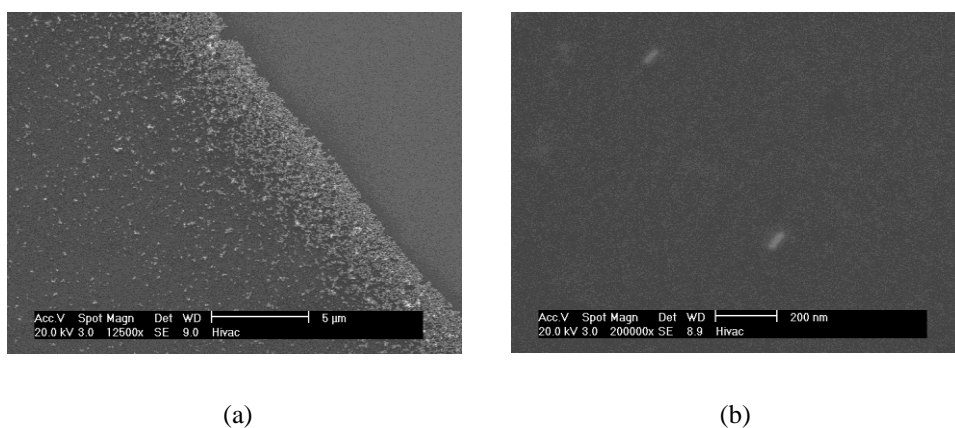
Figure 4.10   SEM images of nanoparticle distribution. (a) High nanoparticle density at

boundary (b) Individual particles

A larger number of particles accumulated at the boundary of the dried pattern but individual particles could be identified within the boundaries, which permitted the implementation of single particle measurements. The pattern of particle distribution is illustrated in Fig. 4.10.

4.3   Spectroelectrochemical experiments
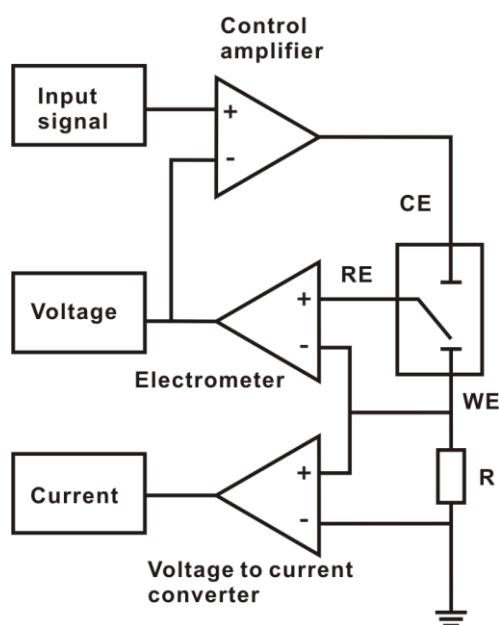
Figure 4.11 Basic potentiostatic circuit. CE: counter electrode. RE: reference electrode.

WE: working electrode.

The electrochemistry is applied to study the chemical reaction taking place at the interface of the working electrode and the electrolyte, which is driven by an external potential to generate the charge transport process at the

interfacial region. Unambiguous information provided by careful control and accurate measurement of electric potential and current is an essential requirement for the investigation of the electrons movement.

Modern electrochemistry takes advantage of potentiostats to hold the potential between the working and reference electrodes at a constant value by adjusting the current through a counter (auxiliary) electrode (Fig. 4.11). In order to maintain a stable potential of the working electrode with respect to the reference electrode, no current is permitted to pass through the reference electrode. Otherwise, this electrode will be polarised and its potential will vary with the current. The primary electronic component of the potentiostat is an operational amplifier. Under normal operation, the working electrode is maintained at ground potential. A preset potential between ground and the reference electrode is connected to the two inputs of the operational amplifier. Due to the high input impedance, there is very little current flow through the reference electrode. The output of the operational amplifier is connected to a counter electrode. Current is forced to flow between the counter electrode and the working electrode and it acts as a feedback signal in the potentiostat circuitry to counteract the difference between the working electrode potential and the desired potential [103].

In this study, the Au nanostructure was arranged as a three-electrode system and its potential was controlled by a potentiostat. Au films and Au nanoparticles prepared on ITO coated coverslips as described in the last section

were used as the working electrode. Ag/AgCl wire and coiled Au wire were employed as reference and counter electrode respectively. The electrochemical cell was integrated into the dark-field imaging spectrometer. Monochromatic light tuned over large wavelength ranges illuminated the objects of interest on the working electrode to produce scattered light. The change in scattered light from the Au nanostructure induced by modulated potential together with the electrochemical measurement from the potentiostat provided the required information to analyse the reactions at the metal nanostructure-solution interface.

4.3.1   The potential of the Ag/AgCl electrode

An ideal nonpolarisable electrode is preferable as the reference electrode, whose potential does not change significantly even if a small current passes through the metal-solution interface. The constant composition of the reference electrode determines its fixed potential.

The potential of a standard hydrogen electrode (SHE) is defined as zero. The potential of a practical reference electrode can be derived on the SHE scale and is quoted as the reference for measurement. Silver-silver chloride is widely used as reference electrodes. The standard potential E^0 of Ag/AgCl is 0.2223 V with respect to SHE in aqueous solution at 25 ℃ [103]. The equilibrium potential of Ag/AgCl during the reversible reaction

99
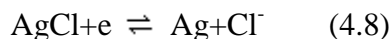
$$AgCl + e \rightleftharpoons Ag + Cl^- \qquad (4.8)$$

is determined by the Nernst equation

$$E_{Ag-AgCl} = E^0_{Ag-AgCl} - \frac{RT}{nF} \ln \frac{[a(Ag)][a(Cl^-)]}{[a(AgCl)]} \qquad (4.9)$$

where $E^0_{Ag-AgCl}$ is the standard potential 0.2223V, R is the gas constant 8.31447 Jmol^{-1}k^{-1}, T is the absolute temperature [K], F is the Faraday constant 9.64853×10^4 C, n is the number of electrons exchanged (1 in this reaction), $[a(Ag)]$, $[a(Cl^-)]$ and $[a(AgCl)]$ are the activities of Ag, Cl$^-$ and AgCl respectively. Since Ag and AgCl are solids, their activities are unity.

At 25 °C (298.15K), the calculation of equilibrium potential can be simplified according to the ion concentration,

$$E_{Ag-AgCl} = 0.2223 - 0.059 \log[n(Cl^-)] \qquad (4.10)$$

which indicates the potential of Ag/AgCl is dependent on the concentration of Cl$^-$ [mol L^{-1}]. The potential of the Ag/AgCl electrode will rise as the concentration of Cl$^-$ decreases.

4.3.2   Construction of the Ag/AgCl reference electrode

Silver wire (0.5 mm diameter, 99.99 % purity, Advent Research Materials Ltd) was used to prepare the Ag/AgCl electrode. The silver was cleaned by immersing in 0.1 M HNO_3 for a few seconds to remove oxide from the surface and thoroughly rinsed with deionised water. One end of the silver wire was heated to form a small bead and was anodised in 1.0 mol L^{-1} HCl solution overnight to coat with a layer of silver chloride.

3 % wt. agar was added to a saturated NaCl solution. The mixture was boiled until the agar dissolved. The agar solution was then sucked into a plastic tube. After the agar mixture was cool and solidified, the end of the silver wire coated with silver chloride was inserted into the plastic tube filled with the gel electrolyte [121-125].

In order to characterise the constructed Ag/AgCl electrode, its potential was measured against a commercial Ag/AgCl electrode (Reichert). Both electrodes were placed in a beaker containing saturated NaCl solution. The potential difference was between 8 and 11 mV, which was considered acceptable.

4.3.3   The electrochemical cell

The electrode configuration is shown in Fig. 4.12. The electrochemical measurements were controlled by a VersaSTAT 3 potentiostat (Princeton

Applied Research). The Au film or ITO coated coverslip with immobilised nanoparticles (working electrode) was sealed by silicon rubber at the bottom of a plastic well to prevent leakage. This reduced the surface area of the working electrode to about 5-7 mm^2. Conducting aluminium adhesive tape was used to ensure a good electrical connection to the working electrode.

The resistance in a solution with a given geometry under a uniform current flow condition is [103]

$$R = \frac{l}{\sigma S} \qquad (4.11)$$

where *l* is the distance of the current path [m], *S* is the surface area at one end of the domain [m^2], and σ is the solution conductivity [Sm^{-1}]. The resistance is therefore proportional to the distance. Hence the Ag/AgCl reference electrode was placed close to the working electrode to minimise the uncompensated resistance. The compact coiled Au counter electrode had a disc-like shape with a diameter of approximately 20 mm. The larger surface area of the counter electrode compared to that of the working electrode is assumed to distribute current uniformly around the working electrode and the contribution of the counter electrode's capacitance to the measurement is negligible [103, 126]. The supporting electrolyte was 0.1M NaCl, which is also the basis of cell culture media.
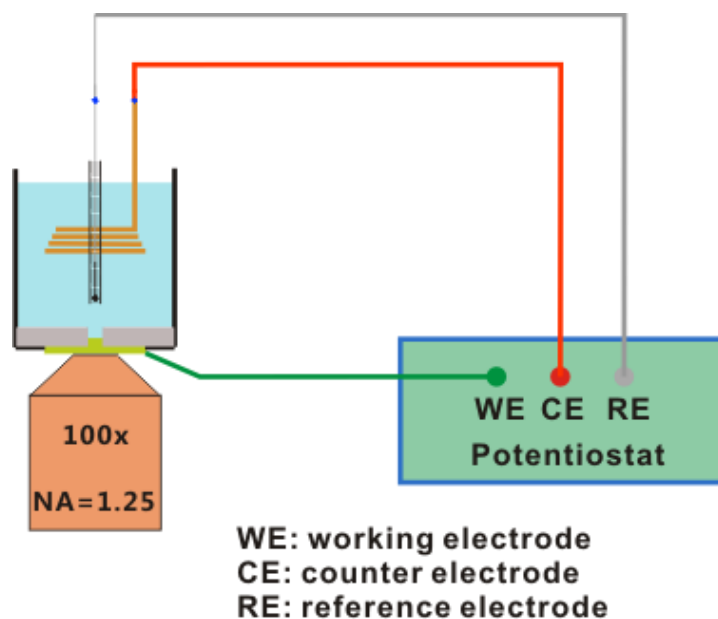
Figure 4.12   Electrochemical cell

4.3.4   Potential modulation

A potential modulation mode denoted bipolar mode A (BMA) was applied to the working electrode with immobilised nanostructure. The potentials were 200 mV and -200 mV. The polarities are defined as positive and negative voltage applied to the working electrode. A square wave of ±200 mV as shown in Fig. 4.13 was applied while the imaging and reference cameras recorded three images during the application of each half period for the purposes of imaging and calibration respectively. The exposure time was dependent on the scattering strength of the Au nanostructure so the duration of each potential was adjusted according to each particular situation.
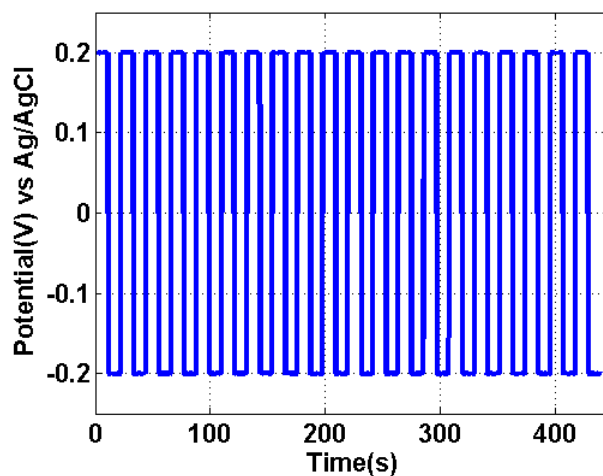
Figure 4.13   Square wave of bipolar mode A. 200mV and -200mV were applied sequentially

to the working electrode for 20 cycles.

Besides BMA, several other modes were used to measure the Au nanostructure's response under applied potential. These modes are denoted BMB, BMC, BMD, BME, BMF and BMG and have the same potential modulation sequence as that of BMA, but magnitudes of ±150, ±100, ±50, ±25, ±10 mV and 0 V respectively.

4.4   Summary

An objective-type dark-field imaging spectrometer was designed and constructed to collect spectral scattering information from Au nanostructures arranged in the electrochemical cell, which not only visualised the spatial distribution of nanoscale objects but enabled the analysis of individual objects under potential control.

Several types of Au nanostructure were prepared for measurement. The thermal evaporation technique was used to construct 16 nm and 50 nm Au films on glass coverslips. 2 μm spheres were used in NSL to make triangular nanoparticle arrays. A commercially obtained nanoparticle suspension was diluted so that nanoparticles could be separately deposited on ITO coated coverslips to allow optical measurement on single, isolated nanoparticles. The morphologies of all samples were evaluated by SEM.

The investigation of Au nanostructure under potential control was implemented by both conventional electrochemical techniques and by dark-field imaging spectrometry. Modulated potential was applied to the Au nanostructure. A range of monochromatic light wavelengths was used as the probe to detect the electrochemical reactions taking place at or near the Au nanostructure's surface. Collection of scattered light induced by the potential from Au nanostructure simultaneously with the electrical signal gathered from electrochemical measurement enabled analysis of the consequence of charge transport on the Au nanostructure's surface.

Chapter 5   Sensing potential with gold films

The unique properties of surface plasmon resonance which depend on the properties of metal and dielectric medium, have been utilised for the development of sensing technology during the last two decades for physical, chemical and biological applications [23, 127-130]. The combination of electrochemical methods and surface plasmon resonance techniques has provided a powerful tool to detect the electrochemical reactions taking place in the vicinity of noble metal films, and is often implemented using the Kretchmann-Raether configuration [131-133]. Interactions of electromagnetic radiation with ultrathin metal islands in film exhibit localised surface plasmon resonance due to the confinement of collective oscillation of the free electrons in these nano-islands, and results in enhanced light scattering [84, 97]. The collection of scattered light from ultrathin metal film using dark-field microscopy provides a relatively convenient technique to detect the electrochemical reactions in a similar way to the electrochemical SPR technique.

In this chapter, the capability of Au film for sensing potential is investigated. Au film supported on a substrate is illuminated by an incident beam. This structure is composed of several layered materials, so the calculation of the reflected and transmitted beams from a multilayer planar

structure by using Fresnel's equations will be described first. Then, an experimental comparison of the wavelength dependent scattering contrast induced by potential from very thin (~16 nm) and thicker (~50 nm) Au films is presented, followed by an investigation of the influence of potential cycling and potential steps on thin Au film (~16 nm) in which a single wavelength was used with a dark-field imaging spectrometer. A commercial SPR system was also employed to explore the effects of potential on thicker gold film (~50 nm) although little response to potential from this thicker gold film was found in the measurements taken by the dark-field spectrometer. Finally, modelling related to sensing potential by using the Au film integrated in a multilayer structure which represents the experimental conditions is presented.

5.1   Reflection and transmission of light in a multilayer planar structure

Light propagates in space as an electromagnetic wave. When s- or p-polarised light transmits from medium 1 with refractive index n_i to medium 2 of refractive index n_t, the interface of these two isotropic media produces a reflected and transmitted beam from the incoming beam. Linearly polarised light will retain its polarisation during reflection and transmission. The electric field amplitude relationships of incident, reflected and transmitted light are given by Fresnel's equations [37]

$$r_{12\_s} = \frac{E_{0r\_s}}{E_{0i\_s}} = \frac{n_i \cos\theta_i - n_t \cos\theta_t}{n_i \cos\theta_i + n_t \cos\theta_t} \qquad (5.1a)$$

$$t_{12\_s} = \frac{E_{0t\_s}}{E_{0i\_s}} = \frac{2n_i \cos\theta_i}{n_i \cos\theta_i + n_t \cos\theta_t} \qquad (5.1b)$$

$$r_{12\_p} = \frac{E_{0r\_p}}{E_{0i\_p}} = \frac{n_t \cos\theta_i - n_i \cos\theta_t}{n_i \cos\theta_t + n_t \cos\theta_i} \qquad (5.1c)$$

$$t_{12\_p} = \frac{E_{0t\_p}}{E_{0i\_p}} = \frac{2n_i \cos\theta_i}{n_i \cos\theta_t + n_t \cos\theta_i} \qquad (5.1d)$$

where $E_{0i\_s}, E_{0r\_s}, E_{0t\_s}$, and $E_{0i\_p}, E_{0r\_p}, E_{0t\_p}$ are the incident, reflected and transmitted electric fields of s- and p- polarised light respectively, θ_i and θ_t are the incident and refracted angle at the interface determined by Snell's law.

The reflectance R and transmittance T for s- and p- polarised light are defined as the ratio of reflected and transmitted to the incident light power respectively, which are

$$R = r^2 \qquad (5.2a)$$

$$T = \frac{n_t \cos\theta_t}{n_i \cos\theta_i} t^2 \qquad (5.2b)$$

When a incident beam strikes a structure consisting of several parallel layers (media 1, 2, 3, …, *j*, …, *m*) embedded between a semi-infinite substrate (medium 0) and a semi-infinite ambient medium (medium *m*+1), with the assumption that all media are homogeneous and isotropic (Fig. 5.1), it produces

a reflected beam in the substrate and a transmitted beam in the ambient medium, whose amplitudes depend upon the multiple reflections suffered by the beam inside the layered medium [134].

Each of the individual interface matrices $I_{j(j+1)}$ and layer matrices L_j characterising the reflection and transmission of light in this structure produce a 2×2 scattering matrix S to connect the wave in medium 0 and $m+1$

$$S = I_{01}L_1I_{10}L_2\cdots I_{(j-1)j}L_jI_{j(j+1)}\cdots L_mI_{m(m+1)} \quad (5.3)$$
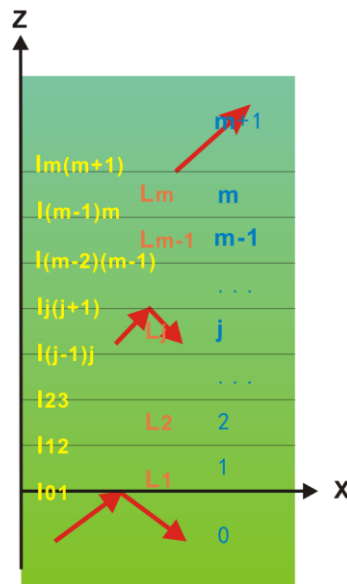
Figure 5.1   Propagation of light in a multilayer planar structure

The interface matrix $I_{j(j+1)}$ characterising the j-$(j+1)$ interface is given by

$$I_{j(j+1)} = \begin{bmatrix} \dfrac{1}{t_{j(j+1)}} & \dfrac{r_{j(j+1)}}{t_{j(j+1)}} \\ \dfrac{r_{j(j+1)}}{t_{j(j+1)}} & \dfrac{1}{t_{j(j+1)}} \end{bmatrix} \quad (5.4)$$

where $t_{j(j+1)}$ and $r_{j(j+1)}$ are the Fresnel reflection and transmission coefficients of the j-$(j+1)$ interface.

The layer matrix L_j for the jth layer is

$$L_j = \begin{bmatrix} e^{j\beta_j} & 0 \\ 0 & e^{-j\beta_j} \end{bmatrix} \qquad (5.5)$$

where $\beta_j = (2\pi/\lambda)d_j n_j \cos\theta_j$ is the phase shift experienced by the light when it travels at angle θ_j in a layer of thickness d_j with a refractive index n_j.

Substituting Fresnel's equations for s- and p-polarised light at each interface into the interface matrix I and multiplying by each layer matrix L forms the final scattering matrix S for s- and p-polarised light respectively. The energetic coefficients of reflected and transmitted light from the multilayer structure are

$$R = (\frac{S_{21}}{S_{11}})^2 \qquad (5.6a)$$

$$T = (\frac{1}{S_{11}})^2 \qquad (5.6b)$$

A detailed description of the derivations of the scattering matrix S is presented in Appendix A.3.

5.2   The effect of potential on Au film

Dark-field imaging spectrometry can detect the scattered light from small objects in a wide wavelengths range. The visibility of the object is enhanced by dark-field microscopy as the bright background is suppressed. Applying a potential generates an electrical double layer on the gold film which allows electrons to be transferred to and from the gold film and modify its relative permittivity. Consequently, scattered light from the surface of the gold film can be recorded to observe this change arising from potential.

5.2.1   Scattering spectra of Au film

(a)   (b)
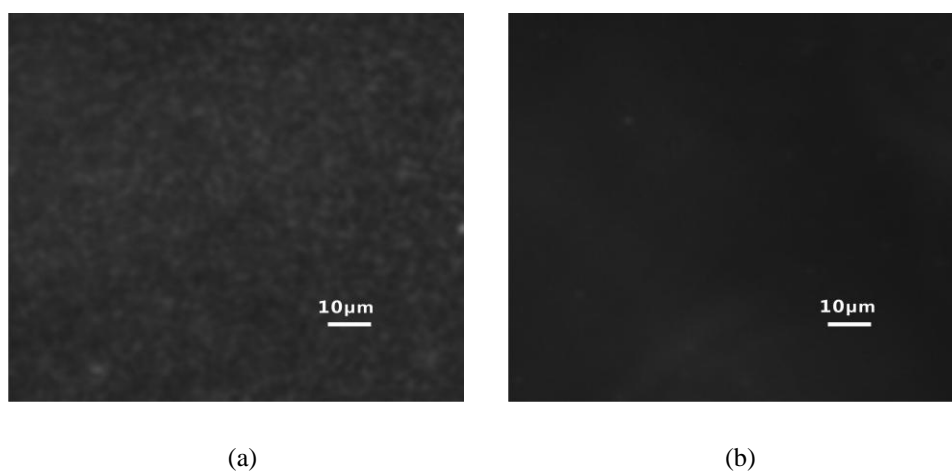
Figure 5.2   Optical images of Au film taken at a wavelength of 707 nm. The mass thickness of Au film was (a) 16 nm and (b) 50 nm respectively.

The deposition of gold onto a coverslip was described in Sec. 4.2.2. Two thicknesses of gold film of approximately 16 nm and 50 nm were used to compare their sensitivity to potential. Scattering from gold film was recorded

with the reflected light dark-field imaging spectrometer. Images of gold film taken at a wavelength of 707 nm are shown in Fig. 5.2. It is possible to visually distinguish the films of thickness 16 and 50 nm. As can be seen, the surface of the thinner Au film is visibly rougher than the thicker one.

Scattering spectra of gold films immersed in aqueous 0.1M NaCl without voltage application are shown in Fig. 5.3. The scattering strength continued to increase with wavelength across the whole instrument range, indicating that the resonance peak was in the IR part of the spectrum. The thinner Au film scattered more strongly than the thicker one due to its rougher surface.
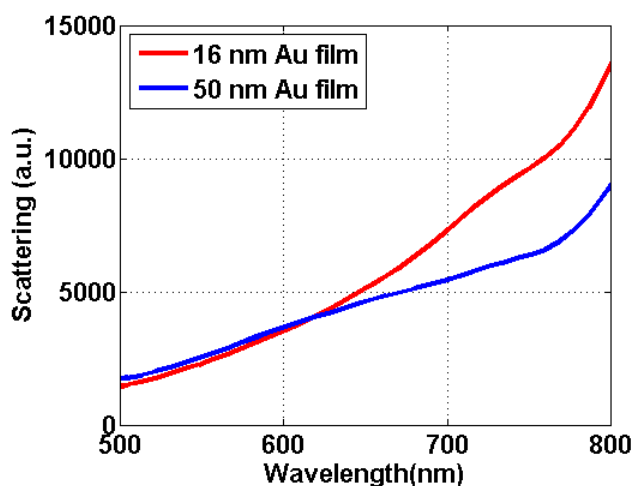
Figure 5.3 Scattering spectra of Au films. Red line is the spectrum of a 16 nm Au film and

the blue line is a 50 nm film

5.2.2   Cyclic voltammetry of the Au film-solution interface

Figure 5.4 depicts the cyclic voltammetry curve of the 16 nm gold film in 0.1 M NaCl. Within the -0.6 V to 1 V potential window (Fig. 5.4a), the gold film experienced an oxidation peak at 0.4 V due to the formation of hydrated AuOH and AuO in the positive-going potential scan [135]

$$Au+2H_2O \rightarrow AuOH \cdot H_2O+H^++e^- \qquad (5.7a)$$

$$AuOH \rightarrow AuO+H^++e^- \qquad (5.7b)$$

(a)   (b)
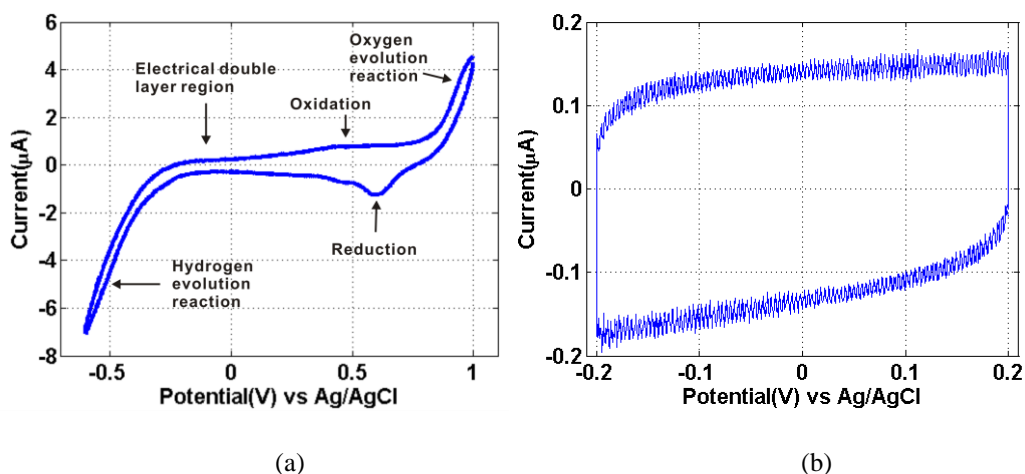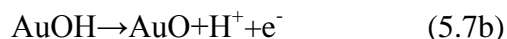
Figure 5.4 Cyclic voltammetry of 16 nm Au film in 0.1 M NaCl with a potential scan rate 0.05

V/s. The oxidation peak and the reduction peak can be observed in (a). The curve of CV in (b)

indicates that potentials between ±200 mV are in the electrical double layer region for this gold

film.

Potential greater than 0.8 V activated oxygen evolution. The reduction

peak at 0.6 V during the cathodic potential scan arose from the reverse reaction

of the above mentioned process. At a potential lower than -0.4 V, the hydrogen

evolution reaction began. The faradaic reactions can be essentially eliminated

by limiting the potential window. The approximately rectangular loop of the

CV plot indicated there was no faradic process between ±200 mV (Fig. 5.4b).

The observed current here was due to the movement of charges taking place in

the electrical double layer, resulting in current displacement.

5.2.3   Potential modulated wavelength-dependent scattering of Au film

The scattering modulated by bipolar voltage mode A (±200 mV) from the thin Au film at wavelength 618 nm is shown in Fig. 5.5. A sequence of 120 images was acquired with 60 corresponding to 200 mV and 60 corresponding to -200 mV. The acquisition time for each image was 3.6 s. In the image of the Au film, eight regions, each corresponding to a sample area of approximately 0.5 μm^2 were selected to investigate their response to potential.
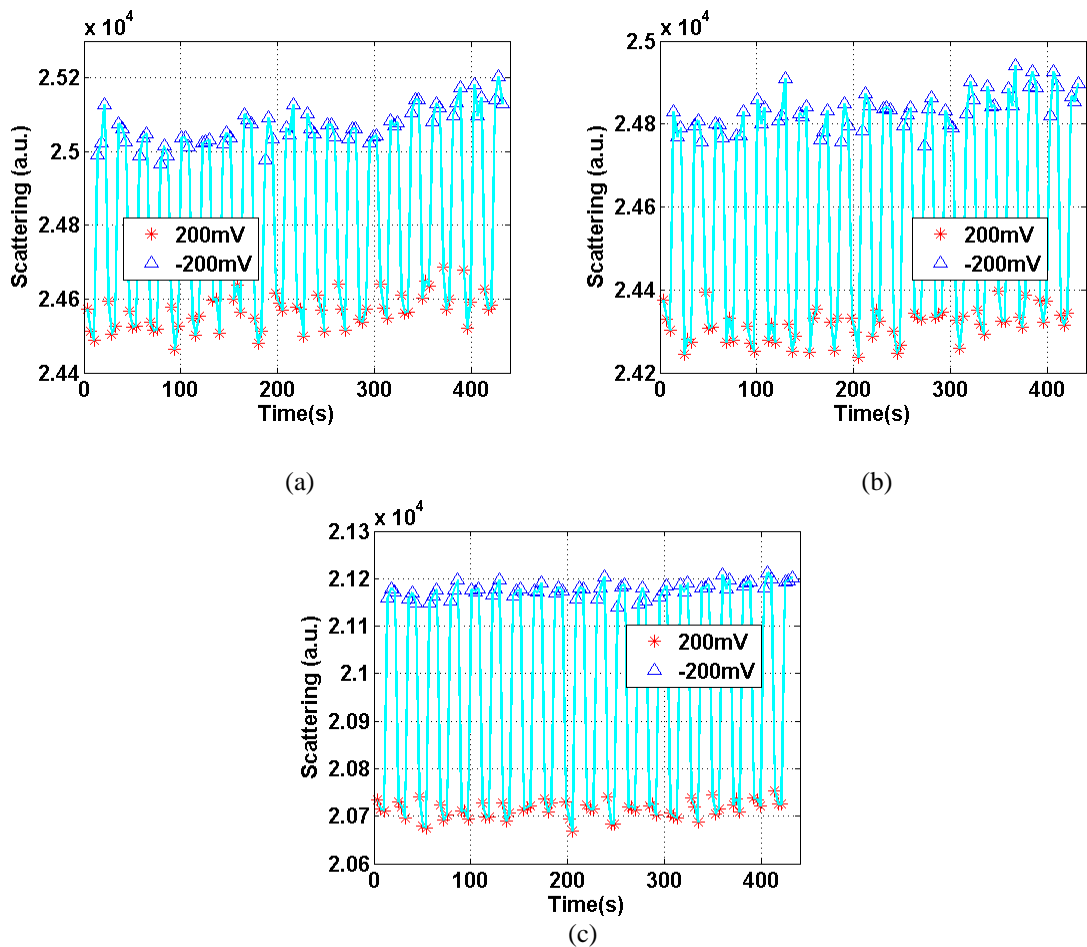
Figure 5.5   Potential modulated scattering from 16 nm Au film. Red stars and blue triangles represent scattering at potentials of 200 mV and -200 mV respectively. The cyan line connects the time. (a) and (b) are the scattering strengths of regions 1 and 2. (c) is the ensemble scattering from all 8 regions.

114

Modulating the applied potential caused a change of the scattering strength. Initially, 200 mV maintained a steady scattering strength of about 2.07×10^4 arbitrary units (AU) for about 11 s. The application of -200 mV made the scattering strength rise to 2.12×10^4 AU and sustained it for a further 11 s. Then the return of potential from -200 mV to 200 mV reduced the scattering strength back to 2.07×10^4 AU again. This modulation of scattering associated with the potential continued throughout the 120 frame sequence.

(a)   (b)
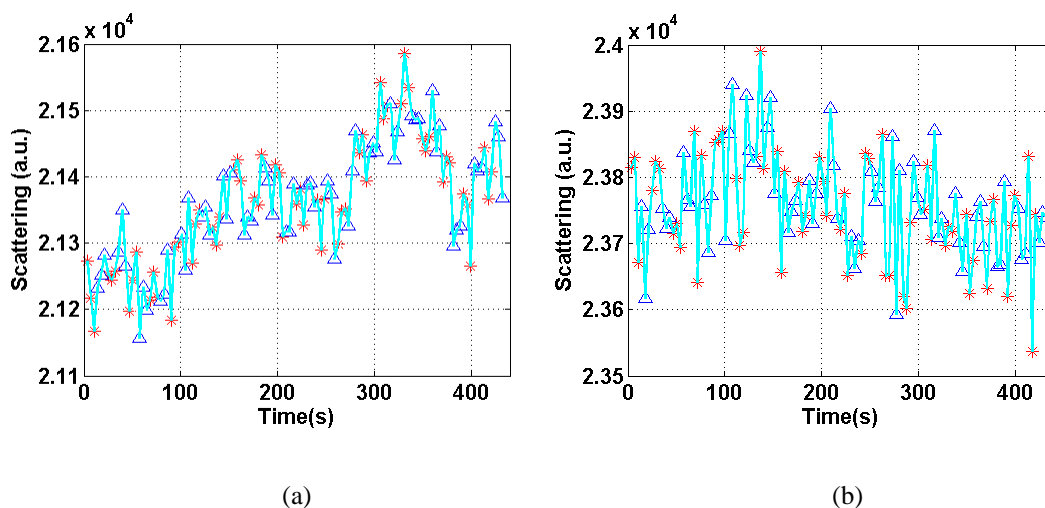
Figure 5.6 Control experiment: irregular scattering trace was due to the absence of potential

Control experiments (Fig. 5.6) conducted under the same experimental conditions but in the absence of potential show that there were no any regular features can be distinguished, indicating that the regular change of the scattering shown in Fig. 5.5 was exclusively caused by the modulated potential.

(a)   (b)

(c)   (d)
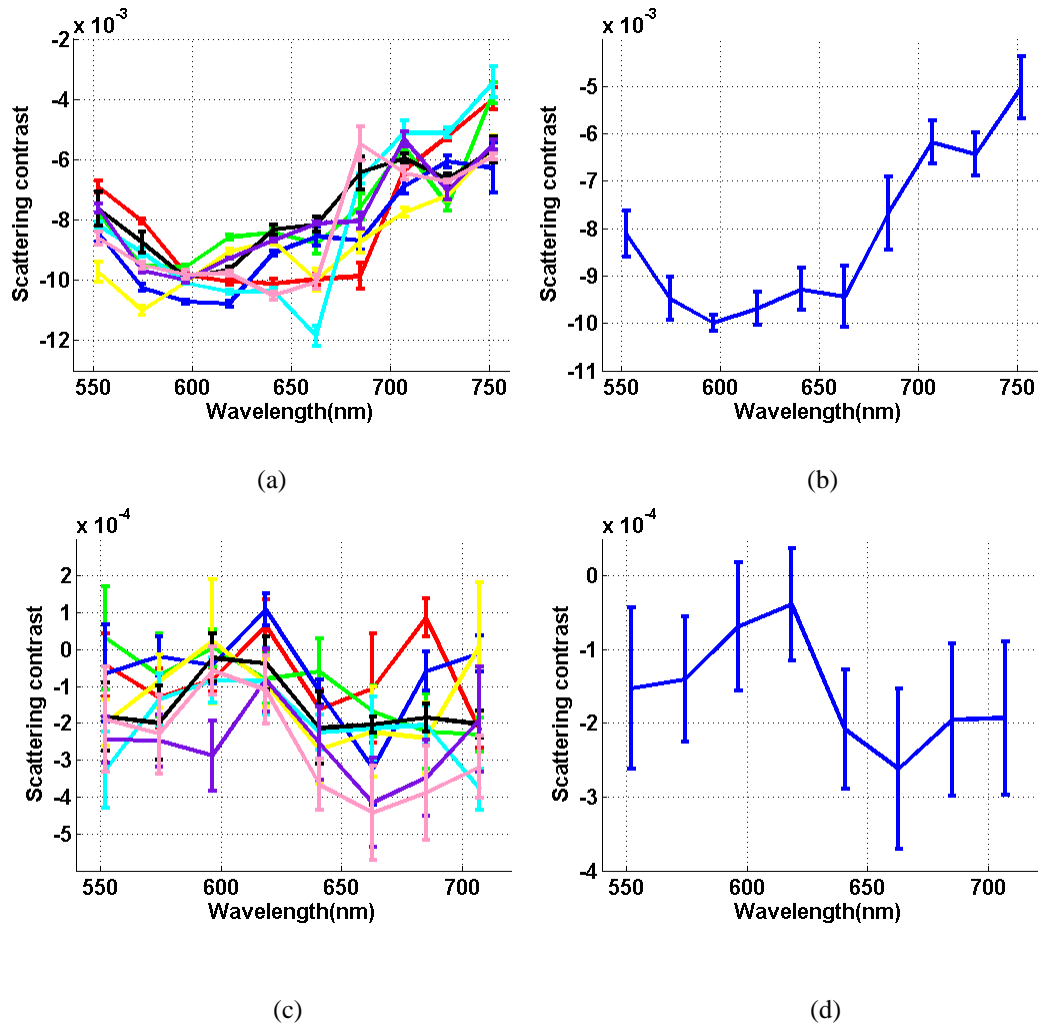
Figure 5.7 Scattering contrast of Au film under the potential applied as bipolar mode A.

(a) and (c) are the individual scattering contrasts from the 8 regions for the 16 nm and 50 nm

film. (b) and (d) are the ensemble scattering contrast of all 8 regions for 16 nm and 50 nm

thickness

To characterise the optical response to potential on the Au film, a measure

of contrast, $C_{scattering}$, is used, defined as the ratio between the difference and

the sum of the scattering at each potential,

$$C_{scattering} = \frac{\displaystyle\sum_{i=1}^{60} I_{higher\_i} - \sum_{i=1}^{60} I_{lower\_i}}{\displaystyle\sum_{i=1}^{60} I_{higher\_i} + \sum_{i=1}^{60} I_{lower\_i}} \qquad (5.8)$$

where I_{higher_i} and I_{lower_i} are the ith scattering intensity recorded at the higher potential and the lower potential respectively.

During the scattered light collection process, the power of scattered light from a region of interest A [m^2] with a irradiance E [Wm^{-2}] is converted to the digital signal value I of the CCD sensor, which can be express as [136]

$$I = \frac{E \cdot t \cdot A \cdot DR \cdot QE \cdot \lambda}{FWC \cdot h \cdot c} \qquad (5.9)$$

where t is the exposure time [s], DR is the maximum white value of the CCD [count], QE is the quantum efficiency of the CCD, λ is the wavelength of the scattered light, FWC is full well capacity (e$^-$), h is Planck constant [Js], and c is the speed of light in vacuum [ms^{-1}]. In a particular measurement, the digital signal value I with an arbitrary units is only proportional to $E \cdot t \cdot A$. The use of Eq. (5.8) allows the characterisation of different samples by one standard, their irradiation E modulated by the potential. Errors due to different exposure times and sample surface areas are eliminated.

In order to determine the maximum scattering contrast that the Au film can produce throughout its spectrum, scattering contrasts corresponding to a series of individual wavelengths were investigated. To ensure that the measured scattering contrast was consistent and stable, the scattering intensity of the Au

film was recorded four times at each wavelength.

Their individual and ensemble scattering contrasts are shown in Fig. 5.7. The maximum ensemble scattering contrast of thin Au film is -1×10^{-2} (-1 %) at about 600 nm. The trend of individual scattering contrast against wavelength was similar in each region, although there were distinct differences between each other. The low resistivity of gold means it is a good choice to be used as an electrical conductor. The potential applied on the working electrode was therefore constant across the surface of the Au film. In practice, each individual region contains many gold clusters. The slightly different scattering contrasts of these 8 regions arose from the collective contributions of these various gold clusters evaporated on the surface of gold. The negative polarity sign of the scattering contrast across the whole measured spectrum implies that scattering intensity was suppressed by a positive potential while it was enhanced by a negative potential, which is also shown in Fig. 5.5. It shows a predictable direction for the change of the scattered intensity of Au film in this spectral region. The spectrum of gold will either be reduced in scattering intensity or red-shifted under the condition of positive potential or vice versa under the condition of negative potential. Comparing with the potential dependent scattering contrast from the thin Au film, the response to potential from the thick film, where the polarisation of incident beam and its angle are unspecific, is much reduced.

5.2.4   Voltage sensitivity of Au film

The scattering contrast of the 16 nm Au film across the spectral range of

the dark field spectrometer had been determined. In order to find out its sensitivity to small potentials, it was necessary to measure its scattering contrast at lower voltages. Potential modulation modes, BMB, BMC, BMD, BME, BMF, and BMG were used for the test of thin Au film with BMA. The magnitudes of the potential in each mode were ±200 mV, ±150 mV, ±100 mV, ±50 mV, ±25 mV, ±10 mV and 0 V respectively. The scattering contrast of the 16 nm Au film resulting from these 7 modulation modes measured at a wavelength of 618 nm is shown in Fig. 5.8.

The relationship between the scattering contrast and the potential was fitted to

$$C(V) = AV^{c} \qquad (5.10)$$

where A is the parameter to scale the fitting value, V is the absolute potential used in each mode, and c is the power to determine the non-linearity. The best fit of (A, c) was (-0.1227, 1.319) and is shown in Fig. 5.9. The fact that the value of c is larger than unity indicates that thin Au film's scattering contrast decreased faster than the potential decreased.

Taking the non-linear capacitance of the electrical double layer into account, the scattered light reflects the amount of charge stored on the surface of Au film. The nonlinear capacitance accumulates a nonlinear quantity of charges as a function of potential, reflected by the voltage sensitivity of Au film as the accelerated decline in contrast with reducing potential.

(a)   (b)
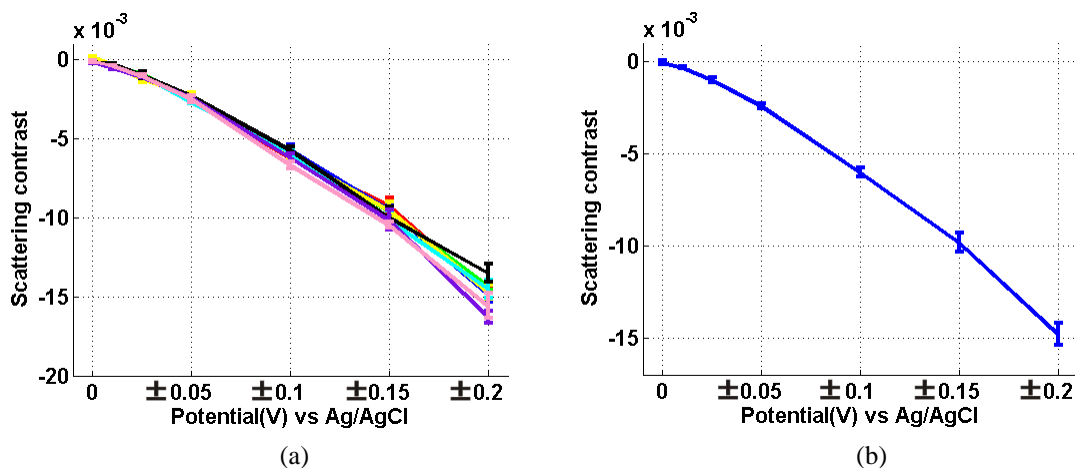
Figure 5.8 Scattering contrast of 16 nm Au film at several potential modulation modes. The

potential was decreased from ±200 mV to 0 V. The individual scattering contrasts from 8

regions are shown in (a) and the ensemble contrast is shown in (b).
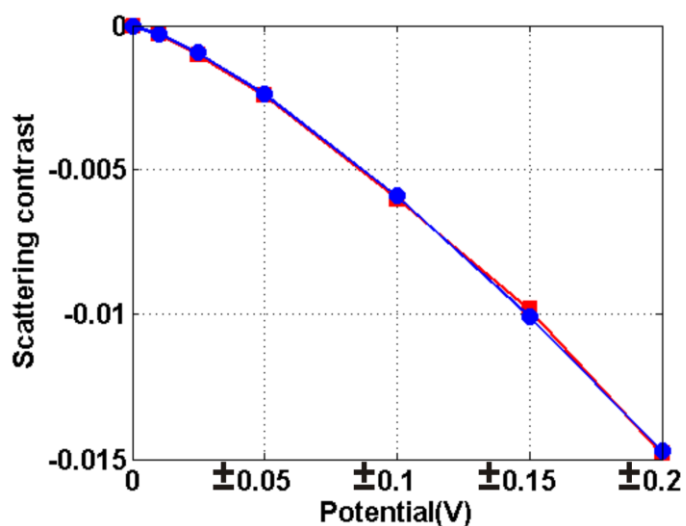
Figure 5.9 Experimental scattering contrast of 16 nm Au film (red squares) and the

corresponding fit (blue circles).

5.2.5   Scattering during cyclic voltammetry

During a linear potential sweep between -0.2 V to 0.2 V and back to -0.2 V,

the potential scan rates were set to 0.0112 V/s, 0.0056 V/s and 0.0028 V/s

allowing 10, 20 and 40 images to be taken in one linear scan.

120

(a)

(b)

(c)
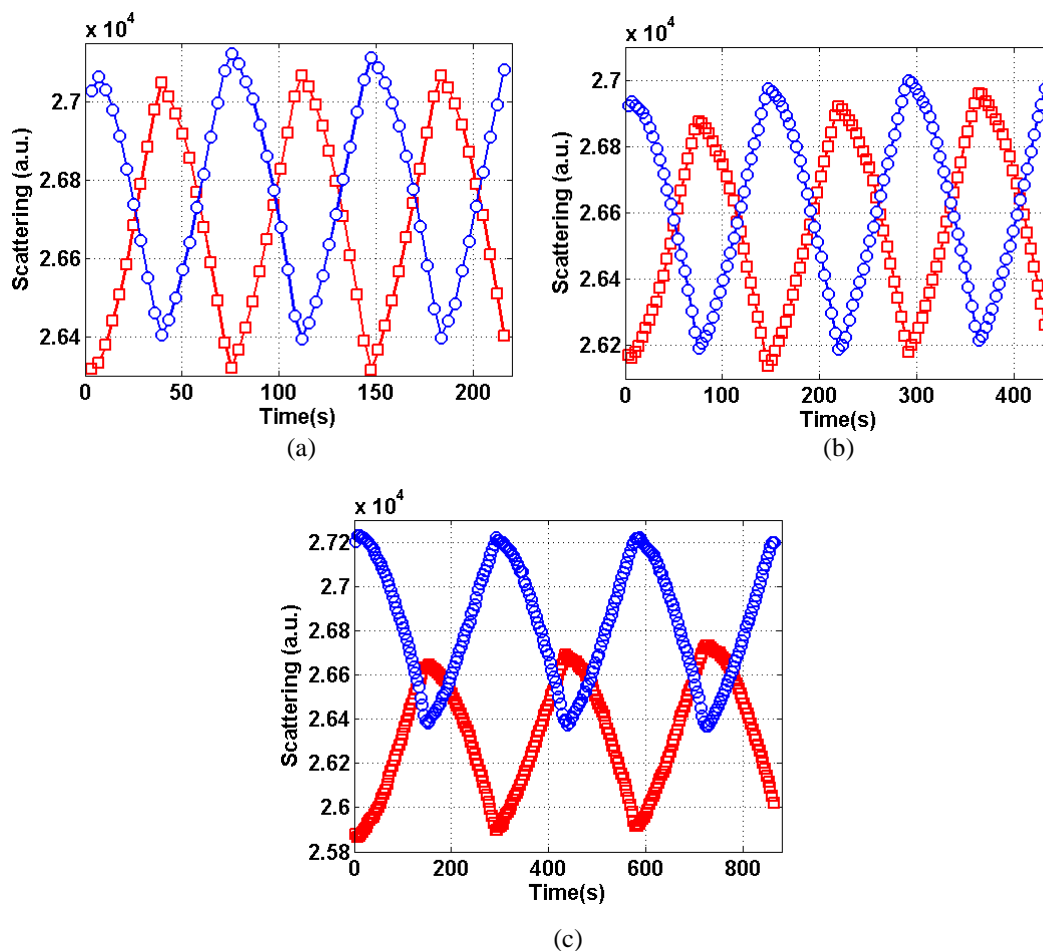
Figure 5.10 Dynamic response of the scattering from 16 nm Au film during cyclic voltammetry. The initial potentials for red squares and blue circles were 0.2 V and -0.2 V respectively. The potential scan rates used in (a), (b) and (c) were 0.0112 V/s, 0.0056 V/s and 0.0028 V/s.

The averaged scattering intensity from 20 regions of 0.5 μm^2 of Au film taken at λ=618 nm is shown in Fig. 5.10. No matter which direction and scan rate, a gradually increasing rate of change in scattering during each linear scan was clearly observed. Determining the rate of change of the scattering within the $\pm$200 mV potential linear sweep was achieved by differentiating the measured samples in these linear potential scans, shown in Fig. 5.11. The scattering transients were fitted to the equation

$$\Delta I(t) = a(1 - e^{-\frac{t}{\tau}}) + b \qquad (5.11)$$

where a is the change of scattering at the final steady state, b is the initial change of scattering after the application of the potential sweep, t is the duration time and τ is the time constant.

(a)
(b)

(c)
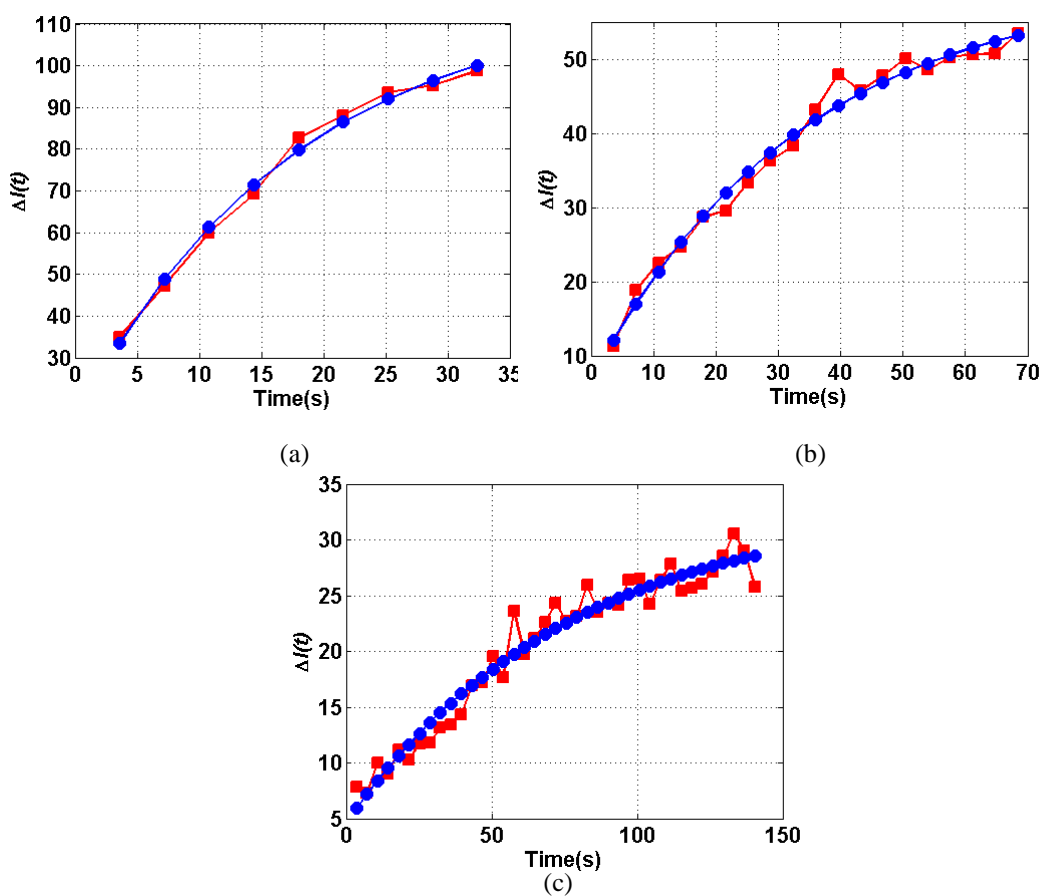
Figure 5.11   The rate of change of scattering in response to the potential scans of ± 200 mV at 0.0112 V/s (a), 0.0056 V/s (b) and 0.0028 V/s (c), calculated by subtracting the $i+1$th scattered intensity from the ith. The change rate of scattering is represented by red squares lines, the blue circles are the a fitted curve using Eq. (5.11)

The red solid squares and blue solid circles lines in Fig 5.11 are the experimental differential scattering and their corresponding fitting curves

respectively. The values of (a, b, τ) for the scan rates of 0.0112 V/s, 0.0056 V/s and 0.0028 V/s were (101.6, 14.56, 17.54 s), (53.65, 6.695, 33.87 s), (28.47, 4.628, 76.15 s) respectively. It is noticeable that the ratio of the three time constants, 17.54:33.87:76.15=1:1.93:4.34, closely matches the reciprocal ratio of the corresponding scan rates 0.0112:0.0056:0.0028=1:1/2:1/4.

The correlation between the time constants and the potential scan rates indicates the rate of change in scattering is able to reflect the rate of charge transfer, which is determined by the potential scan rate. At the beginning of the potential application, the accumulation of counterions outside the gold surface and the assembly of excess charges inside the gold surface construct the double layer at the metal-electrolyte interface. An external electric field induced by the presence of the double layer tends to penetrate into the gold. Meanwhile, an internal electric field is created by the movement of the electrons in the gold's space charge region to resist the influence of the external electric field. Equilibrium was achieved after a certain time depending on the potential scan rate. The balanced interaction between the internal and the external electric fields is reflected by the scattered light, whose rate of change of intensity tends to match the scan rate of the potential. The faster the potential scan rate is, the earlier the equilibration is established and the smaller the time constant will be.

5.2.6   Effect of a potential step on Au film

The scattering from the thin gold film changing with time after the application of different potential steps is shown in Fig. 5.12. The scattering was measured at λ=618 nm and the average scattering was calculated from 20

regions of 0.5 μm^2. The scattering had almost no distinctive feature in the first 36 s application of 0 V. At 36 s, a potential step was applied. Then after a further 180 s, the scattering was switched by reversing the potential step from positive to negative or negative to positive. After another 180 s, the potential was returned to zero for a final 36 s. As the potential step size increased, the level of scattered light stabilised more quickly.

The different scattering intensity at the initial and final applications of 0 V was due to the slow relaxation of charge convection after the gold film suffered a long application of potential, although the application time of the positive and negative potentials was equal. The quantity of charge transferred was limited by the surface area of the gold. Application of a larger potential leads to faster allocation of large charges and an earlier achievement of a balanced electric field at the gold-solution interface. Simultaneous measurements of charge in response to potentials switched between ±200 mV and ±100 mV are shown in Fig. 5.13. The charge was calculated as the time integrated current. Coinstantaneous transients of scattering and charge were synchronised with the potential. The plot of charge was similar to that of the corresponding scattering (with a change in sign). The similarity of traits of scattering and charge was interpreted as that both of them are potential dependent and the product of potential. The charge associated with the current is the outcome of the charging-discharging process of the electrical double layer at the surface of the gold. The electron transfer process caused the scattered light to be synchronised with the potential applied to the gold.

(a)

(b)

(c)

(d)

(e)

(f)

(g)   (h)
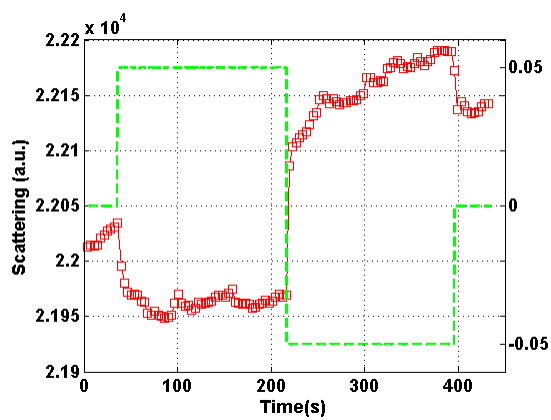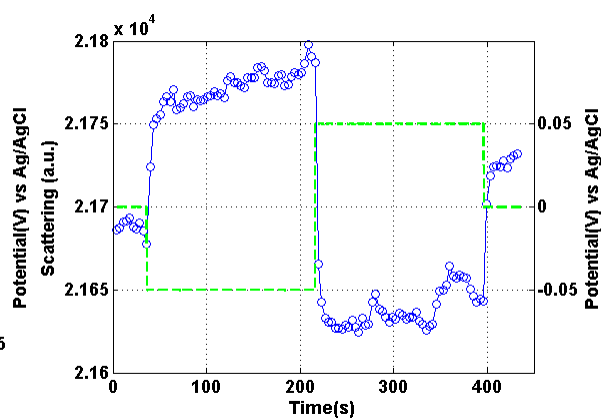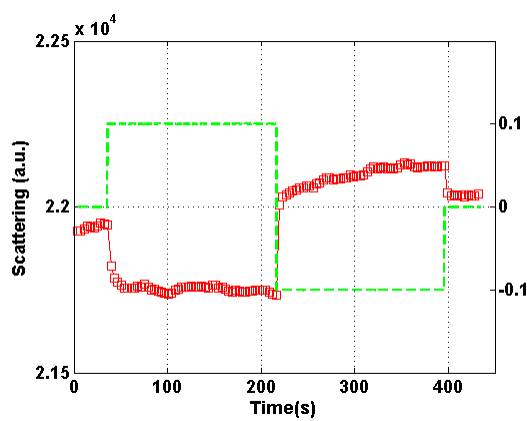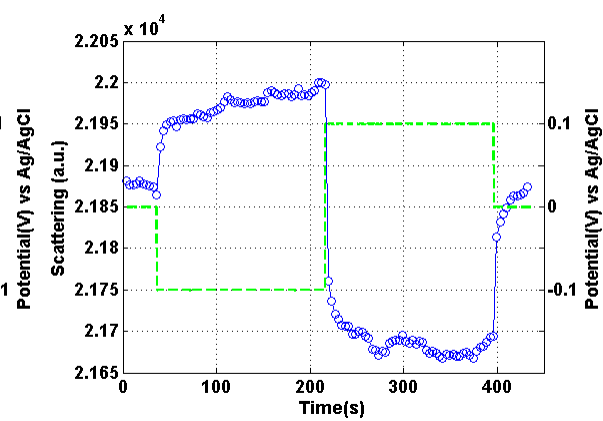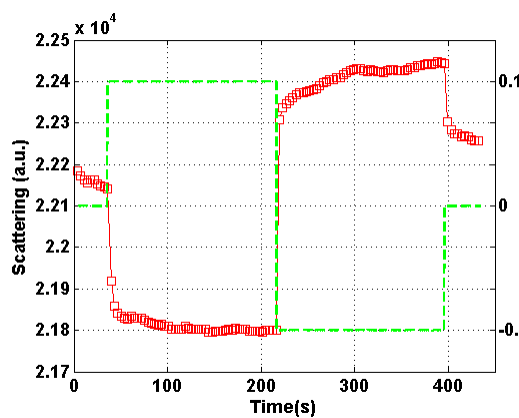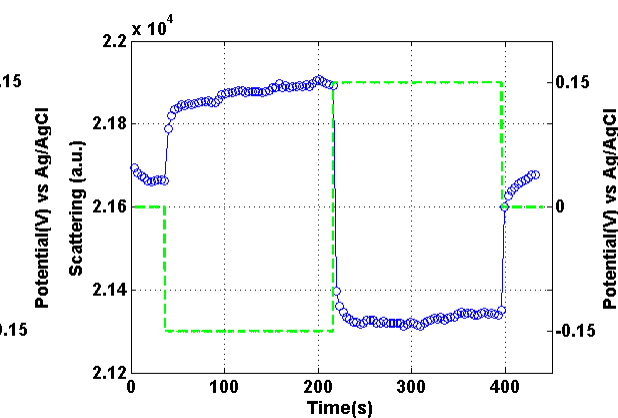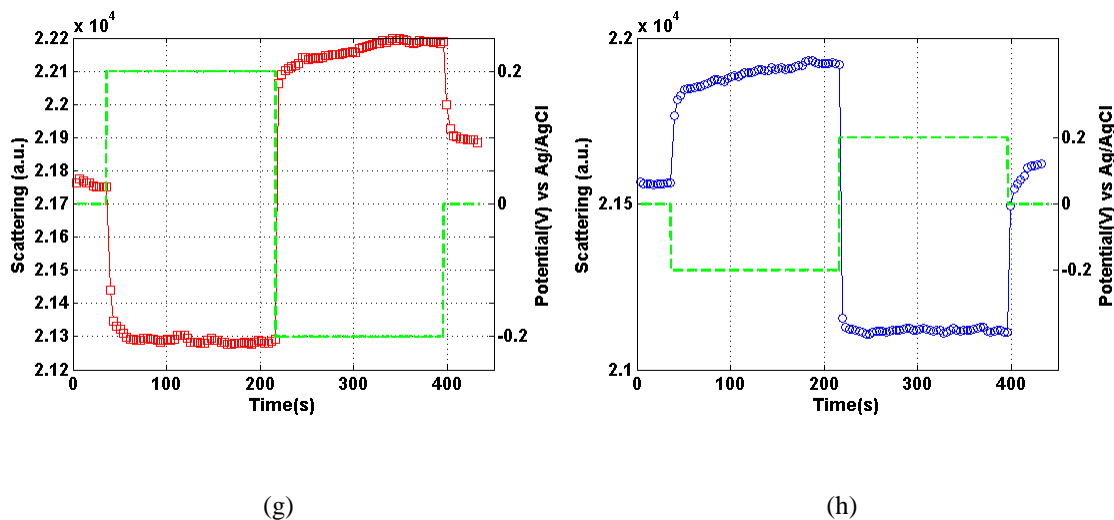
Figure 5.12 The scattering in response to a potential step as the sequence in (a), (c), (e) and (g)

were 0→0.05→-0.05→0 V, 0→0.1→-0.1→0 V, 0→0.15→-0.15→0 V, 0→0.2→-0.2→0 V,

represented as red squares and lines. The potential sequences in (b), (d), (f) and (h) are revered

as 0→-0.05→0.05→0 V, 0→-0.1→0.1→0 V, 0→-0.15→0.15→0 V, 0→-0.2→0.2→0 V,

represented as blue circles and lines.

The potential dependent scattering was not only reflected by the steadier

scattering at larger potential, but is also manifested by the size of scattering

changing at the transition of two different potentials, depicted in Fig. 5.14 as

the differential scattering at each fixed exposure time during the potential

application. The rate of change in scattering was nearly smooth throughout the

total potential application time except for the sharp spikes at the transitions of

two potentials. The different sizes of the spikes when the potential switched at

36 s and 396 s, while the approximately same size of sharp spikes presented at

216 s irrespective to the potentials' polarity, are attributed to the specific

adsorption of chloride ions.

(a)

(b)

(c)

(d)
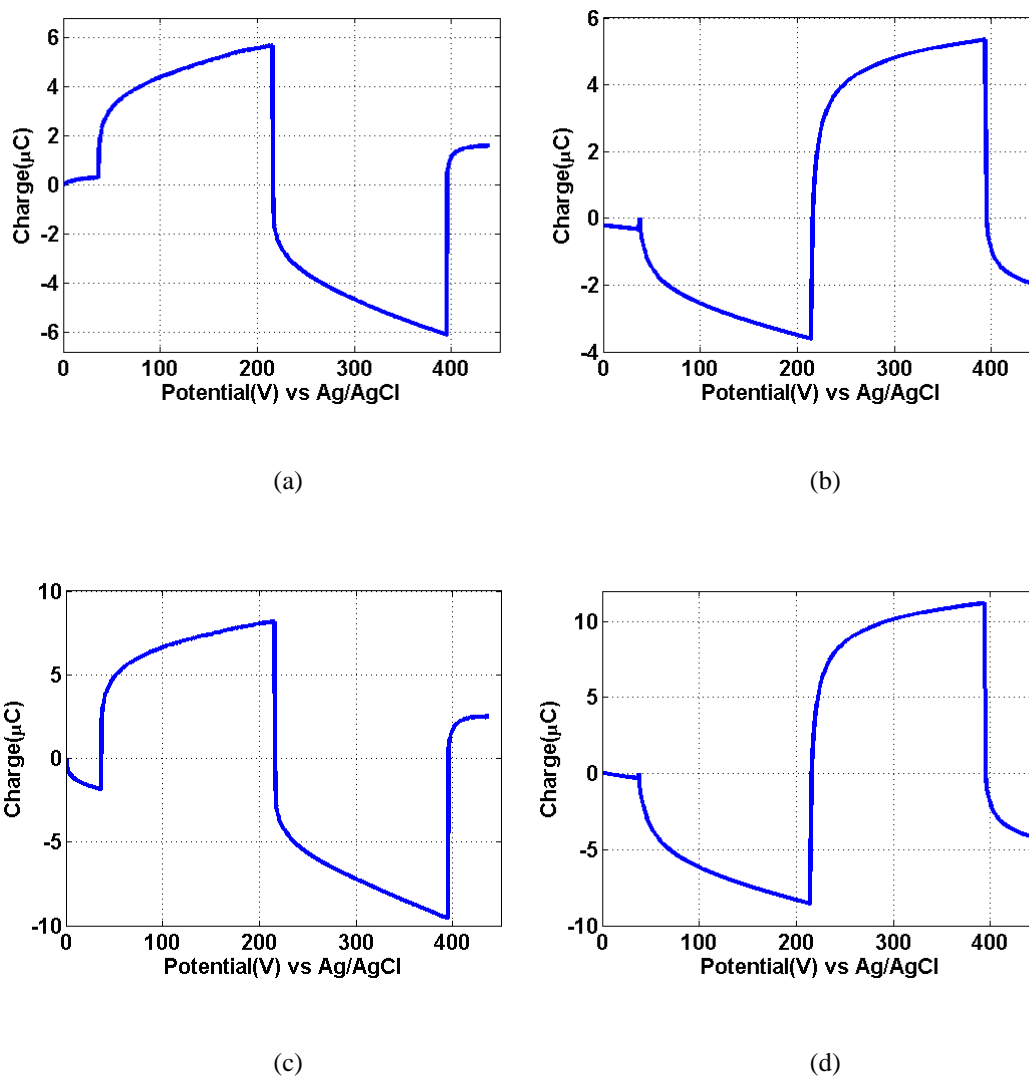
Figure 5.13   Measurements of charge in response to the potential step. The sequences of

potential step for (a), (b), (c) and (d) are, 0→0.1→-0.1→0 V, 0→-0.1→0.1→0 V,

0→0.2→-0.2→0 V, 0→-0.2→0.2→0 V.

(a)

(b)

(c)

(d)
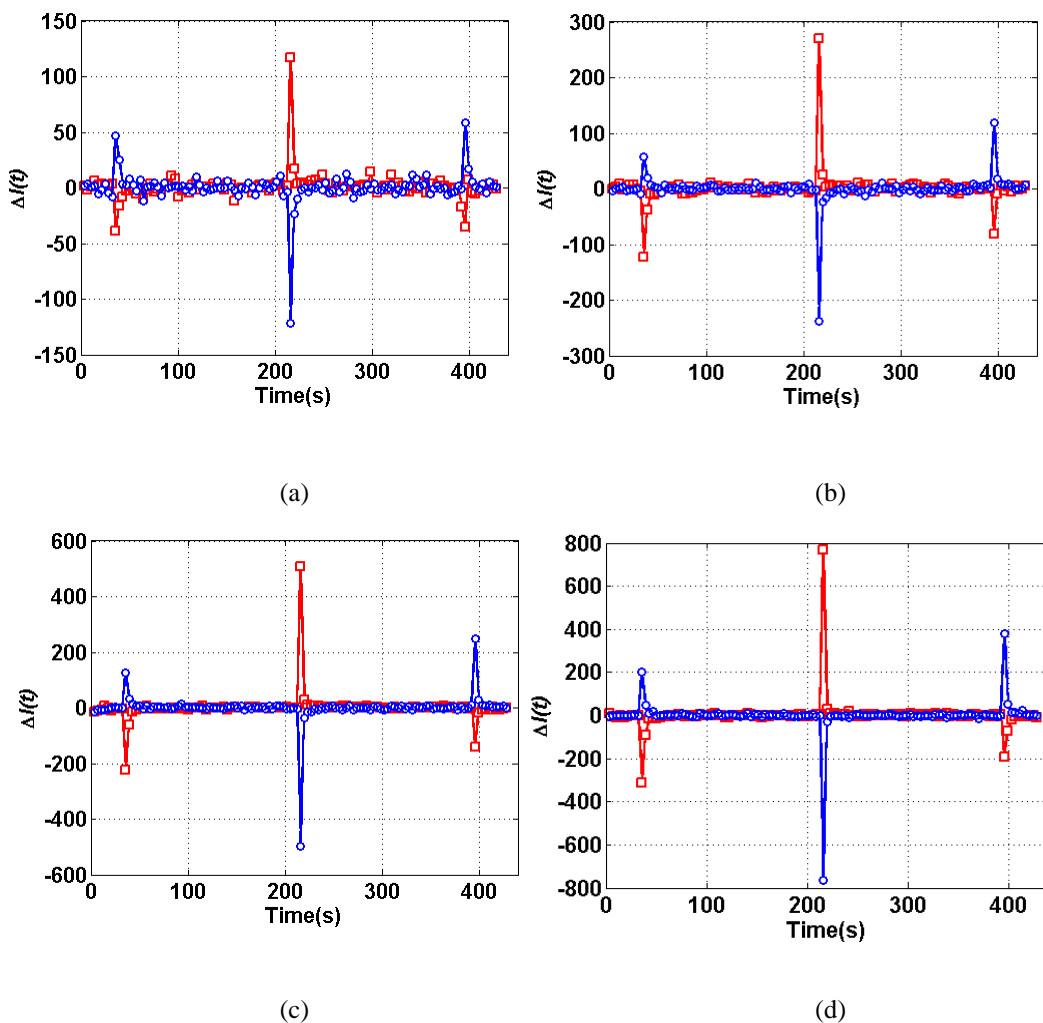
Figure 5.14   The rate of change of scattering from thin Au film during the application of a

potential step. The potential sequence of the red square lines in (a), (b), (c) and (d) are

0→0.05→-0.05→0 V, 0→0.1→-0.1→0 V, 0→0.15→-0.15→0 V, 0→0.2→-0.2→0 V and the

blue circle lines in (a), (b), (c) and (d) are 0→-0.05→0.05→0 V, 0→-0.1→0.1→0 V,

0→-0.15→0.15→0 V, 0→-0.2→0.2→0 V. Each point was obtained by subtracting the i+1th

scattering sampling from the ith scattering sampling.

The equivalent circuit of the electrode-solution interface containing the

specific adsorption process [137] is illustrated in Fig. 5.15. The capacitance

contributed from the adsorption ions is represented by the series of adsorption resistance R_{ad}, adsorption capacitance C_{ad} and a Warburg impedance W_{ad}, related to the specific adsorption ions diffusion to the electrode surface. The total impedance and capacitance of this electrical circuit are given by

$$Z(\omega) = R_s + \cfrac{1}{i\omega C_{dl} + \cfrac{1}{R_{ad} + \cfrac{\sigma_{ad}}{\sqrt{i\omega}} + \cfrac{1}{i\omega C_{ad}}}} \qquad (5.12a)$$

and

$$C(\omega) = \frac{1}{i\omega(Z(\omega)) - R_s)} = C_{dl} + \frac{C_{ad}}{1 + \sigma_{ad}C_{ad}\sqrt{i\omega} + R_{ad}C_{ad}i\omega} \qquad (5.12b)$$

where R_s is the solution resistance, C_{dl} is the double-layer capacitance, $\sigma_{ad}(i\omega)^{-1/2}$ is the diffusional impedance with its coefficient σ_{ad}. Because the adsorbing species Cl$^-$ is a major component of the electrolyte, it approaches the electrode surface by migration instead of diffusion, so the diffusional element W_{ad} is negligible [138]. At high frequencies range, the total capacitance is identified only as C_{dl}, the double-layer capacitance. But at low frequency and DC, $C_{dl}+ C_{ad}$ is present as the total capacitance at the electrode-solution interface.

The anion Cl$^-$ adsorbing at the gold surface in the case of positive potential is stronger than the cation Na$^+$ adsorbing in the case of negative potential. As a result, the application of positive potential induces larger

capacitance than negative potential on the electrode surface, represented by the larger differential scattering spikes at 36 s and 396 s when the potential was altered between the positive and zero. Since the exchange quantity of chloride and sodium ions adsorbed on the electrode surface induced by the switch of potentials at 216 s are almost equal, the same change in the magnitude of adsorption capacitance results in the same size of spikes.
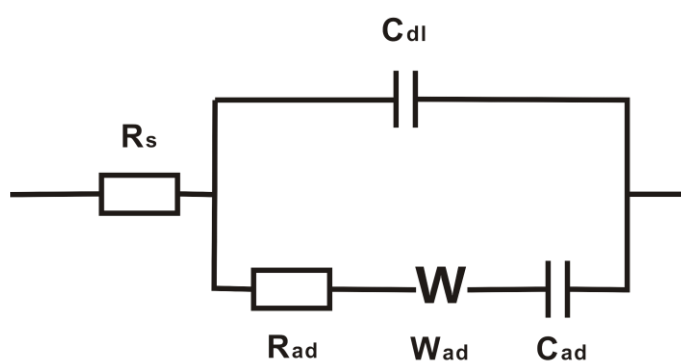
Figure 5.15 Equivalent circuit of the electrode-solution interface in the presence of adsorption ions. R_s and R_{ad} are the solution and adsorption resistances. C_{dl} and C_{ad} are the double layer and adsorption capacitances. W_{ad} is the diffusional (Warburg) impedance.

As the potential step size increased, the size of these spikes at the switch points increased significantly, which demonstrate that the effect of potentials in accordance with their magnitude again. The scattering tendency modulated by the potential steps indicates that the scattering strength depends on both the magnitude of potential and its application time.

5.3   Detection of potential with a SPR platform

Potential detection from thin gold film measured by dark-field spectrometry and microscopy was demonstrated in the last section. At an incident angle of 44 °, the voltage sensitivity of thin (~16 nm) gold film far exceeds that of the thicker (~50 nm) film. In this section, a commercially obtained SPR system (Reichert, SR7000DC) was employed to examine the feasibility of potential detection from thicker gold films (~50 nm) illuminated at the APR angle, which is inaccessible to the custom dark-field instrument.

Surface plasmons are the oscillation of free charges at the interface of a noble metal and a dielectric and are inherently associated with an electromagnetic field. Because of its extreme sensitivity, alteration of the properties of either the dielectric or the metal leads to a significant change in measurement. The configuration of this SPR system of 60 ° to 80 ° incident angle and 780 nm p-polarised illumination provides the correct arrangement to raise surface plasmon resonance propagating on a 50 nm thickness gold film. Observation of the effects of potential on SPR was implemented by recording the refractive index units (RIUs) as a function of the potential applied on the 50 nm gold film with about 2 mm^2 surface area.

5.3.1   Cyclic voltammetry of the Au film-solution interface on SPR system

Cyclic voltammetry from -200 mV to 200 mV was applied to demonstrate

that no redox reaction occurred in this potential range in 0.1 M NaCl (Fig 5.16).

No reduction or oxidation current peak was observed in this potential window

and the presence of current was due to the electrical double layer charging.
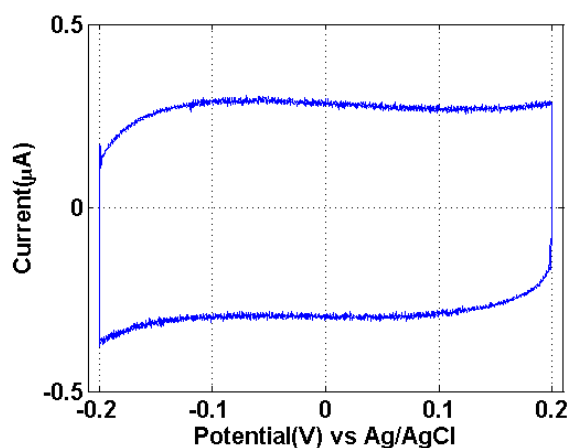
Figure 5.16   Cyclic voltammetry of 50 nm Au film in 0.1 M NaCl at a scan rate of 0.1 V/s

5.3.2   Refractive index units as the function of potential

A series of potential modes from BMA ($\pm$ 200 mV) to BMF ($\pm$ 10 mV)

and BMG (0 V) were applied to a 50 nm gold film deployed on this SPR

system. The electrolyte was 0.1 M NaCl. Figure 5.17 depicts the tendency in

RIU caused by these potentials. The higher and lower RIU induced by the two

polarised potentials clearly indicated that the positive and negative potentials

had opposite effect on the refractive index either in the gold film or its

surrounding medium. An increase of local refractive index in the vicinity of

gold surface is expected due to the adsorption of anions in the case of positive

potential or cations in the case of negative potential applied on the electrode

surface, which are to form the electrical double layer. Transport of charges via

this double layer changes the free electron density in the surface layer of gold.
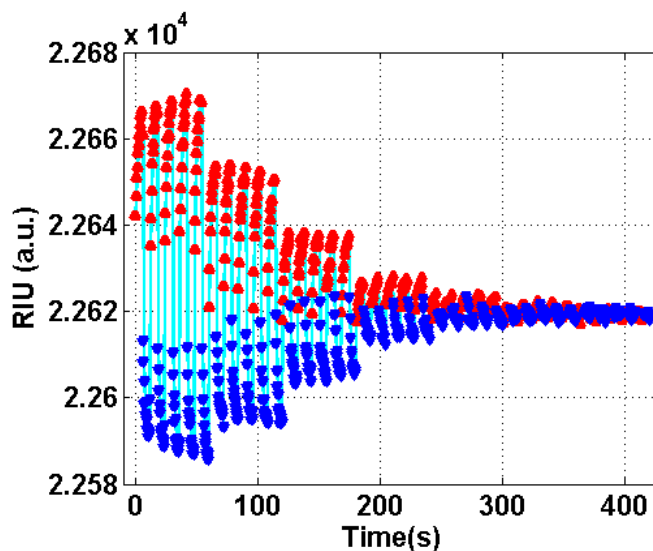
Figure 5.17 Potential induced refractive index unit trace of 50 nm Au film. The sequence of

potential was ±200 mV, ±150 mV, ±100 mV, ±50 mV, ±25 mV, ±10 mV and 0 mV. The

sampling period was 0.5 s. 6 s duration of each pulse resulted in 12 samples. The red and blue

triangles represent positive and negative potentials respectively. The cyan line is drawn as an

eye-guide.

The electron density is increased under the condition of negative potential or

decreased by the application of positive potential. The dielectric function of

gold is dependent on its free electron density, so its change in polarity is altered

with that of the potentials. The symmetric trend of RIU with respect to its value

at 0 V indicated that the RIU was predominantly affected by the change in the

dielectric function of gold due to the alteration of electron density rather than

the increase of the refractive index of surrounding medium of gold because of the ions absorption. The gradually increased RIU in each potential mode, especially apparent in higher potential modes, was accounted for the slow relaxation of charges. In each potential mode, the opposite potential did not completely deplete the charge cumulated by its counterpart. The residual charges pushed the RIU value to a greater level when the same potential was applied again.

The response of Au film to the potential was characterised by its contrast defined as

$$RIU_{contrast} = \frac{\sum\limits_{i=1}^{60} RIU_{higher\_i} - \sum\limits_{i=1}^{60} RIU_{lower\_i}}{\sum\limits_{i=1}^{60} RIU_{higher\_i} + \sum\limits_{i=1}^{60} RIU_{lower\_i}} \qquad (5.13)$$

where RIU_{higher_i} and RIU_{lower_i} represent ith refractive index units value measured at higher and lower potential respectively.

The RIU contrast of 50 nm Au film measured at a series of different potential modes and its fitting curve employing Eq. (5.10) is shown in Fig. 5.18. The value of (A, c) was (0.0113, 1.519). The value of c, 1.519, indicates an increased non-linearity in the RIU contrast which was more severe than the scattering contrast as a function of potential of thin Au film measured by the dark-field system in Sec. 5.2.4, whose value of c was 1.319.
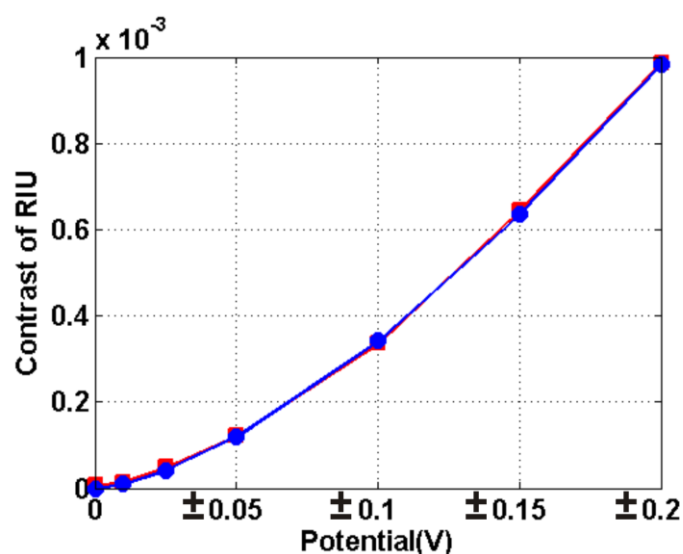
Figure 5.18   The red squares and line is the RIU contrast of 50 nm Au film resulted from

the multi-potential modes where the potential was reduced from ±200 mV to 0 V. The blue

circles and line represents the fitting curve.

5.3.3   The effect of electrolyte concentration

The effect of the bulk NaCl concentration on the potential response of the

50 nm Au film is shown in Fig. 5.19. The contrast decreased from BMA (± 200

mV) to BMB (± 150 mV) and BMC (± 100 mV) as expected. However, at each

potential mode, the contrast value increased from low concentration to a

plateau at moderate concentration then decreased considerably at even higher

concentration.
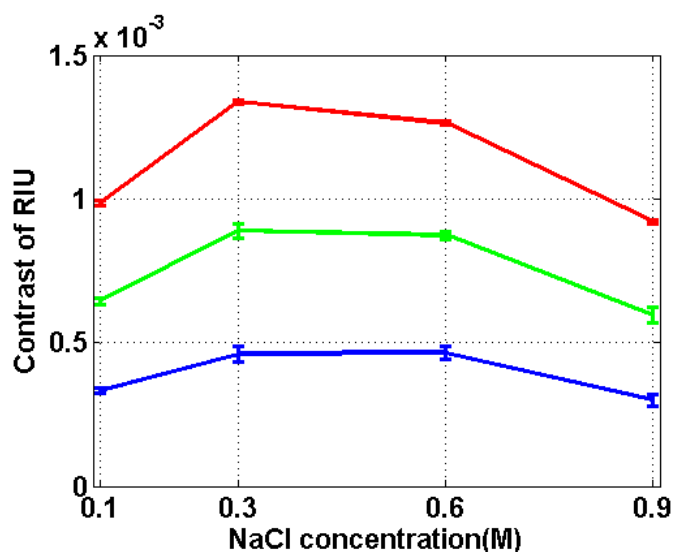
Figure 5.19 Contrast of RIU dependent on the NaCl concentration at 0.1 M, 0.3 M, 0.6 M and

0.9 M. The red, green and blue represent contrast measured for BMA, BMB and BMC.

The electrical double layer capacitance C_D comprises two individual capacitances in series, the inner Helmholtz capacitance C_H whose properties are determined by a layer of solvent and water molecules in the vicinity of the gold surface and the diffuse capacitance C_{diff} dependent on the concentration of bulk electrolyte from the outer Helmholtz layer into bulk of solution. C_D is therefore governed by the smaller of the two capacitances.

At low electrolyte concentration, C_{diff} dominates the total capacitance. The charges accumulated in the electrical double layer increases with increasing electrolyte concentration. Consequently, the displacement of the RIU value induced by two polarised potentials increases with increased concentration. The resultant RIU contrast follows the ascending trend of the

electrolyte concentration. Meanwhile, high electrolyte concentration compresses the thickness of electrical double layer. As one critical concentration is approached, the determination of total capacitance becomes dominated by the Helmholtz capacitance C_H. The presence of 0.9 M NaCl provided abundant cations and anions to adsorb on the gold surface, together with water molecules to realign the Helmholtz capacitance. The binding of cations compensate the negative polarisation of gold while the anions implement an alternate way to decrease the positive potential on the gold surface. The repulsion of coion and attraction of counterion enhance the concentration of counterion, and thereby intensify the neutralisation of gold surface and screen the electrostatic force [139].

5.3.4   Modulation of RIU during cyclic voltammetry

The RIU value related to the CVs of different potential scan rates, 0.01 V/s, 0.005 V/s, 0.001 V/s, in the presence of 0.1 M NaCl are shown in Fig. 5.20. The potential applied was between ±200 mV. The trend of the RIU value followed the same direction as the potential scan when it began from 200 mV.

(a)

(b)

(c)
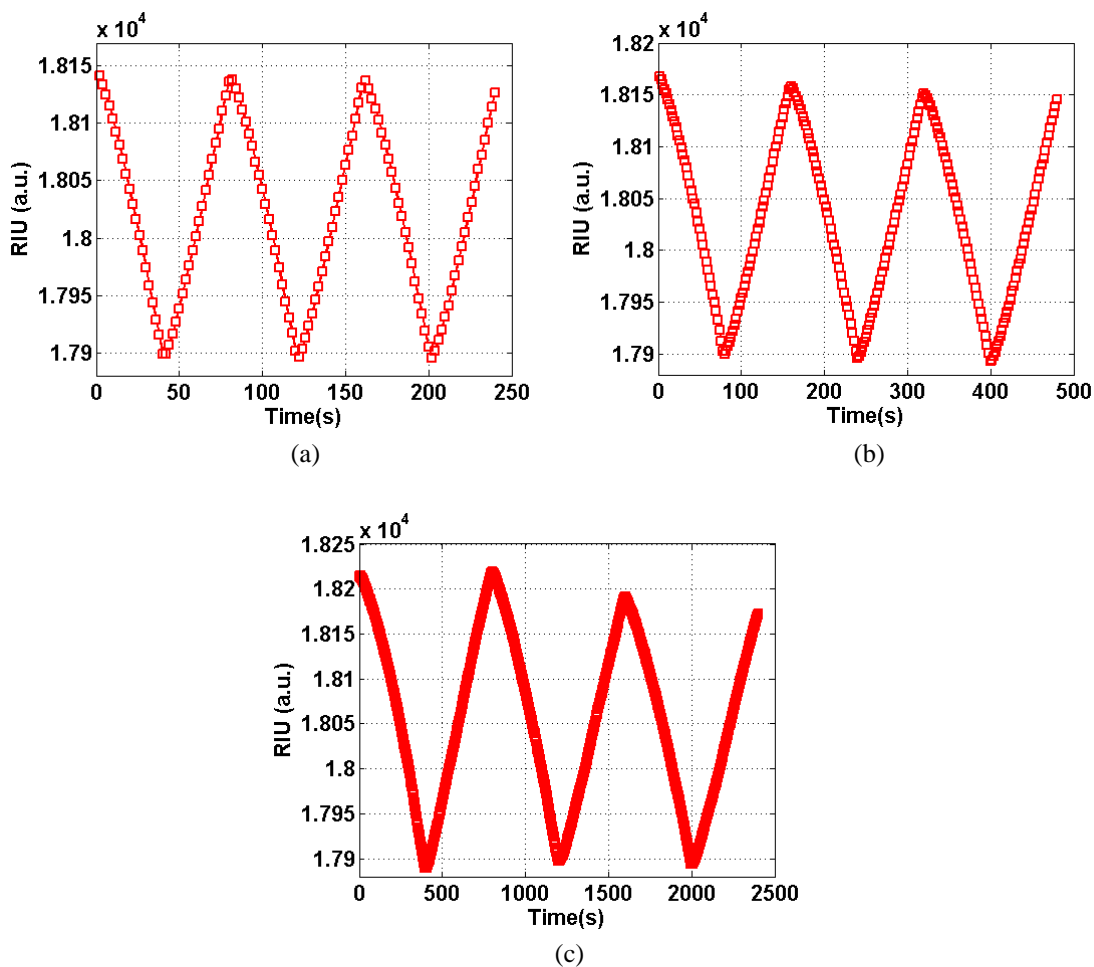
Figure 5.20   RIU traces obtained from cyclic voltammetry. The sampling period for each

RIU value was 2 s. The potential scan rate in (a) was 0.01 V/s, (b) was 0.005 V/s and (c) was

0.001 V/s. The potential began from 200 mV in each measurement.

This behaviour of the RIU transient was strongly dependent on the

potential scan rate. Differentiation of the RIU between ±200 mV as a function

of time gave the details of this transient as shown in Fig. 5.21. The behaviour

was evaluated with Eq. (5.11). The values of (a, b, τ) were (8.305, 6.006, 9.792

s) for 0.01 V/s, (4.058, 3.398, 17.71 s) for 0.005V/s and (1.009, 0.7626, 82.55 s)

for 0.001 V/s. The ratio of time constants 9.792:17.71:82.55=1:1.8:8.43 is

138

proportional   to   the   reciprocal   ratio   of   potential   scan   rates

0.01:0.005:0.001=1:1/2:1/10.

(a)

(b)

(c)
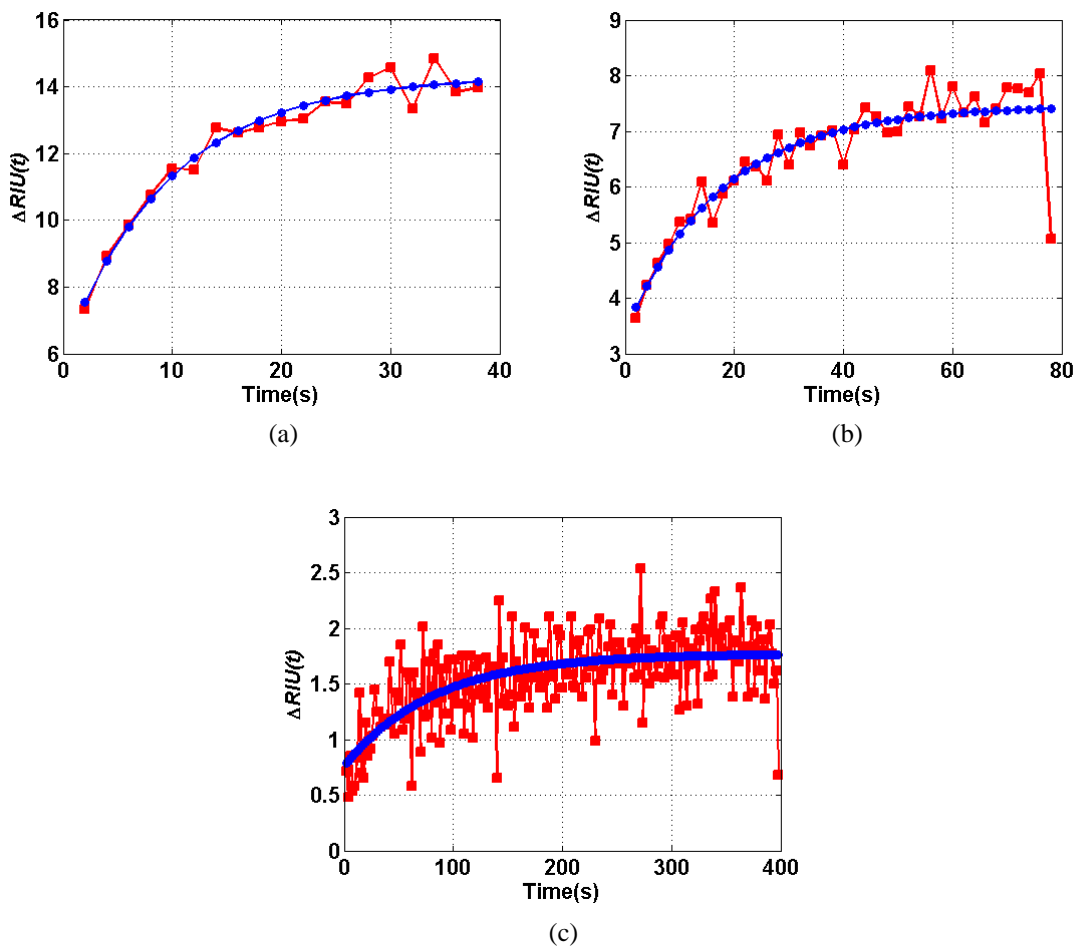
Figure 5.21 Rate of change of RIU by differentiation. The potential scan rate in (a), (b) and (c)

were 0.01 V/s, 0.005 V/s and 0.001 V/s. The red line is the differential value of experiment.

The blue line is a fit to Eq. (5.11).

The time constants of the 50 nm Au film depending on the potential scan

rates detected by SPR system were the same as that found from thin Au film

measured by the dark-field spectrometer. This result reveals that the

charging-discharging process of Au film invoked by a linear potential scan can

be represented by an exponential transition. The faster potential scan results in

139

an earlier equilibrium achievement between Au film and electrolyte.

5.4   Model for electrical induction on gold film

The performance of the gold film under the influence of an applied potential can be explained by applying Fresnel's equations to the multilayer structure as presented in Sec. 5.1. The Thomas-Fermi layer induced by the potential and the rough surface of the gold, both affect the relative permittivity of gold. Consequently, the reflected and transmitted light from the gold varies according to the change in gold structure. Two standards including contrast and signal-to-shot noise ratio are presented to characterise the consequences of the potential in terms of the wavelength and the incident angle of the illumination beam.

5.4.1   Structure of five layer model

The planar gold film is sandwiched between the coverslip and the electrolyte. Meanwhile, the external electric field creates an electrical double layer adjacent to the surface of the gold film. The induced alignment of charges alters the relative permittivity of gold but only extends for a few Ångström from the top surface due to the shield reaction created by the Thomas-Fermi layer, as described in Sec. 3.3. This multilayer model of the experiment is shown schematically in Fig. 5.22. The bottom domain is glass (BK7, $n = 1.517$). The gold is deposited onto the glass and the top domain of electrolyte is 0.1 M NaCl ($n = 1.33$). The gold film comprises three layers, namely a pure bulk gold

layer, an effective medium layer and a Thomas-Fermi layer.
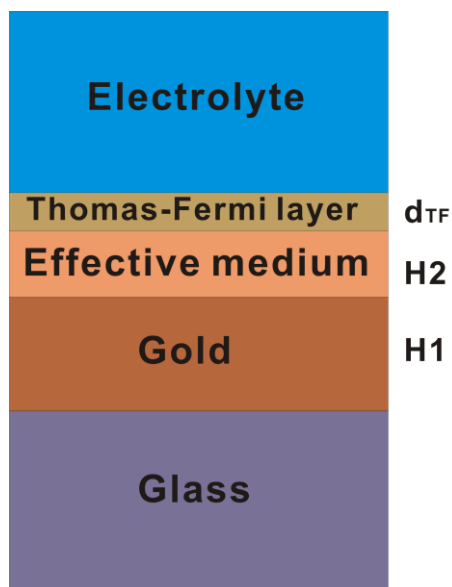
Figure 5.22   Model of gold immersed in electrolyte with applied potential

Due to the thermal evaporation technique employed for depositing the gold film on the coverslip, randomly dispersed gold islands grow on the bare coverslip to aggregate as a continuous film. A plain pure gold layer exists at the bottom of the gold structure. Au islands embedded in the electrolyte aggregate and are represented as an effective medium layer on the top of the pure gold layer. The rough Thomas-Fermi layer caused by the external electric field is positioned above the effective medium layer, separating it from the electrolyte. It is assumed that distributed gold islands in the effective medium are spherical with the depolarisation factor $L = 1/3$ and the volume fraction p of gold is 0.8. The pure plain gold layer ($H1$) and the effective medium layer ($H2$) are estimated to occupy 90 % and 10 % of the total nominal thickness of gold film [96]. Drude-Lorentz theory and Bruggeman model described in Sec. 3.1 was used to calculate the relative permittivity of gold.

5.4.2   Characterisation of the effect of potential on the gold film

The incident beam I_{inc} illuminating the gold structure through the glass results in a portion of light reflected back from its bottom and a portion transmitted from its top surface. Making use of the reflection and the transmission coefficients, *R* and *T* mentioned in Sec. 5.1, the irradiance of the reflected beam I_{ref} and the transmitted beam I_{tran} are obtained as

$$I_{ref} = I_{inc}R \qquad (5.14a)$$

$$I_{tran} = I_{inc}T \qquad (5.14b)$$

In a practical measurement, the detected reflected and transmitted beam energies are constrained by several factors during the beam propagation, including the numerical aperture of the microscope objective lens, the quantum efficiency of the detection devices and the integration time.

Two measures are now introduced to characterise the resultant light from either the reflected or the transmitted field. The first one is the contrast defined as

$$C_{contrast} = \frac{I_{higher} - I_{lower}}{I_{higher} + I_{lower}} \qquad (5.15)$$

With I_{higher} and I_{lower} representing the irradiance of the reflected or the transmitted beam resulting from the applied higher and the lower potentials respectively.

Since the contrast only considers the relative irradiance, the signal-to-shot noise ratio (SSNR) was also utilised to characterise the detected signal determined by the number of detected photons. In the detection system, the overall detection efficiency η is written as

$$\eta = \frac{4\{\sin^{-1}(\frac{NA}{n_{coupling}})\}^2}{\pi^2} \times T_{tran} \times QE_{\lambda} \quad (5.16)$$

where both the numerical aperture of objective *NA* and the refractive index of medium separating the objective and the specimen $n_{coupling}$ determine the detection angle of objective. In addition, the optical transmission of T_{tran} and the quantum efficiency QE_{λ} of detection sensor contribute to the overall detection efficiency η as well.

The minimum distance that the objective lens can resolve two closely spaced point elements according to the Rayleigh criterion is

$$d_{Rayleigh} = \frac{0.61\lambda}{NA} \quad (5.17)$$

where $d_{Rayleigh}$ is the Rayleigh resolution distance [m], λ is the wavelength of the illumination beam [m] and *NA* is the objective lens numerical aperture.

Nyquist-Shannon sampling theorem states that in order to fully reconstruct the image, the resolvable element is required to be sampled twice. To satisfy the Nyquist requirement, the sampling interval is half of the

Rayleigh distance. The minimum required sampling area S_{area} [m^2] is therefore

$$S_{area} = (\frac{d_{Rayleigh}}{2})^2 \qquad (5.18)$$

The reflected and transmitted beams emerged from this sampling area S_{area} are delivered as photons to the detection device. Assuming the gold film's temperature does not rise too much due to the energy absorbed from the illuminated beam, the energy of the detected reflected and transmitted beam is

$$I_{det\_ref} = I_{ref} S_{area} \eta T_{integration} \qquad (5.19a)$$

$$I_{det\_tran} = I_{tran} S_{area} \eta T_{integration} \qquad (5.19b)$$

where $T_{integration}$ is the integration time of detection sensor.

The numerous advantages of CCD sensors allow them to be applied widely. But CCD's are of course subject to noise, with the three primary components being photon noise, dark noise and readout noise. In general, the effect of dark noise and readout noise can be reduced by the design of the CCD sensor. The shot noise generated by the arrival of photons within the sensor determines the fundamental limit of detection sensitivity. The magnitudes of the detected beams in terms of photon number are

$$N_{det\_ref} = \frac{I_{det\_ref}}{E_{photon}} \qquad (5.20a)$$

$$N_{\mathrm{det\_tran}} = \frac{I_{\mathrm{det\_tran}}}{E_{photon}} \qquad (5.20b)$$

where E_{photon} is the energy of one photon, equivalent to hc/λ, h is the Planck's constant [Js], λ is the wavelength of beam [m] and c is the speed of light [ms^{-1}].

The magnitude of the shot noise is governed by Poisson statistics and is equivalent to the square-root of the signal in an integrating detector, so the signal-to-shot noise ratio (SSNR) is

$$SSNR_{ref} = \frac{N_{\mathrm{det\_ref}}}{\sqrt{N_{\mathrm{det\_ref}}}} = \sqrt{N_{\mathrm{det\_ref}}} \qquad (5.21a)$$

$$SSNR_{tran} = \frac{N_{\mathrm{det\_tran}}}{\sqrt{N_{\mathrm{det\_tran}}}} = \sqrt{N_{\mathrm{det\_tran}}} \qquad (5.21b)$$

The procedure for the utilisation of SSNR to investigate the influence of the potential on the gold film is described as follow. Spectra for the reflected or the transmitted light in terms of the detected photon numbers induced by a higher potential and a lower potential were calculated. The difference of the detected photon numbers due to the two potentials is the signal and the numerator of this ratio. The square-root of the total photon numbers is the noise, the denominator of this ratio. The division of the numerator and the denominator is the SSNR related with the potential, which is defined as

$$SSNR = \frac{N_{higher} - N_{lower}}{\sqrt{N_{higher} + N_{lower}}} \qquad (5.22)$$

where N_{higher} and N_{lower} are the number of photons detected as the reflected

or the transmitted beam at the higher and the lower potential respectively.

In the following sections, contrast and SSNR will be utilised to characterise the gold film's sensitivity to the change of potential.

5.4.3   Contrast as a function of potential

The response of the light reflected from the gold film at different potentials is transferred as contrast to quantify its sensitivity to potential. The reflected light is unpolarised light which is defined as the sum of half p- and half s- polarised light. In accordance with the conditions of the experiment, the thin gold film represented by 15 nm thickness was illuminated at a 44 ° angle of incidence and potentials of ±200 mV, ±150 mV, ±100 mV, ±50 mV, ±25 mV, ±10 mV and 0 V respectively were applied. Beside the case mentioned at beginning that the pure plain gold layer (*H*1) and the effective medium layer (*H*2) are estimated to occupy 90 % and 10 % (case a) of the total nominal thickness of gold film, three other cases, the pure plain gold layer and the effective medium layer occupy 70 % and 30 % (case b), 40 % and 60 % (case c), 0 % and 100 % (case d) of the total nominal thickness of gold film, are considered in this section for comparison. The calculated contrast recorded at 3

wavelengths, 550 nm, 600 nm and 650 nm marked by red, purple and green squares and their corresponding best-fit curves indicated by blue triangles are shown in Fig. 5.23.

(a)

(b)

(c)

(d)
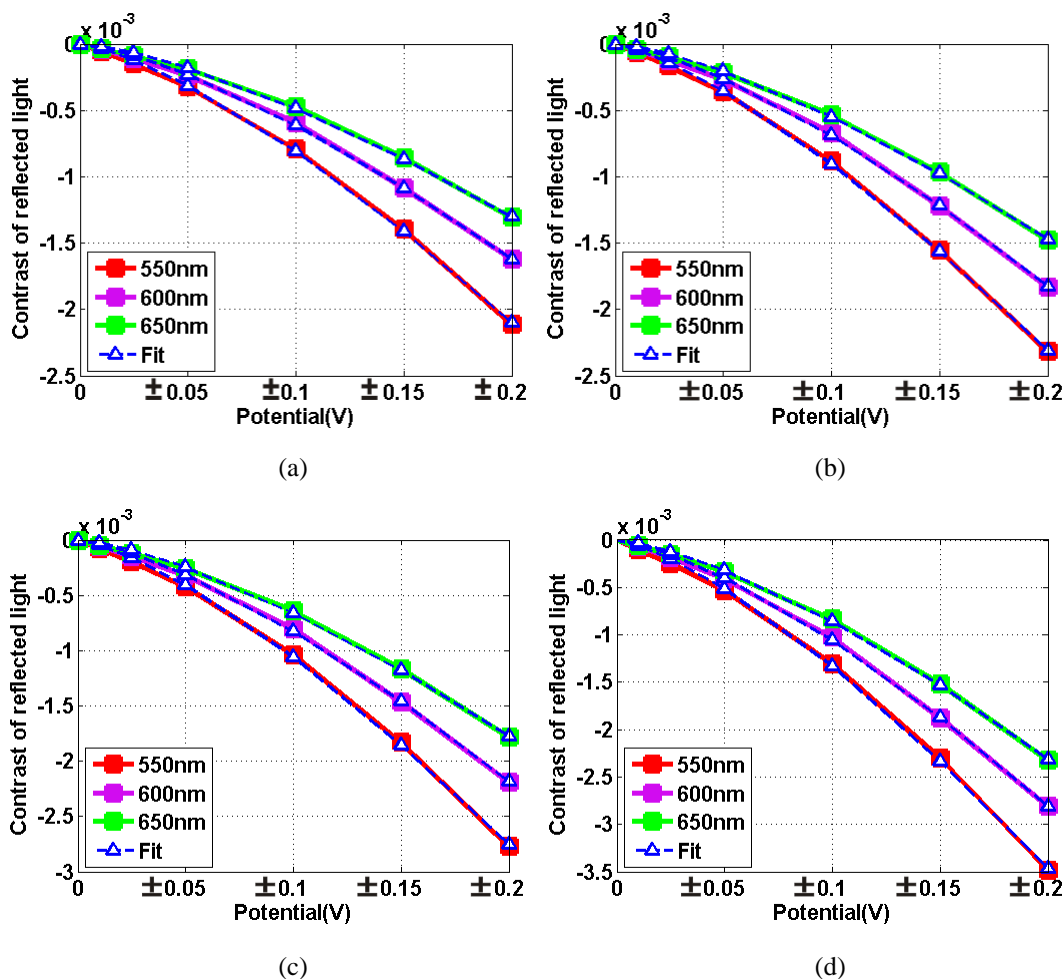
Figure 5.23 Contrast calculated from the reflected light and the corresponding best-fit curve.

The red, purple and green squares and solid lines are the contrasts calculated from the reflected

light at 550 nm, 600 nm and 650 nm. The blue triangle dashed lines represent their

corresponding best-fit curve for Eq. (5.10). The thicknesses of the pure plain gold layer and the

effective medium layer in (a), (b), (c) and (d) are described in case a, b, c and d respectively.

See Fig. (5.9) for the curve derived from experimental data.

All of them decrease with the corresponding potentials as expected. The fitted values of (A, c) for the calculated contrast at 550 nm, 600 nm and 650 nm were (-0.0193, 1.378), (-0.0156, 1.409), (-0.0129, 1.428) in case a, (-0.0205, 1.357), (-0.0176, 1.41), (-0.0147, 1.429) in case b, (-0.0254, 1.381), (-0.0209, 1.405), (-0.0177, 1.43) in case c and (-0.032, 1.381), (-0.027, 1.408),   (-0.0231, 1.432) in case d. The values of c of larger than unity in all cases is consistent with the fitting value 1.319 for the experimental result illustrated in Fig. 5.9, showing that both experimental and calculated contrasts reduce nonlinearly with decreasing potential.

The difference between the experimental and calculated contrast is probably due to the heterogeneous gold layer and the effect of the electrical double layer. In spite of the addition of the effective medium layer, which takes the roughness of gold surface into consideration, the estimation of the consequences of thermal evaporation during the whole process of gold deposition is insufficient. The gold nano-islands scatter strongly on gold film surface while this consideration in the simulation is inadequate. The magnitude of contrast increases with increasing effective medium thickness as shown in Fig. 5.23. The properties of gold may need to be considered from the glass substrate to its top surface [96]. The computation of the electrical double layer could be improved by considering the specific, and nonspecific adsorbed ions' impacts on the gold.

5.4.4   Wavelength dependent contrast and SSNR

Although the quantitative prediction of this modelling is insufficient, it could provide the general trends and illustrate the qualitative effect. The reflected and transmitted spectra of the gold film depend on both the wavelength and the incident angle of the illumination beam. In this section, the potential dependent contrast and SSNR as a function of wavelength will be investigated first. Four incident angles, 0 °, 44 °, 70 ° and 80 ° were chosen to use for the comparison of the effects resulting from the potential applied on the gold film of thickness from 1 nm to 80 nm. Because the reflected and the transmitted spectra are mainly dependent on the thickness of gold film and the angle of incident beam, the transition of the angle from below to above the total internal reflection angle 61 ° will have significant effect on the results.

Figures 5.24 and 5.25 illustrate the contrast and the SSNR of the reflected and the transmitted light at these four different angles, calculated from the unpolarised light stimulated by 200 mV and -200 mV respectively. The contrast and SSNR are shown as their absolute values.

(a)   (b)

(c)

(d)

(e)

(f)

(g)

(h)
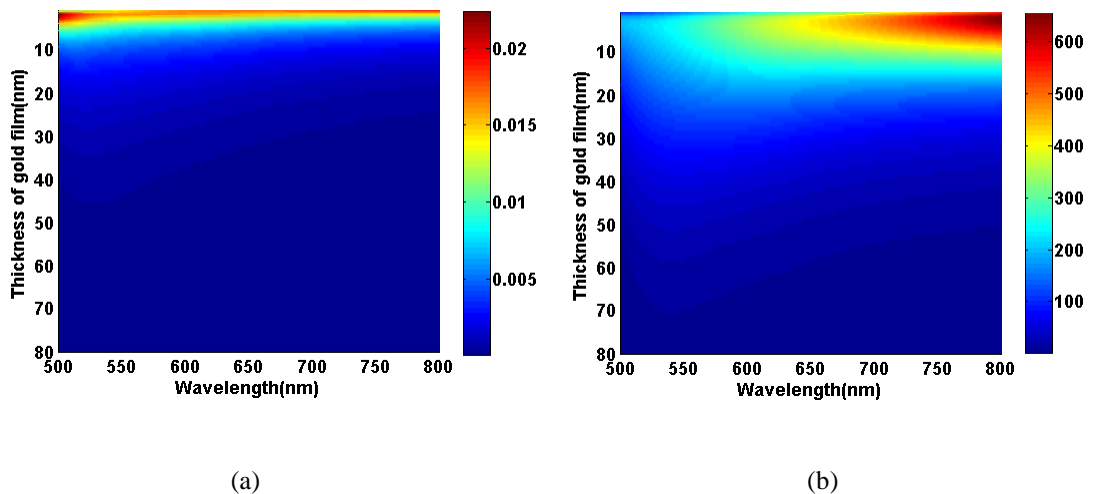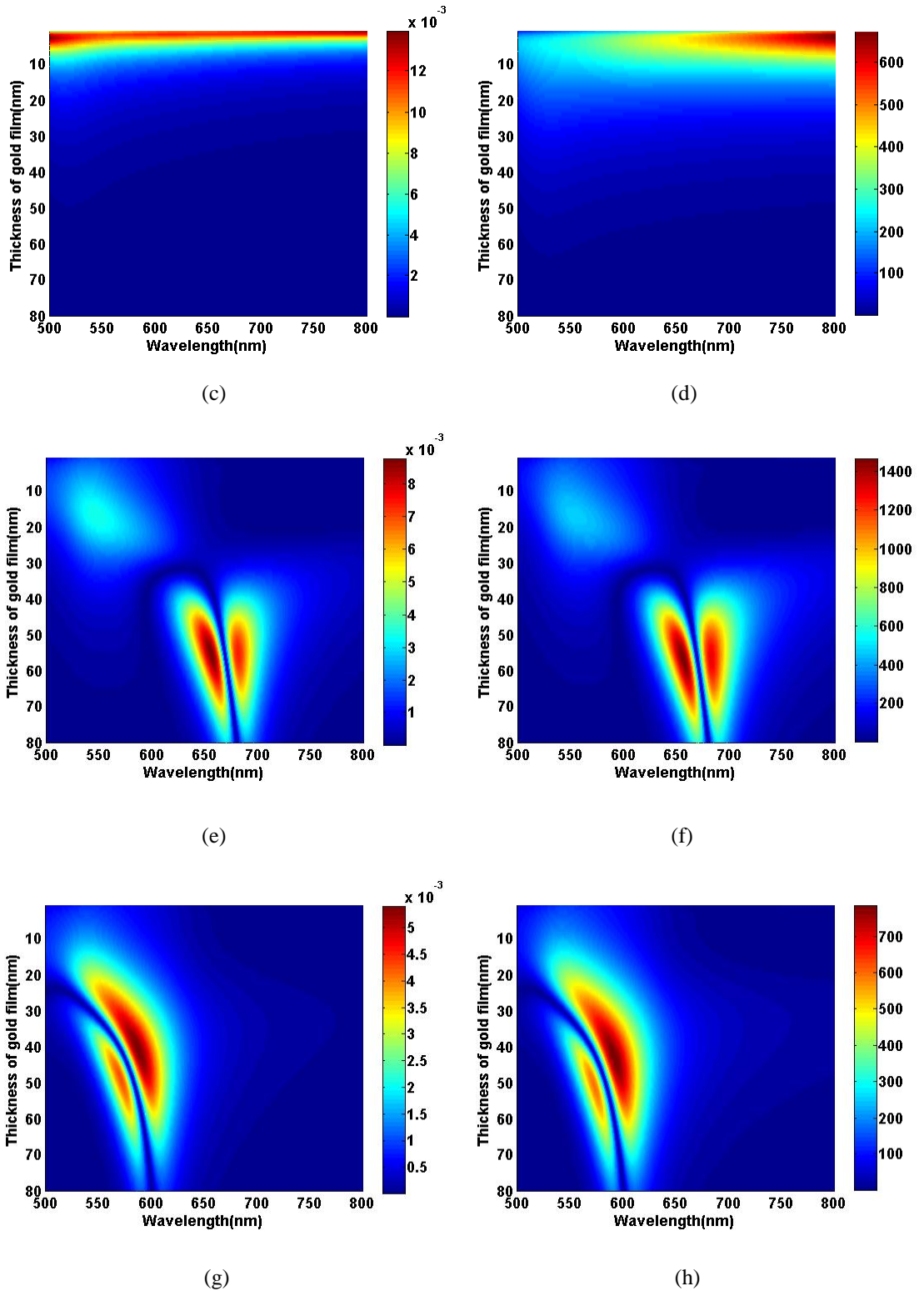
Figure 5.24 The contrast and SSNR of the reflected light from the gold film. (a),(c),(e) and (g) show the contrast of the reflected light at the incident angles of 0 °, 44 °, 70 °and 80 ° respectively. (b), (d), (f) and (h) show the SSNR of the reflected light at the incident angle of 0 °, 44 °, 70 °and 80 °respectively.

The contrast and the SSNR of the reflected light presented in Fig. 5.24 have the same trend for the different thickness of gold film for incident wavelengths from 500 nm to 800 nm. For incident angles less than the total internal reflection angle, namely 0 ° and 44 °, the thinner gold films have better contrast and SSNR compared to the thicker ones, especially at small incident angles. The optimum thickness for voltage sensitivity transfers from thin gold films to the thicker ones as the incident angles increases. Gold films with thickness in the range of 40 nm to 60 nm outperform the others. P-polarised beams whose incident angles are larger than the total internal reflection angle have the chance to raise SPR, which has been demonstrated as an outstanding sensing technology to monitor the change of refractive index near the surface of gold film. The 'butterfly like' features of the contrast and the SSNR presented within the wavelength range of 630 nm to 680 nm in Figs. 5.24 (e) and (f) imply the voltage sensitivity is partially contributed by the SPR. If only the contrast is considered as the criteria to select the best sensitivity platform, thin gold film illuminated at small incident angles performs best. However, taking the number of detected photons into account, thick gold film illuminated at the higher incident angles can provide more photons, which can overcome the lower contrast in a practical measurement.

Usually, reflected light from the gold film is utilised due to the mature methods of investigation for the reflection in the far field. However, there is also a possibility to enhance the electric field near the gold-electrolyte interface due to the evanescent wave. Although this field enhancement takes place in the near field, the near field signal is able to be transferred to the far field by the assistance of the presence of nanostructure at the interface. Considering

making use of the light detected in transmission provides an additional method to detect the potential, even if there are more complex factors that need to be evaluated for the transmitted field, such as the energy loss transfer from the near to far field, which is not taken into account in this model. The light detected in transmission of thick gold films illuminated by higher incident angles is better than all the other arrangements according to the magnitude of both contrast and SSNR. The extraordinary SSNR, which is more than 10,000 in the case of 70° incident angle, indicates proper optical alignment could achieve higher voltage sensitivity by observing 50 to 70 nm gold films due to the field intensity enhancement.

(a)

(b)

(c)

(d)

(e)

(f)

(g)

(h)
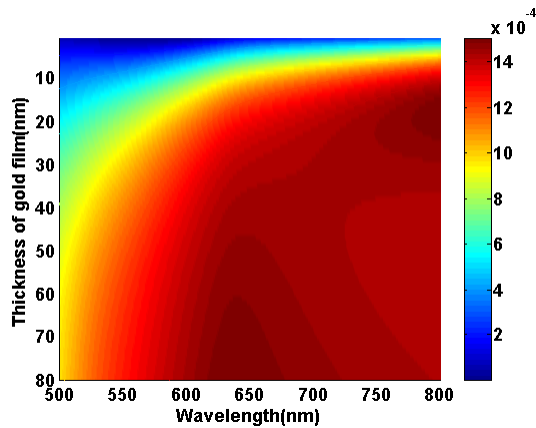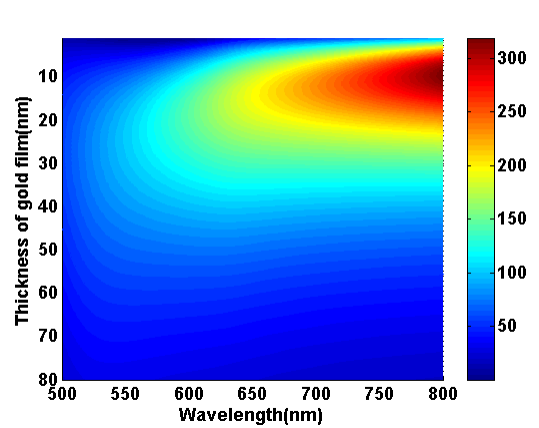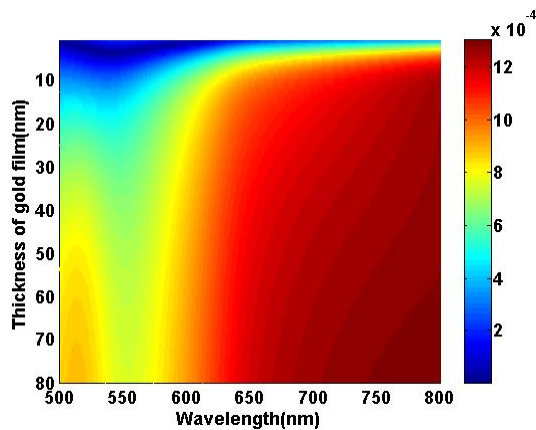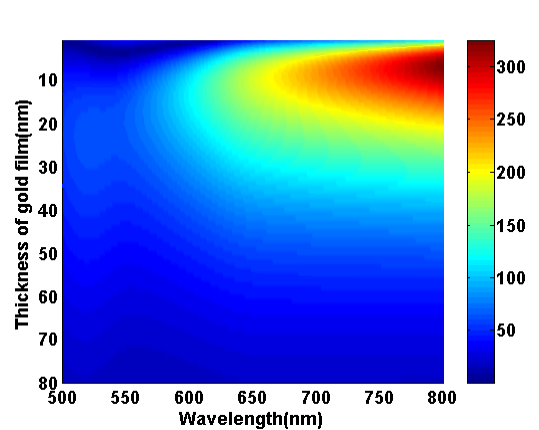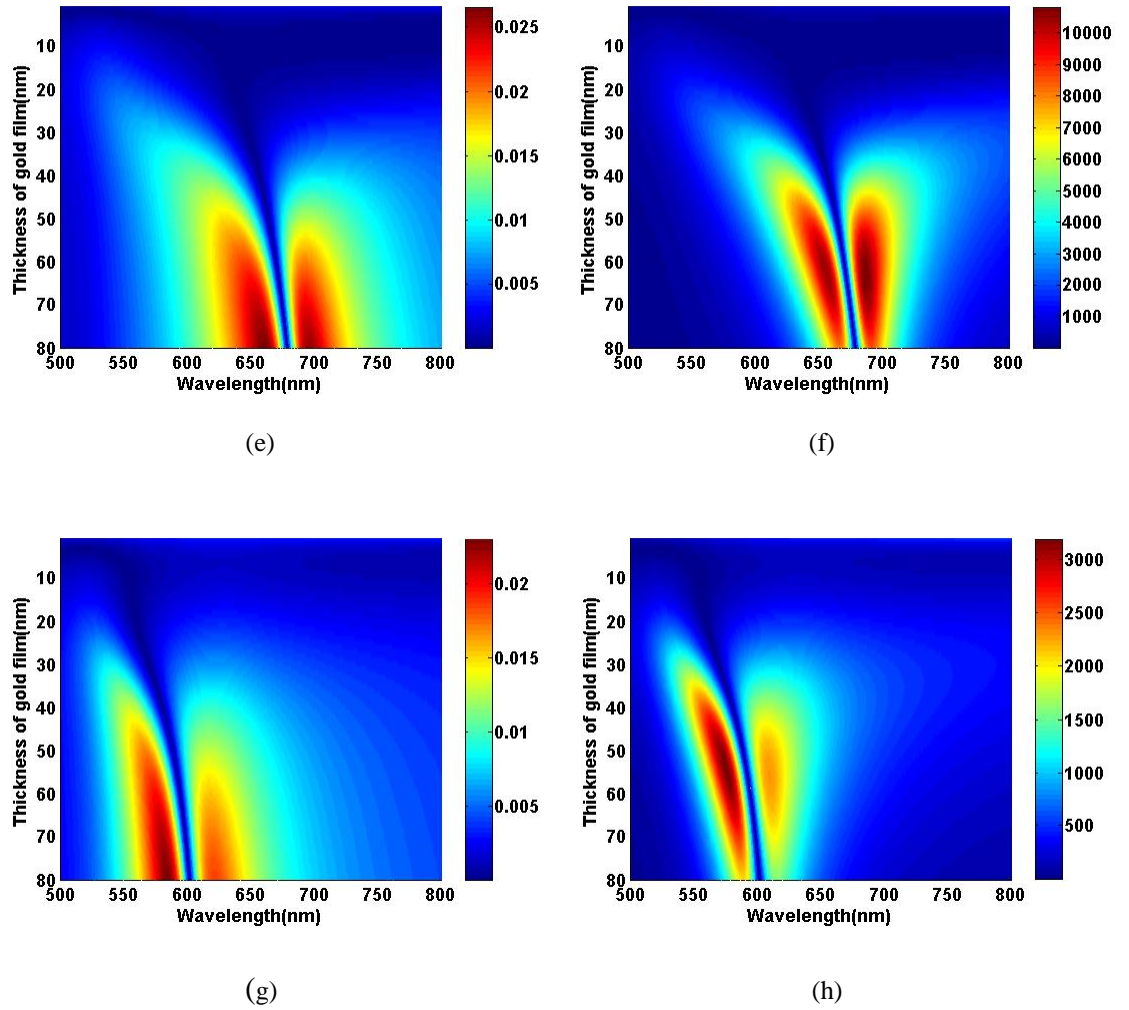
Figure 5.25 The contrast and SSNR of transmitted light from the gold film. (a),(c),(e) and (g) show the contrast of the transmitted light at the incident angles of 0 °, 44 °, 70 °and 80 ° respectively. (b), (d), (f) and (h) show the SSNR of the transmitted light at the incident angle of 0 °, 44 °, 70 °and 80 °respectively.

5.4.5   Incident angle dependent contrast and SSNR

In this section, the contrast and SSNR will be investigated as a function of incident angle. The performance of gold film under the application of ±200 mV was computed by selecting incident beams with wavelengths of 550 nm, 650 nm and 750 nm respectively.

153
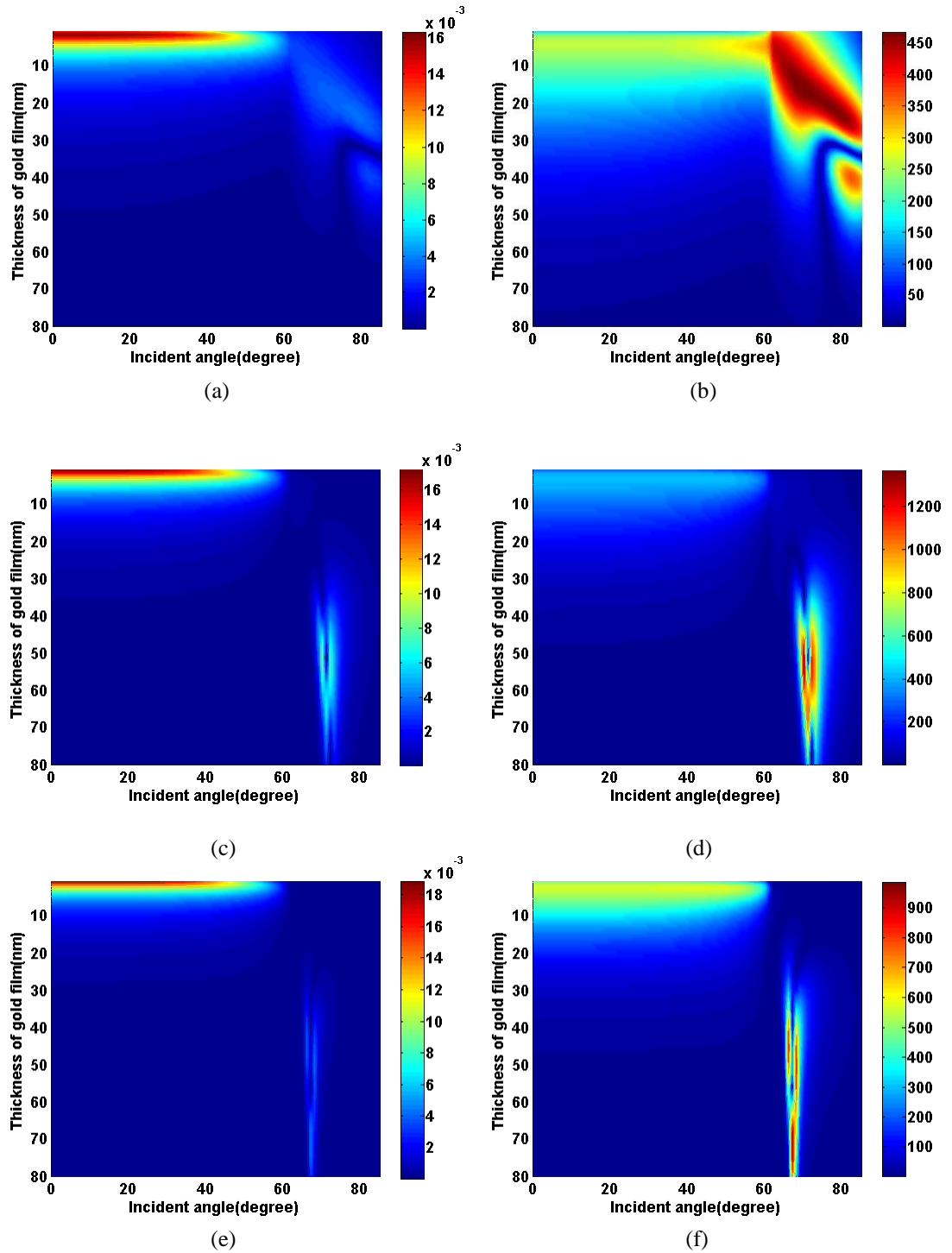
Figure 5.26 The contrast and SSNR of the reflected light from the gold film. (a),(c) and (e) show the contrast of the reflected light at the wavelengths of 550 nm, 650 nm and 750 nm respectively. (b), (d) and (f) show the SSNR of the reflected light at wavelengths of 550 nm, 650 nm and 750 nm respectively.

(a)

(b)

(c)

(d)

(e)

(f)
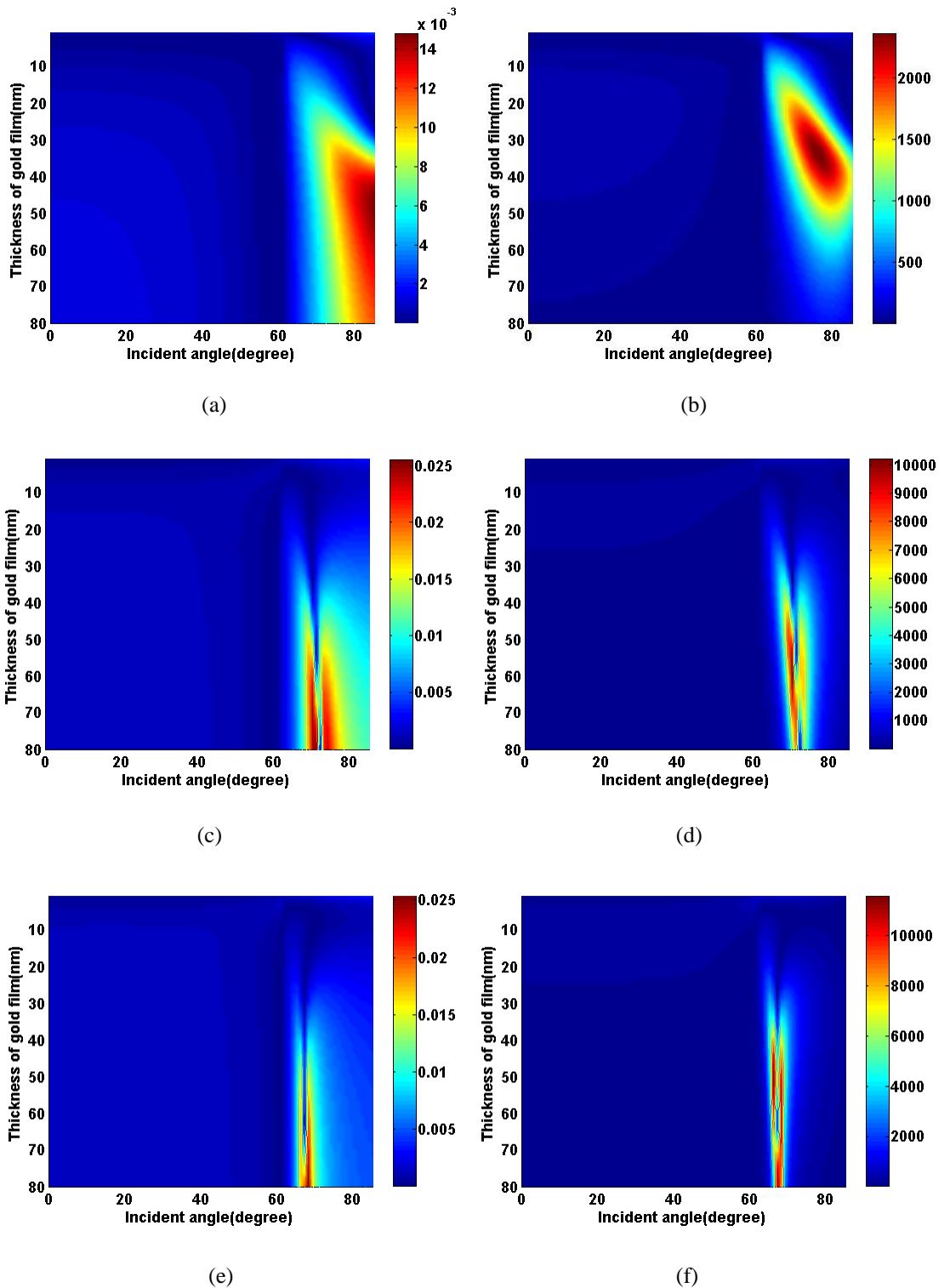
Figure 5.27 The contrast and SSNR of the transmitted light from the gold film. (a), (c) and (e)

show the contrast of the transmitted light at the wavelengths of 550 nm, 650 nm and 750 nm

respectively. (b), (d) and (f) show the SSNR of the transmitted light at the corresponding

wavelengths.

155

According to the depiction in Figs 5.26 and 5.27, considering the reflected light, good contrast and SSNR are exhibited by 1 to 20 nm thin gold films illuminated at shorter wavelength and lower incident angles and by 40 to 60 nm medium thickness gold films in the case of the longer wavelength and higher incident angles. Considering the light detected in transmission, 40 to 60 nm gold films associated with higher incident angles produce higher contrast and SSNR at longer wavelengths. The conditions including medium thickness of 40 to 60 nm gold films, wavelengths and angles of incident beams that produce high contrast and SSNR coinciding with the requirement to raise the SPR, prove the sensitivity of surface plasmons resonance again, where the evanescent wave enhances the field intensity dramatically. Meanwhile, the narrow zones of high contrast and SSNR require very high scanning angle resolution. In order to achieve the high response to the potential from thick gold films, it is necessary to slightly adjust the incident angle to locate at the correct angle, which is a rigorous requirement compared to the slight smaller contrast and SSNR but a relaxed alignment if the thin Au film is chosen as the platform.

5.5   Conclusions

The ±200 mV potential window was proved to be within the electrical double layer range for gold film by using the cyclic voltammetry technique. There was no redox reaction at these potentials, just electron transfer between the electrical double layer and the gold film.

The custom built spectrometer was utilised to compare the wavelength

dependent scattering contrast of thin (~16 nm) and thicker gold film (~50 nm) under the conditions of 0.1 M NaCl and ±200 mV potential range. At the lower incident angle, the thin gold film afforded higher scattering contrast than the thick one. The wavelength 618 nm at which the thin gold film had good scattering contrast was selected for the subsequent single wavelength measurements.

The scattering of thin Au film had been modulated by a series of potential application modes, from ±200 mV to ±10 mV, to determine the tendency of scattering contrast. The magnitude of scattering contrast decreased non-linearly with decreasing potentials. The application of a linear potential sweep at three scan rates resulted in three kinds of scattering plot. The differential scattering change rates of these three plots were well fitted by an exponential equation. The exponential change rate of scattering implies the completion of the equilibrium between the gold and electrolyte is influenced by the velocity of potential applied on the Au film. The potential dependent scattering was also examined by several types of potential step mode. The similar traces of scattering strength and charge calculated by time integration of current are further proofs that the modulated scattering is governed by the electron transfer process at the surface of Au film.

A commercial SPR system provides an alternative way to investigate the potential response of thick gold film. The potential dependent RIU contrast and potential cycling induced RIU presented similar tendencies as these of thin Au film measured by dark-field spectrometer. This similarity proves that the kinetic of Au film's response to potential is independent of their thickness and is predominantly contributed by the alteration of electron density in gold.

Two criteria, contrast and SSNR, were introduced to assess the ability of rough Au film sensing the potential in a modelling employing Fresnel's equations. The calculated reflected light contrast induced by the potential applied on a 15 nm thickness Au film deviated from a linear ratio and coincided with the measured scattering contrast of thin Au film. It is known that the magnitude of potential, thickness of Au film, the incident angle and the wavelength of beam could determine the response of Au film to the potential. Alternative usage of the last three parameters in the modelling under the same condition of ±200 mV, the simulation qualitatively predicted the trend of contrast and SSNR. Generally speaking, thin gold film less than 30 nm have good contrast and SSNR under the conditions of lower incident angle and shorter wavelength. Conversely, 40 nm to 60 nm Au film are recommended to detect the potential with higher incident angle and longer wavelength.

The experimental results presented in this chapter demonstrate the potential dependent scattering strength from thin Au film (~16 nm) and RIU from thick Au film (~50 nm) are governed by the charging-discharging process at the surface of gold. The modelling results point out the direction to utilise the Au film to sensing potential under certain circumstances.

Chapter 6   Sensing potential using nanoparticles

As described in earlier sections, collective oscillation of conduction electrons at the surface of nanoparticles due to optical irradiation is known as localised surface plasmon resonance (LSPR). The size, shape, material and aggregative state dependence of the LSPR spectrum provides analogous sensitivity to change in the local dielectric environment as commercially established SPR platforms using smooth Au films [7, 19, 28-29, 140]. Furthermore, a wide range of spectral tunability from the visible to infrared spectrum offer additional benefits and flexibility in configuration as compared to the classical SPR platform[21].

The interesting optical attributes of metal nanoparticles, specifically their intense scattering and absorption of light are the result of their unique interaction with light. Although Mie theory and Gans' theory have a long history, the reason why they have remained important today is their simple and exact solutions which can explain the anomalous and striking colours exhibited by small metallic particles [3, 40]. Therefore, an explanation of Mie theory and Gans' theory for the scattering and absorption of metal particle will be briefly described first. Then, an experimental investigation of Au NPs in the presence of potential will be compared with modelling results obtained by applying these theories. Their scattering spectra and response to potential were recorded

159

by the dark-field imaging spectrometer and used to quantitatively compare spherical and rod-shaped NPs. The effect of the essential factors that influence a particle's voltage sensitivity, namely the surface area to volume ratio and the NPs geometrical aspect ratio, are demonstrated in both experimental and simulation results.

6.1   Gans' theory and Mie theory

The complete explanation of the various colour effects from colloids had been speculated by several scientists before Mie's famous 1908 publication [141]. Mie firstly introduced his theory to qualitatively correlate the properties of a single colloidal particle made of arbitrary material and its scattering and absorption of light [41, 142-143]. The interaction between an incident wave and a homogeneous spherical particle was rigorously explained by solving Maxwell's equations. The applicability of Mie's solution to the colour phenomena of noble metal colloids smaller than or comparable to wavelength was realised by Mie as well, and is now known as plasmon resonance. The size of a spherical particle and its surrounding environment strongly influence the spectral position and width of the localised surface plasmon resonance.

Gans extended Mie's theory from spherical to ellipsoidal particles, which are much smaller than the illuminating wavelength [41]. Gans' theory revealed that in addition to size, NP shape is a very important factor in determining the

resonance properties. Different lengths of axes in ellipsoidal and spheroidal particles lead to different magnitudes of electron oscillation and split the plasmon resonance along each corresponding axis [41].

6.1.1   Gans' theory

Gans' theory simplifies the response of an elliptical particle to irradiation by applying a quasi-static model (dipole approximation). Considering an isotropic particle embedded in a non-absorbing medium, and much small compared to the incident wavelength, the magnitude of the electric field is approximately constant throughout the particle. The macroscopic electric field E over the particle comprises the incoming radiation field E_0 and the depolarisation electric field E_1 caused by the perturbation from the particle, which tends to oppose the external applied electric field. The dipole moment of this particle is [85]

$$p = \frac{4\pi abc}{3} \frac{\varepsilon_1 - \varepsilon_m}{\varepsilon_m + (\varepsilon_1 - \varepsilon_m)L} \varepsilon_m E_0 \qquad (6.1)$$

where a, b, c are the three semiaxes of the ellipsoidal particle, ε_1 is the complex permittivity of the particle's material, ε_m is the relative permittivity of the surrounding medium and L is the depolarisation factor related to the depolarisation field.

Therefore, the polarisability of the ellipsoid at one of its axes is

$$\alpha = \frac{4\pi abc}{3} \frac{\varepsilon_1 - \varepsilon_m}{\varepsilon_m + (\varepsilon_1 - \varepsilon_m)L} \qquad (6.2)$$
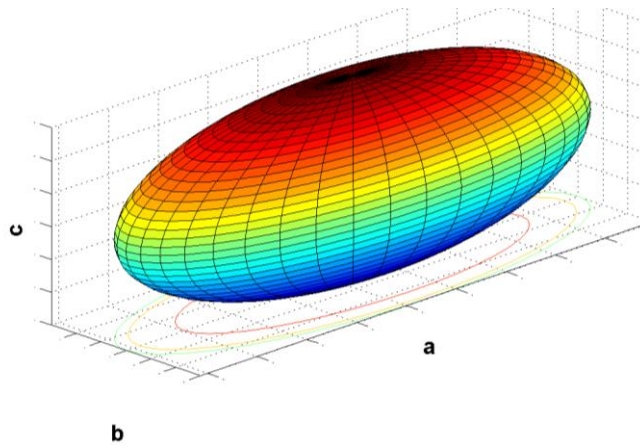
Figure 6.1   Prolate or "rod-like" spheroid

The depolarisation factor L is characterised by the ratio of the three

principal semiaxes, a, b and c. For an arbitrary ellipsoid, such as the prolate

spheroid shown in Fig. 6.1, the depolarisation factor L_a along the semiaxis a

is [144]

$$L_a = \int_0^\infty \frac{abc}{2(s+a^2)^{\frac{3}{2}}(s+b^2)^{\frac{1}{2}}(s+c^2)^{\frac{1}{2}}} ds \qquad (6.3)$$

where a, b and c are the length of the corresponding semiaxes, and s is the

surface area of the ellipsoid.

Depolarisation factors L_b and L_c are obtained by the same formula

with a cyclical changes of semiaxes. The sum rule $L_a + L_b + L_c = 1$ always holds.

Here, spherical particles ($a = b = c$), and prolate spheroids ($a > b = c$) are the interesting cases to be investigated. A sphere has $L_a = L_b = L_c = 1/3$. The depolarisation factors of a prolate spheroid are

$$L_a = \frac{1-e^2}{e^2}[\frac{1}{2e}\ln(\frac{1+e}{1-e})-1] \qquad (6.4a)$$

$$L_b = L_c = \frac{1-L_a}{2} \qquad (6.4b)$$

$$e = \sqrt{1-\frac{b^2}{a^2}} \qquad (6.4c)$$

The scattering, absorption and extinction cross sections in the dipole approximation are

$$C_{sca} = \frac{k^4}{18\pi}[|\alpha_a|^2 + |\alpha_b|^2 + |\alpha_c|^2] \qquad (6.5a)$$

$$C_{abs} = \frac{k}{3}\text{Im}(\alpha_a + \alpha_b + \alpha_c) \qquad (6.5b)$$

$$C_{ext} = C_{sca} + C_{abs} \qquad (6.5c)$$

where α_a, α_b and α_c are the polarisability of three axes and k is the wave vector in the surrounding medium $\left(2\pi\sqrt{\varepsilon_m}/\lambda\right)$.
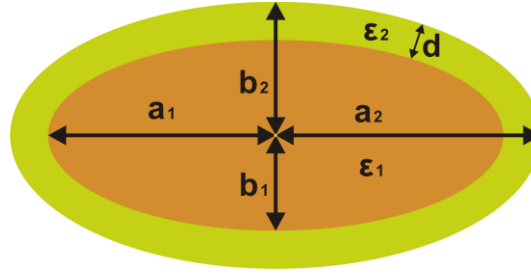
Figure 6.2   Ellipsoidal shell

In the case that the ellipsoid is covered by a different material with a thickness d (Fig. 6.2), the depolarisation factors of the inner and outer ellipsoids are also determined by the length of corresponding semiaxes. The expression of polarisability for the total particle is [85]

$$\alpha_i = \frac{4\pi a_2 b_2 c_2}{3} \frac{(\varepsilon_2 - \varepsilon_m)[\varepsilon_2 + (\varepsilon_1 - \varepsilon_2)(L_i^1 - fL_i^2)] + f\varepsilon_2(\varepsilon_1 - \varepsilon_2)}{[\varepsilon_2 + (\varepsilon_1 - \varepsilon_2)(L_i^1 - fL_i^2)][\varepsilon_m + (\varepsilon_2 - \varepsilon_m)L_i^2] + fL_i^2\varepsilon_2(\varepsilon_1 - \varepsilon_2)}$$

(6.6)

where subscript i denotes the three axes, ε_1 is the relative permittivity of the inner ellipsoid, ε_2 is the relative permittivity of the outer coating, ε_m is the relative permittivity of surrounding medium, a_1, b_1 and c_1 are the lengths of the semiaxes of the inner ellipsoid, a_2, b_2 and c_2 are the lengths of the semiaxes of the outer ellipsoid, $f = a_1 b_1 c_1 / a_2 b_2 c_2$ is the fraction of the total particle occupied by the inner ellipsoid, and L_i^1 and L_i^2 are the depolarisation factors of the inner and outer ellipsoids respectively. By substituting the

polarisability of the ellipsoidal shell into Eq. (6.5), its scattering and absorption

cross section are available for calculation.

It should be noted that the spectral response of a particle in the dipole

approximation is only dependent on the permittivity of the material and the

particle's shape. The size of the particle only determines the magnitudes of

C_{sca}, C_{abs} and C_{ext}.

6.1.2   Mie theory

An   exact   analysis   of   the   response   of   a   spherical   particle   to

electromagnetic radiation in a homogeneous dielectric medium is feasible by

using Mie theory, performed here using custom programmes based upon

functions written by Christian Mätzler [145]. Mie theory considers several

factors involving the determination of the response from a spherical particle,

such as electric and magnetic dipoles [47, 85, 140]. The Mie coefficients a_n

and b_n are the key factors for the calculation of scattering and extinction

efficiencies.

$$a_n = \frac{m^2 j_n(mx)[xj_n(x)]' - \mu_1 j_n(x)[mxj_n(mx)]'}{m^2 j_n(mx)[xh_n^{(1)}(x)]' - \mu_1 h_n^{(1)}(x)[mxj_n(mx)]'} \quad (6.7a)$$

$$b_n = \frac{\mu_1 j_n(mx)[xj_n(x)]' - j_n(x)[mxj_n(mx)]'}{\mu_1 j_n(mx)[xh_n^{(1)}(x)]' - h_n^{(1)}(x)[mxj_n(mx)]'} \quad (6.7b)$$

where m is the refractive index of sphere relative to the medium, $m = \sqrt{\varepsilon_{sphere}} / \sqrt{\varepsilon_{medium}}$, $x = kr = 2\pi\sqrt{\varepsilon_{medium}}\, r / \lambda$ is the size parameter, λ is the wavelength and r is the radius of the sphere. μ_1 is the magnetic permeability of the sphere relative to the magnetic permeability of the medium. Usually, μ_1 is approximated as unity. $j_n(z)$ and $h_n^{(1)}(z)$ are spherical Bessel functions of order n and argument $z = x$ or mx.

The scattering and extinction efficiencies derived from the Mie coefficients are

$$Q_{sca} = \frac{2}{x^2} \sum_{n=1}^{\infty} (2n+1)(|a_n|^2 + |b_n|^2) \qquad (6.8a)$$

$$Q_{ext} = \frac{2}{x^2} \sum_{n=1}^{\infty} (2n+1)\,\text{Re}(a_n + b_n) \qquad (6.8b)$$

Absorption efficiency follows the rule of energy conservation as

$$Q_{abs} = Q_{ext} - Q_{sca} \qquad (6.8c)$$

Multiplying the efficiencies by the geometrical cross section πr^2 yields the scattering, absorption and extinction cross sections of the spherical particle.

6.2   Scattering spectra of nanoparticles

The scattering of three types of nanoparticle including spheres and rods were measured with the dark-field spectrometer. Their distinct spectra and sensitivity to change in the surrounding environment was considered in relation to their shape. The scattering spectra of particles of the same dimensions as used in the experiment were also calculated with Mie and Gans' theories. Both simulation and experiment showed the tendency of spectra to red-shift in response to increasing refractive index of the surrounding medium, and for the sensitivity to refractive index to increase with the particle aspect ratio.

6.2.1   Experimental nanoparticle scattering spectra

Spectrometers are frequently used to observe localised surface plasmon resonance in nanoparticles. Generally, the wavelength-shift of the spectra is the primary measurement to detect a change in the local environment.

Individual Au NPs were isolated on an ITO coated coverslip as described in Sec. 4.2.4 to avoid plasmonic coupling and to allow the resolution of individual particles. The scattering spectra of the nanoparticles were acquired by using the dark-field imaging spectrometer. To ensure the measured scattering spectrum originated from the expected NP, it was compared with the nominal resonance peak in data provided by the NP manufacturer. According to the NP manufacturer's spectra measurement, the peak wavelength for

nanospheres ($d = 100$ nm) in distilled water is 569 nm. The longitudinal peak

wavelengths of nanorods in distilled water are 650 nm ($L = 60$ nm, $d = 25$ nm)

and 700 nm ($L = 73$ nm, $d = 25$ nm) respectively [146]. The Au particles were

supported on a ITO coated coverslip. The presence of the coated coverslip (the

refractive index of the coated coverslip is about 2 [147]) increases the local

refractive index of the particle's surrounding medium, shifting the LSPR

wavelength to the red as compared to when it is only exposed in solvent [29, 44,

81].

(a)   (b)
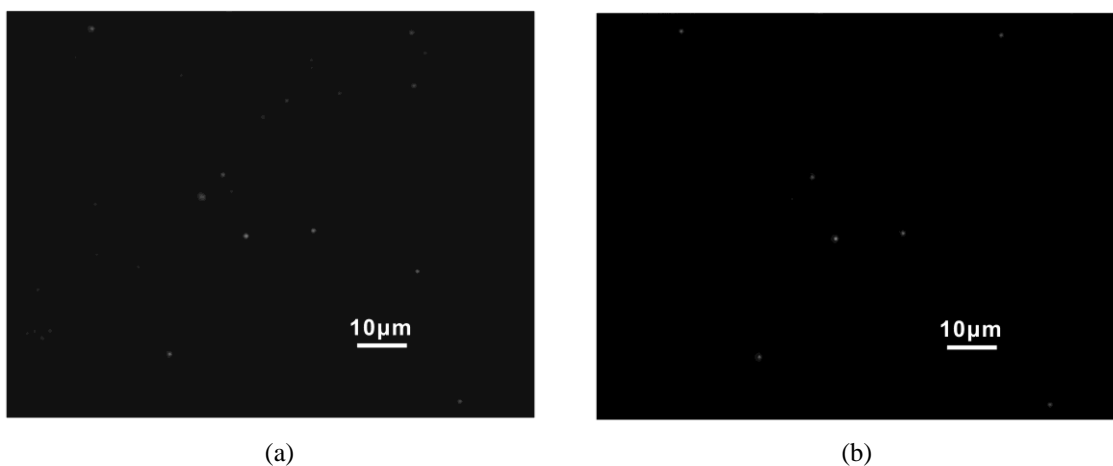
Figure 6.3 Dark-field images of nanorods at a wavelength of 680 nm in (a) air and (b)

water. (Nanorod dimensions were L=60 nm, d=25 nm)

Taking the substrate effect on the LSPR into consideration, particles

whose scattering peak wavelengths agreed with the red-shifted nominal peak

wavelength were selected as the objects for further investigation, ensuring that

individual particles rather than cluster are used in the subsequent analysis. Gold

nanorods at an illumination wavelength of 680 nm, close to the resonance of

their scattering spectra, are shown in Fig. 6.3. The nanorods were well distributed and isolated, reducing the probability of plasmonic interactions. Since the dimensions of the nanorods were less than the optical resolution of the microscope, the diffraction limited point spread function of the imaging spectrometer determined their size in the image plane.

As described above, the scattering spectra of Au NPs depend on several factors, such as their size, shape, and in particular, the embedding environment, which is of course the motivation behind investigating the potential of nanoparticles for sensing applications. The shift of scattering spectra of three kinds of nanoparticles (nanospheres of diameter $d = 100$ nm, nanorods with dimensions of $L = 60$ nm, $d = 25$ nm, and $L = 73$ nm, $d = 25$ nm), induced by adding 0.1 M NaCl and comparing to previously recorded spectra when the NPs were exposed to air are illustrated in Fig. 6.4. The red-shift of their scattering spectra and the decrease in scattering magnitude when the nanoparticles were immersed in solvent are very noticeable.

It is anticipated that the spectra of nanorods has two plasmon resonance peaks instead of the single peak observed from spherical particles. The first is a longitudinal plasmon resonance, because the plasmon oscillates along its long axis, and is dependent on its geometrical shape. The second is a transverse resonance, the plasmon oscillating perpendicularly to its long axis, but is polarisation independent and weak compared to the longitudinal resonance peak [148].
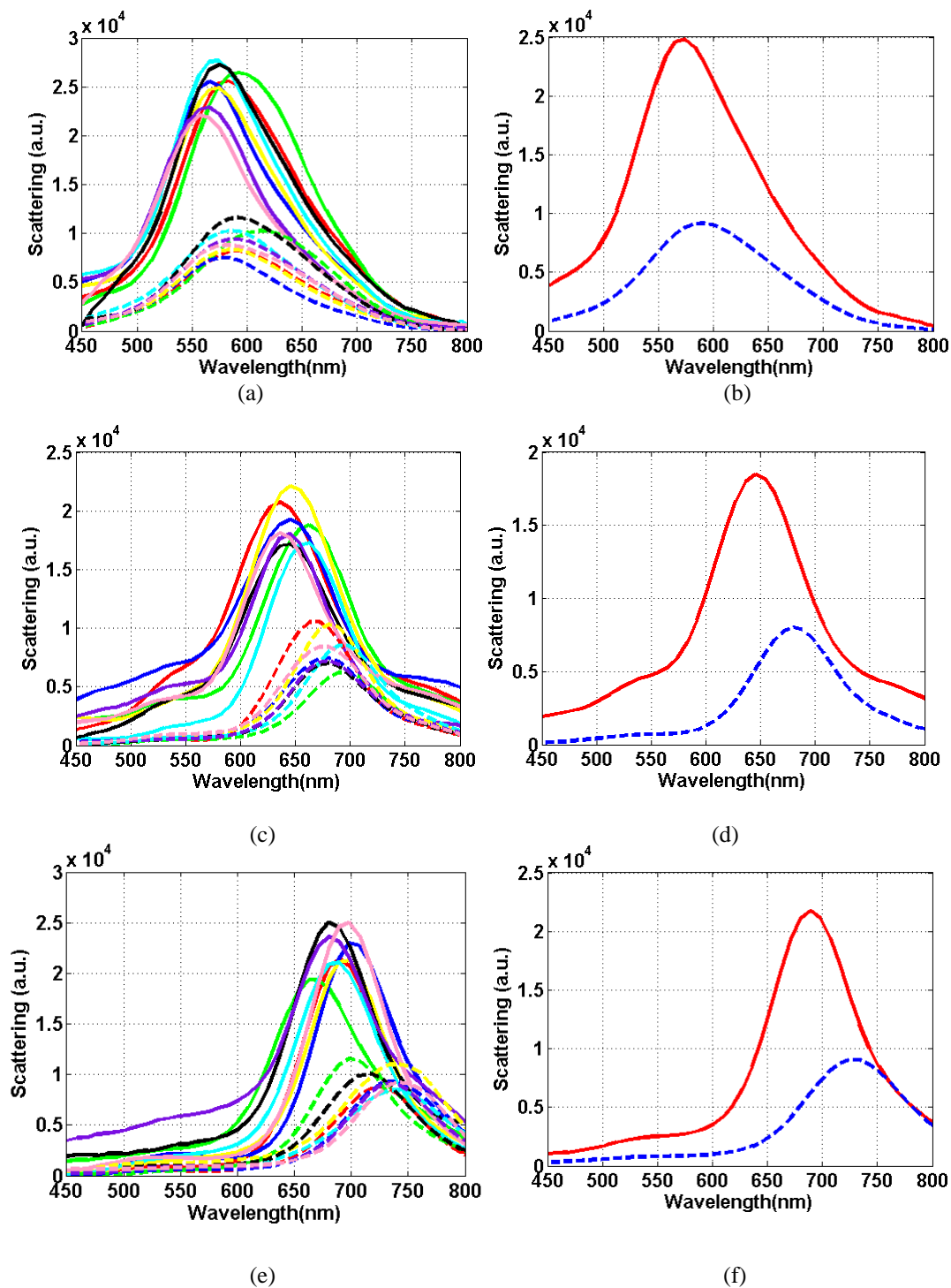
Figure 6.4 Scattering spectra of (a,b) nanospheres with d=100 nm, (c,d) nanorods with $L = 60$ nm, $d = 25$ nm and (e,f) nanorods with $L = 73$ nm, $d = 25$ nm. (a), (c) and (e) display the scattering spectra of 8 individual particles. (b), (d) and (f) are ensemble spectra. Solid and dashed lines represent nanoparticles exposed to air and immersed in solvent respectively.

However, the scattering spectra of nanorods exhibited a pronounced longitudinal resonance peak but a barely visible transverse resonance around 510-520 nm even for the larger nanorods. This is different from the two resonance peaks observed in the absorption spectra. It is reasonable to take the absorption into account, as it dominates the spectral response. The region of transverse resonance overlaps with the gold interband absorption threshold of 2.5 eV. The contribution of electron interband transition results in the weak transverse resonance amplitude compared to the remarkable longitudinal resonance amplitude [82, 143, 149].

6.2.2 Calculated scattering spectrum

Mie theory and Gans' theory were utilised to calculate the spectra of spherical and spheroidal particles. A size dependent adjustment to Drude-Lorentz theory (see Sec. 3.1.2 for details) was employed to calculate the dielectric function of the gold nanoparticles.

The shift of calculated scattering spectra from air ($n = 1$) to water ($n = 1.33$, the refractive index of 0.1 M NaCl was assumed to be the same as that of water) is illustrated in Fig. 6.5. The resonance wavelength λ^* and the sensitivity defined as the relative changes in peak wavelength to a change in refractive index of medium, $\Delta\lambda^*/\Delta n$, along with experimental results are depicted in Fig. 6.6 as a function of aspect ratio, AR=L/d. Both the resonance

wavelength and the sensitivity increased monotonically with the aspect ratio of

the NPs.

(a)

(b)

(c)
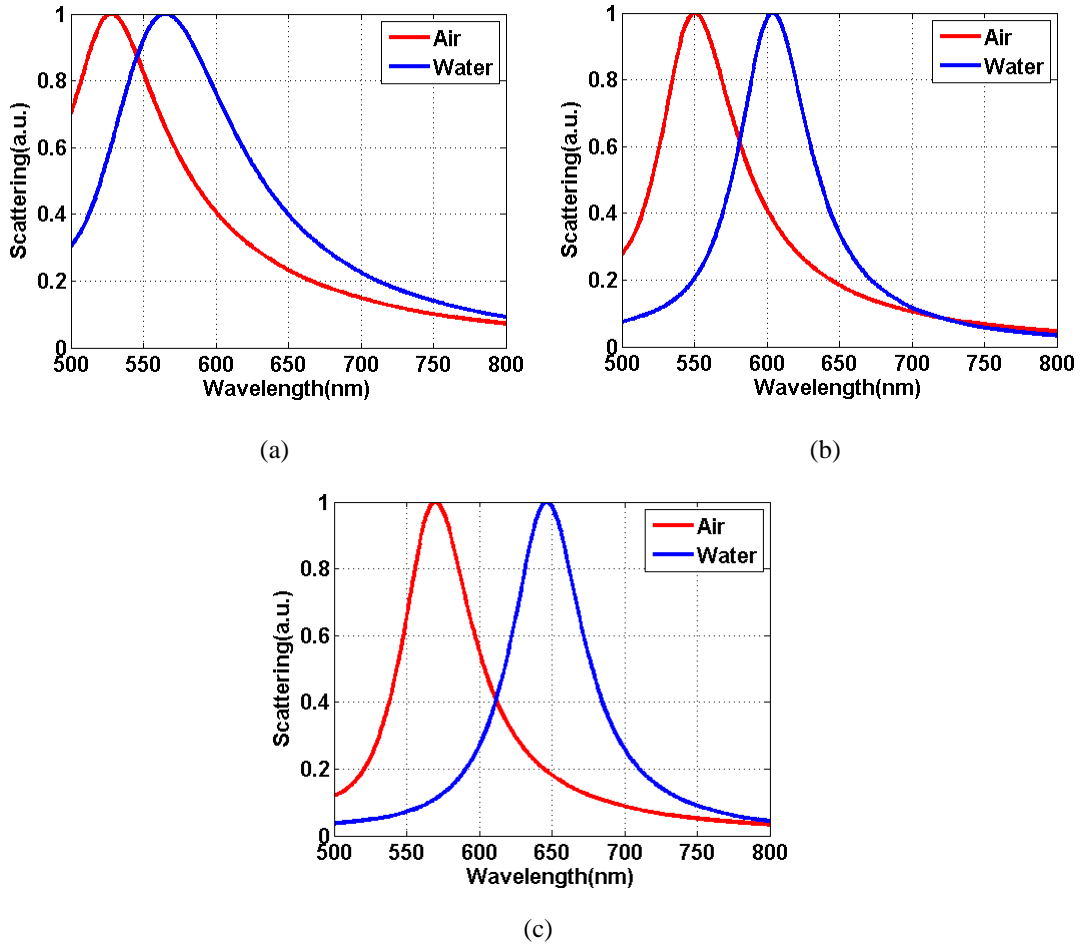
Figure 6.5   Calculated scattering spectra of (a) nanosphere, $d = 100$ nm, (b) nanorod $L = 60$

nm, $d = 25$ nm and (c) nanorod $L = 73$ nm, $d = 25$ nm in air and water respectively.

The relationship between the sensitivity and the aspect ratio can be fitted as

41.84AR + 5.698 [nm/RIU] for experiment and 56.4AR + 49.87 [nm/RIU] for

simulation respectively. The value of slope obtained from calculation is close

to the experimental one, although a difference exists between the magnitudes

of their intercepts. A more than twofold improvement of the sensitivity of

nanorods relative to that of nanosphere implies that nanorods have potential to be employed as sensors.

The peak wavelength of the experimental result is located at a longer wavelength than the calculated value. This discrepancy is most probably explained by the fact that the effect of the substrate was not considered in the calculation of scattering. A homogeneous environment [150] was assumed to surround the particle in the simulation whereas in the experiment, there was an asymmetric environment including an ITO coated glass substrate to support the particle and a second medium encloses it.
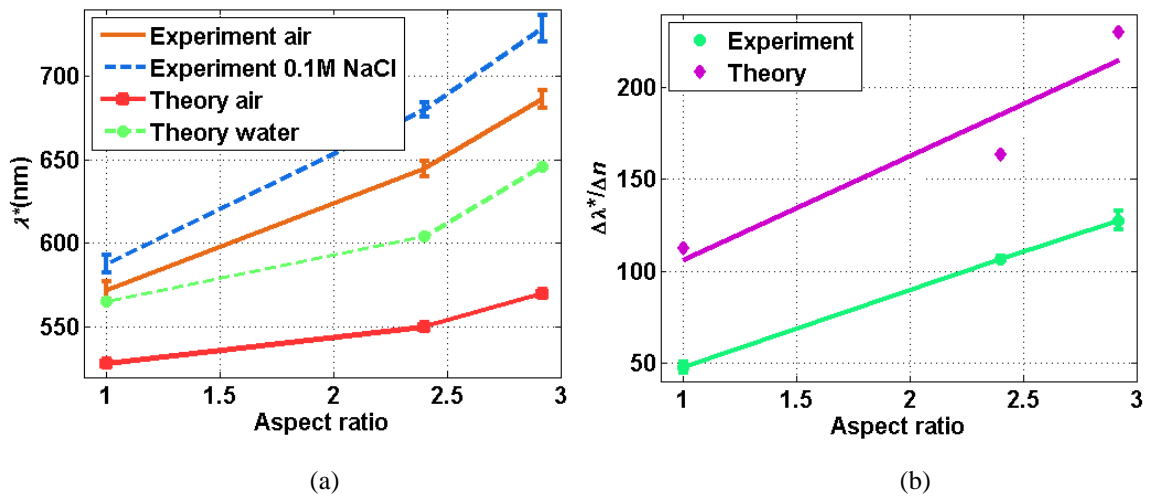
Figure 6.6 (a) Peak wavelengths of particles.

(b) The sensitivity for nanospheres of $d = 100$ nm, and nanorods of $L = 60$ nm, $d = 25$ nm and $L = 73$ nm, $d = 25$ nm as a function of aspect ratio according to their scattering spectra.

6.3   Potential modulated scattering

Electron transfer between nanoparticles and the electrical double layer was studied by using nanoparticles immobilised on an ITO coated coverslip in 0.1 M NaCl bulk solution (NP size and shape as in the previous section). The formation of an electrical double layer around the surface of the NPs as a consequence of the applied potential performs as a tunnel for electron transfer to and from the particles. The voltage sensitivity of these three kinds of NPs were characterised by their scattering contrast.

6.3.1   Cyclic voltammetry
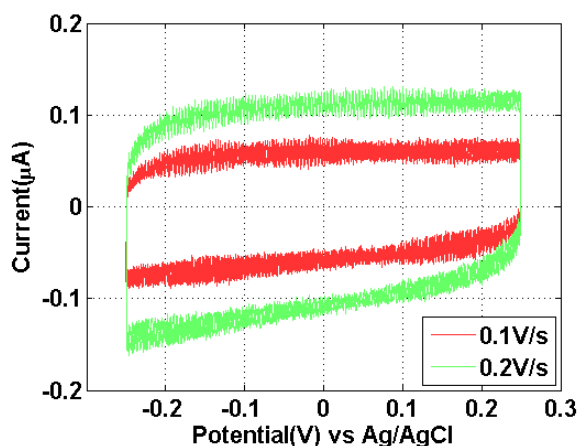
Figure 6.7 Cyclic voltammogram with nanorods ($L = 60$ nm, $d = 25$ nm) immobilised on ITO

in 0.1 M NaCl with 0.1 V/s (red line) and 0.2 V/s (green line) scan rate

Cyclic voltammetry was used to determine the potential range for the redox reaction. The cyclic voltammogram (CV) of nanorods ($L = 60$ nm, $d = 25$

nm) immobilised on an ITO coated coverslip at two potential scan rates (0.1

and 0.2 V/s) are shown in Fig. 6.7. The absence of cathodic and anodic current

peaks proofs that no faradic current was observed and the CV curves were

nearly symmetrical relative around zero current.

6.3.2   Scattering contrast as a function of wavelength

To discern the potential response of each kind of NP, bipolar voltage mode

A (± 200 mV) was applied after the scattering spectra of these NPs had been

collected as shown in Fig. 6.4. The acquisition time for each image was 4 s.

Scattering contrast (Sec. 5.2.3) was used to characterise their response to

potential. Since their resonance wavelength is detectable in the visible range, it

is interesting to notice that the sign of the response to potential alters on the

either side of scattering peak of nanorods ($L = 60$ nm, $d = 25$ nm, $\lambda^* = 680\text{-}690$

nm) shown in Fig. 6.8.

A positive potential reduced the scattering at 662 nm which was at the left

side of the spectral peak, while it enhanced the scattering at 729 nm, located at

the right side of the peak. The absence of a response around the spectral peak

indicated neither positive nor negative potential affected scattering in this

region.

The wavelength dependent scattering contrast of the nanoparticles is

shown in Fig. 6.9, including 8 individual nanoparticles and their ensemble

average contrast. Scattering contrast from nanorods is clearly greater than for

100 nm diameter nanospheres. The different sign at either side of the nanorods'

spectral peak coincides with the modulated scattering observed in Fig. 6.8.

(a)

(b)

(c)

(d)

(e)

(f)

(g)

(h)

(i)
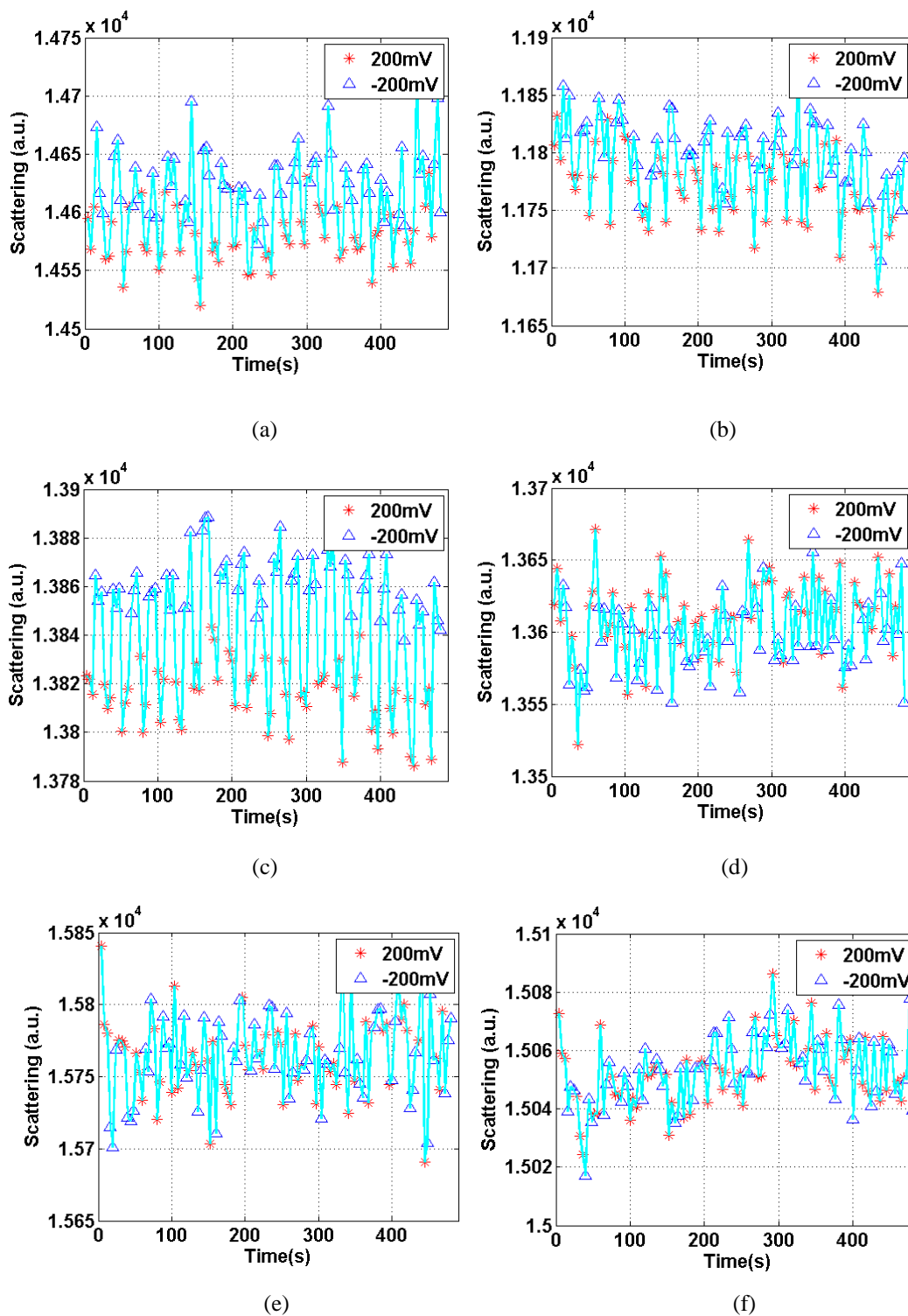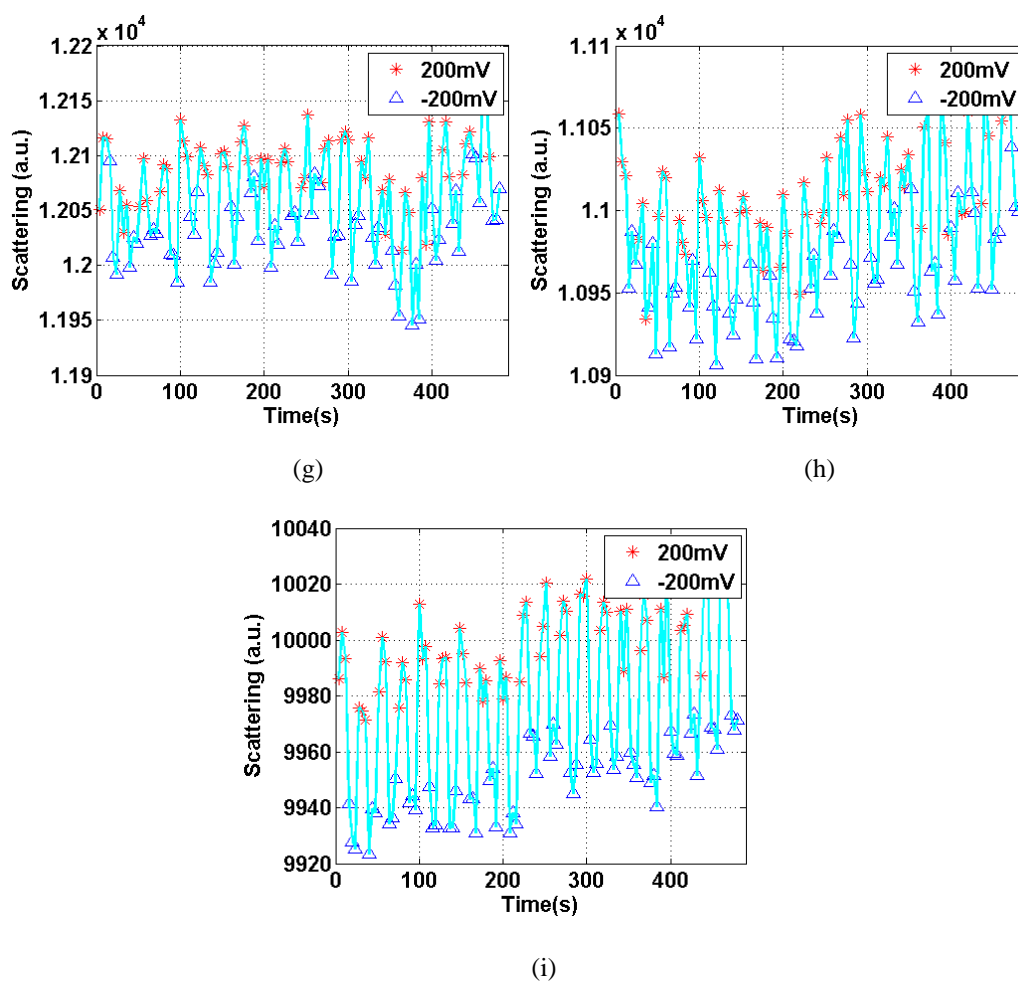
Figure 6.8 Scattering of nanorods ($L = 60$ nm, $d = 25$ nm) (a), (b), (c) at a wavelength of 662

nm, (d), (e), (f) at 684 nm, (g), (h) and (i) at 729 nm. (a), (b), (d), (e), (g) and (h) depict the

scattering response to ±200 mV from two individual nanoparticles. (c), (f) and (i) show the

ensemble response of 8 individual particles at their corresponding wavelength. The cyan line is

for eye guidance.
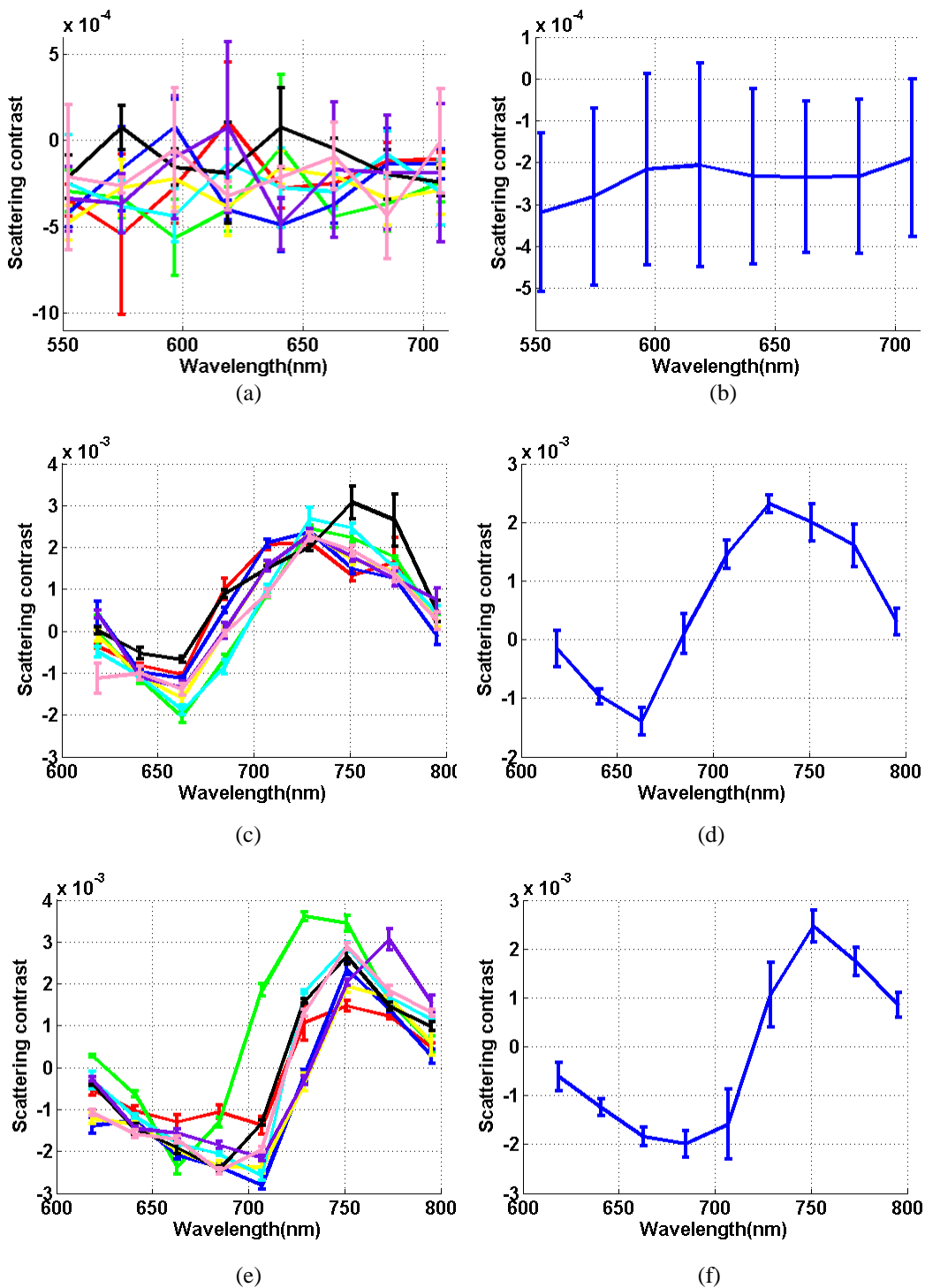
Figure 6.9 The scattering contrast of (a, b) nanosphere($d = 100$ nm) , (c, d) nanorod ($L = 60$ nm, $d = 25$ nm) and (e, f) nanorod ($L = 73$ nm, $d = 25$ nm). (a), (c) and (e) are the scattering contrast of 8 single individual particles and (b), (d) and (f) are their corresponding ensemble scattering contrast calculated as the average contrast of 8 individual particles.

178

A positive potential produces the opposite effect on the particle's scattering at the left and right of the spectral peak. This is further evidence that a positive potential red-shifts the spectrum while a negative potential induces it to blue-shift. Taking the scattering spectra collected in Fig 6.4 into account, the largest contrast is detectable at the shoulder of the spectrum whereas the spectral peak is the least sensitive. The aspect ratio of the nanospheres ($d = 100$ nm) and nanorods ($L = 60$ nm, $d = 25$ nm and $L = 73$ nm, $d = 25$ nm) increases as 1, 2.4 and 2.92 respectively, which corresponds to the same order as their scattering contrast. It implies that their sensitivity to potential is correlated to their aspect ratio.

6.4   Simulation of potential modulated scattering

It is known that an electrical double layer is created on the surface of nanoparticles immobilised on the ITO coverslip as the result of applied potential. Perturbation of the electric field near the surface of Au NPs induces the movement of electrons between the gold and the electrolyte. The charging-discharging process taking place in the Thomas-Fermi layer of an Au NP alters the free electron density of this superficial region. The alteration of the free electron density dependent plasmon frequency induces a change in the Au NP's scattering as a consequence of voltage application.

Nanospheres and nanorods under the circumstance of voltage application

in 0.1 M NaCl (n =1.33) were modelled by Mie theory and by Gans' theory

respectively. The influence of the Thomas-Fermi layer was modelled by

regarding it as a superficial layer coating the particle.

Scattering contrast and signal-to-shot noise ratio (SSNR) were again

utilised to characterise their sensitivity to potential. The scattering contrast of

the particle was defined as

$$C_{contrast} = \frac{C_{sca\_higher} - C_{sca\_lower}}{C_{sca\_higher} + C_{sca\_lower}} \qquad (6.9)$$

where C_{sca_higher} and C_{sca_lower} represent the scattering cross section at the

higher and the lower potential respectively.

The signal-to-shot noise ratio (SSNR) considered the energy loss caused

by propagation of the scattered light through the imaging optics before it

approaches the sensor. Its calculation procedure is the same as described in Sec.

5.4.2.

The total power of scattered light from the particle in all directions I_{sca}

[W] is equal to the incident power falling on its scattering cross section,

$$I_{sca} = I_{inc}C_{sca} \qquad (6.10)$$

where I_{inc} is the irradiation of the incident beam [Wm^{-2}] and C_{sca} is the

particle's scattering cross section [m^2].   Then, I_{sca} is substituted for the

$I_{ref}S_{area}$ and $I_{tran}S_{area}$ in Eq. (5.19) and used to calculate the photon number

and the SSNR .

6.4.1   Potential modulated scattering of specified particles

The particles' scattering spectra and the contrast induced by a potential of

200 and -200 mV are presented in Fig. 6.10. In terms of the calculated

scattering spectra, red-shifted spectra by positive potential and blue-shifted

spectra by negative potential result in the asymmetric 'butterfly shaped'

contrast plot that is consistent with the profile of experimental contrast shown

in Fig. 6.9.   The scattering contrast of the sphere is 10 times less than that of

the nanorod shown in Fig. 6.10, emphasising that shape plays a crucial role in

determining a particle's response to an applied potential. To achieve the

experimental scattering contrast of Au nanorod, only about 1.6 % change in the

electron density was required, which means that the double layer capacitance

per unit surface area of nanorod was 0.0222 Fm^{-2}. This value is much smaller

than the anticipation (see Appendix A.4 for the calculation of capacitance).

The qualitative agreement between experimental and theoretical results

indicates there are some uncertain factors that influence the particle's response

to potential. They are possibly due to the absence of consideration of protective

coating CTAB and additional specific adsorption species that are tightly bound

to the Au NP's surface and change the structure of double layer capacitor.

(a)

(b)

(c)

(d)

(e)

(f)
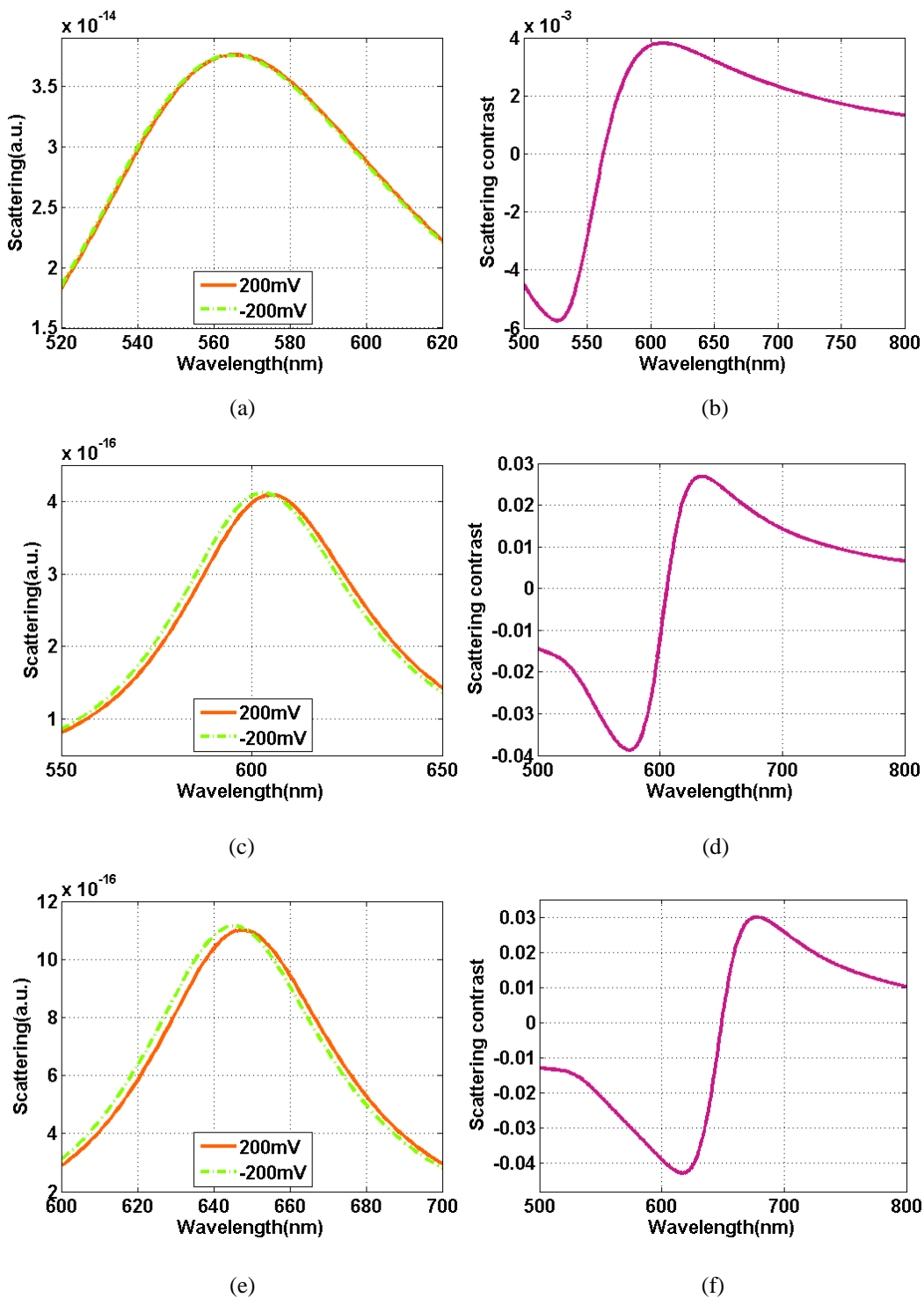
Figure 6.10   Spectra of nanoparticle modulated by 200 mV, -200 mV and their

corresponding scattering contrast. (a, b) are for a nanosphere(d = 100 nm), (c, d) are for

nanorods (L = 60 nm, d = 25 nm) and (e, f) are for nanorod (L = 73 nm, d = 25 nm).

6.4.2   Shape and size dependent voltage response of particles

As the particles' sensitivity to the change of bulk environment is related to their size and shape, their sensitivity to the potential should also be dependent on their geometry.

Figure 6.11 illustrates the scattering contrast and SSNR of spherical particles subjected to the potentials of 200 mV and -200 mV. The diameter of sphere was modelled from 1 nm to 100 nm. Two features are apparent from this figure. First, smaller particles have a larger scattering contrast. Second, as the diameter increases, the effect of potential on larger particles is more easily detectable due to the higher SSNR. Similar features are also exhibited by the scattering contrast and SSNR of spheroidal particles with the same aspect ratio of 2 as shown in Fig. 6.12, which were generated by ± 200 mV. The scattering contrast and SSNR resulting from ± 200 mV for spheroidal particles with equivalent volume to a 20 nm diameter sphere are presented in Fig. 6.13. Both scattering contrast and SSNR vary proportional to the aspect ratio increased from 1 to 8.

High scattering contrast for a sphere is attained when its surface area to volume ratio increases from 6.837×10^7 m^{-1} to 8.377×10^{12} m^{-1} as its diameter decreases from 100 nm to 1 nm. In the case of spheroids with the same aspect ratio of 2, their scattering contrast increases with increasing surface area to volume ratio ranging from 3.259×10^8 m^{-1} to 4.698×10^9 m^{-1}. The proportional relationship between the scattering contrast and the surface area to volume

ratio is the same as that of sphere, the smaller particle resulting in larger

scattering contrast.

<div align="center">(a)</div>

<div align="center">(b)</div>
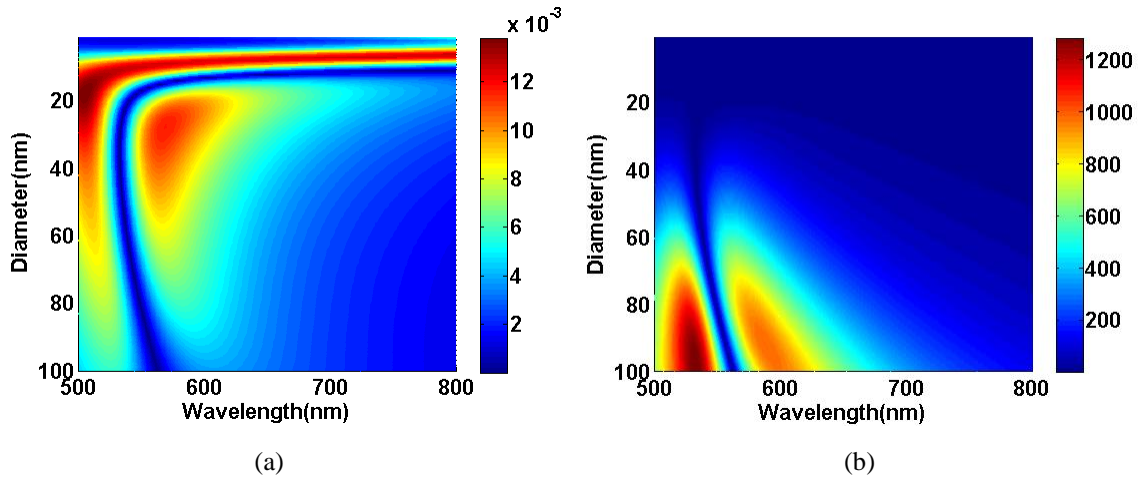
<div align="center">Figure 6.11   Scattering contrast and SSNR of spherical particles. The diameter of sphere</div>

<div align="center">increases from 1 nm to 100 nm</div>

<div align="center">(a)</div>

<div align="center">(b)</div>
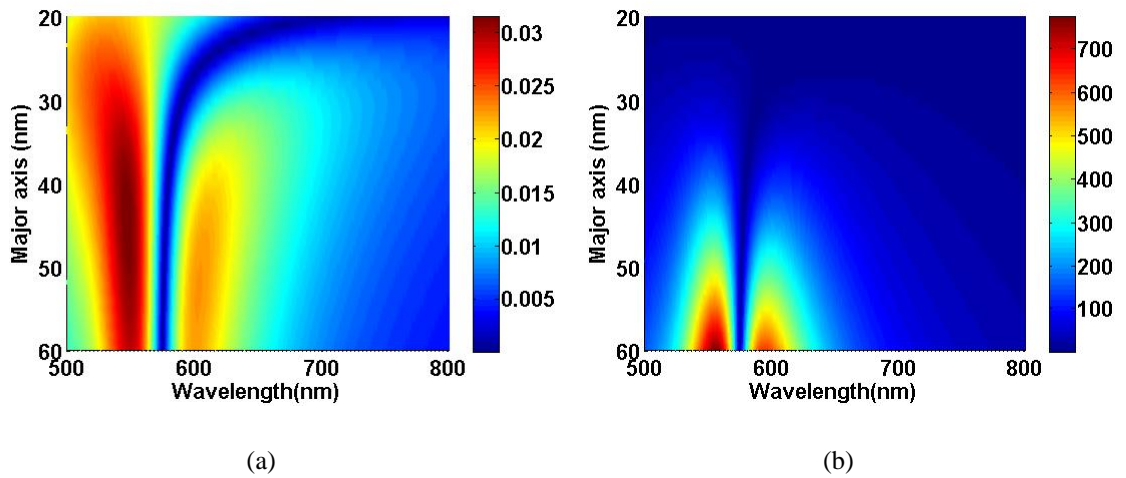
<div align="center">Figure 6.12   Scattering contrast and SSNR of spheroid particles with the same aspect ratio</div>

of 2. The major axis (*a*) and minor axis (*b* = *c*) increases from 20 nm to 60 nm and from 10 nm

<div align="center">to 30 nm respectively.</div>

In addition, the scattering contrast of a spheroid with equivalent volume to a 20

<div align="center">184</div>

nm diameter sphere jumps to 0.04 with enlarging aspect ratio. The increase in aspect ratio of a spheroid caused a corresponding increase in the surface area to volume ratio from 1.346×10^9 m^{-1} to 1.521×10^9 m^{-1}.

(a)   (b)
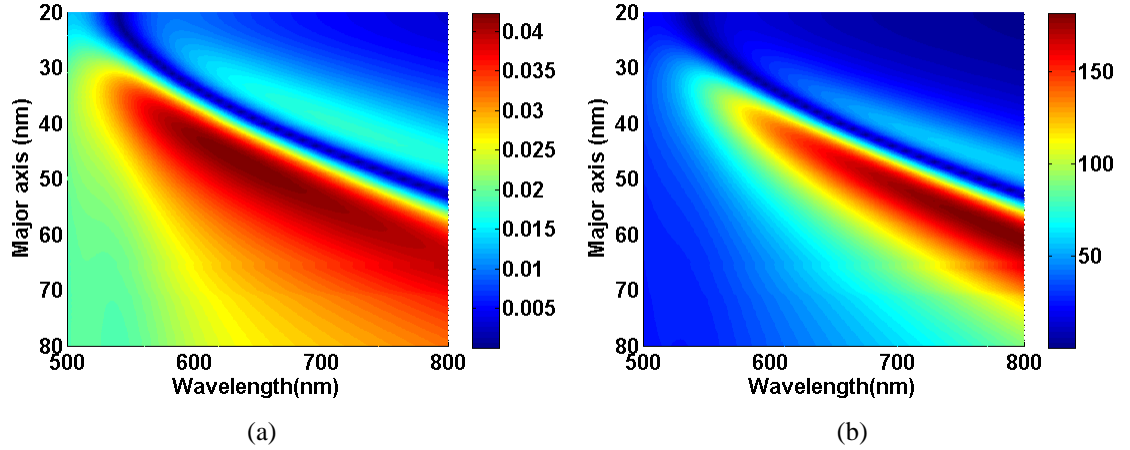
Figure 6.13   Scattering contrast and SSNR of spheroid particles, all with the same equivalent volume to a sphere diameter of 20 nm. The major axis (*a*) increases from 20 nm to 80 nm. The minor axis (*b = c*) decreases from 20 nm to 10 nm.

For simplicity, the Drude model and Eq. (6.2) are utilised to express the dielectric function of gold in the absence of electron interband transition and the particle's polarisability respectively.

The dielectric function of gold described by the Drude model is

$$\varepsilon(\omega) = \varepsilon_\infty - \frac{\omega_D^2}{\omega(\omega + i\gamma_D)} \qquad (6.11)$$

and the plasmon frequency ω_D is given by

$$\omega_D = \sqrt{\frac{Ne^2}{m^* \varepsilon_0}} \qquad (6.12)$$

which is determined by the free electron density N.

Applying potential to the particle alters its free electron density and the consequent plasmon frequency can be written as

$$\omega_{D\_f} = \sqrt{\frac{(N + \Delta N)e^2}{m^* \varepsilon_0}}$$

$$= \sqrt{(1 + \frac{\Delta N}{N})\omega_D} \qquad (6.13)$$

The ellipsoidal particle modelled by Gans' theory has the polarisabiltiy as shown in Eq. (6.2)

$$\alpha = \frac{4\pi abc}{3} \frac{\varepsilon_1 - \varepsilon_m}{\varepsilon_m + (\varepsilon_1 - \varepsilon_m)L} \qquad (6.14)$$

At wavelengths where the imaginary part of dielectric function of gold has weak dispersion, the condition for the presence of the longitudinal wavelength peak λ_p is that the denominator of the polarisability α corresponding to the major axis vanishes

$$\text{Re}(\varepsilon_1) = \frac{L-1}{L}\varepsilon_m \qquad (6.15)$$

Using Eqs. (6.11) and (6.15), the longitudinal wavelength peak is then expressed as

$$\lambda_p = \frac{2\pi c}{\sqrt{\dfrac{\omega_D^2}{\varepsilon_\infty + \dfrac{1-L}{L}\varepsilon_m} - \gamma_D^2}} \approx \frac{2\pi c}{\sqrt{\dfrac{\omega_D^2}{\varepsilon_\infty + \dfrac{1-L}{L}\varepsilon_m}}}$$

(6.16)

where c is the speed of light in vacuum, and $\gamma_D \ll \omega_D$

The change in the longitudinal wavelength peak as the result of applied potential is

$$\Delta\lambda_p = \lambda_{p\_f} - \lambda_{p\_i}$$

$$= \frac{2\pi c}{\sqrt{\dfrac{\omega_{D\_f}^2}{\varepsilon_\infty + \dfrac{1-L}{L}\varepsilon_m}}} - \frac{2\pi c}{\sqrt{\dfrac{\omega_D^2}{\varepsilon_\infty + \dfrac{1-L}{L}\varepsilon_m}}}$$

$$= -\frac{2\pi c}{\omega_D}(1 - \frac{1}{\sqrt{1 + \dfrac{\Delta N}{N}}})\sqrt{\varepsilon_\infty + \frac{1-L}{L}\varepsilon_m}$$

(6.17)

The shift of longitudinal wavelength peak is assumed to represent the shift

187

of whole spectrum. Therefore, Eq. (6.17) indicates the relationship between the shift of spectrum and the alteration of electron density and particle's aspect ratio. Since $\Delta\lambda_p$ is proportional to ΔN and to the aspect ratio (aspect ratio is inversely proportional to *L* and is proportional to (1-*L*)/*L*), a larger value of ΔN and a higher aspect ratio are expected to achieve greater spectral shift.

For particles of the same aspect ratio, the change of electron density determines the spectral shift. The perturbed scattering in the presence of an applied potential is attributed to the electrical double layer that provides the charging and discharging process of electrons to the particle. The change of electron density is confined in the domain of the Thomas-Fermi screening layer. The surface charging of the particle is dependent on the size-independent double layer capacitance per unit surface area [66]. The capability of accumulating electrons is elevated by a larger surface area while the electron density is inversely proportional to the volume of this tiny domain. A particle of larger surface area but smaller volume experiences an enormous alteration of its electron density as a function of applied potential. Considering a particle much smaller than the wavelength of light, the electric field is quasi-constant throughout the particle and the incident light induces all the electrons in the particle including the electrons in the Thomas-Fermi layer to have a collective oscillation and give rise to the surface plasmons at particle's surface. Although the change of electron density only takes place in the Thomas-Fermi layer, this alteration is expressed by the change of scattered light from the whole particle.

Hence, the surface area to volume ratio has a positive correlation with the scattering contrast, despite the fact that the volume of the Thomas-Fermi layer changes only slowly with particle morphology.

The influence of surface area to volume ratio is weaker compared to that of the particle's aspect ratio. As predicted by Eq. (6.17), for a fixed surface area to volume ratio which results in a constant ΔN, the wavelength shift is higher for particles with larger aspect ratio. In the dipole approximation, the depolarisation factor L represents the ease with which electron cloud can be polarised to the particle surface against the Coulombic restoring force of positive atomic lattice by light[51, 151]. From Eq. (6.14), a smaller value of L produced by a higher aspect ratio results in a larger polarisability of the particle, and the electron cloud will be displaced easier. The larger aspect ratio leads to a greater ease of the polarisation of the particle, which compensates the same electron density modification. Thereby, a particle with a higher aspect ratio can exhibit greater scattering contrast, even if its geometry constrains its change of electron density.

In contrast, larger particles result in overwhelmingly greater SSNR whatever the scattering contrast, especially for spheres that only have weak scattering contrast. This is due to larger particle scattering much stronger so that there are more photons available for detection even if the larger particle only has a small spectral shift.

Particles have been applied in a wide range of sectors. There are specific

requirements for the usage of particle in some specialised sectors, such as, cell labelling particle. Considering this application, small particles are preferable as they are less invasive, but have the drawback of fewer photons. Larger particles provide strong scattering signal but may be invasive to cell. This means that the choice of optimum particle is determined by the specific application. However, it is clear that in most cases nanorods will outperform nanospheres.

6.5   Conclusions

Mie theory presents a solution to describe the spectral properties of spherical particles of arbitrary size. Although Mie theory has more than one hundred years of history, its exact and accurate calculations are still important today. The demand to characterise the optical properties of nonspherical particles motivated the development of Gans' theory to explain the behaviour of ellipsoid particles, which regards the interaction between an electromagnetic wave and nanoparticle smaller than a wavelength as a quasi-static model.

The red-shifted scattering spectrum of three kinds of nanoparticles, including one nanosphere ($d = 100$ nm) and two nanorods ($L = 60$ nm, $d = 25$ nm and $L = 73$ nm, $d = 25$ nm) induced by changing its surrounding environment from air to water, experimentally measured by the dark-field spectrometer had qualitative agreement with the modelling using Mie theory and Gans' theory.

The expectation of observing potential induced scattering from nanoparticles was fulfilled by applying ±200 mV on nanorods. The voltage sensitivity of nanorods exceeded that of nanospheres. The relation between their response to potential and aspect ratio discovered in this experimental measurement was demonstrated in the modelling. Although particles have different geometry, surface area to volume ratio and its aspect ratio govern the particle's potential scattering contrast. Particles with larger surface area to volume ratio undergo a drastic change in their electron density under an applied potential. Higher aspect ratio provides one additional and predominant factor to determine the particle's response to potential. Consequently, the combination of these factors leads to considerable modification to their optical properties and the spectral response.

However, the trend of SSNR is more complicated than scattering contrast. Because large particles are capable of scattering much more light than smaller ones, consequence induced by potential becomes more convenient by observing large particle. However, taking the limitations in practical application of particle into account, choosing a particle with a suitable geometry for a particular case is necessary to achieve optimal performance.

Chapter 7   Gold nanoprisms for sensing potential

Nanosphere lithography (NSL) is a cost-effective and high throughput technique to fabricate periodic, weakly coupled triangular nanoparticle arrays. Tuning the LSPR of triangular nanoparticles can be achieved by varying their size and height which depend on the diameter of nanosphere and the thickness of deposited metal respectively [19, 80]. The appreciable sensitivity of triangular nanoprisms fabricated by NSL to chemical and biological measurements has been study recently relying on its LSPR spectral shift. Nanoprism LSPR biosensing and detection capabilities have been demonstrated in a variety of potential applications in environmental monitoring, proteomics and drug discovery [46].

In this chapter, the electrochemical properties of Au nanoprisms produced by NSL are explored using the dark-field spectrometer. The spectral location where Au triangular nanoparticles possess the best sensitivity to potential was detected by measuring its scattering contrast at several wavelengths under one modulated potential mode, bipolar mode A. When this wavelength was identified, Au nanoprism's scattering behaviour under several other potential modulation modes was probed at this wavelength. Its properties of potential dependent scattering differ from Au film, spherical and rod-shaped nanoparticles and indicate the structural effect on the capability of sensing potential.

7.1   Spectra of Au nanoprisms

(a)   (b)
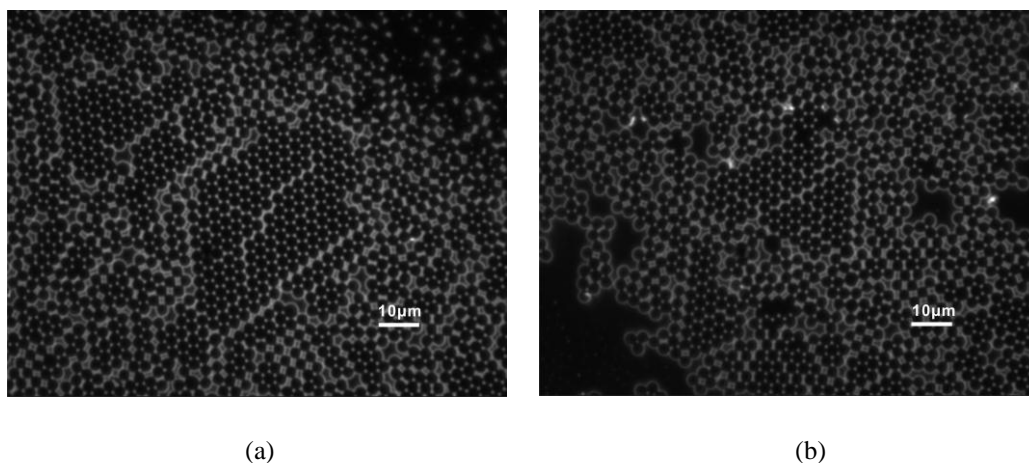
Figure 7.1 Dark-field images of Au nanoprisms in water at a wavelength of 653 nm. The

in-plane length of triangular nanoparticle was ~ 466 nm. The interparticle spacing was about

1.1 μm. The out-of-plane heights of nanoparticles were (a) ~ 16 nm and (b) ~50 nm

respectively.

Two types of Au triangular nanoparticle were fabricated by NSL as described in Sec. 4.2.3. The in-plane length and interparticle spacing of the triangular particles were about 466 nm and 1.1 μm using 2 μm spheres as a mask. The out-of-plane heights of the two kinds of triangular particle were about 16 nm and 50 nm. These dimensions result in their aspect ratio (in-plane length/out-of-plane height) as 29.1 and 9.3 respectively [44]. Dark-field images of these Au triangular particles are shown in Fig. 7.1. Regions of approximately 200-300 μm^2 of well-ordered, low defect Au nanotriangle array were located in the centre of the images.
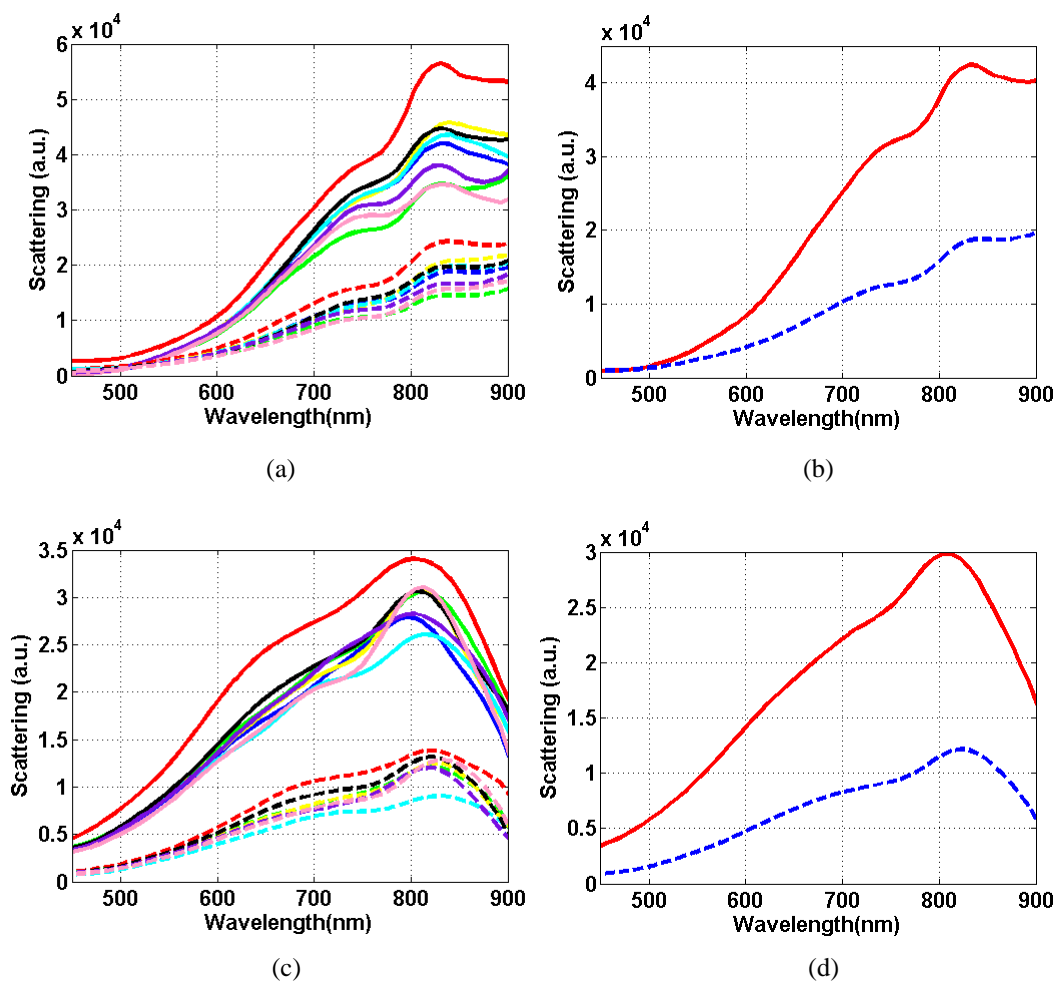
Figure 7.2 Scattering spectra of (a, b) 16 nm height and (c, d) 50 nm height nanoprisms. (a) and

(c) show the scattering spectra of 8 individual particles. (b) and (d) are the corresponding

ensemble spectra. Spectra correspond to nanoprisms exposed to air (solid) and immersed in

water (dashed).

Eight single Au triangular nanoparticles' scattering spectra in air and water,

and their corresponding ensemble spectra are shown in Fig. 7.2. About 14 nm

red-shift was caused by changing the nanoprisms' surrounding environment

from air ($\lambda_{max} = 808$ nm) to water ($\lambda_{max} = 822$ nm) was observed from the

ensemble 50 nm height nanoprisms' spectra. Since the aspect ratio of 16 nm

height nanoprism is larger than that of the 50 nm height nanoprism, its peak

wavelength in water was shifted further into the infrared region from it

spectrum in air ($\lambda_{max} = 832$ nm), outside of the wavelength range of analysis.

7.2   Scattering under potential control

Both types of Au nanoprism were fabricated on ITO coated coverslip and

used as the working electrode in three-electrode electrochemical system. The

electrolyte was 0.1 M NaCl. The application of potential perturbed the Au

nanoprism's surface and the vicinal environment. The change of LSPR

depending on the properties of the nanoparticles and its imbedding

environment was consequently observed as the result of voltage application.

The surface curvature and topology play important roles in determining the

nature of their potential-induced scattered light.

7.2.1   Cyclic voltammetry of Au nanoprism-solution interface

Initially, cyclic voltammetry was used to determine the non-Faradic

reaction potential range. The lack of oxidation and reduction current peaks in

the cyclic voltammogram shown in Fig. 7.3 indicated that the potential window

between ±250 mV was within the double layer charging region for the

nanoprism array.
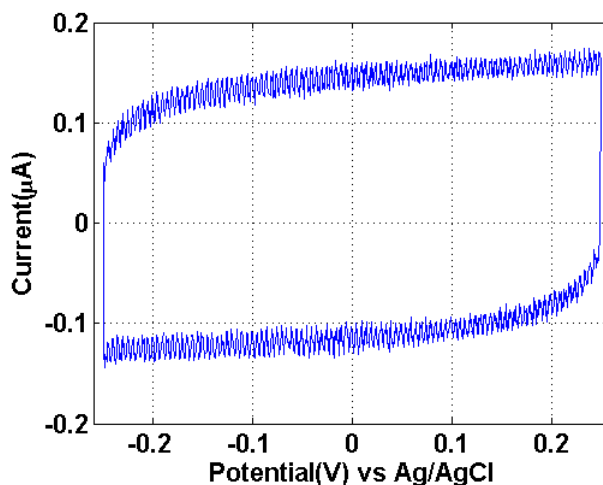
Figure 7.3   Cyclic voltammogram of 16 nm height Au nanoprisms on an ITO coated

coverslip. The scan rate was 0.1 V/s.

7.2.2   Wavelength dependent scattering contrast

Potential modulation mode, BMA (±200 mV) was applied to the nanoprism array. The acquisition time for each image was 1.4 s. Since the range of illumination wavelengths employed were to the left side of the Au nanoprisms' spectral peak, positive potential decreased the scattering (by causing a red shift) while negative potential enhanced it (corresponding to a blue shift), as shown in Fig. 7.4. The effect of potential on the 16 nm height nanoprisms was distinct, exhibiting a contrast of almost -0.7 %. The effect of potential on the 50 nm height nanoprisms was recognisable from their individual scattering, and comparable to the response of the nanorods presented in Chapter 6, but was more easily distinguished from their ensemble average
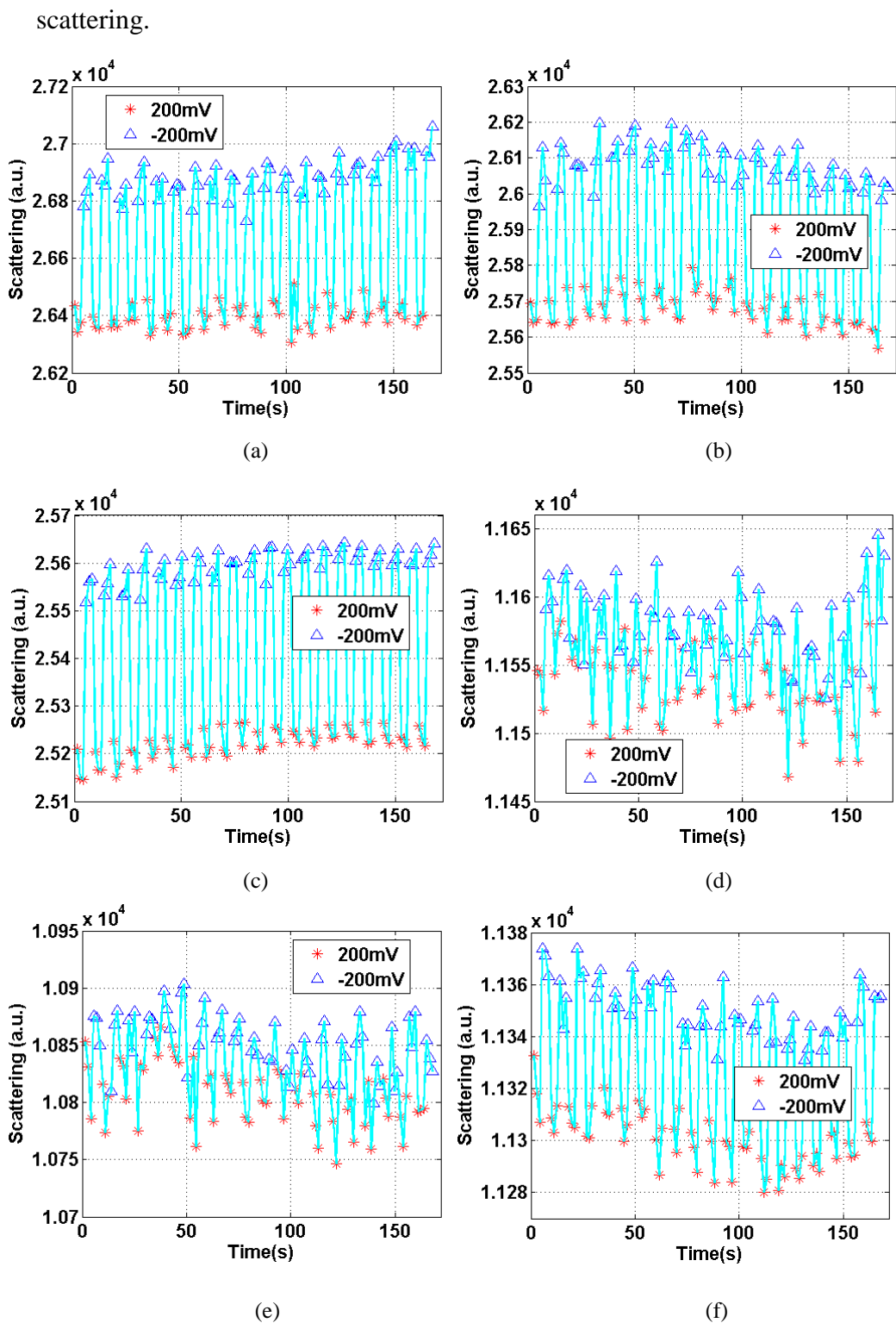
scattering.

Figure 7.4 Modulated scattering of (a), (b), (c) 16 nm height nanoprisms at wavelength=640

nm, (d), (e), (f) 50 nm height nanprimsms at wavelength=618 nm. (a), (b), (d), (e) represent the

scattering response to ±200 mV from two individual nanoprisms. (c) and (f) depict the

197

ensemble average scattering response of eight individual nanoprisms. The cyan line is for eye

guidance.

The wavelength dependent scattering contrast (Sec. 5.2.3) of these two types of Au nanoprisms is illustrated in Fig. 7.5. Comparing the 16 nm height nanoprisms' redshifted spectra in water to that of the 50 nm height nanoprisms, the largest scattering contrast of the 16 nm nanoprisms is located at a longer wavelength than the 50 nm nanoprisms, consistent with the rule that largest scattering contrast presents at the spectral shoulder. Both the 16 nm and the 50 nm height nanoprisms have sharp tips and corners [152], which leads to high charge density at the surface region and a large enhancement of the electric field intensity [6, 47]. The 50 nm height nanoprisms' high curvature leads to a large scattering cross section, and results in scattering contrast comparable to that of nanorods and much better than 50 nm thickness Au film as measured in this dark-field spectrometer. The higher aspect ratio of the 16 nm height nanoprisms led to a scattering contrast of nearly three times that of its counterpart. When two noble metal nanoparticles approach closer together, the plasmon resonance oscillations on the individual nanoparticle overlap and couple with each other, strongly affecting the plasmonic resonance energies. The Au nanoprisms array is a periodic tip-to-tip structure with 1.1 μm interparticle spacing (approximate separation between the centers of the two particles), and two neighbouring particles could produce weak electromagnetic

coupling [44].

(a)

(b)

(c)

(d)
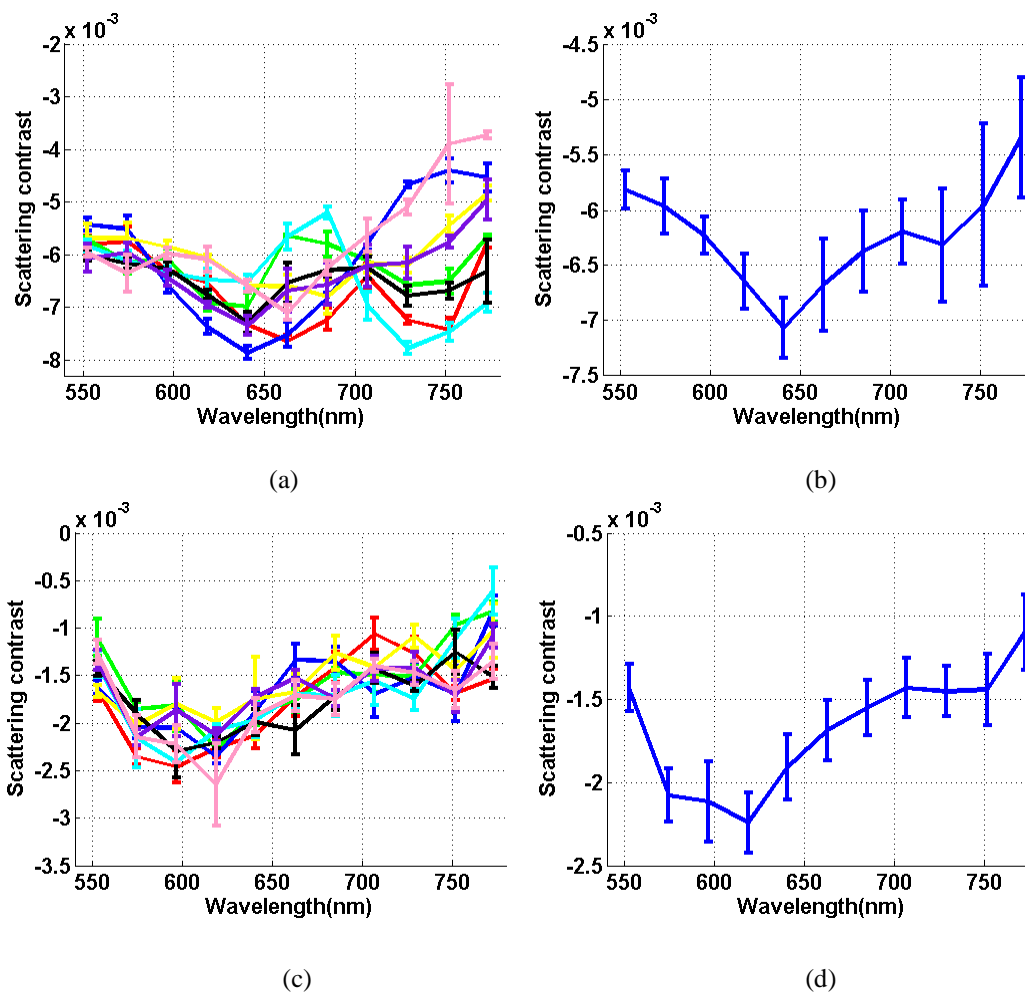
Figure 7.5   The wavelength dependent scattering contrast of (a, b) 16 nm height nanoprisms

and (c, d) 50 nm height nanoprisms. (a) and (c) are the scattering contrast of eight individual

nanoprisms. (b) and (d) are their corresponding ensemble scattering contrast.

This is different from the continuous 16 nm Au film, where conductively

overlapped nano-islands produce a stronger plasmonic coupling. Stronger

coupling leads to a higher value of particle polarisability and a greater ease of

electron cloud displacement [51], which has a similar effect to the higher

aspect ratio and improves the particle's response to the potential. Possibly as a result of the weakly coupled-particle system, the scattering contrast of the 16 nm height Au nanoprisms is somewhat lower than that of the 16 nm Au film.

7.2.3   Sensitivity to potential of the Au nanoprisms

Because high scattering contrast was provided by the 16 nm height Au nanoprism at illumination angles accessible to the spectrometer, it was selected as the platform to investigate its sensitivity to lower potential. The scattering contrast detected from the seven potential modulated modes, whose potential decreases from ± 200 mV, ± 150 mV, ± 100 mV, ± 50 mV, ± 25 mV, ± 10 mV to 0 V and the fitting curve using Eq. (5.10) are shown in Figs. 7.6 and 7.7 respectively.

(a)   (b)
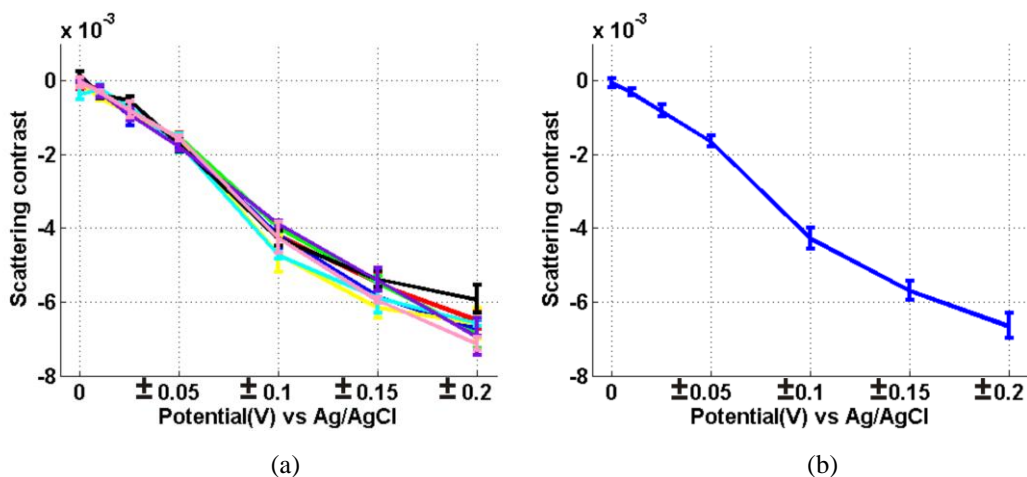
Figure 7.6   Scattering contrast of 16 nm height nanoprisms under the application of seven potential modulated modes. (a) and (b) are the scattering contrast of eight individual nanoprisms and their corresponding ensemble contrast respectively.
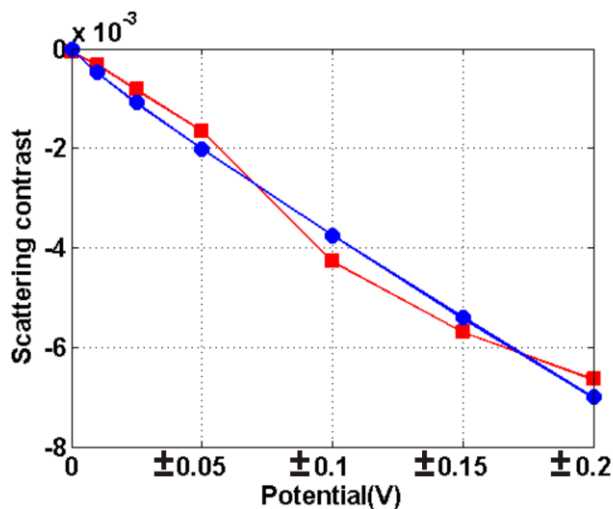
Figure 7.7 Experimental 16 nm height nanoprisms' ensemble scattering contrast in red square

and the corresponding fit in blue circles using Eq. (5.10)

The measurement was implemented at 640 nm wavelength because this was the location of the highest scattering contrast induced in BMA (± 200 mV) as shown in Fig. 7.5. The fitted values of (A, c) were (-0.0298, 0.901). The value of c is less than the unity, implying that the sensitivity of Au nanoprism improves slightly at lower potential and is much more linear than that of the 16 nm Au film ($c = 1.319$). The quasi-linear trend of nanoprisms' scattering contrast as a function of potential could be attributable to the field enhancement due to the higher charge densities in the surface region, which decelerates the effect of reduced charges on the light scattered by the nanoprisms. Although the scattering contrast of the Au nanoprisms is lower than that of the 16 nm Au film, its linearity, especially at the very low voltages

indicates the shape effect on the particle's potential sensing capability.

7.2.4   Potential cycling dependent scattering

(a)

(b)

(c)
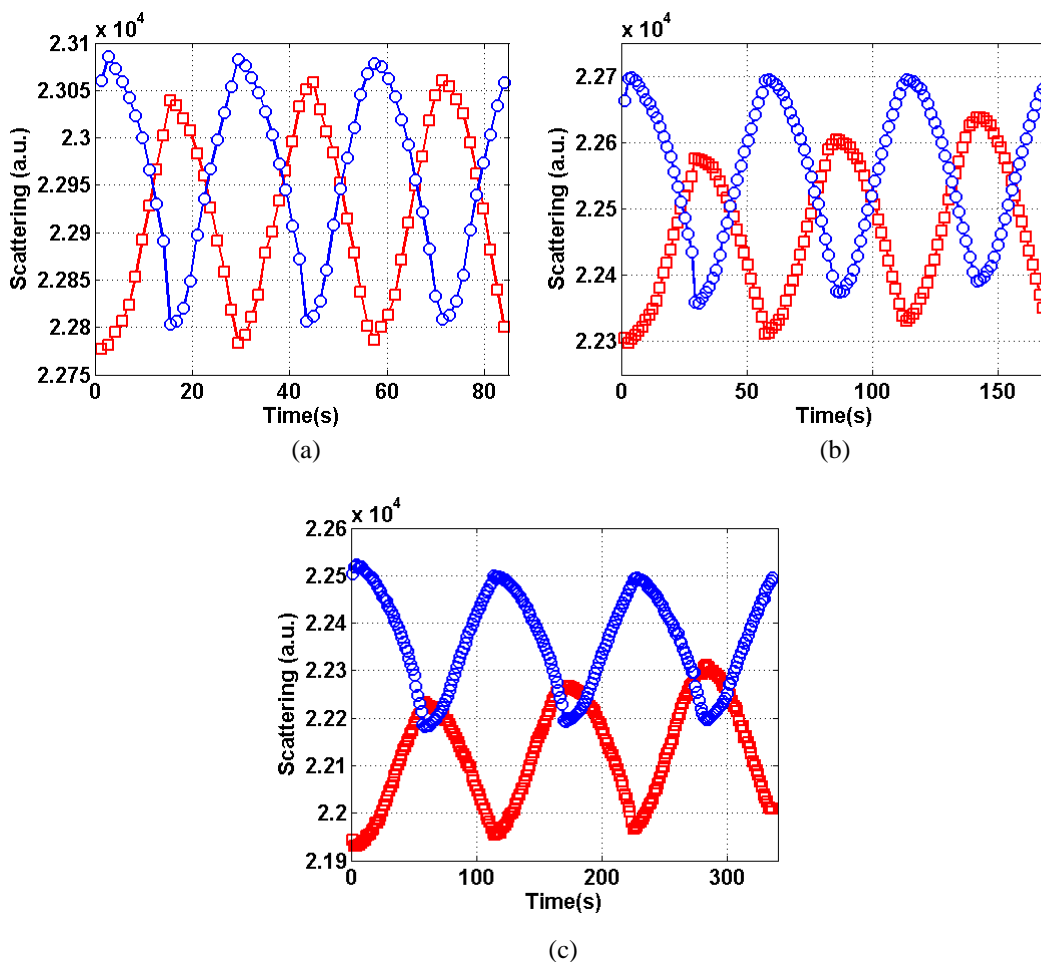
Figure 7.8   Scattering of 16 nm height nanoprisms induced by cyclic voltammetry. The initial

potentials for red squares and blue circles were 200 mV and -200 mV respectively. The

potential scan rates used in (a), (b) and (c) were 0.0276 V/s, 0.0138 V/s and 0.0071 V/s

respectively.

The scattering of 16 nm height Au nanoprism under a linear potential

sweep was studied by cyclic voltammetry at an illumination wavelength of 640

nm. The potential scan range was between +200 mV and −200 mV and the scan

rates were set as 0.0276 V/s, 0.0138 V/s, 0.0071 V/s and accommodated 10, 20

and 40 images in each potential scan. The perturbed scattering collected from

60-70 nanoprisms illustrated in Fig. 7.8 demonstrate that Au nanoprisms are

able to distinguish the rate of potential change in different linear scans. The

initial delay of some scattering transients in the first few seconds of the scan

was due to the potential instantly stepping to 200 mV or -200 mV from its

open-circuit potential (70-90 mV).

The differential scattering caused by the three potential scan rates is

shown in Fig. 7.9 along with the best fit to the Eq. (5.11). The fitted values of

(a, b, τ) were (44.7, -7.524, 3.607 s) for 0.0276 V/s, (23.19, -1.335, 8.796 s) for

0.0138 V/s and (9.612, 0.3883, 13.92 s) for 0.0071 V/s. The ratio of time

constants evaluated in three scan rates, 3.607:8.796:13.92=1: 2.43:3.86 also

nearly matches the same reciprocal ratio of the three potential sweep rates,

0.0276:0.0138:0.0071=1:1/2:1/3.88.

The inversely proportional relationship between time constants and

potential sweep rates discovered in Au nanoprisms and Au films implies the

universality of the interpretation for the potential's perturbation on Au

nanostructures. The potential perturbs the initial equilibrium between the gold

and the solution by inducing the accumulation of charges inside and ions

outside of the gold surface, which constitutes the double layer. In order to

prevent the penetration of the external electric field created by the double layer into the bulk gold, the gold's electrons adjust their location within the space charge region to create an internal electric field. A new equilibrium is established when the electrons are able to adapt to the complex electric field environment in terms of the dynamic potential.

(a)

(b)

(c)
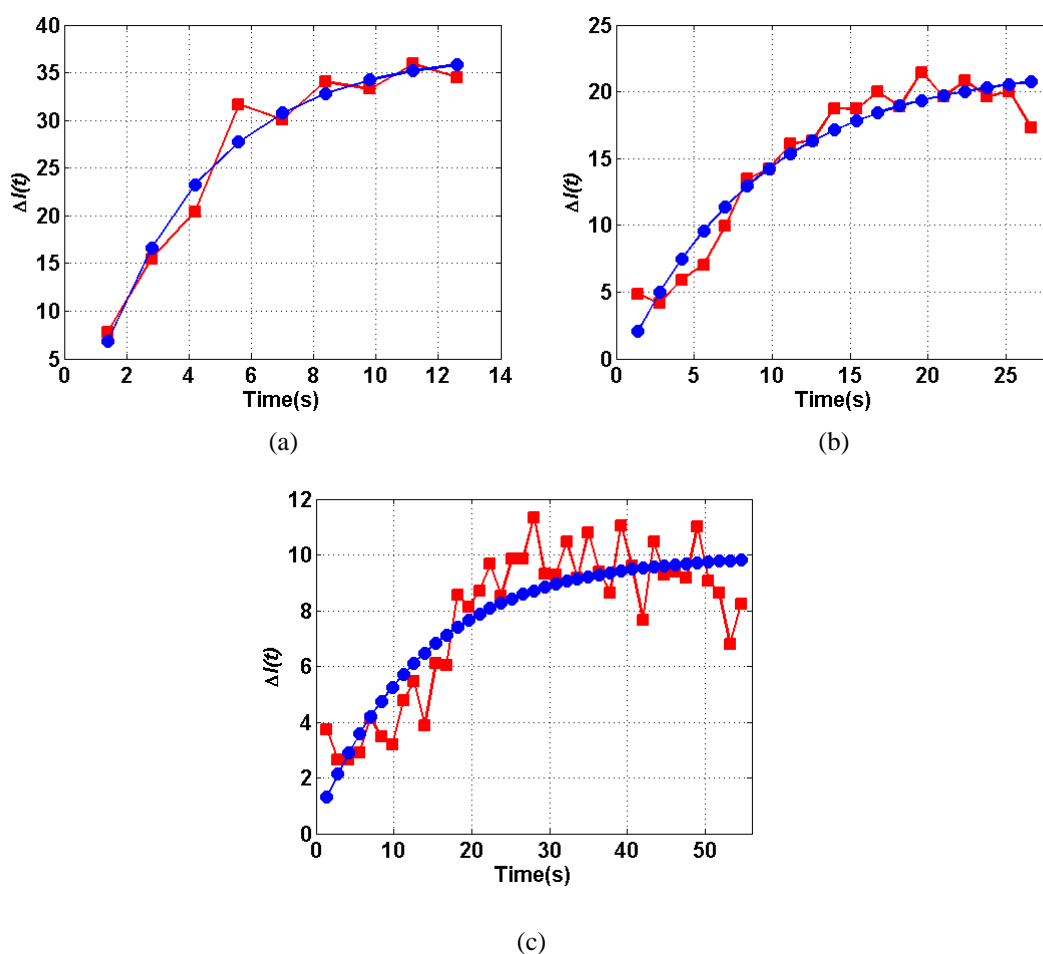
Figure 7.9 Differential scattering of 16 nm height nanoprisms. The red square line and blue circle line were experimental differential value and the corresponding fitting curve for Eq. (5.11) respectively. The potential scan rates in (a), (b) and (c) were 0.0276 V/s, 0.0138 V/s and 0.0071 V/s.

7.2.5   Potential step dependent scattering

The scattering response to the application of a potential step maintained for 168 s is illustrated in Fig. 7.10. 0 V was applied for the first and the last 14 s. Reversed potentials including ±50 mV, ±100 mV, ±150 mV and ±200 mV, were applied on the Au nanoprisms for 70 s after the first 14 s of 0 V. Steady state scattering was achieved with a high magnitude of potential and a long application time, indicated by the differential scattering shown in Fig. 7.11 is the greater change of scattering at the potential switching points when the magnitude of potential increased from ±50 mV to ±200 mV in each potential step mode.

The affect on scattering strength of the specific adsorption of Cl^- anions on the Au nanoprism's surface was less than for the 16 nm Au film as indicated by the almost equal size of differential scattering spikes at 14 s and 154 s when the magnitude of potential was switched between 0 V and a positive or 0 V and a negative potential. When a positive potential is applied, the capacitance of the Au nanoprism's surface is considered to be larger than the case of negative potential, due to the contribution from the absorption capacitance caused by the specific adsorption of Cl^- on the Au surface. Therefore, a negative potential will lead to a smaller change in scattering because of the smaller quantity of accumulated charges in the absence of the specific adsorption ions. The electromagnetic field extends further out from the 16 nm Au nanoprism compared to the nanospheres of similar size, due to the sharp curvature

[152-153], so its decay length is longer than that of 16 nm Au film. Although the specific adsorption anions Cl⁻ is capable of increasing the capacitance of the Au nanoprism's surface in the case of positive potential, more cations Na^+ at the vicinity of Au nanoprism's surface are detectable due to the longer EM field decay length in the case of negative potential. The presence of more detected cations is transduced as an increase of local refractive index and consequently increases the scattering strength when the negative potential is used. The field enhancement resulting from the Au nanoprism's sharp curvature is considered to compensate the smaller scattered light in the case of negative potential and enhances it to match the scattered light caused by the positive potential. As a result, the change of scattering was almost equal when the potential were switched between 0V and any other levels.

(a)   (b)

(c)

(d)

(e)

(f)

(g)

(h)
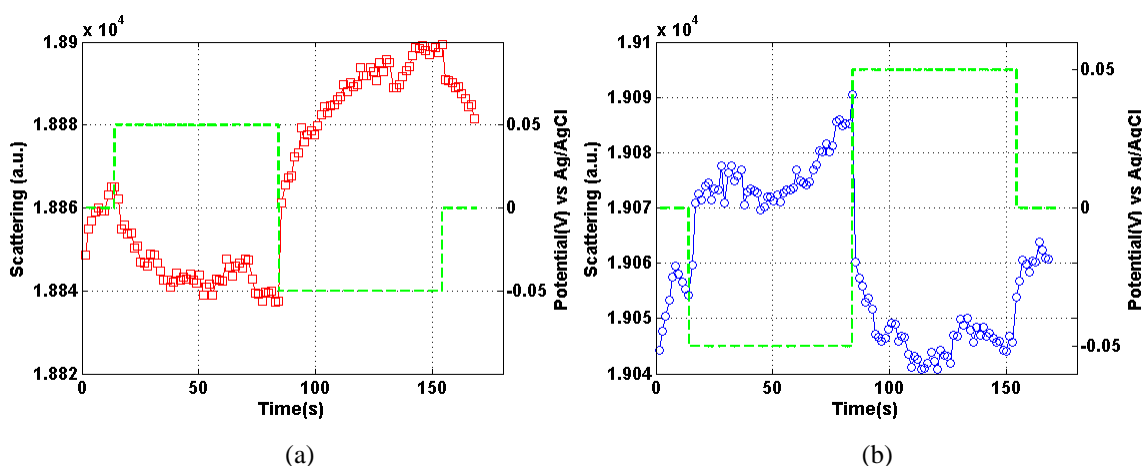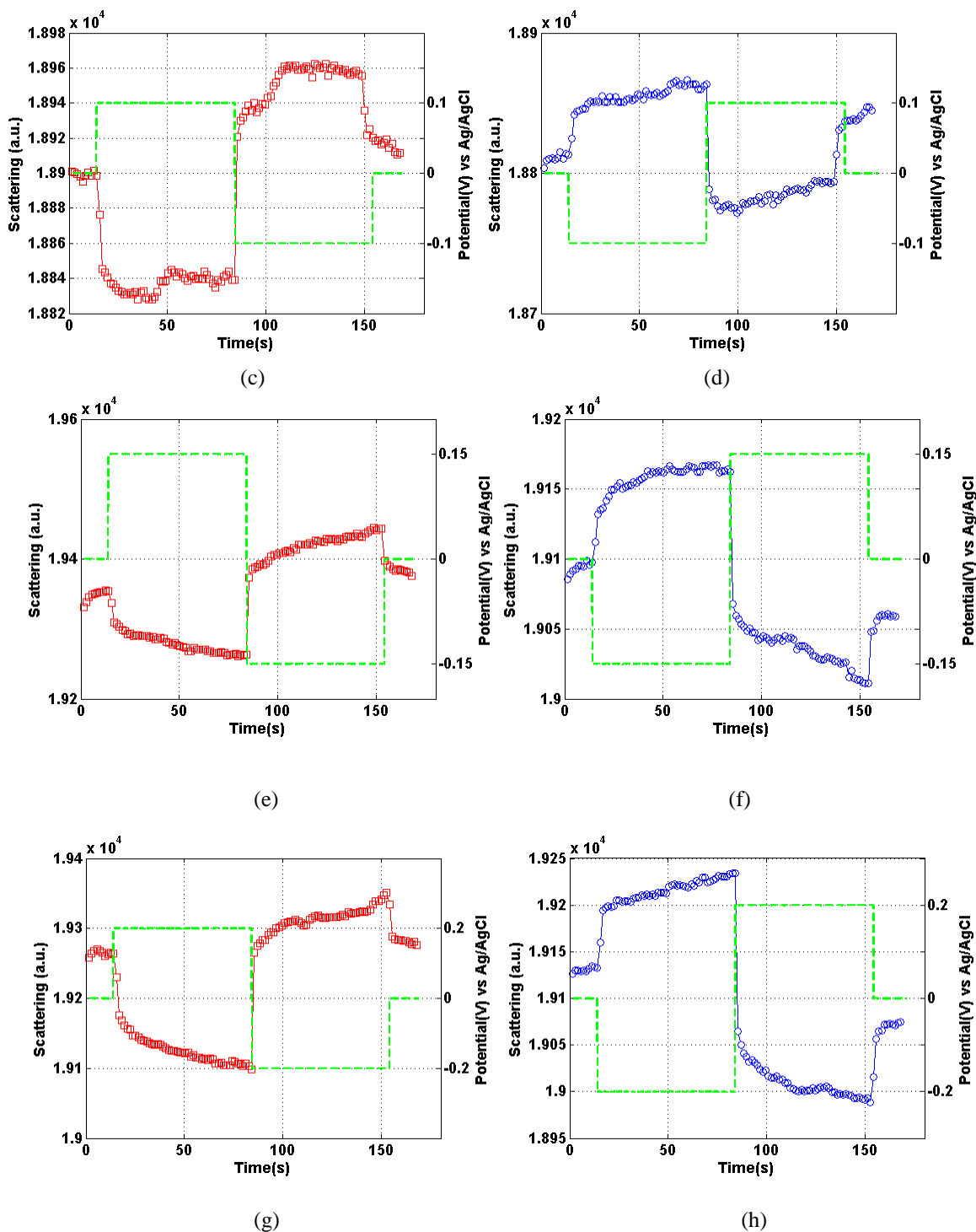
Figure 7.10   Scattering resulted from a potential step, collected from 60-70 nanoprisms. The potential sequences in (a), (c), (e) and (g) are 0 →0.05 →-0.05 →0 V, 0 →0.1 →-0.1 →0 V, 0 →0.15 →-0.15 →0 V, 0 →0.2 →-0.2 →0 V, represented as red lines. The potential sequences in (b), (d), (f) and (h) are revered as 0 →-0.05 →0.05 →0 V, 0 →-0.1 →0.1 →0 V, 0 →-0.15 →0.15 →0 V, 0 →-0.2 →0.2 →0 V, represented as blue lines.

207

(a)

(b)

(c)

(d)
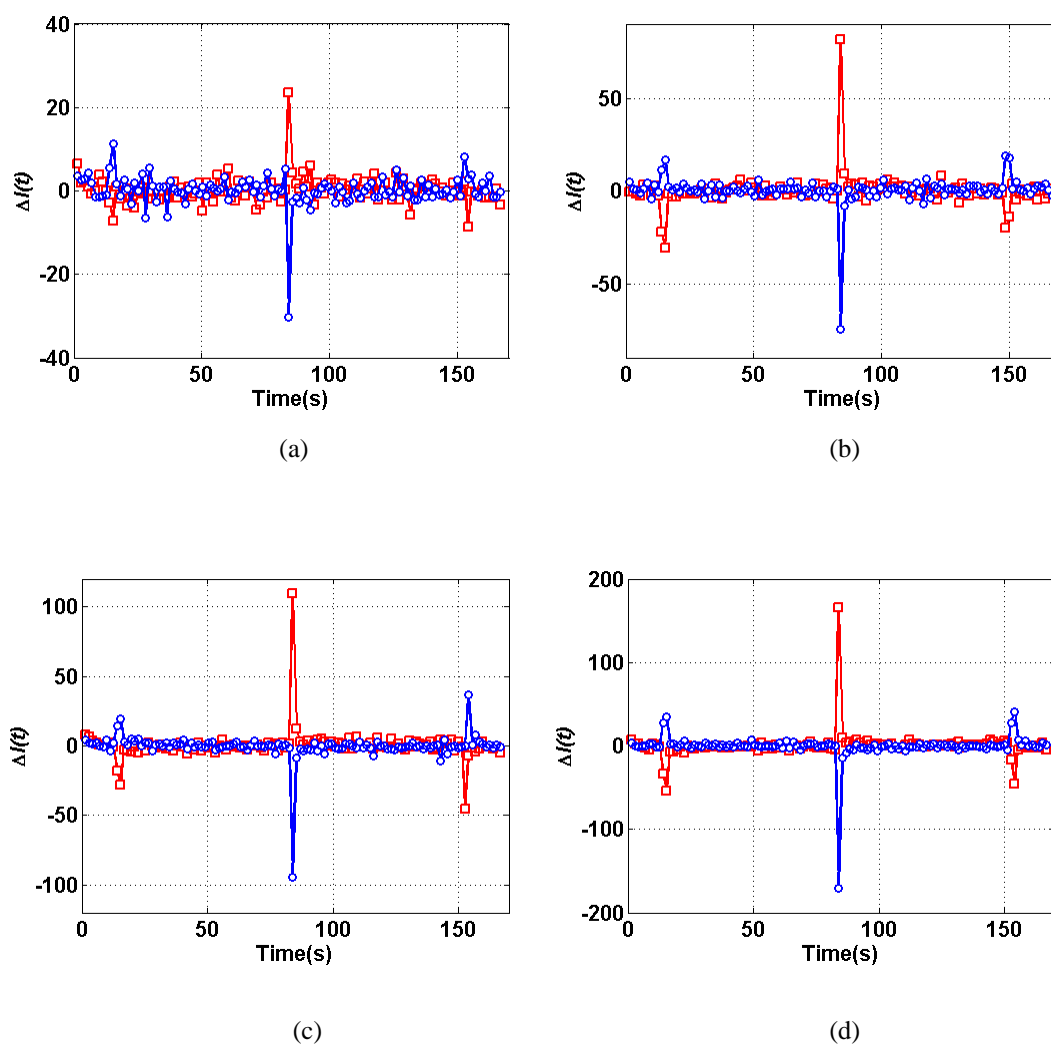
Figure 7.11   The differential scattering of Au nanoprisms during the application of potential step. The potential sequence of red lines in (a), (b), (c) and (d) are 0 →0.05 →-0.05 →0 , 0 V→0.1 →-0.1 →0 V, 0 →0.15 →-0.15 →0 V, 0 →0.2 →-0.2 →0 V and blue lines in (a), (b), (c) and (d) are 0 →-0.05 →0.05 →0 V, 0 →-0.1 →0.1 →0 V, 0 →-0.15 →0.15 →0 V, 0 →-0.2 →0.2 →0 V.

7.3   Conclusions

The scattering of Au nanoprisms was induced by the implementation of several modulated potentials modes. The wavelength dependent scattering contrast of 16 nm and 50 nm height Au nanoprisms has been measured. 16 nm height Au nanoprisms exhibited higher scattering contrast than that of the 50 nm height nanoprisms. The scattering contrast of the 16 nm height Au nanoprisms is slightly lower than 16 nm Au film, but far more linear with voltage. The electric field enhancement generated by the Au nanoprisms morphology is attributed to the smaller effect from specific absorption ions. The differential scattering of the 16 nm height nanoprism observed under cyclic voltammetry exhibited a similar exponential trend as the Au films. The similar ratio of time constants deduced from the exponential fits as the reciprocal ratio of the three potential sweep rates reveals that the electrons in gold have the same mechanism to respond to dynamic potential even if they have different morphologies.

The different scattered light performance between Au nanoprisms, Au nanorods and Au film under potential control confirms the size and shape effect on the surface plasmons and the important role morphology plays in the determination of potential detection capability. Sharp curvature results in an enhancement of electric field intensity. The increase in aspect ratio and plasmonic coupling strength lead to larger polarisability and subsequently stronger voltage sensitivity. This is the reason why the 50 nm height

nanoprisms had comparable capability to that of nanorods. The voltage sensitivity of nanorods ($L = 73$ nm, $d = 25$ nm) and 16 nm height nanoprisms is better than nanospheres ($d = 100$ nm), nanorods ($L = 60$ nm, $d = 25$ nm) and 50 nm height nanoprism because of their high aspect ratio. Stronger plasmonic coupling leads the 16 nm Au film having the best voltage sensitivity in the range of these Au nanostructures.

Chapter 8　　Conclusions and future work

This thesis has presented the optical response of Au nanostructure to potential measured by using the electrochemical method. The potential applied to the nanostructure was limited within Au nanostructure's double layer charging region to avoid any redox reaction taking place between the Au nanostructure and the electrolyte solution. The dynamic scattering of Au nanostructures resulting from several types of potential modulation mode was collected from a custom designed objective-type dark-field imaging spectrometer, which enabled the simultaneous acquisition of spatial and spectral information.

A potential modulation mode, denoted bipolar mode A, was applied to a variety of Au nanostructures to characterise their capabilities to detect potential. When potential was applied between 200 mV and -200 mV, the increase and decrease of scattering along with the Au nanostructures' spectra indicated their scattering was potentially manipulable and wavelength dependent. The morphology of the nanostructure plays an important role to determine the voltage sensitivity of these Au nanostructures. Plamonic coupling and aspect ratio are able to increase the polarisability of Au nanostructure and subsequently improve the voltage sensitivity. Sharp surface curvature is an additional factor which improves the sensitivity due to the electric field

enhancement. Au nano-islands randomly orientated and conductively overlapped on 16 nm Au film induced strong plasmonic coupling. Therefore, 16 nm Au film had the greatest sensitivity among the Au nanostructures which were investigated. 16 nm height Au nanoprims had a weak coupling compared to the 16 nm Au film but a higher aspect ratio than 50 nm height Au nanoprism, and its voltage sensitivity was between that of 16 nm Au film and 50 nm height Au nanoprism. Due to 50 nm height Au nanoprism's sharp curvature and Au nanorod's aspect ratio, they had comparable voltage sensitivity. Au nanospheres with the smallest aspect ratio were the least appropriate choice to be selected as a potential sensing platform. It should be noted that the experimental conditions can also determine the measurement result. 50 nm Au film had little response to the potential by using the dark-field spectrometer in the case of a non-resonant incident wave-vector. But its response to the potential was detectable when it was employed on a surface plasmon resonance system with the Kretchmann-Raether configuration.

Time dependent scattering has been studied by the application of potential cyclic voltammetry and potential steps. An exponential expression for the differential scattering induced by the potential cyclic voltammetry can be applied to Au film and Au nanoprism. The faster the potential scan is, the earlier steady state of the scattering transients will settle. The universality of the exponential fit for Au film and Au nanoprism indicates the mechanism of potential on the Au nanostructure is the same, whatever the morphologies are.

The similar trend of the scattering generated by the potential step and the charge measured by the electrochemical method implied the scattering of Au nanostructure was a good indicator to the charges produced by the charging and discharging process on the Au nanostructure.

Electron transport between the Au nanocrystals and electrolyte solution was accounted for the electrical double layer at their interface. The application of potential induces excessive but opposite charges to accumulate at the Au nanostructure-solution interface, which comprises the double layer capacitance. The formation of the double layer capacitance induces a movement of electrons in gold's space charge region. The consequence of this change in the electron density of gold is the alteration of its dielectric constant, which depends on the electron density, and subsequently the change in the nanostructure's optical properties. Theoretical simulations related to the potential and Au nanostructures were developed to understand their relationship. The nanoparticle's spectrum was red-shifted by positive potential and blue-shifted by negative potential in simulation which was consistent with the experimental observations. The tendency of reflected light contrast with potential calculated from the modeling of Au film agreed with the scattering contrast decreasing as a function of potential which was measured from the Au film experimentally. The nonlinear trend with respect to the decreasing potential is the result of nonlinear accumulated charges on the gold surface. Furthermore, the calculations illustrate the key role of the morphology of the nanoparticles to

213

determine their potential detection abilities. A high aspect ratio means it is easier to polarise the particle and produces greater voltage sensitivity. This rule points out the direction to select the particle to achieve high potential sensing capability.

Future work of noble metallic nanostructure will be more exciting because of its intriguing potential application in monitoring cellular activity. The small magnitude of neural cell spiking and the fast transient of the signal is a major challenge for design of this sensor.

Selecting a nanostructure with a suitable morphology is a good beginning. The advances in synthesis methods enable the design and fabrication of nanostructure to suit specific applications. According to the rules discovered in this thesis, large surface area to volume ratio, high aspect ratio, strong coupling, to chose nanostructure are useful to find the effective nanostructure. Electron beam lithography can be used to fabricate nanoparticles of homogeneous size, shape and interparticle separation, such as conductively overlapped gold and silver nanoprisms with different orientations. This will allow the properties of nanoparticles to be tailored in a much more controlled way.

The experimental condition is a further factor to determine the measurement results. The different measurement results of the 50 nm thickness Au film due to the beam with different incident angles is an example. In this thesis, the dark-field spectrometer only provided the beam with a lower (sub-critical) incident angle. Therefore, it is necessary to measure the response

of nanostructure to the potential at different incident angles, from below to above the critical angle, to identify the best condition for the potential detection.

The camera used in this thesis was capable of collecting spatial information from the sample but the slow response was a drawback. An improvement in the temporal resolution of the instrument by increasing the sampling frequency and signal-to-noise ratio would enable the detection of the tiny electron transport process produced by nerve cells.

The seed-mediated-synthesised gold nanorods are typically coated with CTAB, which maintains the gold nanorods in a finely dispersed state but is detrimental to biological molecules. To reduce the toxicity of CTAB, the surface of gold nanoparticles can be modified such that CTAB is either replaced by centrifugation or covered by biocompatible molecules, such as polyelectrolyte and silica.

To sense a change in tran-membrane potential, the surface of gold nanostructure need to be hydrophilic so that gold nanoparticles bind to the surface of the membrane of all cells without interrupting cellular normal functions. Gold nanostructures immobilised on substrate are suitable for the external sensing of cell response, but this method will be only effective in situations when the neurons are in a monolayer and is restricted to a narrow region in the z-axis. Removing nanoparticles from the substrate and releasing them into solution by adding surfactant and sonicating the sample provide extra

flexibilities for biological applications. Intracellular application of gold nanoparticle is more sensitive to membrane potential change. The analysis of membrane potential transient from multiple sites in neuronal processes and the initiation and propagation of electrical signals in whole ganglion preparation become achievable.

Further theoretical study on the response of nanostructure to the potential should also be carried out for a deeper understanding of this unexplored world. Plenty of precise experimental data used as input for the improved theory could give more detailed insight into the fascinating charge transport in noble metal nanostructure and create more accurate guideline to design and develop plasmonic nanoparticle sensors.

Appendix   A

A.1   Surface plasmon resonance theory

The surface charges and the electromagnetic wave interact at the metal-dielectric interface, when light propagates from metal medium 1 to dielectric medium 2, with relative permittivities ε_1 ($n_1 = \sqrt{\varepsilon_1}$, $\varepsilon_1 = \varepsilon_1^{'} + i\varepsilon_1^{''}$) and ε_2 ($n_2 = \sqrt{\varepsilon_2}$) respectively. Under specified conditions, Maxwell's Equations without an external source can be expressed as follows:

$$\begin{cases} \nabla \cdot D = 0 \\ \nabla \times E = -\dfrac{\partial B}{\partial t} \\ \nabla \cdot B = 0 \\ \nabla \times H = \dfrac{\partial D}{\partial t} \end{cases} \qquad (A.1a)$$

$$D = \varepsilon_r \varepsilon_0 E \qquad (A.1b)$$

$$B = \mu_r \mu_0 H \qquad (A.1c)$$

where the charge density ρ_0 and current density J are assumed as approximately equal to zero, ε_r and ε_0 are the relative permittivity and the permittivity of vacuum respectively, μ_r and μ_0 are relative permeability and the permeability of vacuum respectively.

Since only a p-polarised beam induces a discontinuity of the electric field E at the interface of these two media (z=0), penetrating into both sides. The electric and magnetic fields in the two media can be written as:

$$E_j = \begin{pmatrix} E_{xj} \\ 0 \\ E_{zj} \end{pmatrix} \text{exp}^{i(k_{xj}x - k_{z_j}|z| - \omega t)} \qquad (A.2a)$$

$$H_j = \begin{pmatrix} 0 \\ H_{yj} \\ 0 \end{pmatrix} \text{exp}^{i(k_{xj}x - k_{zj}|z| - \omega t)} \qquad (A.2b)$$

where the index j represents the media, $j=1$ at negative direction ($z<0$) and $j=2$ at positive direction ($z>0$).

Introducing Eq.(A.2) into Eq. (A.1) results in the i component as

$$iH_{y1}k_{z1} = -i\omega\varepsilon_1\varepsilon_0 E_{x1} \qquad (A.3a)$$

$$-iH_{y2}k_{z2} = -i\omega\varepsilon_2\varepsilon_0 E_{x2} \qquad (A.3b)$$

According to the boundary condition, the tangential component of E and H are continuous,

$$E_{x1} = E_{x2} \qquad (A.4a)$$

$$H_{y1} = H_{y2} \qquad (A.4b)$$

So $\qquad \dfrac{\varepsilon_1}{k_{z1}} + \dfrac{\varepsilon_2}{k_{z2}} = 0 \qquad (A.5)$

The wave vectors in medium 1, k_1, and medium 2, k_2, can be written

as

$$k_1^2 = k_{x1}^2 + k_{z1}^2 \qquad\qquad \text{(A.6a)}$$

$$k_2^2 = k_{x2}^2 + k_{z2}^2 \qquad\qquad \text{(A.6b)}$$

where $k_{x1} = k_{x2} = k_x$

Substituting Eq. (A.5) into Eq.(A.6) obtains

$$k_x^2 = (\frac{\omega}{c})^2 \frac{\varepsilon_1 \varepsilon_2}{\varepsilon_1 + \varepsilon_2} \qquad\qquad \text{(A.7a)}$$

$$k_{z1}^2 = (\frac{\omega}{c})^2 \frac{\varepsilon_1^2}{\varepsilon_1 + \varepsilon_2} \qquad\qquad \text{(A.7b)}$$

$$k_{z2}^2 = (\frac{\omega}{c})^2 \frac{\varepsilon_2^2}{\varepsilon_1 + \varepsilon_2} \qquad\qquad \text{(A.7c)}$$

Because the relative permittivity of metal 1 is complex, Eq. (A.7a) is written as

$$k_x^2 = (\frac{\omega}{c})^2 \varepsilon_2 \frac{\varepsilon_1^{'}(\varepsilon_2 + \varepsilon_1^{'}) + \varepsilon_1^{''2} + i\left[\varepsilon_1^{''}(\varepsilon_2 + \varepsilon_1^{'}) - \varepsilon_1^{'}\varepsilon_1^{''}\right]}{(\varepsilon_2 + \varepsilon_1^{'})^2 + \varepsilon_1^{''2}} \qquad \text{(A.8a)}$$

$$\text{Real part } \operatorname{Re}(k_x) = (\frac{\omega}{c})\sqrt{\varepsilon_2 \frac{\varepsilon_1^{'}(\varepsilon_2 + \varepsilon_1^{'}) + \varepsilon_1^{''2}}{(\varepsilon_2 + \varepsilon_1^{'})^2 + \varepsilon_1^{''2}}} \qquad \text{(A.8b)}$$

$$\text{Imaginary part } \operatorname{Im}(k_x) = (\frac{\omega}{c})\sqrt{\varepsilon_2 \frac{\varepsilon_1^{''}(\varepsilon_2 + \varepsilon_1^{'}) - \varepsilon_1^{'}\varepsilon_1^{''}}{(\varepsilon_2 + \varepsilon_1^{'})^2 + \varepsilon_1^{''2}}} \qquad \text{(A.8c)}$$

The imaginary part of k_x leads the amplitude of the surface plasmons to exponentially decay in the x direction as $\exp[\pm \mathrm{Im}(k_x)x]$.

Usually, the real part of the metallic permittivity ε_1' is negative but its absolute value is larger than its imaginary part ε_1'' and the dielectric permittivity ε_2. Assuming $|\varepsilon_1'| > \varepsilon_1''$ and $|\varepsilon_1'| > \varepsilon_2$ results in purely imaginary k_{z1} and k_{z2} because of negative $\varepsilon_1' + \varepsilon_2$

$$k_{z1} = \frac{\omega}{c}\sqrt{\frac{\varepsilon_1'^2}{\varepsilon_1' + \varepsilon_2}} \qquad (A.9a)$$

$$k_{z2} = \frac{\omega}{c}\sqrt{\frac{\varepsilon_2^2}{\varepsilon_1' + \varepsilon_2}} \qquad (A.9b)$$

Besides decaying in the x direction, surface plasmons also decay into the metal and dielectric at z direction respectively. The penetration depth is defined as $1/k_{zj}$.

A.2 The capacitance of the electrical double layer

The structure of the electrical double layer is depicted in Fig. 3.4. The charge density at the electrode surface, $\sigma^M = -\sigma^S$, the charge density in the solution at all times.

The structure in the region $0 \le x \le x_2$ resembles a parallel-plate capacitor. In the assumption that there are no specially adsorbed ions on the

metal electrode, the charges distribute at the metal surface ($x = 0$) and the counterions' closest approach distance ($x = x_2$) as a uniform layer with opposite sign. The charge density σ^M of the electrode surface at a potential ψ_0 [V] is

$$\sigma^M = \frac{\varepsilon_0 \varepsilon_r}{x_2} \psi_0 \qquad \text{(A.10)}$$

where ε_0 is the permittivity of vacuum, ε_r is the relative static permittivity of the medium and x_2 is the closest distance that the counterion can approach the metallic surface.

The capacitance C_H of the Helmholtz layer depends on the nature of the ions in the electrolyte. It is expressed per unit area [Fm^{-2}] as

$$\frac{d\sigma^M}{d\psi_0} = C_H = \frac{\varepsilon_0 \varepsilon_r}{x_2} \qquad \text{(A.11)}$$

For distances $x \geq x_2$, the distribution of ions is assumed to obey Boltzmann's law,

$$n_i(x) = 10^3 N_A n_i^0 \exp\left(-\frac{z_i e \psi(x)}{kT}\right) \qquad \text{(A.12)}$$

where $n_i(x)$ is the concentration of ions of species i, n_i^0 is the bulk

concentration [mol L^{-1}], N_A is Avogadro's number, z_i is the valence of species i ion, e is the electron charge [C], $\psi(x)$ [V] is the electrical potential at position x, k is Boltzmann's constant [JK^{-1}] and T is the absolute temperature [K].

The charge density $\rho(x)$ at x is given by

$$\rho(x) = \sum_i 10^3 N_A n_i z_i e = \sum_i 10^3 N_A n_i^0 z_i e \exp(-\frac{z_i e \psi(x)}{kT}) \qquad (A.13)$$

The potential $\psi(x)$ at position x is related to the charge density. Their relationship is given by the Poisson equation

$$\rho(x) = -\varepsilon_0 \varepsilon_r \frac{d^2 \psi(x)}{dx^2} \qquad (A.14)$$

Combining Eqs. (A.13) and (A.14) gives the electric field strength at range $x \geq x_2$ for a symmetrical $z:z$ electrolyte with the bulk concentration n^0 [mol L^{-1}]

$$\frac{d\psi}{dx} = -\sqrt{\frac{8kT10^3 N_A n^0}{\varepsilon_0 \varepsilon_r}} \sinh(\frac{ze\psi(x)}{2kT}) \qquad (A.15)$$

Considering that specially adsorbed ions are absent in the region

$0 \leq x \leq x_2$, the charge density is zero. The electric field $d\psi / dx$ is constant and the potential varies linearly in the Helmholtz layer. The potential ψ_2 at position x_2 is

$$\psi_0 = \psi_2 - (\frac{d\psi}{dx})_{x=x_2} x_2 \qquad (A.16)$$

The geometry of charges distributed at $x \geq x_2$ is supposed to be a Gaussian surface. The electric field extends from one boundary $(x = x_2)$ adjacent to and perpendicular to the electrode surface, into the bulk solution where its value decreases to zero. The charge distribution profile at this boundary with a surface area A is integrated to give

$$q = \varepsilon_0 \varepsilon_r \oint_{surface} \frac{d\psi}{dx} dS$$

$$= \varepsilon_0 \varepsilon_r (\frac{d\psi}{dx})_{x=x_2} A \qquad (A.17)$$

The charge density at the electrode surface ($\sigma^M = -q/A$) is

$$\sigma^M = -\sigma^S = \varepsilon_0 \varepsilon_r (\frac{d\psi}{dx})_{x=x_2} = \sqrt{\frac{8kT10^3 N_A n^0}{\varepsilon_0 \varepsilon_r}} \sinh(\frac{ze\psi_2}{2kT}) \quad (A.18)$$

The potential ψ_2 in Eq. (A.16) can be solved graphically and substituting it into Eq. (A.18) can obtain the capacitance of this double layer

C_D [Fm^{-2}] $(C_D = d\sigma^M / d\psi)$

$$\frac{1}{C_D} = \frac{x_2}{\varepsilon_0\varepsilon_r} + \frac{1}{\sqrt{\dfrac{2\varepsilon_0\varepsilon_r z^2 e^2 10^3 N_A n^0}{kT}} \cosh(\dfrac{ze\psi_2}{2kT})} = \frac{1}{C_H} + \frac{1}{C_{diff}}$$

(A.19)

A.3 Calculation of the reflection and transmission of light in a multilayer structure

The multi-reflected wave traversing in the structure depicted in Fig. 5.1 along the z axis comprises a forward-travelling plane wave denoted by (+) and backward-travelling plane wave denoted by (-) whose destinations are the ambient medium and the substrate respectively. Considering two neighbouring planes $z^{'}$ and $z^{''}$, the amplitudes of the forward travelling $E^+(z^{'})$ and the backward travelling $E^-(z^{'})$ waves in plane $z^{'}$ can be described by a 2×2 matrix related to the amplitudes of the forward $E^+(z^{''})$ and the backward $E^-(z^{''})$ travelling waves in plane $z^{''}$

$$\begin{bmatrix} E^+(z^{'}) \\ E^-(z^{'}) \end{bmatrix} = \begin{bmatrix} S_{11} & S_{12} \\ S_{21} & S_{22} \end{bmatrix} \begin{bmatrix} E^+(z^{''}) \\ E^-(z^{''}) \end{bmatrix}$$

(A.20)

or $\qquad E(z^{'}) = SE(z^{''}) \qquad$ for a concise style

If the locations of planes $z^{'}$ and $z^{''}$ are just opposite the interface of

layers j and $j+1$, the relationship between the waves in planes z' and z'' can be written as

$$E(z_j) = I_{j(j+1)}E(z_j) \qquad \text{(A.21)}$$

where interface matrix $I_{j(j+1)}$ characterises the j-$(j+1)$ interface. On the other hand, if the planes z' and z'' are chosen to locate at the two boundaries of jth layer, the relationship between the wave in plane z' and z'' is described as

$$E(z_j) = L_j E(z_j + d_j) \qquad \text{(A.22)}$$

where layer matrix L_j is the characteristic of jth layer and d_j is its thickness.

Since only the resultant reflected and transmitted waves are accessible in practice, combining the individual interface matrix and layer matrix in the structure to bridge the wave in medium 0 and $m+1$

$$E(z_0) = SE(z_{m+1}) \qquad \text{(A.23)}$$

Scattering matrix S is the combination of the properties of all interfaces and layers beginning from the interface of medium 0 and 1, following several internal layers and interfaces, and ending at the interface of medium m and $m+1$.

$$S = I_{01}L_1 I_{10}L_2 \cdots I_{(j-1)j}L_j I_{j(j+1)} \cdots L_m I_{m(m+1)} \qquad \text{(A.24)}$$

(a)   (b)
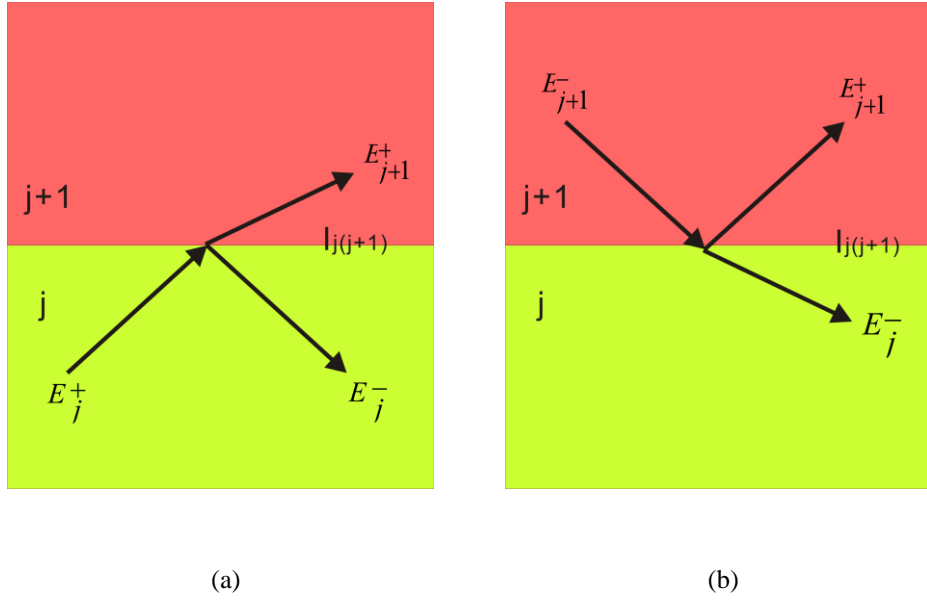
Figure A.1 Reflection and transmission of light transmits from (a) layer *j* to layer *j*+1, (b)

from layer *j*+1 to layer *j*

Considering the special case when the incident beam E_j^+ travelling to the

j-*j*+1 interface results in a reflected beam E_j^- and a transmitted beam E_{j+1}^+, as

shown in Fig. A.1 (a), the interface matrix $I_{j(j+1)}$ related to this field is written

as

$$
\begin{bmatrix} E_j^+ \\ E_j^- \end{bmatrix} = \begin{bmatrix} I_{11} & I_{12} \\ I_{21} & I_{22} \end{bmatrix} \begin{bmatrix} E_{j+1}^+ \\ E_{j+1}^- \end{bmatrix}
\tag{A.25}
$$

their amplitude relationships can be simply described as

$$
E_{j+1}^+ = t_{j(j+1)} E_j^+
\tag{A.26a}
$$

226

$$E_j^- = r_{j(j+1)} E_j^+ \qquad\qquad \text{(A.26b)}$$

$$E_{j+1}^- = 0 \qquad\qquad \text{(A.26c)}$$

where $t_{j(j+1)}$ and $r_{j(j+1)}$ are the Fresnel's reflection and transmission coefficients of *j-j+1* interface. Solving Eq. (A.25) by substituting Eq.(A.26) could get

$$I_{11} = \frac{1}{t_{j(j+1)}} \qquad\qquad \text{(A.27a)}$$

$$I_{21} = \frac{r_{j(j+1)}}{t_{j(j+1)}} \qquad\qquad \text{(A.27b)}$$

Reversing the propagation direction of this beam as transmitting from layer *j+1* to layer *j* through the *j+1-j* interface, the amplitude relationships of each beam are

$$E_j^- = t_{(j+1)j} E_{j+1}^- \qquad\qquad \text{(A.28a)}$$

$$E_{j+1}^+ = r_{(j+1)j} E_{j+1}^- \qquad\qquad \text{(A.28b)}$$

$$E_j^+ = 0 \qquad\qquad \text{(A.28c)}$$

where $t_{(j+1)j}$ and $r_{(j+1)j}$ are the Fresnel coefficients of *j+1-j* interface. Substituting Eq. (A.28) to Eq. (A.25) leads to

$$I_{12} = -\frac{r_{(j+1)j}}{t_{j(j+1)}} \qquad \text{(A.29a)}$$

$$I_{22} = \frac{(t_{j(j+1)}t_{(j+1)j} - r_{j(j+1)}r_{(j+1)j})}{t_{j(j+1)}} \qquad \text{(A.29b)}$$

When the light travels from layer j to $j+1$, and then reverses direction from layer $j+1$ to j as shown in Fig. A.1 (b), the reflection and transmission coefficients are related as

$$r_{(j+1)j} = -r_{j(j+1)} \qquad \text{(A.30a)}$$

$$r_{(j+)j} = -r_{j(j+1)} \qquad \text{(A.30b)}$$

$$t_{(j+1)j} = \frac{1 - r_{j(j+1)}^2}{t_{j(j+1)}} \qquad \text{(A.30c)}$$

$$t_{(j+1)j} = \frac{1 - r_{j(j+1)}^2}{t_{j(j+1)}} \qquad \text{(A.30d)}$$

So the interface matrix $I_{j(j+1)}$ is solved as

$$I_{j(j+1)} = \begin{bmatrix} \dfrac{1}{t_{j(j+1)}} & \dfrac{r_{j(j+1)}}{t_{j(j+1)}} \\[2ex] \dfrac{r_{j(j+1)}}{t_{j(j+1)}} & \dfrac{1}{t_{j(j+1)}} \end{bmatrix} \qquad \text{(A.31)}$$

Besides the interface matrix *I*, the second component of the scattering matrix is layer matrix *L*. Considering the situation depicted in Fig. A.2 where the beam E_e^+ propagates at z^+ direction in *j*th layer of thickness d_j from the

interface *e* until be resiled by interface *f*, the beams at both interfaces are maintained the same amplitude except a phase shift β_j, E_f^+ and E_e^- are phase lag β_j compared to E_e^+ and E_f^- respectively,
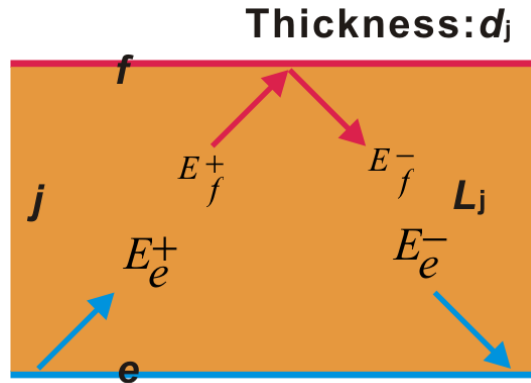
Figure A.2   Light travelling in the *j*th layer

$$E_f^+ = e^{-j\beta_j} E_e^+ \qquad \text{(A.32a)}$$

$$E_e^- = e^{-j\beta_j} E_f^- \qquad \text{(A.32b)}$$

where phase shift β_j is caused by light when it travels in the layer with refractive index n_j at angle θ_j
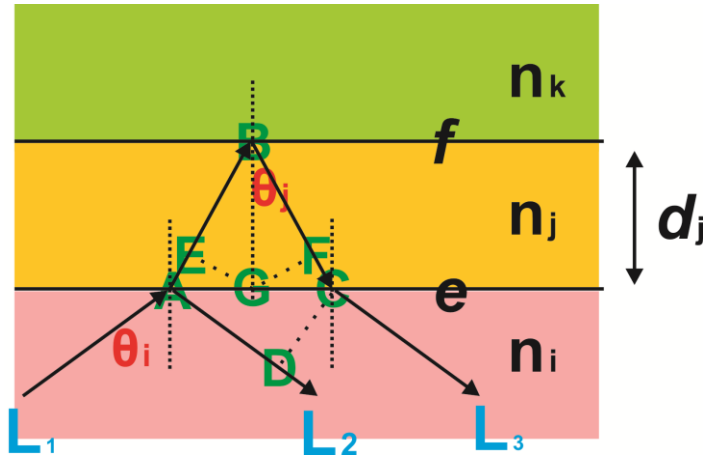
Figure A.3 Schematic diagram of light reflection between interface *e* and *f*

The detail of the phase shift is depicted in Fig. A.3. When the beam L_1 impinges on the interface *e* at point *A* between two layers *i* and *j* with dielectric constant n_i and n_j respectively, one part of *L*1 is reflected back to the *i*th layer, indicated as beam L_2, with the same incident angle θ_i. The rest of L_1 is refracted into the *j*th layer with a refracted angle θ_j. It is reflected at interface *f* (point *B*) and transmits to the *i*th layer (point *C*) represented by beam L_3.

The optical path length difference between beam L_2 and L_3 is

$$\Delta = n_j(AB + BC) - n_i AD$$

$$= n_j(AE + EB + BF + FC) - n_i AD$$

$$= n_j(AE + FC) - n_i AD + n_j(EB + BF) \qquad \text{(A.33)}$$

According to the geometry,

$$\sin\theta_j = AE / AG$$

$$AE = AG\sin\theta_j = \frac{AC}{2}\sin\theta_j \qquad (A.34)$$

$$\sin\theta_i = \frac{AD}{AC} \qquad (A.35)$$

Because of Snell's law,

$$n_i \sin\theta_i = n_j \sin\theta_j$$

$$\sin\theta_j = \frac{n_i \sin\theta_i}{n_j} \qquad (A.36)$$

Substituting Eqs.(A.35) and (A.36) to Eq. (A.34) leads to

$$AE = \frac{AC}{2}\frac{n_i \sin\theta_i}{n_j} = \frac{AC}{2}\frac{n_i}{n_j}\frac{AD}{AC} = \frac{AD}{2}\frac{n_i}{n_j}$$

$$ADn_i = 2AEn_j = AEn_j + FC n \qquad (A.37)$$

Now, considering Eq. (A.37), Eq. (A.33) is rearranged as

$$\Delta = n_j(EB + BF) = 2n_j EB = 2n_j d_j \cos\theta_j \quad (A.38)$$

So the change of the phase due to the propagation of light between A and B, B and C, which is equivalent to the phase shift between the beam E_f^+ and E_e^+,

231

E_e^- and E_f^-, is given by

$$\beta_j = \frac{2\pi}{\lambda} d_j n_j \cos\theta_j \qquad (A.39)$$

Therefore, the layer matrix L can be written as

$$L_j = \begin{bmatrix} e^{j\beta_j} & 0 \\ 0 & e^{-j\beta_j} \end{bmatrix} \qquad (A.40)$$

The overall scattering matrix S is the multiplication of interface matrix I and layer matrix L representing each interface and layer. For a practical multilayer structure, the scattering matrix S is

$$\begin{bmatrix} E_0^+ \\ E_0^- \end{bmatrix} = \begin{bmatrix} S_{11} & S_{12} \\ S_{21} & S_{22} \end{bmatrix} \begin{bmatrix} E_{m+1}^+ \\ 0 \end{bmatrix} \qquad (A.41)$$

The scattering matrix S for p- and s-polarised light is produced by substituting Fresnel's equation of p- and s-polarised light for the interface matrix I of each interface and multiplying by every layer's matrix L respectively. The energetic coefficients of reflection and transmission light from the multilayer structure are

$$R = (\frac{E_0^-}{E_0^+})^2 = (\frac{S_{21}}{S_{11}})^2 \qquad (A.42a)$$

$$T = (\frac{E_{m+1}^+}{E_0^+})^2 = (\frac{1}{S_{11}})^2 \qquad \text{(A.42b)}$$

A.4 Simple capacitance calculation

L=73nm

d=25nm

H
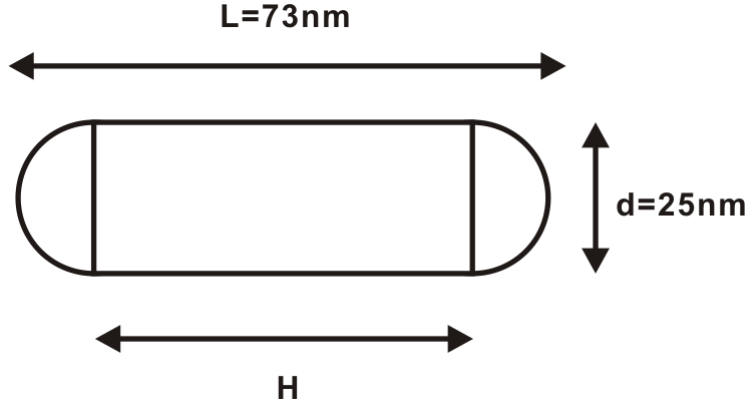
Figure A.4 Illustration of nanorod

In the case of rod (*L*= 73 nm, *d*= 25 nm, *H*= 48 nm) with two spherically-capped ends as shown in Fig. A.4, the surface area of the rod *SA* [m^2] is

$$SA = 4\pi(\frac{d}{2})^2 + 2\pi H \frac{d}{2} = 5.7334 \times 10^{-15} \qquad \text{(A.43)}$$

The volume of the rod *VOL* [m^3] is

$$VOL = [H\pi(\frac{d}{2})^2 + (\frac{d}{2})^3 \times 4\pi/3] = 3.1743 \times 10^{-23} \quad \text{(A.44)}$$

The electrons are assumed to distribute uniformly inside the rod and its density

N [m^{-3}] is 5.9×10^{28}.

The maximum experimental scattering contrast of this nanorod resulted from the perturbed potential E of 0.4 V was about 2.5×10^{-3}. 1.6 % change of electron density ΔN [m^{-3}] in the domain of Thomas-Fermi layer leads to the same magnitude of scattering contrast for this type of nanorod in simulation. The thickness of Thomas-Fermi layer d_{TF} is 5.8744×10^{-11} m and the electron charge e is 1.6022×10^{-19} C, so the charge transferred ΔQ [C] in this domain is

$$\Delta Q = e \times d_{TF} \times SA \times 0.016 \times N$$

$$= 1.6022 \times 10^{-19} \times 5.8744 \times 10^{-11} \times 5.7334 \times 10^{-15} \times 0.016 \times 5.9 \times 10^{28}$$

$$= 5.0941 \times 10^{-17}$$

(A.45)

Hence, the capacitance per unit surface area C [Fm^{-2}] at the surface of rod is

$$C = \frac{\Delta Q}{E \cdot SA} = \frac{5.0789 \times 10^{-17}}{0.4 \times 5.7334 \times 10^{-15}} = 0.0222$$

(A.46)

According to the GCS model, the anticipated double layer capacitance at the surface of electrode is 0.9205 Fm^{-2} when the potential is 0.2 V or -0.2 V.

A.5   Symbols and abbreviations

Symbol	Description	Value	Units
ω	angular frequency		rad s^{-1}
ε_∞	high frequency limit	5.9673	
r_D	damping coefficient for bulk metal	15.92×10^{12}	Hz
ω_D	plasmon frequency	2113.6×10^{12}	Hz
N	free electron density	5.9×10^{28}	m^{-3}
e	charge of an electron	1.602×10^{-19}	C
ε_0	permittivity of vacuum	8.854×10^{-12}	Fm^{-1}
m^*	effective mass of an electron		kg
m_e	mass of an electron	9.109×10^{-31}	kg
Ω_L	strength of Lorentz oscillator	650.07×10^{12}	Hz
Γ_L	spectral width of Lorentz oscillator	104.86×10^{12}	Hz
$\Delta\varepsilon$	weight factor	1.09	
v_F	Fermi velocity	1.4×10^6	ms^{-1}
λ_τ	mean free path for electron		m
L_{eff}	effective mean free path		m
A	dimensionless parameter	1	
V	volume of particle		m^3
S	surface area of particle		m^2

ε_{eff}	effective dielectric constant		
ε_p	relative permittivity of particle		
ε_i	relative permittivity of insulating medium		
L_p	depolarization factor		
f_p	volume fraction of metal particles		
ε_r	relative static permittivity of water	78.5	
x_2	thickness of Helmholtz layer	5×10^{-10}	m
ψ_0	potential at electrode surface		V
n^0	Bulk concentration of electrolyte		mol Ł$^{-1}$
N_A	Avogadro's number	6.02×10^{23}	
z	valence of species		
k	Boltzmann's constant	1.38×10^{-23}	JK^{-1}
T	absolute temperature		K
C_D	double layer capacitance		Fm^{-2}
C_H	capacitance of Helmholtz layer		Fm^{-2}
C_{diff}	capacitance of diffuse layer		Fm^{-2}
h	Planck's constant	6.626×10^{-34}	Js
I_{inc}	power of incident beam	1×10^{9}	Wm^{-2}
NA	numerical aperture of objective lens	1.49	
$n_{coupling}$	refractive index of coupling medium	1.52	
T_{tran}	optical transmittion		

QE_λ	quantum efficiency	0.5	
λ	wavelength of light		m
$T_{integration}$	integration time of detection sensor	1×10^{-3}	s
c	speed of light	2.99×10^{8}	ms^{-1}
a	semiaxes of the ellipsoidal particle		m
b	semiaxes of the ellipsoidal particle		m
c	semiaxes of the ellipsoidal particle		m

ITO	indium tin oxide
CTAB	cetyltrimethylammonium bromide
RIU	refractive index unit

Bibliography

1.   Huang, X.H., S. Neretina, and M.A. El-Sayed, *Gold Nanorods: From Synthesis and Properties to Biological and Biomedical Applications.* Advanced Materials, 2009. **21**(48): p. 4880-4910.

2.   Jain, P.K., X. Huang, I.H. El-Sayed, and M.A. El-Sayad, *Review of some interesting surface plasmon resonance-enhanced properties of noble metal nanoparticles and their applications to biosystems.* Plasmonics, 2007. **2**(3): p. 107-118.

3.   Perez-Juste, J., I. Pastoriza-Santos, L.M. Liz-Marzan, and P. Mulvaney, *Gold nanorods: Synthesis, characterization and applications.* Coordination Chemistry Reviews, 2005. **249**(17-18): p. 1870-1901.

4.   Bukasov, R. and J.S. Shumaker-Parry, *Highly tunable infrared extinction properties of gold nanocrescents.* Nano Letters, 2007. **7**(5): p. 1113-1118.

5.   Wang, H., D.W. Brandl, F. Le, P. Nordlander, and N.J. Halas, *Nanorice: A hybrid plasmonic nanostructure.* Nano Letters, 2006. **6**(4): p. 827-832.

6.   Lee, K.S. and M.A. El-Sayed, *Gold and silver nanoparticles in sensing and imaging: Sensitivity of plasmon response to size, shape, and metal composition.* Journal of Physical Chemistry B, 2006. **110**: p. 19220-19225.

7.   Eustis, S. and M.A. El-Sayed, *Why gold nanoparticles are more precious than pretty gold: Noble metal surface plasmon resonance and its enhancement of the radiative and nonradiative properties of nanocrystals of different shapes.* Chemical Society Reviews, 2006. **35**(3): p. 209-217.

8.   Venkataramani, S., K.M. Davitt, J.Y. Zhang, H. Xu, Y.K. Song, B.W. Connors, and A.V. Nurmikko, *Compact semiconductor light-emitting diodes for dynamic imaging of neuronal circuitry.* Ieee Journal of Selected Topics in Quantum Electronics, 2005. **11**(4): p. 785-790.

9.   Zhang, J.Y., T. Atay, and A.V. Nurmikko, *Optical Detection of Brain Cell Activity Using Plasmonic Gold Nanoparticles.* Nano Letters, 2009. **9**(2): p. 519-524.

10.   Jain, P.K., X.H. Huang, I.H. El-Sayed, and M.A. El-Sayed, *Noble Metals on the Nanoscale: Optical and Photothermal Properties and Some Applications in Imaging, Sensing, Biology, and Medicine.* Accounts of Chemical Research, 2008. **41**(12): p. 1578-1586.

11.   Novo, C. and P. Mulvaney, *Charge-induced Rayleigh instabilities in small gold rods.* Nano Letters, 2007. **7**(2): p. 520-524.

12.   Toyota, A., N. Nakashima, and T. Sagara, *UV-visible transmission-absorption spectral study of Au nanoparticles on a*

modified ITO electrode at constant potentials and under potential modulation. Journal of Electroanalytical Chemistry, 2004. **565**(2): p. 335-342.

13. Lippert, M.T., K. Takagaki, W.F. Xu, X.Y. Huang, and J.Y. Wu, *Methods for voltage-sensitive dye imaging of rat cortical activity with high signal-to-noise ratio.* Journal of Neurophysiology, 2007. **98**(1): p. 502-512.

14. Chemla, S. and F. Chavane, *Voltage-sensitive dye imaging: Technique review and models.* Journal of Physiology-Paris, 2010. **104**(1-2): p. 40-50.

15. Miyazaki, T., R. Hasegawa, H. Yamaguchi, H. Oh-Oka, H. Nagato, I. Amemiya, and S. Uchikoga, *Electrical Control of Plasmon Resonance of Gold Nanoparticles Using Electrochemical Oxidation.* Journal of Physical Chemistry C, 2009. **113**(19): p. 8484-8490.

16. Wang, T.J. and C.W. Hsieh, *Surface plasmon resonance biosensor based on electro-optically modulated phase detection.* Optics Letters, 2007. **32**: p. 2834-2836.

17. Odom, T.W. and C.L. Nehl, *How gold nanoparticles have stayed in the light: The 3M's principle.* Acs Nano, 2008. **2**(4): p. 612-616.

18. Leong, H.S., J.P. Guo, R.G. Lindquist, and Q.H. Liu, *Surface plasmon resonance in nanostructured metal films under the Kretschmann configuration.* Journal of Applied Physics, 2009. **106**(12).

19. Willets, K.A. and R.P. Van Duyne, *Localized surface plasmon resonance spectroscopy and sensing.* Annual Review of Physical Chemistry, 2007. **58**: p. 267-297.

20. Englebienne, P., A. Van Hoonacker, and M. Verhas, *Surface plasmon resonance: principles, methods and applications in biomedical sciences.* Spectroscopy-an International Journal, 2003. **17**(2-3): p. 255-273.

21. Sepulveda, B., P.C. Angelome, L.M. Lechuga, and L.M. Liz-Marzan, *LSPR-based nanobiosensors.* Nano Today, 2009. **4**(3): p. 244-251.

22. Jiang, Z.L., S.J. Sun, A.H. Liang, and C.J. Liu, *A new immune resonance scattering spectral assay for trace fibrinogen with gold nanoparticle label.* Analytica Chimica Acta, 2006. **571**(2): p. 200-205.

23. J.Tudos, A. and R.B.M. Schasfoort, *Introduction to surface plasmon resonance*, in *Handbook of surface plasmon resonance* R.B.M. Schasfoort and A.J. Tudos, Editors. 2008, RSC Publishing: Cambridge. p. 1-13.

24. P.H.Kooyman, R., *Physics of surface plasmon resonance*, in *Handbook of surface plasmon resonance* R. B.M.Schasfoort and A.J. Tudos, Editors. 2008, RSC Publishing: Cambridge. p. 15-31.

25. Homola, J., S.S. Yee, and G. Gauglitz, *Surface plasmon resonance sensors: review.* Sensors and Actuators B-Chemical, 1999. **54**(1-2): p. 3-15.

26. Barnes, W.L., A. Dereux, and T.W. Ebbesen, *Surface plasmon subwavelength optics.* Nature, 2003. **424**(6950): p. 824-830.

27. Homola, J., *Electromagnetic theory of surface plasmons*, in *Surfae plasmon resonance based sensors*, O.S. Wolfbeis and J.Homola, Editors. 2006, Springer: Berlin. p. 3-44.

28. Noguez, C., *Surface plasmons on metal nanoparticles: The influence of shpae and physical environment.* Journal of Physical Chemistry C, 2007. **111**: p. 3806-3819.

29. Kelly, K.L., E. Coronado, L.L. Zhao, and G.C. Schatz, *The optical properties of metal nanoparticles: The influence of size, shape, and dielectric environment.* Journal of Physical Chemistry B, 2003. **107**(3): p. 668-677.

30. Xiao, M.F., *Competing intra- and inter-band transitions in quantum dots as manifested in optical absorption spectra.* Physics Letters A, 2001. **288**(1): p. 37-40.

31. Beversluis, M.R., A. Bouhelier, and L. Novotny, *Continuum generation from single gold nanostructures through near-field mediated intraband transitions.* Physical Review B, 2003. **68**(11).

32. Hopkins, P.E., *Effects of electron-boundary scattering on changes in thermoreflectance in thin metal films undergoing intraband excitations.* Journal of Applied Physics, 2009. **105**(9).

33. Qu, S.L., Y.W. Zhang, H.J. Li, J.R. Qiu, and C.S. Zhu, *Nanosecond nonlinear absorption in Au and Ag nanoparticles precipitated glasses induced by a femtosecond laser.* Optical Materials, 2006. **28**(3): p. 259-265.

34. Pawlik, S., M. Bauer, and M. Aeschlimann, *Lifetime difference of photoexcited electrons between intraband and interband transitions.* Surface Science, 1997. **377**(1-3): p. 206-209.

35. Charles, K. Eighth ed. Introduction to Solid State Physics. 2005: John Wiley & Sons.Inc.

36. Ball, D.W., *Rayleigh and Raman scattering.* Spectroscopy, 2001. **16**(2): p. 28-30.

37. Hecht, E. Fourth ed. Optics. 2002: Addison Wesley.

38. Zijlstra, P., J.W.M. Chon, and M. Gu, *Five-dimensional optical recording mediated by surface plasmons in gold nanorods.* Nature, 2009. **459**(7245): p. 410-413.

39. Khlebtsov, N.G. and L.A. Dykman, *Optical properties and biomedical applications of plasmonic nanoparticles.* Journal of Quantitative Spectroscopy & Radiative Transfer, 2010. **111**(1): p. 1-35.

40. Sharma, V., K. Park, and M. Srinivasarao, *Colloidal dispersion of gold nanorods: Historical background, optical properties, seed-mediated synthesis, shape separation and self-assembly.* Materials Science & Engineering R-Reports, 2009. **65**(1-3): p. 1-38.

41. Link, S., M.B. Mohamed, and M.A. El-Sayed, *Simulation of the optical absorption spectra of gold nanorods as a function of their aspect ratio and the effect of the medium dielectric constant.* Journal of Physical

Chemistry B, 1999. **103**(16): p. 3073-3077.

42. Link, S., M.A. El-Sayed, and M.B. Mohamed, *Simulation of the optical absorption spectra of gold nanorods as a function of their aspect ratio and the effect of the medium dielectric constant (vol 103B, pg 3073, 1999).* Journal of Physical Chemistry B, 2005. **109**(20): p. 10531-10532.

43. Brioude, A., X.C. Jiang, and M.P. Pileni, *Optical properties of gold nanorods: DDA simulations supported by experiments.* Journal of Physical Chemistry B, 2005. **109**(27): p. 13138-13142.

44. Haynes, C.L. and R.P. Van Duyne, *Nanosphere lithography: A versatile nanofabrication tool for studies of size-dependent nanoparticle optics.* Journal of Physical Chemistry B, 2001. **105**(24): p. 5599-5611.

45. Chen, C.D., S.F. Cheng, L.K. Chau, and C.R.C. Wang, *Sensing capability of the localized surface plasmon resonance of gold nanorods.* Biosensors & Bioelectronics, 2007. **22**(6): p. 926-932.

46. Zhao, J., X.Y. Zhang, C.R. Yonzon, A.J. Haes, and R.P. Van Duyne, *Localized surface plasmon resonance biosensors.* Nanomedicine, 2006. **1**(2): p. 219-228.

47. Miller, M.M. and A.A. Lazarides, *Sensitivity of metal nanoparticle surface plasmon resonance to the dielectric environment.* Journal of Physical Chemistry B, 2005. **109**(46): p. 21556-21565.

48. Miller, M.M. and A.A. Lazarides, *Sensitivity of metal nanoparticle plasmon resonance band position to the dielectric environment as observed in scattering.* Journal of Optics a-Pure and Applied Optics, 2006. **8**(4): p. S239-S249.

49. Chen, H.J., L. Shao, K.C. Woo, T. Ming, H.Q. Lin, and J.F. Wang, *Shape-Dependent Refractive Index Sensitivities of Gold Nanocrystals with the Same Plasmon Resonance Wavelength.* Journal of Physical Chemistry C, 2009. **113**(41): p. 17691-17697.

50. Chen, H.J., X.S. Kou, Z. Yang, W.H. Ni, and J.F. Wang, *Shape- and size-dependent refractive index sensitivity of gold nanoparticles.* Langmuir, 2008. **24**(10): p. 5233-5237.

51. Jain, P.K. and M.A. El-Sayed, *Noble Metal Nanoparticle Pairs: Effect of Medium for Enhanced Nanosensing.* Nano Letters, 2008. **8**(12): p. 4347-4352.

52. Burda, C., X.B. Chen, R. Narayanan, and M.A. El-Sayed, *Chemistry and properties of nanocrystals of different shapes.* Chemical Reviews, 2005. **105**: p. 1025-1102.

53. Grand, J., M.L. de la Chapelle, J.L. Bijeon, P.M. Adam, A. Vial, and P. Royer, *Role of localized surface plasmons in surface-enhanced Raman scattering of shape-controlled metallic particles in regular arrays.* Physical Review B, 2005. **72**(3).

54. Kolb, D.M., *Electrochemical surface science.* Angewandte Chemie-International Edition, 2001. **40**(7): p. 1162-1181.

55. Ritchie, I.M., S. Bailey, and R. Woods, *The metal-solution interface.* Advances in Colloid and Interface Science, 1999. **80**(3): p. 183-231.

56. Jory, M.J., G.W. Bradberry, P.S. Cann, and J.R. Sambles, *Surface-plasmon opto-electrochemistry.* Sensors and Actuators B-Chemical, 1996. **35**(1-3): p. 197-201.

57. McIntyre, J.D., *ELECTROCHEMICAL MODULATION SPECTROSCOPY.* Surface Science, 1973. **37**(1): p. 658-682.

58. Gordon Ii, J.G. and S. Ernst, *Surface plasmons as a probe of the electrochemical interface.* Surface Science, 1980. **101**(1-3): p. 499-506.

59. Tadjeddine, A., *INFLUENCE OF THE ELECTRICAL-POLARIZATION ON THE SURFACE-PLASMON DISPERSION AT METAL-ELECTROLYTE INTERFACES.* Electrochimica Acta, 1989. **34**(1): p. 29-33.

60. Iwasaki, Y., T. Horiuchi, M. Morita, and O. Niwa, *Analysis of electrochemical processes using surface plasmon resonance.* Sensors and Actuators B-Chemical, 1998. **50**(2): p. 145-148.

61. Lioubimov, V., A. Kolomenskii, A. Mershin, D.V. Nanopoulos, and H.A. Schuessler, *Effect of varying electric potential on surface-plasmon resonance sensing.* Applied Optics, 2004. **43**(17): p. 3426-3432.

62. Ung, T., M. Giersig, D. Dunstan, and P. Mulvaney, *Spectroelectrochemistry of colloidal silver.* Langmuir, 1997. **13**(6): p. 1773-1782.

63. Qu, X.H., Z.Q. Peng, X. Jiang, and S.J. Dong, *Surface charge influence on the surface plasmon absorbance of electroactive thiol-protected gold nanoparticles.* Langmuir, 2004. **20**: p. 2519-2522.

64. Chapman, R. and P. Mulvaney, *Electro-optical shifts in silver nanoparticle films.* Chemical Physics Letters, 2001. **349**(5-6): p. 358-362.

65. Daniels, J.K. and G. Chumanov, *Spectroelectrochemical studies of plasmon coupled silver nanoparticles.* Journal of Electroanalytical Chemistry, 2005. **575**(2): p. 203-209.

66. Toyota, A. and T. Sagara, *Particle size dependence of the charging of Au nanoparticles immobilized on a modified ITO electrode.* Electrochimica Acta, 2008. **53**(5): p. 2553-2559.

67. Mulvaney, P., J. Perez-Juste, M. Giersig, L.M. Liz-Marzan, and C. Pecharroman, *Drastic surface plasmon mode shifts in gold nanorods due to electron charging.* Plasmonics, 2006. **1**: p. 61-66.

68. Novo, C., A.M. Funston, and P. Mulvaney, *Direct observation of chemical reactions on single gold nanocrystals using surface plasmon spectroscopy.* Nature Nanotechnology, 2008. **3**(10): p. 598-602.

69. Toyota, A. and T. Sagara, *Time dependent spectral change upon potential step perturbation for Au nanoparticles immobilized on an organic monolayer-modified ITO electrode.* Colloids and Surfaces a-Physicochemical and Engineering Aspects, 2006. **286**(1-3): p. 62-69.

70. van Dijk, M.A., A.L. Tchebotareva, M. Orrit, M. Lippitz, S. Berciaud, D. Lasne, L. Cognet, and B. Lounis, *Absorption and scattering microscopy of single metal nanoparticles.* Physical Chemistry Chemical Physics, 2006. **8**(30): p. 3486-3495.

71. Sardar, R., A.M. Funston, P. Mulvaney, and R.W. Murray, *Gold Nanoparticles: Past, Present, and Future.* Langmuir, 2009. **25**(24): p. 13840-13851.

72. Sonnichsen, C., S. Geier, N.E. Hecker, G. von Plessen, J. Feldmann, H. Ditlbacher, B. Lamprecht, J.R. Krenn, F.R. Aussenegg, V.Z.H. Chan, J.P. Spatz, and M. Moller, *Spectroscopy of single metallic nanoparticles using total internal reflection microscopy.* Applied Physics Letters, 2000. **77**(19): p. 2949-2951.

73. Cognet, L., C. Tardin, D. Boyer, D. Choquet, P. Tamarat, and B. Lounis, *Single metallic nanoparticle imaging for protein detection in cells.* Proceedings of the National Academy of Sciences of the United States of America, 2003. **100**(20): p. 11350-11355.

74. Van Duyne, R.P., A.J. Haes, and A.D. McFarland, *Nanoparticle optics: sensing with nanoparticle arrays and single nanoparticles.* Physical Chemistry of Interfaces and Nanomaterials Ii, 2003. **5223**: p. 197-207.

75. Novo, C., A.M. Funston, A.K. Gooding, and P. Mulvaney, *Electrochemical Charging of Single Gold Nanorods.* Journal of the American Chemical Society, 2009. **131**(41): p. 14664-14666.

76. Stuart, D.A., A.J. Haes, C.R. Yonzon, E.M. Hicks, and R.P. Van Duyne, *Biological applications of localised surface plasmonic phenomenae.* IEE Proceedings Nanobiotechnology, 2005. **152**(1): p. 13-32.

77. Yu, C.X. and J. Irudayaraj, *Multiplex biosensor using gold nanorods.* Analytical Chemistry, 2007. **79**(2): p. 572-579.

78. Zabet-Khosousi, A. and A.A. Dhirani, *Charge transport in nanoparticle assemblies.* Chemical Reviews, 2008. **108**(10): p. 4072-4124.

79. Scaffardi, L.B., N. Pellegri, O. de Sanctis, and J.O. Tocho, *Sizing gold nanoparticles by optical extinction spectroscopy.* Nanotechnology, 2005. **16**(1): p. 158-163.

80. Haes, A.J., S.L. Zou, J. Zhao, G.C. Schatz, and R.P. Van Duyne, *Localized surface plasmon resonance spectroscopy near molecular resonances.* Journal of the American Chemical Society, 2006. **128**(33): p. 10905-10914.

81. Curry, A., G. Nusz, A. Chilkoti, and A. Wax, *Substrate effect on refractive index dependence of plasmon resonance for individual silver nanoparticles observed using darkfield micro-spectroscopy.* Optics Express, 2005. **13**(7): p. 2668-2677.

82. Del Fatti, N., D. Christofilos, and F. Vallee, *Optical response of a single gold nanoparticle.* Gold Bulletin, 2008. **41**(2): p. 147-158.

83. Su, H.M., Y.S. Li, X.Y. Li, and K.S. Wong, *Optical and electrical properties of Au nanoparticles in two-dimensional networks: an*

effective cluster model. Optics Express, 2009. **17**(24): p. 22223-22234.

84.   Doron-Mor, I., Z. Barkay, N. Filip-Granit, A. Vaskevich, and I. Rubinstein, *Ultrathin gold island films on silanized glass. Morphology and optical properties.* Chemistry of Materials, 2004. **16**(18): p. 3476-3483.

85.   F.Bohren, C. and D.R. Huffman. Absorption and Scattering of Light by Small Particles. 1983, New York: John Wiley & Sons, Inc. .

86.   Szczyrbowski, J., *A NEW SIMPLE METHOD OF DETERMINING THE EFFECTIVE MASS OF AN ELECTRON OR THE THICKNESS OF THIN METAL-FILMS.* Journal of Physics D-Applied Physics, 1986. **19**(7): p. 1257-1263.

87.   Hopkins, P.E., *Contributions of Inter- and Intraband Excitations to Electron Heat Capacity and Electron-Phonon Coupling in Noble Metals.* Journal of Heat Transfer-Transactions of the Asme, 2010. **132**(1).

88.   Johnson, P.B. and R.W. Christy, *OPTICAL-CONSTANTS OF NOBLE-METALS.* Physical Review B, 1972. **6**(12): p. 4370-4379.

89.   Hohlfeld, J., S.S. Wellershoff, J. Gudde, U. Conrad, V. Jahnke, and E. Matthias, *Electron and lattice dynamics following optical excitation of metals.* Chemical Physics, 2000. **251**(1-3): p. 237-258.

90.   Alvarez, M.M., J.T. Khoury, T.G. Schaaff, M.N. Shafigullin, I. Vezmar, and R.L. Whetten, *Optical absorption spectra of nanocrystal gold molecules.* Journal of Physical Chemistry B, 1997. **101**(19): p. 3706-3712.

91.   Vial, A., A.S. Grimault, D. Macias, D. Barchiesi, and M.L. de la Chapelle, *Improved analytical fit of gold dispersion: Application to the modeling of extinction spectra with a finite-difference time-domain method.* Physical Review B, 2005. **71**(8).

92.   Link, S. and M.A. El-Sayed, *Shape and size dependence of radiative, non-radiative and photothermal properties of gold nanocrystals.* International Reviews in Physical Chemistry, 2000. **19**(3): p. 409-453.

93.   Sonnichsen, C., T. Franzl, T. Wilk, G. von Plessen, J. Feldmann, O. Wilson, and P. Mulvaney, *Drastic reduction of plasmon damping in gold nanorods.* Physical Review Letters, 2002. **88**(7).

94.   Coronado, E.A. and G.C. Schatz, *Surface plasmon broadening for arbitrary shape nanoparticles: A geometrical probability approach.* Journal of Chemical Physics, 2003. **119**(7): p. 3926-3934.

95.   Mark, C.B., K. Doh-Y, and H.N. M, *The mechanism of gold deposition by thermal evaporation.* Journal of Ceramic Processing Research, 2000. **1**: p. 45-52.

96.   Zhang, S., L. Berguiga, J. Elezgaray, T. Roland, C. Faivre-Moskalenko, and F. Argoul, *Surface plasmon resonance characterization of thermally evaporated thin gold films.* Surface Science, 2007. **601**(23): p. 5445-5458.

97.   Xu, G., M. Tazawa, P. Jin, and S. Nakao, *Surface plasmon resonance of sputtered Ag films: substrate and mass thickness dependence.* Applied Physics a-Materials Science & Processing, 2005. **80**(7): p. 1535-1540.

98.   Gao, L., L.P. Gu, and Y.Y. Huang, *Effective medium approximation for optical bistability in nonlinear metal-dielectric composites.* Solid State Communications, 2004. **129**(9): p. 593-598.

99.   V.S.BAGOTSKY. Fundamentals of electrochemistry. 2006: John Wiley & Sons.Inc.

100.   Oldham, K.B., *A Gouy-Chapman-Stern model of the double layer at a (metal)/(ionic liquid) interface.* Journal of Electroanalytical Chemistry, 2008. **613**(2): p. 131-138.

101.   Bohinc, K., V. Kralj-Iglic, and A. Iglic, *Thickness of electrical double layer. Effect of ion size.* Electrochimica Acta, 2001. **46**(19): p. 3033-3040.

102.   Lamperski, S. and C.W. Outhwaite, *Differential capacitance of the solvent primitive model diffuse layer using the inhomogeneous Poisson-Boltzmann theory with an exclusion volume term.* Journal of Electroanalytical Chemistry, 2004. **567**(2): p. 263-267.

103.   Allen, J.B. and R.F. Larry. Second ed. Electrochemical Methods: Fundamentals and Applications 2001, New York: John Wiley & Sons, Inc. .

104.   H.Hamman, C., A. Hamnett, and W. Vielstich. Electrochemistry. 2007, Weinheim: Wiley-VCH.

105.   di Caprio, D., Z. Borkowska, and J. Stafiej, *Simple extension of the Gouy-Chapman theory including hard sphere effects. Diffuse layer contribution to the differential capacity curves for the electrode vertical bar electrolyte interface.* Journal of Electroanalytical Chemistry, 2003. **540**: p. 17-23.

106.   Mönch, W. Third ed. Semiconductor surface and interfaces. 2001, Berlin: Springer.

107.   Stephen, E. The physics and chemistry of solids. 1998, New York: John Wiley & Sons Ltd,.

108.   Novo, C., D. Gomez, J. Perez-Juste, Z.Y. Zhang, H. Petrova, M. Reismann, P. Mulvaney, and G.V. Hartland, *Contributions from radiation damping and surface scattering to the linewidth of the longitudinal plasmon band of gold nanorods: a single particle study.* Physical Chemistry Chemical Physics, 2006. **8**(30): p. 3540-3546.

109.   Hu, M., C. Novo, A. Funston, H.N. Wang, H. Staleva, S.L. Zou, P. Mulvaney, Y.N. Xia, and G.V. Hartland, *Dark-field microscopy studies of single metal nanoparticles: understanding the factors that influence the linewidth of the localized surface plasmon resonance.* Journal of Materials Chemistry, 2008. **18**(17): p. 1949-1960.

110.   Ali, A.H. and C.A. Foss, *Electrochemically induced shifts in the plasmon resonance bands of nanoscopic gold particles adsorbed on*

transparent electrodes. Journal of the Electrochemical Society, 1999. **146**(2): p. 628-636.

111. Muskens, O.L., P. Billaud, M. Broyer, N. Fatti, and F. Vallee, *Optical extinction spectrum of a single metal nanoparticle: Quantitative characterization of a particle and of its local environment.* Physical Review B, 2008. **78**(20).

112. B.Murphy, D. Fundamentals of light microscopy and electronic imaging. 2001, New York: John Wiley & Sons,Inc.

113. Pawley, J. Third ed. The Handbook of Biological Confocal Microscopy. 2006, New York: Springer Science+Busness Media,LLC.

114. Braslavsky, I., R. Amit, B.M.J. Ali, O. Gileadi, A. Oppenheim, and J. Stavans, *Objective-type dark-field illumination for scattering from microbeads.* Applied Optics, 2001. **40**(31): p. 5650-5657.

115. Stout, A.L. and D. Axelrod, *EVANESCENT FIELD EXCITATION OF FLUORESCENCE BY EPI-ILLUMINATION MICROSCOPY.* Applied Optics, 1989. **28**(24): p. 5237-5242.

116. Mock, J.J., D.R. Smith, and S. Schultz, *Local refractive index dependence of plasmon resonance spectra from individual nanoparticles.* Nano Letters, 2003. **3**: p. 485-491.

117. Riboh, J.C., A.J. Haes, A.D. McFarland, C.R. Yonzon, and R.P. Van Duyne, *A nanoscale optical biosensor: Real-time immunoassay in physiological buffer enabled by improved nanoparticle adhesion.* Journal of Physical Chemistry B, 2003. **107**(8): p. 1772-1780.

118. Curry, A., W.L. Hwang, and A. Wax, *Epi-illumination through the microscope objective applied to darkfield imaging and microspectroscopy of nanoparticle interaction with cells in culture.* Optics Express, 2006. **14**(14): p. 6535-6542.

119. Hulteen, J.C., D.A. Treichel, M.T. Smith, M.L. Duval, T.R. Jensen, and R.P. Van Duyne, *Nanosphere lithography: Size-tunable silver nanoparticle and surface cluster arrays.* Journal of Physical Chemistry B, 1999. **103**(19): p. 3854-3863.

120. Hulteen, J.C. and R.P. Vanduyne, *NANOSPHERE LITHOGRAPHY - A MATERIALS GENERAL FABRICATION PROCESS FOR PERIODIC PARTICLE ARRAY SURFACES.* Journal of Vacuum Science & Technology a-Vacuum Surfaces and Films, 1995. **13**(3): p. 1553-1558.

121. Fajac, I., J. Lacronique, A. Lockhart, J. Dall'Ava-Santucci, and D.J. Dusser, *Silver/silver chloride electrodes for measurement of potential difference in human bronchi.* Thorax, 1998. **53**(10): p. 879-881.

122. Yu, P.G. and S.J. Dong, *The fabrication and performance of an Ag/AgCl reference electrode in human serum.* Analytica Chimica Acta, 1996. **330**(2-3): p. 167-174.

123. Cieslak, W.R. and F.M. Delnick, *THE FABRICATION AND PERFORMANCE OF A AG/AGCL REFERENCE ELECTRODE IN THIONYL CHLORIDE ELECTROLYTE.* Journal of the Electrochemical

Society, 1987. **134**(1): p. 132-134.

124. Hassel, A.W., K. Fushimi, and M. Seo, *An agar-based silver vertical bar silver chloride reference electrode for use in micro-electrochemistry.* Electrochemistry Communications, 1999. **1**(5): p. 180-183.

125. Inamdar, S.N., M.A. Bhat, and S.K. Haram, *Construction of Ag/AgCl Reference Electrode from Used Felt-Tipped Pen Barrel for Undergraduate Laboratory.* Journal of Chemical Education, 2009. **86**(3): p. 355-356.

126. Lockett, V., R. Sedev, J. Ralston, M. Horne, and T. Rodopoulos, *Differential capacitance of the electrical double layer in imidazolium-based ionic liquids: Influence of potential, cation size, and temperature.* Journal of Physical Chemistry C, 2008. **112**(19): p. 7486-7495.

127. Bally, M., M. Halter, J. Voros, and H.M. Grandin, *Optical microarray biosensing techniques.* Surface and Interface Analysis, 2006. **38**(11): p. 1442-1458.

128. Bardin, F., A. Bellemain, G. Roger, and M. Canva, *Surface plasmon resonance spectro-imaging sensor for biomolecular surface interaction characterization.* Biosensors & Bioelectronics, 2009. **24**(7): p. 2100-2105.

129. Ho, H.P., C.L. Wong, K.S. Chan, S.Y. Wu, and C.L. Lin, *Application of two-dimensional spectral surface plasmon resonance to imaging of pressure distribution in elastohydrodynamic lubricant films.* Applied Optics, 2006. **45**(23): p. 5819-5826.

130. Wong, C.L., H.P. Ho, Y.K. Suen, S.K. Kong, Q.L. Chen, W. Yuan, and S.Y. Wu, *Real-time protein biosensor arrays based on surface plasmon resonance differential phase imaging.* Biosensors & Bioelectronics, 2008. **24**(4): p. 606-612.

131. Toyama, S., O. Takei, M. Tsuge, R. Usami, K. Horikoshi, and S. Kato, *Surface plasmon resonance of electrochemically deposited Au-black.* Electrochemistry Communications, 2002. **4**(7): p. 540-544.

132. Panta, Y.M., J. Liu, M.A. Cheney, S.W. Joo, and S.Z. Qian, *Ultrasensitive detection of mercury (II) ions using electrochemical surface plasmon resonance with magneto hydrodynamic convection.* Journal of Colloid and Interface Science, 2009. **333**(2): p. 485-490.

133. Zhang, N., R. Schweiss, Y. Zong, and W. Knoll, *Electrochemical surface plasmon spectroscopy - Recent developments and applications.* Electrochimica Acta, 2007. **52**(8): p. 2869-2875.

134. R.M.A, A. and B. N.M. Ellipsometry and polarized light. 1987, Amsterdam: Elsevier

135. Garland, J.E., K.A. Assiongbon, C.M. Pettit, and D. Roy, *Surface plasmon resonance transients at an electrochemical interface: time resolved measurements using a bicell photodiode.* Analytica Chimica Acta, 2003. **475**(1-2): p. 47-58.

136. Janesick, J.R. Photon Transfer: DN -λ. 2007, Washionton: SPIE

137. Pajkossy, T., T. Wandlowski, and D.M. Kolb, *Impedance aspects of anion adsorption on gold single crystal electrodes.* Journal of Electroanalytical Chemistry, 1996. **414**(2): p. 209-220.

138. Pajkossy, T. and D.M. Kolb, *Double layer capacitance of the platinum group metals in the double layer region.* Electrochemistry Communications, 2007. **9**(5): p. 1171-1174.

139. Matsumura, H. and K. Furusawa, *Phospholipid membranes*, in *Electrical phenomena at interfaces: fundamentals, measurements, and applications*, H. Ohshima and K. Furusawa, Editors. 1998, Marcel Dekker, Inc. p. 531-532.

140. Kooij, E.S. and B. Poelsema, *Shape and size effects in the optical properties of metallic nanorods.* Physical Chemistry Chemical Physics, 2006. **8**(28): p. 3349-3357.

141. Horvath, H., *Gustav Mie and the scattering and absorption of light by particles: Historic developments and basics.* Journal of Quantitative Spectroscopy & Radiative Transfer, 2009. **110**(11): p. 787-799.

142. Zhu, J., *Shape dependent full width at half maximum of the absorption band in gold nanorods.* Physics Letters A, 2005. **339**(6): p. 466-471.

143. Qiu, L., T.A. Larson, D.K. Smith, E. Vitkin, S.H. Zhang, M.D. Modell, I. Itzkan, E.B. Hanlon, B.A. Korgel, K.V. Sokolov, and L.T. Perelman, *Single gold nanorod detection using confocal light absorption and scattering spectroscopy.* Ieee Journal of Selected Topics in Quantum Electronics, 2007. **13**(6): p. 1730-1738.

144. van de Hulst, H.C. Light scattering by small particles 1981, New York: John Wiley & Sons,Inc.

145. Christian, M.; Available from: http://arrc.ou.edu/~rockee/NRA_2007_website/Mie-scattering-Matlab.pdf.

146. Nanopartz. Available from: http://www.nanopartz.com/index.htm.

147. SPI. Available from: http://www.2spi.com/catalog/standards/ITO-coated-substrates-refractive-index-values.html.

148. van der Zande, B.M.I., M.R. Bohmer, L.G.J. Fokkink, and C. Schonenberger, *Colloidal dispersions of gold rods: Synthesis and optical properties.* Langmuir, 2000. **16**(2): p. 451-458.

149. Muskens, O.L., G. Bachelier, N. Del Fatti, F. Vallee, A. Brioude, X.C. Jiang, and M.P. Pileni, *Quantitative absorption spectroscopy of a single gold nanorod.* Journal of Physical Chemistry C, 2008. **112**(24): p. 8917-8921.

150. Murray, W.A., B. Auguie, and W.L. Barnes, *Sensitivity of Localized Surface Plasmon Resonances to Bulk and Local Changes in the Optical Environment.* Journal of Physical Chemistry C, 2009. **113**(13): p. 5120-5125.

151. Jain, P.K. and M.A. Ei-Sayed, *Surface plasmon resonance sensitivity of metal nanostructures: Physical basis and universal scaling in metal nanoshells.* Journal of Physical Chemistry C, 2007. **111**: p. 17451-17454.

152. Tabor, C., R. Murali, M. Mahmoud, and M.A. El-Sayed, *On the Use of Plasmonic Nanoparticle Pairs As a Plasmon Ruler: The Dependence of the Near-Field Dipole Plasmon Coupling on Nanoparticle Size and Shape.* Journal of Physical Chemistry A, 2009. **113**(10): p. 1946-1953.

153. Haes, A.J., S.L. Zou, G.C. Schatz, and R.P. Van Duyne, *A nanoscale optical biosensor: The long range distance dependence of the localized surface plasmon resonance of noble metal nanoparticles.* Journal of Physical Chemistry B, 2004. **108**: p. 109-116.